MASS ESTIMATION, DYNAMICS AND FEEDBACK IN GALAXY GROUPS

RICHARD JOHN PEARSON

A thesis submitted to the
University of Birmingham
for the degree of
DOCTOR OF PHILOSOPHY

Astrophysics and Space Research
School of Physics and Astronomy
College of Engineering and Physical Sciences
University of Birmingham
November 2014

STATEMENT OF ORIGINALITY

The contents of this thesis are original work produced by the author. Any non-original content has been referenced throughout.

Chapters 1 and 2 constitute review chapters whereby literature results and methodologies have been summarised with sources listed at all times.

Chapter 3 is based on a paper submitted to the Monthly Notices of the Royal Astronomical Society. I wrote the paper with collaborative input into the interpretation from Trevor Ponman and, at later stages, other co-authors, Peder Norberg, Aaron Robotham and Will Farr. I note that paragraph five of Section 3.4.1 was contributed by Will Farr, who also provided substantial assistance throughout that section. Modifications from the submitted manuscript are to improve readability, formatting and address examiners comments. The data used in this chapter are either available from survey data (Sloan Digital Sky Survey) and from the literature [Sun et al., 2009], or made available for use by Peder Norberg and Aaron Robotham. The analysis of this data, with the exception of the development and testing of the generative model fitting (again, Section 3.4.1) by Will Farr, was performed by me.

Chapter 4 is derived from a manuscript currently in preparation with input in the interpretation from Trevor Ponman, but is yet to be distributed to other co-authors. Data used in this chapter were either acquired specifically for this work by the *Chandra* X-ray observatory, drawn from the *Chandra* archive, or were made available for use by Peder Norberg and Aaron Robotham. Equation (4.1) was provided by Aaron Robotham. The OWLS entropy ranges in Figure 4.5 are based on results provided by Ian McCarthy. Additional work for determining

the feasibility of X-ray observation targets, such as final exposure times, was performed by Alastair Sanderson and Ewan O'Sullivan.

Chapter 5 is based upon a large collaborative project, the Galaxy Cluster Mass Reconstruction project. The mock data used in this chapter was provided by the project leads, Lyndsay Old and Frazer Pearce. The results discussed are original output for the methods described in this thesis, with assistance in the interpretation from Trevor Ponman.

The analysis described in this work uses standard tools such as the R statistical package and the CIAO and SHERPA tools for X-ray analysis. When required I implement methods described in the literature to perform our analysis, referencing the original method description. I additionally make use of tools developed by Alastair Sanderson and Aurelia Pascut for the reduction and analysis of X-ray data.

ABSTRACT

Accurate mass estimates for galaxy groups and clusters are important for understanding the evolution of matter within the universe. In this thesis we first discuss methods of mass estimation currently used within the literature, and introduce a set of scaling relations for mass estimation in cases where literature methods are not applicable. We find that methods based on group richness provide the best (i.e. lowest scatter) mass estimator.

Secondly, we study the impact of feedback on hot group gas for a sample of optically selected groups. We refine the group selection using their dynamical state, identified through substructure in the distribution of member galaxies. We find this sample to be underluminous compared to an X-ray selected sample. Furthermore, with two groups showing high 2σ lower limits on entropy, the population of high entropy groups predicted by hydrodynamical simulations may have been detected.

Finally, we combine measures of dynamical state and mass estimation scaling relations to understand how the presence of substructure can impact upon the ability to reliably estimate group and cluster masses. We find that substructure introduced through poor group identification has the largest effect on the quality of the final mass estimates.

To Mom and Dad

ACKNOWLEDGEMENTS

I would like to thank my parents and friends for their continued support and encouragement.

I would also like to thank the many past and present members of Birmingham's Extragalactic Research Group, as well as the many students of G26, for their assistance, guidance and merriment over the years. For their help in the early days, I would like to especially thank Alastair Sanderson, Aurelia Pascut and Paul May. For their support, friendship and the occasional welcome distraction during the challenging period as I conclude this work I would like to also thank Sarah Mulroy, Maggie Lieu and Melissa Gillone.

Thanks also go to David Stops for his tremendous skill for any computer related problems.

Finally, I would like to thank my supervisor, Trevor Ponman, for all his help, support and patience throughout. I have learnt a lot from him over the years, and am truly grateful. I wish him well on his recent retirement.

To everyone, once again, thank you.

Contents

List of Figures

List of Tables

Chapter 1

INTRODUCTION

Galaxy groups and clusters are the largest gravitationally bound structures in the Universe. Containing around half of all galaxies [Tully, 1987], they are excellent laboratories for understanding the formation, evolution and distribution of structure. An early example of their utility is the role that the dynamics and total light of cluster galaxies played when dark matter was first inferred [e.g. Zwicky, 1937], demonstrating that luminous matter makes up a small fraction of the Universe's matter content.

As measured by galaxy redshift surveys [e.g. 2dFGRS and SDSS, Colless et al., 2001; York et al., 2000], the distribution of galaxies has shown that they exist within the large scale structure of the Cosmic Web (e.g. Figure 1.1). Comparing the observed galaxy distribution to the dark matter structures produced in simulations such as the Millennium Simulation [Springel et al., 2005] have further improved our understanding of how these structures form — i.e. through the hierarchical, bottom-up assembly of dark matter halos. Group and cluster halos form at the nodes in the Cosmic Web, and grow through accretion of matter

falling in along connected filaments.

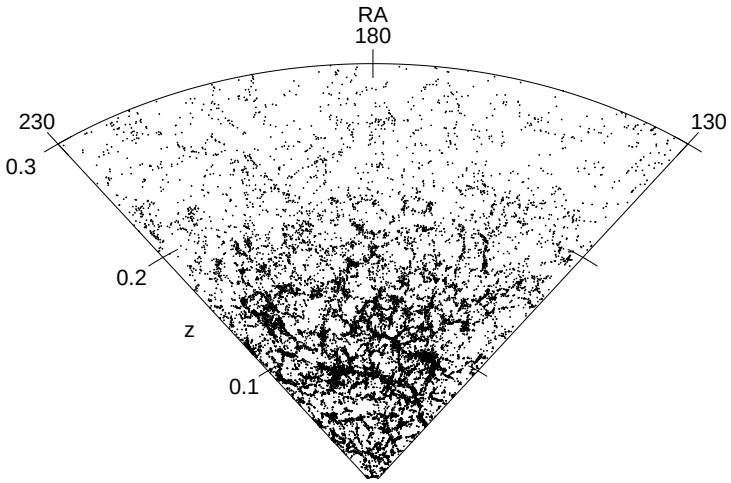

Figure 1.1: The Cosmic Web as observed by the Sloan Digital Sky Survey [York et al., 2000]. Galaxies were taken from the New York University Value Added Galaxy Catalogue [Blanton et al., 2005] with redshifts $z < 0.3$ and declination $|\delta| < 1\,\mathrm{deg}$.

Dark matter only interacts gravitationally with ordinary matter, and therefore observational constraints on the properties of the dark matter distribution can only be inferred from this gravitational influence on observable matter. This introduces the concept of a mass tracer, such as the galaxies within the halo, whose properties or distribution are influenced by the mass and distribution of the underlying dark matter halo. As the mass of a halo is a fundamental property of a group or cluster, knowledge of which is important for cosmology [e.g. the mass function of halos, Murray et al., 2013; Press and Schechter, 1974] and the study of group and cluster evolution [e.g. cosmic feedback and breaking of

self-similarity, Bower et al., 2006; McCarthy et al., 2010], understanding and estimating halo masses is important.

Current methods for mass estimation work best for large halos where the signal-to-noise is highest. In these large halos, non-gravitational effects and dynamical disturbances also have a reduced impact on their baryonic properties and masses estimated through such tracers. In low mass halos statistics can be poor and disturbances significant. Coupled with selection methods that can have various selection effects, it can be difficult to understand the properties of low mass halos.

The aim of this thesis is to understand how unbiased mass estimation can be extended to the scale of galaxy groups, and to understand how scatter in mass estimates can be linked to dynamical disturbances within groups and clusters. Additionally, we present a pilot study to illustrate an alternative to traditional, X-ray selection methods, using substructure to define a sample in which the effect of feedback on galaxy groups can be studied.

1.1 Galaxy Groups and Clusters

Optically, galaxy groups and clusters appear as a local excess, or overdensity, of galaxies. Groups and clusters vary in scale from radii of a few hundred kpc for the lowest mass groups with a few tens of galaxies ($\sim 10^{13}$ $M_{\odot}$) to several Mpc for the highest mass clusters which can contain thousands of galaxies ($\sim 10^{15}$ $M_{\odot}$).

A simple expectation is that groups and clusters scale in similar ways with mass (self-similarity, see Section 1.2), showing a smooth continuum of properties. This makes it difficult to split samples into groups and clusters. In studies that

aim to characterise the behaviour of groups and clusters it can sometimes be informative to broadly split a population, defining clusters to be objects above some appropriate limit such as halo mass (e.g. $M_{500} > 10^{14}$ $M_{\odot}$), or by gas properties such as temperature (e.g. $kT_{gas} > 2$ keV). We adopt a loose definition of the terms "group" and "cluster", using them to simply indicate the scale of objects, where groups are structures with masses of a few 10^{13} $M_{\odot}$, whilst galaxy clusters have masses of several 10^{14} $M_{\odot}$ and higher.

1.1.1 Formation

The galaxy groups and clusters we see today are believed to have grown from Gaussian density perturbations in the otherwise homogeneous matter distribution of the early universe [e.g. Press and Schechter, 1974; van de Weygaert and Bond, 2008]. Observationally we see these perturbations as small temperature variations on the Cosmic Microwave Background, corresponding to regions of slight matter overdensity and underdensity relative to the mean at the time of recombination. These overdensities will collapse through gravitational instability, forming dark matter halos. Hierarchical formation describes the collapse of the smallest halos first, later merging with larger structures as they collapse.

For a given initial perturbation, the simplest model describing the collapse of a halo is the spherical collapse model [e.g. van de Weygaert and Bond, 2008]. Briefly, in this model a spherical overdensity is embedded within a uniform density matter distribution. This sphere will expand linearly with the universe until it reaches some maximum extent and critical overdensity where its evolution becomes non-linear. At this point it separates from the Hubble flow (turnaround)

and begins to collapse into a relaxed halo.

As these halos collapse, baryonic matter is also accreted, ultimately forming stars and galaxies. As hierarchical formation continues, these baryons evolve with the halo through mergers and subsequent relaxation.

1.1.2 Contents

To understand the evolution of groups and clusters, it is important to understand their contents (dark matter, hot gas and stars/galaxies) and how this matter is distributed and evolves within the halo. In the following sections we will briefly cover these mass components, building to the concept of the baryon budget.

Dark Matter

Dark matter, as the name implies, is a form of matter that negligibly interacts electromagnetically (i.e. it neither absorbs nor emits electromagnetic radiation), and therefore is unobservable beyond its gravitational effects. However, from studies of the Cosmic Microwave Background (CMB) it is well established that dark matter also makes up $\sim 83.5\%$ of the universe's matter content [Hinshaw et al., 2013], with baryonic matter making up the remainder. Though the exact proportion of dark matter to baryons is subject to discussion [Giodini et al., 2009; Gonzalez et al., 2007; Sanderson et al., 2013], the majority of the mass within groups and clusters is similarly made up of dark matter.

Dark matter was first inferred on large, cluster scales by Zwicky [1937] whilst attempting to determine the mass of the Coma cluster of galaxies. The mass inferred from the luminous galaxies within the cluster was found to be substantially less than that determined from the dynamics of those galaxies. Though we

would now expect $\sim 10\%$ of the total mass to be contributed by hot intracluster gas [e.g. Sanderson et al., 2013] which was unknown at this time, the difference between dynamical mass and luminous mass implied that there was an unseen form of matter present within the potential well.

The dominance of this dark matter, and its simple gravitational interactions, have made it a fundamental component of cosmological simulations [e.g. Klypin et al., 2011; Springel et al., 2005]. By simulating the primordial distribution of dark matter as a distribution of N massive particles, the growth of structure through gravitational collapse can be modelled. Simulated predictions for the clustering of structures and the mass function can then be compared to observations, allowing cosmological models to be tested. Such N-body simulations have demonstrated that structures form following the hierarchical scenario [e.g. Springel et al., 2005]. This formation requires "cold" dark matter (i.e. non-relativistic), such that the initial perturbations are not smoothed out as would be seen in a "hot" (i.e. relativistic) dark matter universe.

In addition to predicting the large scale distribution of dark matter, studies of N-body simulations such as Navarro et al. [1996] have shown how dark matter is distributed within a halo. This is described by the Navarro-Frenk-White (NFW) density profile,

$$\rho = \frac{\rho_0}{\frac{r}{r_s}\left(1+\frac{r}{r_s}\right)^2} \quad , \tag{1.1}$$

where ρ_0 is a characteristic density and r_s is the scale radius. The scale radius is related to an overdensity radius such as r_{200} (the radius enclosing a mean density 200 times the critical density of the universe, ρ_c[1]) by the concentration

[1]The critical density at redshift z is $\rho_c(z) = 3H(z)^2/8\pi G$, where $H(z) = H_0\sqrt{\Omega_m(1+z)^3+\Omega_\Lambda} = H_0 E(z)$.

$c_{200} = r_{200}/r_s$. Dark matter halos have been found to follow this shape at all mass scales, though a mass dependency in the concentration is observed [see, e.g. Duffy et al., 2008]. As massive halos collapse at later times [van de Weygaert and Bond, 2008], this mass-concentration relation is likely due to the evolution of the density of the universe.

The increase in computing power over the last decade, as well as improvements in our understanding of the universe, have allowed simulations to grow significantly and to include baryonic physics on cosmological scales [e.g. the OverWhelmingly Large Simulations project, Schaye et al., 2010]. For dark matter N-body simulations improvements in mass resolutions have allowed smaller dark matter particles to be tracked throughout the simulation. For example, the Millennium Simulation [Springel et al., 2005], followed 10 billion particles of mass $\sim 8.6 \times 10^8\ h^{-1}\ \mathrm{M}_\odot$ within a cube with sides of length 500 h^{-1} Mpc (where $h = H_0/100$ km s^{-1} Mpc^{-1}). The more recent Bolshoi simulation [Klypin et al., 2011] followed only 8 billion particles in a smaller cube (250 h^{-1} Mpc), but tracked much smaller particles of $\sim 1.35 \times 10^8\ h^{-1}\ \mathrm{M}_\odot$.

These simulations allow the study of the formation and evolution of structure in the universe. As each dark matter particle is tracked, the merger history of simulated halos is easily obtained. Provided they can be simulated, this can be extended to testing models for the evolution of the baryonic component of the universe, simulating the formation of galaxies and evolution of cluster gas. Full hydrodynamic simulations can include the baryons as a further particle to trace. Though as baryon physics, such as gas cooling and star formation, are complicated processes that act on smaller scales than usually seen in large cosmological simulations, robust hydrodynamic simulations can still be difficult to produce.

A simpler alternative is to map galaxies onto the dark matter distribution using Semi-Analytic Models [SAM, e.g. Bower et al., 2006] or models of the Halo Occupation Distribution [HOD, e.g. Skibba et al., 2006].

Gas

When observed at X-ray wavelengths, galaxy clusters are found to contain large, diffuse sources of emission due to the presence of a hot gas reservoir in the halo, the intracluster medium (ICM, e.g. Figure 1.2). As gas is accreted into the halo, it will shock on any gas already present, raising its temperature to several million Kelvin, hot enough for the ICM to radiate via X-ray emission [Sarazin, 2008]. Gas within a stable, undisturbed halo will reach a condition of hydrostatic equilibrium where the gas pressure provides sufficient support to prevent any further gravitational collapse. This equilibrium condition is an important concept for measuring halo mass through the gas properties, as discussed in Chapter 2.

Gas temperature is usually measured in terms of the internal energy of the gas, $k_B T$, in keV, where k_B is the Boltzmann constant. A typical sample of groups and clusters will have gas temperatures in the range $\sim 1 - 10$ keV, with gas forming $\sim 10\%$ of the halo mass [Gonzalez et al., 2013; Sanderson et al., 2013]. Despite the substantial gas mass present, it is also highly rarefied, with typical number densities of $10^{-2} - 10^{-4}$ cm^{-3} [Sarazin, 2008].

The high temperature of the gas reservoir results in the gas being a highly ionised plasma radiating through the *bremsstrahlung* emission mechanism. Consisting mostly of hydrogen and helium, the ICM can also be contaminated by metals (elements heavier than helium) produced by the galaxies within the halo, either ejected into the ICM by galactic winds [Baumgartner and Breitschwerdt,

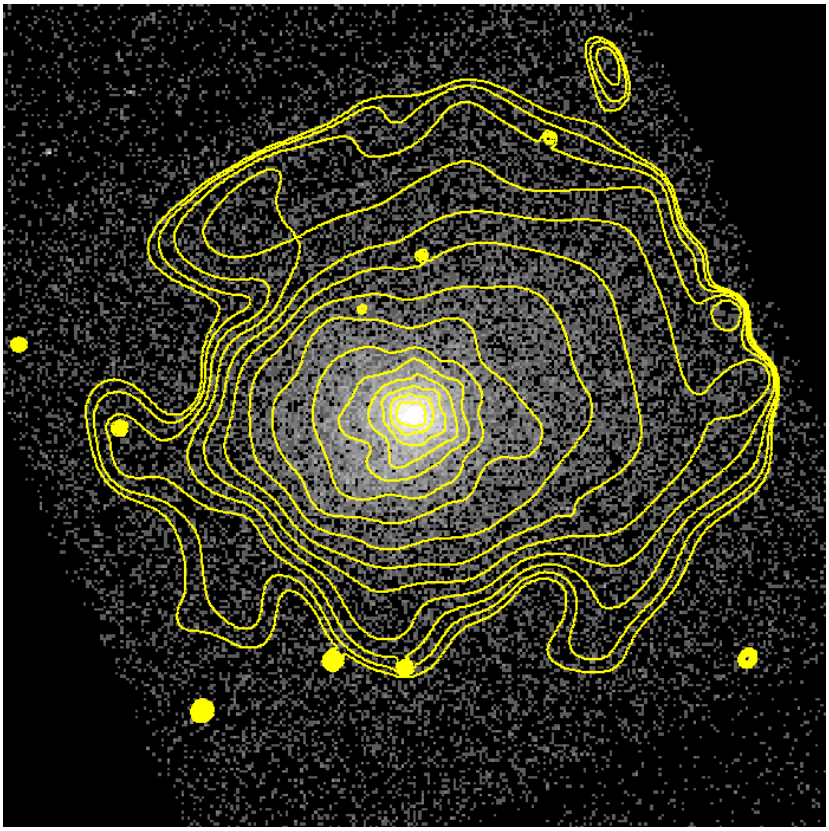

Figure 1.2: X-ray image for the group MKW4 in the energy range 0.5–2 keV as observed by the *Chandra* X-ray Observatory. Overlaid onto the image are adaptively smoothed contours of emission that relate to the projected distribution of gas within the group.

2009; Rasmussen and Ponman, 2009; Schindler and Diaferio, 2008] or stripped out of the galaxy by ram pressure stripping [Schindler and Diaferio, 2008]. This contamination of ICM gas by metals, referred to as the gas metallicity, allows a second emission mechanism, *line emission*. The balance of these two mechanisms is driven by the temperature and metallicity of the ICM.

For high temperature gas (e.g. $\gtrsim 3$ keV), the observed emission is dominated by bremsstrahlung radiation. Sometimes referred to as free-free emission, this radiation is due to electrons passing close to ions within the plasma, radiating as

their paths are deflected. The emissivity is $\epsilon \propto n_e n_i T^{1/2}$, where bremsstrahlung emission has a cooling function $\Lambda(T) \propto T^{1/2}$. The X-ray luminosity from a spherical source of radius r emitting bremsstrahlung radiation is then $L_X \propto r^3 n^2 T^{1/2}$, assuming $n_e \propto n_i = n$. With a mean density ρ and a relation between mass and X-ray temperature this can be reduced to $L_X \propto T^2$.

At lower temperatures line-emission becomes important. Despite the low density of the plasma, collisional excitation is a dominant mechanism where free electrons excite electrons still bound in the metals contaminating the ICM. The amount of emission due to line-emission will depend on the temperature and composition of the plasma, though approximations to the cooling function show that at as temperature decreases, cooling becomes more efficient [e.g. $\lambda(T) \propto T^{-0.6}$, McKee and Cowie, 1977], flattening the $L - T$ relation.

In a relaxed halo with gas that is not experiencing significant central cooling, the surface brightness profile of gas emission is observed to follow a cored density profile, the β-profile, [Cavaliere and Fusco-Femiano, 1976]

$$S(r) = S_0 \left(1 + \left(\frac{r}{r_c}\right)^2\right)^{-3\beta+0.5} , \tag{1.2}$$

where S_0 is the central, characteristic emission and r_c is the radius of an observed emission core. In comparison to the dark matter NFW distribution, the β-profile features a substantial core, rather than a cusp. This core is associated with gas that has been non-gravitationally heated by, for example, active-galactic-nuclei (AGN). This heating results in gas being redistributed evenly throughout central regions [Sarazin, 2008], smoothing out the central gas distribution and forming a core.

In practice, a number of galaxy clusters have been found to have excess emission in their cores. The increased central luminosity is associated with dense, rapidly cooling gas. These "cool core" clusters are readily identified by short (substantially less than the age of the universe) gas cooling times in the central regions and a drop in the inner gas temperature. Non-cool core clusters, where no cool core is observed, may be systems where recent disturbances have destroyed a cool core, such as mergers or AGN activity heating cluster gas.

Stellar Mass

The third component of a galaxy cluster is its stellar mass — the stars in hosted galaxies (e.g. Figure 1.2). The mass held in stars contributes the least to the total mass in clusters, though the stellar fraction may be comparable to the gas fraction for galaxy groups [Gonzalez et al., 2013].

Galaxies, like other cosmological structures, are thought to grow hierarchically, both by accreting cold gas and converting it into stars and through direct galaxy-galaxy mergers. Galaxies also represent collisionless tracers of the dark matter distribution within which they are embedded and can therefore help illustrate any recent dynamical activity, such as cluster mergers.

In addition to the galaxy dynamics, falling into a cluster potential will also affect the activity and state of a galaxy or group of galaxies. The most obvious effect is the loss of star forming gas as it is stripped out of the stellar system by ram pressure against existing halo gas [e.g. Eckert et al., 2014; Russell et al., 2014], quenching any star formation and resulting in cluster galaxies being dominated by old, red stars. Tidal disruption may also occur in recently merged systems when two or more galaxies move close enough to gravitationally disturb one another,

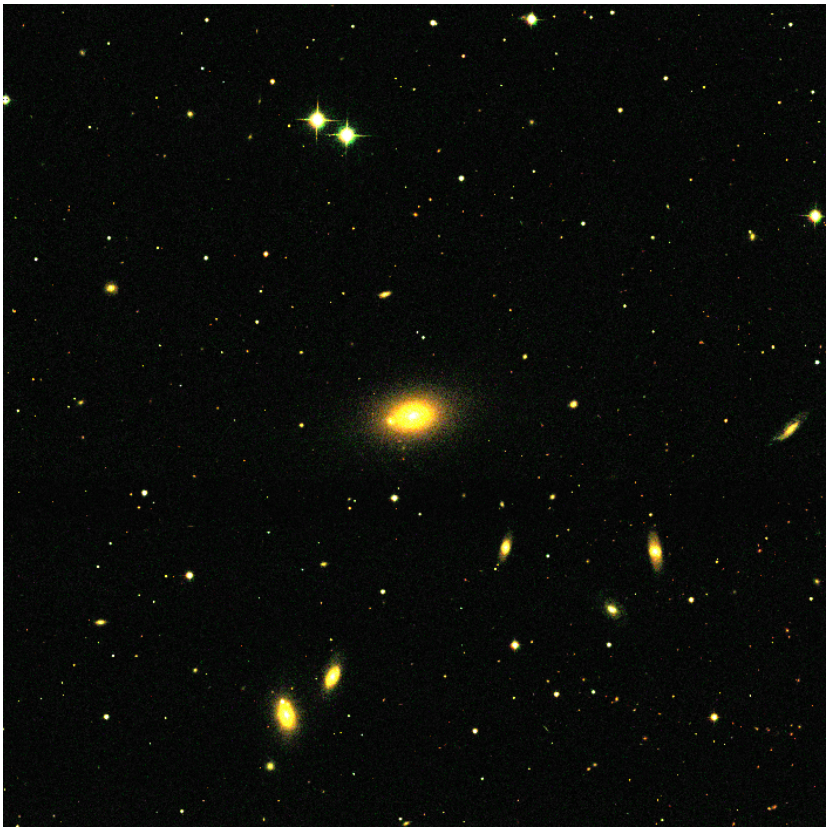

Figure 1.3: Composite SDSS u, g, r-image of the central region of MKW4 showing its central galaxies.

disrupting galaxy morphology.

The above processes, star formation quenching and morphological disruption, convert active, blue, spiral galaxies (late-type galaxies) into populations of dead, red, elliptical galaxies (early-type galaxies). These processes are more prominent in high density environments such as clusters, than in the field, resulting in galaxy populations at high and low density environments being significantly different [Balogh et al., 2004; Hogg et al., 2004]. This difference in population can be useful when identifying galaxy groups and clusters (see Section 1.4.3).

Another consequence of the tidal disruption of galaxies in close approaches or

galaxy-galaxy mergers is the potential to strip stars from galaxies, forming the intracluster light [ICL Burke et al., 2012; Gonzalez et al., 2005; Zibetti et al., 2005]. Estimates of the exact amount of light held in the ICL is debated but imply that at least $\sim 10\%$ of light is in a low surface brightness stellar population between galaxies. This component is extremely difficult to measure due to its low surface brightness, compounded by the need to define where galaxies end and the ICL begins, an otherwise smooth distribution. The study of Gonzalez et al. [2005] find a substantial fraction of the BCG+ICL light is contained within the ICL $(80-90\%)$, which is itself a large fraction of the total cluster light at low redshifts [$\sim 40\%$ at $z \lesssim 0.13$, Gonzalez et al., 2007]. Examining the ICL fraction at high redshift ($z \approx 1$), Burke et al. [2012] find that the BCG contributes a much greater fraction of light to the BCG+ICL luminosity ($\sim 60\%$), than at low redshift [e.g. Gonzalez et al., 2005].

The Baryon Budget

The fraction of a group or cluster's mass contributed by baryons is important for understanding their evolution. Studies of the baryon fraction using large samples of groups and clusters have conflicting results, with work such as Giodini et al. [2009] finding a significant, mass dependent deficiency. Gonzalez et al. [2007] instead imply a constant baryon fraction only marginally deficient relative to the universal fraction, though update this result in Gonzalez et al. [2013] to also find a mass dependent deficiency.

The observed baryon deficiency, usually measured within r_{500}, implies that baryons have been ejected from within r_{500}. This is plausibly due to heating by feedback processes [Giodini et al., 2009; McCarthy et al., 2010], also explaining

potential mass dependencies. Feedback processes such as AGN heating will have a greater impact on group scale halos than clusters due to the shallower potential well.

Accurately determining the baryon fraction is difficult as it requires reliably measuring the masses of both the stellar and gas phase baryons as well as the total mass of the halo. Biases in estimates of the total mass will clearly bias measured fractions, as shown by Sanderson et al. [2013] when comparing the dynamical based masses used by Gonzalez et al. [2007] to X-ray based masses, finding them to be substantially underestimated. However, Gonzalez et al. [2007] also provided excellent constraints on the stellar mass by robustly including the intracluster light. When the ICL is not measured as part of the study, stellar mass can be rescaled to account for the unobserved ICL luminosity [e.g. Giodini et al., 2009]

Decomposing the baryon fraction into a stellar and gas fraction, these components have been observed to show trends with halo mass [e.g. Figure 1.4, Giodini et al., 2009; Gonzalez et al., 2007, 2013]. The gas mass fraction is seen to decrease towards lower masses, possibly due to the action of feedback inflating gas halos. The stellar mass fraction is observed to increase towards low mass [see also Budzynski et al., 2014; Leauthaud et al., 2012; Moster et al., 2010], implying a greater efficiency of star formation at lower masses (peaking at halo masses of $\sim 10^{12}\mathrm{M}_{\odot}$), and providing another sink for halo gas as it cools into a stellar phase.

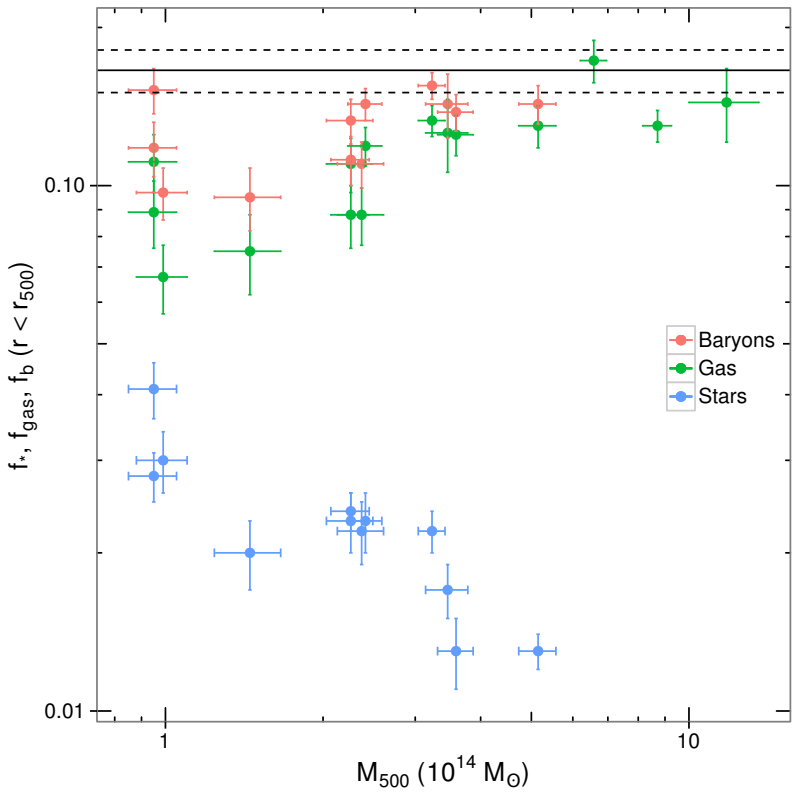

Figure 1.4: Gas, stellar and total baryon fraction (f_{gas}, f_* and f_b) of galaxy clusters as found from the analysis of Gonzalez et al. [2013]. The horizontal line at ~ 0.17 shows the universal baryon fraction from WMAP 9 [Hinshaw et al., 2013].

1.2 Self-Similarity and Mass

The defining feature of a galaxy group or cluster is its mass. Massive clusters, in excess of 10^{15} $M_\odot$, should show significantly different properties compared to small groups of $\sim 10^{13}$ $M_\odot$. However, if the processes that give rise to cluster properties, such as luminosity or gas temperature, are purely dependent on the total gravitating mass, there should be a simple, *self-similar* evolution with halo mass — i.e. clusters would simply be scaled up groups [e.g. Kaiser, 1991].

A simple example of this can be seen in the mass-temperature and X-ray

luminosity-temperature relations. Assuming a cluster is virialised (i.e. $K = -\frac{1}{2}U$) with a hot, ideal gas reservoir at temperature T, the kinetic energy of a particle of gas is simply $\frac{3}{2}k_BT$, where k_B is the Boltzmann constant. For a system of gas mass $M_{gas} = Nm$ where N is the number of particles and m is the mass per particle, the total kinetic energy of the gas is $K \propto M_{gas}k_BT$. In a self-similar system one would expect $M_{gas} \propto M_{halo}$, and assuming the usual form of gravitational binding energy, $U \propto GM_{halo}^2/r$, the equilibrium of this system gives rise to the relation

$$M_{halo}k_BT \propto \frac{M_{halo}^2}{r} \quad . \tag{1.3}$$

Assuming cluster mass and radius is measured within a region enclosing a mean density $\rho = \Delta\rho_c \propto M_{halo}r^{-3}$ (where Δ is the overdensity of the region relative to the critical density) and that the cluster collapsed at the present day, $z \approx 0$, the mass-temperature relation is then

$$M_{halo} \propto (k_BT)^{3/2} \quad . \tag{1.4}$$

Similarly, the luminosity-temperature relation, assuming that the X-ray emissivity is dominated by thermal bremsstrahlung emission with emissivity $\propto n_e n_i T^{1/2}$ is found to be $L_X \propto T^2 \propto M_{halo}^{4/3}$. As a group or cluster's mass increases, these results imply that the X-ray temperature and luminosity should scale in a simple manner with the accreted mass.

In reality, observations of these scaling relations have shown that self-similarity is broken, especially in lower mass systems. The $L_X - T$ relation especially shows this, with measured slopes of ~ 3 [e.g. Slack and Ponman, 2014], steepening to ~ 4 for groups [e.g. Osmond and Ponman, 2004]. To study similarity breaking,

it is important to be able to determine the mass of the systems being studied, or to at least have a reliable mass proxy, such as temperature.

The variety of mass estimators used today, discussed further in Chapter 2, can be roughly grouped by the matter they rely upon. The virial theorem and caustic mass estimates determine mass through the dynamics and distribution of stellar material, whilst hydrostatic X-ray analyses and Sunyaev-Zel'dovich estimates rely on the gas properties. Gravitational lensing mass estimation is the most direct method for estimating halo mass, sensitive to the effect the total, predominantly dark matter mass distribution has on the light of background galaxies.

However, these mass estimates are often impractical for low mass systems ($M \lesssim 10^{14}\mathrm{M}_{\odot}$). Low halo masses result in little detectable lensing signal, and with shallow potential wells disturbances to the equilibria for virial and hydrostatics based masses can be more significant. Furthermore, as many methods rely on specialised observatories to acquire their data (e.g. *Chandra* and *XMM-Newton* X-ray Observatories), acquiring data of sufficient quality for such analyses often requires a substantial dedication of time. The exception to this are dynamical based mass estimates which benefit instead from the many wide and increasingly deep redshift surveys [Colless et al., 2001; Driver et al., 2011; York et al., 2000] that have been performed in recent years.

1.3 Cosmic Feedback

In the previous sections we presented a simple view of the universe whereby groups and clusters are self-similar and gas readily cools into stars. In fact, gas should so easily cool out of the ICM that by the present day, large amounts of

the universe's baryons should be contained within stars [the cooling catastrophe, e.g. Balogh et al., 2001]. However, as we observe large, X-ray emitting halos of gas at low redshifts, this is an over-simplified view.

Therefore, some process is required to not only reheat group and cluster gas, disrupting cooling, but also to introduce non-gravitational physics (i.e. independent of the gravitational collapse of the halo) that would break the simple self-similar models. This is especially true at early times when the mean density of the universe was higher than now and therefore cooling processes more efficient.

A plausible solution is heating of the ICM by "feedback" [e.g. Voit and Bryan, 2001]. Very simply, as material cools, feedback processes would inject energy and entropy into the gas. This entropy injection would act to reduce gas density, increasing the cooling time of the gas, either turning off cooling or limiting its efficiency. If done at high redshift, this *pre-heating* would raise gas entropy, which would then be further boosted by shocks during subsequent hierarchical mergers, overcoming the cooling catastrophe.

Through the decreased density of high entropy gas, entropy injection will also cause gas to redistribute itself within the cluster. This has the effect of flattening the density profile in the core, lowering the X-ray emissivity of the gas. Due to the shallower potential of groups injected entropy will be more significant in low mass systems compared to high mass clusters, and will therefore lower the emissivity more strongly in groups, steepening the $L_X - T$ relation.

Prominent sources of heating are considered to be either galactic winds driven by supernovae from recent gas fed star formation [e.g. Ponman et al., 1999], or energy injection from active galactic nuclei [e.g. Bower et al., 2006; McCarthy et al., 2010, 2011, and references therein]. In addition to heating the intracluster

medium, these processes also constrain models for galaxy formation, explaining the difference observed between the predicted mass function and the galaxy luminosity function. Galaxy winds, for example, will tend to inhibit star formation in low mass halos, blowing material out of dwarf galaxies, whilst AGN would heat gas to prevent it cooling onto more massive galaxies.

1.3.1 Entropy

The entropy of group and cluster gas is an important diagnostic for quantifying their thermal history and measuring the impact of feedback on a halo [e.g. Cavagnolo et al., 2009; McCarthy et al., 2010; Ponman et al., 1999; Voit and Bryan, 2001; Voit et al., 2002, 2005]. As entropy can only be raised by heating (such as merger shocks or feedback) and lowered by radiative cooling, entropy is a much more sensitive probe of the history of a group than, for example, temperature or energy. Changes in energy and temperature can be concealed by hydrostatic equilibrium as gas moves to re-establish pressure support following feedback.

In astrophysics, the gas adiabat, K, is a convenient alternative to the standard thermodynamic entropy, S, and is often referred to as "entropy". As described in, for example, Sarazin [2008] if we consider the specific entropy of gas, i.e. the entropy per particle, s, and assume the gas to be a monatomic ideal gas, the gas adiabat is

$$K = \frac{k_B T}{n_e^{2/3}} \quad , \tag{1.5}$$

where n_e is the electron number density, T is the temperature of the gas and k_B is the usual Boltzmann constant. We can relate K to the specific entropy as $s \propto \ln(K)$. In a self-similar description, where $n_e \propto \rho = \Delta\rho_c$ — again, where Δ is

the factor by which the cluster mean density is greater than the critical density, its overdensity — one would expect $K \propto T$, though in the core ($r \sim 0.1 r_{200}$) where gas is densest and radiative cooling can be efficient, entropy has been observed to scale as $K \propto T^{2/3}$ [Ponman et al., 2003].

Within a given cluster, entropy is expected to monotonically increase with radius. As gas is heated and has its entropy raised, the cluster will convectively redistribute it to maintain a radial entropy gradient with the lowest entropy gas in the core. Outside the core, entropy is expected to follow a radial profile $\propto r^{1.1-1.2}$ [Voit et al., 2005].

Reproducing the distribution of gas entropies has been very important for hydrodynamic simulations, helping to constrain feedback models. For example, simulations by the OverWhelmingly Large Simulations project [OWLS, Schaye et al., 2010] have shown that models that preheat group gas by AGN give the best match to the observed distribution of entropy, as well as other halo properties such as its stellar mass [McCarthy et al., 2010, 2011]. However, this model also predicts a wide range of central group entropies, of which existing measurements only probe the low entropy population. As high entropy groups would have reduced X-ray luminosities, they would also be less likely to be covered by existing X-ray group selection.

In Chapter 4 we present a pilot study looking for high entropy galaxy groups using an optically selected sample. By selecting groups independently of their X-ray properties, we avoid selecting only the brightest, low entropy population of groups. However, optical selection can also select groups in a variety of dynamical states. A group that is yet to fully virialise, for example, will not feature gas at virial densities and will therefore mimic high entropy groups. We discuss this

more, and strategies for group selection, in the next section.

1.4 Dynamical State and Substructure

1.4.1 Virialisation

The spherical collapse model discussed previously is a conceptually useful way to understand the collapse of overdense regions in an expanding universe. However, this is an idealised example of collapse whereby the overdense region collapses to a point. In reality the overdensity will collapse until it reaches an equilibrium state and virialises. In a universe where $\Omega_m = 1$, the overdensity of a virialised region is $\delta \approx 178$ [e.g. van de Weygaert and Bond, 2008]. This typical virialised overdensity motivates several measures of halo properties, such as r_{vir}, the radius enclosing a mean matter density of δ times the critical density.

In practice it is convenient to adopt a fixed overdensity threshold, Δ (relative to the critical density of the universe), as a means of characterising halos. $\Delta = 200$ is often used synonymously with the virial overdensity. Other overdensities used, such as $\Delta = 500$ or 2500, are observationally motivated. X-ray emission, for example, is difficult to trace to large radius due to the drop in gas density at large radius, though is much more easily detected within r_{2500} and, in some cases, r_{500}.

In addition to the dark matter halo reaching a characteristic overdensity, virialisation also affects the gas and galaxies within a halo which similarly relax into a state of equilibrium. We have already discussed the hydrostatic equilibrium of gas, where the thermal gas pressure balances further gravitational collapse.

This relaxation also allows group and cluster gas to reach the densities required for the observed X-ray emission. Gas in a halo that is still collapsing will be of a much lower density and therefore will be much less luminous than one would expect for the mass of the halo. Galaxies reach a similar virialised state in which their motion reflects the motion of the dark matter and its kinematic support against further collapse. They will therefore satisfy the Virial Theorem and Jean's Equation (see Section 2.1.1). In virialised halos, the velocity of cluster galaxies are consistent with a Gaussian distribution [e.g. Yahil and Vidal, 1977].

1.4.2 Substructure

The spherical collapse description only considers the initial collapse of a halo, and not the subsequent merger events that follow as structures hierarchically build. As larger halos collapse, they accrete matter through the infall of smaller, pre-existing halos, resulting in a number of small subhalos being hosted within the halo until they can be completely disrupted and mixed into the main halo. Additionally, as the collapse of a halo is unlikely to be spherical in practice, a structured distribution of matter may also indicate that the halo is still in the process of collapsing for the first time.

Therefore, the presence of substructure is a strong indication of disturbances to the equilibria and symmetries required by many mass estimators. Identifying individual substructure can be difficult due to the small size of subhalos relative to the structure within which they are embedded. Instead, as substructures introduce deviations from the expected distribution of matter within clusters, a statistical approach can be taken whereby this deviation, and its significance, is

measured [e.g. Pinkney et al., 1996].

Optically, substructure tests are sensitive to the spatial and velocity distribution of member galaxies, for example, testing for "clumpy" distributions of the galaxies or irregularities in the velocity histogram. Similar arguments can be applied to the X-ray emitting gas where X-ray substructures or disturbances can manifest as a simple offset between the peak emission and some centroid of emission, or between emission centroids measured within incrementally larger radii. X-ray based substructure has the advantage over galaxy based measures as, unlike galaxies which are discrete probes of the halo structure, the ICM forms a continuous tracer of the matter distribution.

1.4.3 Group Selection

Selection effects from the construction of group and cluster samples are important to account for when interpreting the results of the sample. For example, many modern group and cluster samples are X-ray selected, selecting objects based on known X-ray luminosities. As discussed previously, this selection can result in missing a population of high entropy – and therefore low luminosity – groups. However, as non-virialised halos will also likely have low X-ray luminosity, X-ray selection can produce samples which tend towards largely relaxed halos.

An alternative to X-ray selection is to construct an optically selected sample, a sample of groups and cluster identified from optical redshift surveys and selected by their optical properties. Naturally this will introduce selection effects if one were interested in how optical properties are related. Instead, as optical selection methods are independent of their X-ray properties, they protect against X-ray se-

lection effects when studying the X-ray properties. Indeed, X-ray observations of optically selected samples, such as the *XMM-IMACS* [XI, Rasmussen et al., 2006] sample or the low redshift sample of groups from Balogh et al. [2011], have shown that the population of groups is more varied than previously observed. Both samples, drawn from a Friends-of-Friends analysis of galaxy surveys, Merchán and Zandivarez [2002] and Eke et al. [2004] respectively, found that a large fraction of their groups were undetected, whilst most others were X-ray underluminous compared to X-ray selected samples. These studies attribute these underluminous groups to either uncollapsed groups or spurious, chance associations, or that their hot gas has been strongly affected by feedback processes that suppress X-ray luminosity.

It is potentially very interesting if these non-detections are a result of feedback processes as it would add further support to feedback models such as those of McCarthy et al. [2011]. However, further work needs to both detect the gas in these systems (i.e. targeting with deep X-ray observations) and to reliably separate relaxed optical groups from unvirialised or spurious groups. As part of the study in Chapter 4 where we look for evidence of a population of high entropy groups, we examine the issue of group selection when selecting a sample.

1.4.4 Group and Member Identification

Samples of groups and clusters are usually constructed from a broader sample of group and cluster candidates and their member galaxies. Historically samples were constructed from clusters identified as an excess of bright galaxies in photographic plates [e.g. Abell, 1958]. However, as redshift information was sparse, if

available at all, many of the identified clusters suffered heavy interloper contamination due to the projection effects including foreground and background galaxies [Lucey, 1983; van Haarlem et al., 1997].

The lack of projection concerns with X-ray observations, where detectability is dominated by gas near the centre of the cluster — and is therefore densest (for a given temperature, $L_X \propto n^2$) — made X-ray based identification a simple alternative when constructing a cluster catalogue. All sky surveys such as the ROSAT All Sky Survey [RASS, Voges et al., 1999], identified over 18,000 bright X-ray sources which could later be examined to construct catalogues of point-like and extended sources. This survey has been the starting point for many X-ray selected cluster samples.

To associate galaxies to clusters identified as above, a simple approach is to use data from a galaxy redshift survey, and apply a velocity cut about the galaxies at the redshift of the cluster [e.g. Mamon et al., 2010; Yahil and Vidal, 1977]. By excluding galaxies more than 3σ (where σ is the velocity dispersion of the group) it is possible to substantially reduce the contamination of the cluster by unassociated, interloper galaxies. However, as shown by Mamon et al. [2010] it is not possible to completely remove interloper galaxies.

This X-ray detection with optical follow-up is one approach to cluster and member identification. Other approaches make use of optical observations only, using galaxy properties and distribution to both identify clusters and their members simultaneously.

FoF Group Identification

Outlined by Huchra and Geller [1982], the Friends-of-Friends (FoF) algorithm aims to identify associated galaxies through their spatial and velocity information only, noting that groups and clusters constitute a 3D overdensity. The FoF algorithm proceeds by first determining a linking length for each galaxy, related to the mean number density of galaxies n as, e.g. $\propto n^{-1/3}$. For any pair of galaxies, separation of these galaxies in projection and along the line-of-sight are compared to their linking lengths. If the separation of these galaxies is less than a criterion based on the linking lengths, the algorithm considers them to be linked. Whilst unlinked galaxies are interpreted as isolated galaxies that make up the field, linked galaxies, and the galaxies that they are linked to, are considered associated, forming groups and clusters.

The choice of linking length controls the efficiency of the linking algorithm. Small linking lengths will break halos into small associations, potentially ignoring galaxies at large radius, whilst large linking lengths will extend the linking volume into the field, adding field galaxies into the estimated halo. Survey flux limits or variation in survey completeness further affect the observed density of galaxies, though this can be accounted for when determining the linking lengths. The exact linking lengths used and their scaling are often tuned on mock realisations of the survey to which the FoF algorithm is to be applied to [e.g. Eke et al., 2004; Robotham et al., 2011]. By tuning on a sample of galaxies whose true halo membership is known, the user can optimise their implementation.

Whilst this algorithm should produce a more robust estimate of a halo's membership than a simple σ clip, it will not be completely free of interlopers and spu-

rious groups. By searching for overdensities, the FoF algorithm can, for example, link together merging structures or line-of-sight superpositions. Furthermore, there is no guarantee that the identified groups are virialised or fully collapsed.

MaxBCG

An alternative to the FoF group finder that is well suited to multiband photometric surveys is the MaxBCG algorithm, described fully in Koester et al. [2007] and summarised below. This algorithm takes a likelihood approach to identifying group and cluster galaxies based on their luminosity, colour and spatial distribution. Rather than linking together neighbouring galaxies, the MaxBCG algorithm examines each galaxy in a survey for its likelihood of being a brightest cluster galaxy (BCG) in a typical cluster environment.

To determine the likelihood of a galaxy being part of a cluster, cluster galaxies are assumed to have colours consistent with galaxies on the red sequence. The red sequence, an area of the colour-magnitude diagram populated with luminous, red galaxies, is most prominent in rich clusters, though Koester et al. [2007, and references therein] indicate that it is observed to some extent on group scales, despite the decreasing fraction of red galaxies [Weinmann et al., 2006]. Koester et al. [2007] define the likelihood of a region being a cluster assuming colour is distributed as a Gaussian about the red sequence, and also that galaxies are radially distributed following an NFW density profile.

A similar, colour dependent argument is made for the likelihood of a galaxy being a BCG. Koester et al. [2007] again assume that colours are Gaussian distributed, additionally including a scale that ensures these galaxies are bright. The product of these likelihoods is calculated for each galaxy assuming a red-

shift to determine the colour of the red-sequence. The highest likelihood object within a spatial and velocity range is identified as the BCG with members identified within an aperture about this BCG and a colour about the red sequence. These likelihoods are maximised with respect to redshift, allowing the MaxBCG algorithm to be run on photometric surveys without any prior need to constrain redshift. It can therefore be applied to deeper, more distant objects than group finders such as the Friends-of-Friends.

The use of the red-sequence for MaxBCG clusters results in objects that are inherently different and less diverse than those from a FoF grouping. Furthermore, as groups at high redshift may not have red, early type BCGs [e.g. Ascaso et al., 2014], this algorithm may be less effective at identifying high redshift structures. However, as the processes that transform blue, late-type galaxies into red galaxies are most efficient in real, collapsed structures, MaxBCG clusters likely represent real galaxy associations. This is in contrast to FoF groups which attempts to link together an overdensity of galaxies and, whilst likely to detect a more diverse range of groups, are also much more likely to detect groups that are still collapsing or spurious.

1.5 Sources of data for this thesis

The data used for this thesis cover both optical and X-ray wavelengths. The optical data are drawn from galaxy redshift surveys, the Sloan Digital Sky Survey [SDSS, York et al., 2000] and the Galaxy And Mass Assembly project [GAMA, Driver et al., 2011]. X-ray data are derived entirely from *Chandra* observations with results from literature results, archived observations or from observations

for time granted specifically for the work described here. Additionally, we make use of mock datasets constructed from N-body simulations and populated with galaxies. This section briefly describes the origin of the data used for this work.

1.5.1 Sloan Digital Sky Survey

The Sloan Digital Sky Survey [SDSS, York et al., 2000, and references therein] began as a large, deep photometric survey mostly of the north galactic cap with medium depth spectroscopic follow up of point and extended sources. Now in its 10th data release [Ahn et al., 2014] the SDSS covers $14,555\,\mathrm{deg}^2$ including a large area of the southern galactic cap. The survey has catalogued more than 469 million objects with photometry better than a 5σ detection, generating spectra for over 1.8 million galaxies with a nominal depth of $m_r \approx 17.7$. Recent upgrades to the instrumentation for the study of baryon oscillations have allowed SDSS spectroscopy to target fainter sources.

The SDSS spectrometer spans 3800 to 9200 Å and is fibre fed with a minimum separation of fibres of $55''$. Any spectroscopic candidates that are closer than this limit will therefore not be simultaneously observable in a single exposure ("fibre collision") and will require repeat visits with different fibre permutations. However, overlap regions do not constitute a significant fraction of the observations, resulting in regions of high projected density — such as the centres of groups and clusters — being less complete than the nominal completeness.

Photometrically the survey extends to $m_r \approx 22$ spanning five bands, u, g, r, i and z with effective wavelengths at 3560, 4680, 6180, 7500 and 8870 Å respectively. A number of magnitude definitions are used, where, for example, flux can

be measured within a fixed angular aperture or modelled using galaxy surface brightness profiles. An alternative is to use the *Petrosian* magnitude, where the flux is measured within a radius where the ratio of the flux within an annulus of radius r' and the mean galaxy flux within r' reaches some threshold value.

We specifically use the reprocessed SDSS galaxy data available from the New York University Value Added Galaxy Catalogue [NYU-VAGC, Blanton et al., 2005, and references therein], derived from the 7th data release [Abazajian et al., 2009]. This catalogue includes a number of refinements to the galaxy photometry [Padmanabhan et al., 2004] and provides k-corrected absolute magnitudes [Blanton and Roweis, 2007]. It additionally provides catalogues that account for fibre collisions, allowing improved completeness in regions of high spatial density. In Chapter 3 we use these data to provide optical members for a sample of X-ray selected groups and clusters.

1.5.2 Galaxy And Mass Assembly Project

Though large in scale, a limitation of the SDSS is its spectroscopic depth. The Galaxy And Mass Assembly project [GAMA, Driver et al., 2011], by contrast, focused initially on three smaller $\sim 12 \times 4\,\mathrm{deg}^2$ regions of the sky, extending spectroscopic coverage to cover galaxies to $m_r = 19.8$, two magnitudes fainter than the SDSS. This additional depth allows GAMA to observe a complete population of galaxies to much higher redshifts than possible with the SDSS, Figure 1.5). Their science goals, to study the evolution and assembly of galaxy scale structures, additionally requires data covering a broad wavelength range spanning ultraviolet, infrared and radio frequencies. This makes GAMA a significant

resource for tying together a diverse range of galaxy properties.

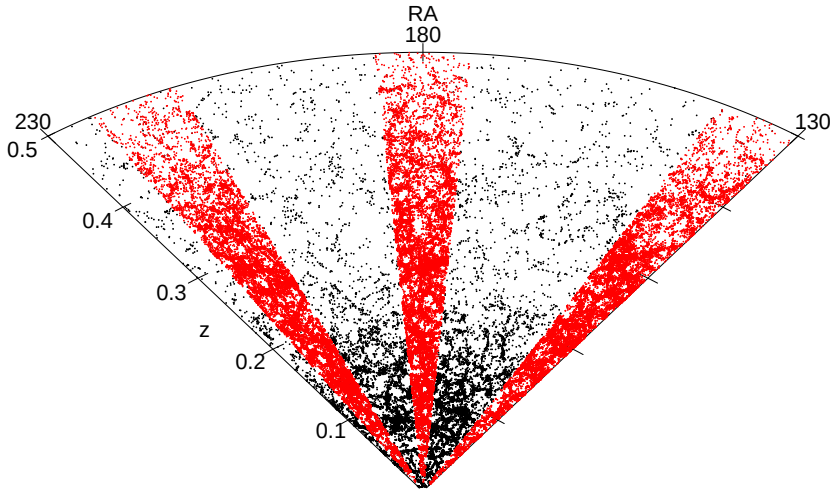

Figure 1.5: As Figure 1.1, extending out to $z = 0.5$, with galaxies observed by the GAMA project overlaid (*red points*).

In Chapter 4 of this thesis we make use of the deep spectroscopic data and the galaxy groups identified by Robotham et al. [2011]. The groups were identified using a FoF group finder calibrated on a set of mock galaxies derived from a semi-analytic model of galaxy formation [Bower et al., 2006] applied to the dark matter halos from the N-body Millennium Simulation [Merson et al., 2013; Springel et al., 2005]. These mocks are also used in this work, allowing for a useful comparison with observations in Chapter 3 and forming the calibration sample for the group selection in Chapter 4.

1.5.3 *Chandra* X-ray Observatory

The *Chandra* X-ray Observatory is one of two currently operating major X-ray observatories, the other being *XMM-Newton*. *Chandra*, whilst not as sensitive as its counterpart, has substantially better spatial resolution with Full-Width at Half-Maximum (FWHM) of $\sim 0.5''$ for on-axis sources. This greater resolution makes *Chandra* a good choice for studies that require robust separation of point sources from diffuse emission as well as work that aims to examine radial trends in observed emission or to look for substructures.

The primary *Chandra* instrument used here is the Advanced CCD Imaging Spectrograph (ACIS). This instrument allows high resolution imaging of X-ray sources with simultaneous, spatially resolved X-ray spectroscopy in the range $0.1 - 10$ keV using two CCD arrangements denoted ACIS-I and ACIS-S. The ACIS-I uses four front-illuminated CCDs in a 2×2 grid spanning an area of $16.9' \times 16.9'$.

The ACIS-S configuration uses four front-illuminated chips and two back-illuminated chips in a strip spanning $8.3' \times 50.6'$ which can be used for imaging, but also as the detector for any spectroscopic observations using the high and low energy transmission gratings. The ACIS-S nominal aim point coincides with one of the two back-illuminated CCDs. These CCDs are more sensitive than the front illuminated chips due to the pixel control structures being placed behind the photosensitive material rather than in the optic path as is usual. ACIS-S observations can therefore make a good choice when the user wishes to observe a concentrated diffuse source, such as a nearby cluster core. Further technical discussion is available within the *Chandra* Proposer's Observatory Guide[1].

[1] http://cxc.cfa.harvard.edu/proposer/POG/html/index.html

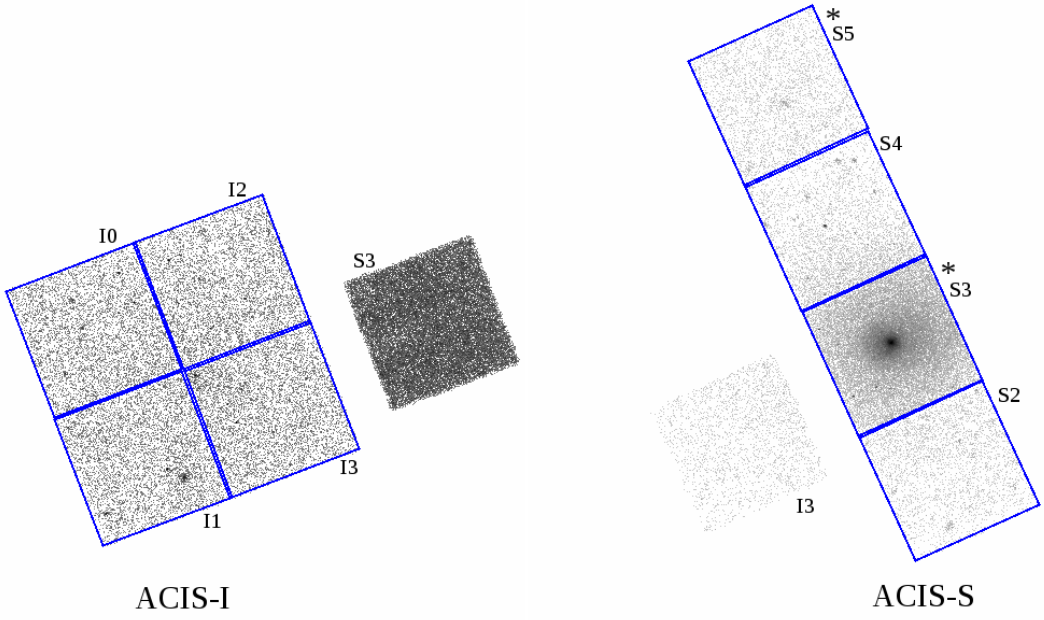

Figure 1.6: Example configuration of the *Chandra* Advanced CCD Imaging Spectrograph (ACIS) instrument with typical setup in the I configuration (*left*) and S configuration (*right*). The chips marked with $*$ show the more sensitive, back-illuminated CCD chips.

Whilst the ACIS instrument nominally allows for 6 CCDs to operate, only 4 are required for observations. Up to two additional CCDs from either ACIS-I or ACIS-S configurations can be specified as optional with their use dependant on the thermal condition of the observatory. Example exposures in ACIS-I and S modes are shown in Figure 1.6 with the main CCDs used highlighted.

The work in Chapter 4 of this thesis primarily uses ACIS-I imaging data acquired for this project. One target in Chapter 4 makes use of archived ACIS-S observations. In Chapter 3 we make use of literature results based upon both *Chandra* ACIS-I and ACIS-S observations.

1.5.4 Simulations

Finally, this thesis makes use of two separate sets of mock realisations of galaxy surveys. The first of these, as noted in Section 1.5.2, was generated for the GAMA project and is derived from the Millennium N-body simulation [Springel et al., 2005]. Galaxies were populated within the dark matter simulation using a Semi-Analytic Model (SAM) of galaxy formation based on the Bower et al. [2006] prescription, adjusted to match the luminosity function of GAMA galaxies [Merson et al., 2013]. With reference to the N-body dark matter merger trees and the baryonic physics expected during halo formation such as star formation and feedback, the semi-analytic models will produce a population of galaxies with realistic, physically motivated properties. Again, we make use of these mocks in Chapters 3 and 4.

The second set of simulations generate a mock light-cone using both a SAM (using an updated version of the Croton et al. [2006] galaxy model) and a Halo Occupation Distribution model (HOD, using updates to the Skibba et al. [2006]; Skibba and Sheth [2009] distributions) applied to the Bolshoi dark matter simulation [Klypin et al., 2011] for the Galaxy Cluster Mass Reconstruction project [Old et al., 2014, Old et al., submitted, and references therein]. These mocks, the details of which are described in Old et al. (submitted), were created for evaluating the performance of a variety of mass estimators on rich clusters, and to compare their behaviour under two different methods for generating a galaxy population. The HOD model, unlike the SAM, distributes galaxies within halos to statistically reproduce the observed distributions of galaxy properties such as the luminosity function. In Chapter 5 we use the SAM realisation of these mocks.

1.6 Thesis Outline

This chapter has demonstrated the importance of reliably estimating the masses of groups and clusters. Well constrained masses from large samples are useful for understanding the evolution and assembly of matter in the universe. However, reliable mass estimates on such large scales are difficult to achieve, either due to poor statistics at low masses, or the finite time available at the specialised observatories required to acquire data. In Chapter 2 we examine the diverse methods available for estimating group and cluster masses. We follow this in Chapter 3 with a discussion of mass estimation through mass-proxy scaling relations calibrated on an X-ray selected sample of groups and clusters.

We note however that these calibrations are only as good as the samples that they were constructed from. As we have also discussed, the use of X-ray selected samples can introduce selection effects that will miss distinct populations of groups that, for example, have low X-ray luminosity due to high gas entropy. In Chapter 4 we work to overcome this limitation in selection, using optical substructure (or lack thereof) to define a sample of galaxy groups from a FoF group catalogue, independent of their X-ray properties. We then use these groups as a pilot study to examine if there is indeed a population of groups with high central entropy gas.

Finally, in Chapter 5 we ask how substructure, already used for defining a sample of groups, can affect the reliability of mass estimates. For a sample of 1000 groups and clusters drawn from a SAM mock galaxy catalogue, we examine the degree to which substructure influences the scatter and bias of the mass estimators discussed in Chapter 3.

Chapter 2

METHODS FOR ESTIMATING GROUP AND CLUSTER MASSES

The previous chapter highlighted the importance of reliably measuring the mass of galaxy groups and clusters. This chapter will discuss the mass estimation methods that are used in the literature and the basic principles behind them. The aim of this discussion is to not only illustrate the diverse range of methods available, but to also present their limitations, motivating the study in Chapter 3. The following sections approach this topic from the fundamental property of a cluster that the methods rely upon. Firstly we discuss the dynamics of member galaxies and applying the virial theorem or determining caustics. Secondly, we examine the hot intracluster medium and its observed X-ray emission or Sunyaev-Zel'dovich effect. Thirdly, we give a brief overview of the gravitational lensing effect due to the large dark matter halos within these clusters. We conclude this

chapter with a brief discussion of mass estimation through scaling relations and their associated mass proxies.

2.1 Galaxy Dynamics

2.1.1 Virial Theorem

The use of galaxy dynamics, the motion and distribution of galaxies within a group or cluster, for estimating the mass of their host halo via the virial theorem is one of the oldest methods available to us today [Smith, 1936; Zwicky, 1937]. Whilst the projected radial distribution of galaxies is easy to measure from imaging data, constraints on their velocity are less trivial, requiring that the redshift of galaxies are known. This redshift is a combination of cosmological redshift from the Hubble expansion of the universe, and the Doppler shift due to the line-of-sight component of the motion of the galaxy within the group or cluster (its peculiar velocity). If the redshift of the cluster is known, the spread of member redshifts about this central value can be assumed to be representative of the peculiar velocities of the galaxies.

The virial theorem assumes that, if a cluster is relaxed, the various cluster components are in virial equilibrium,

$$\langle K \rangle = -\frac{\langle U \rangle}{2} \quad , \tag{2.1}$$

where $\langle K \rangle$ is the kinetic energy of a cluster component and $\langle U \rangle$ is its gravitational binding energy. Though the dark matter halo forms the majority of the cluster's mass, the dynamics of the member galaxies trace this larger component. Assump-

tions of virial equilibrium can therefore be applied to the galaxy population. The details of this methodology are explained in Biviano [2008], which we summarise here. Redshift can only estimate galaxy velocity along the line-of-sight, resulting in there being an unmeasurable component of velocity in the plane of the sky. Assuming we could measure both components, and that the galaxies are collisionless particles (i.e. significant gravitational interactions between galaxies are rare) in a spherical potential, we can describe this equilibrium via the Jeans' Equation,

$$\frac{\mathrm{d}(\rho\sigma_r^2)}{\mathrm{d}r} + 2\rho\frac{\sigma_r^2 - \sigma_t^2}{r} = -\rho\frac{\mathrm{d}\Phi}{\mathrm{d}r} \quad , \tag{2.2}$$

where σ_r and σ_t are the radial and tangential velocity dispersions, ρ is the density of the system and $-\mathrm{d}\Phi/\mathrm{d}r = -GM(<r)/r^2$ describes the gravitational potential of the cluster. This can be rewritten to find the mass within a radius r, M,

$$M = -\frac{r\sigma_r^2}{G}\left[\frac{\mathrm{d}\ln\rho}{\mathrm{d}\ln r} + \frac{\mathrm{d}\ln\sigma_r^2}{\mathrm{d}\ln r} + 2\beta(r)\right] \quad , \tag{2.3}$$

where $\beta = 1 - \sigma_t^2/2\sigma_r^2$ is the velocity anisotropy, describing how the galaxy velocities are distributed in the system. With knowledge of the density profile, velocity dispersion profile and the velocity anisotropy, it is possible to calculate the mass profile and determine the group mass.

In practice, a simplifying assumption of isotropic galaxy motions is often made ($\beta = 0$), reducing Equation (2.2) to

$$\frac{\mathrm{d}(\rho\sigma_r^2)}{\mathrm{d}r} = -\rho\frac{\mathrm{d}\Phi}{\mathrm{d}r} \quad . \tag{2.4}$$

This leads to the virial theorem,

$$M = 3\pi P \sigma_v^2 R_h / G \quad , \tag{2.5}$$

where σ_v is the line-of-sight velocity dispersion, 3π is a correction factor for projection, P is a correction factor analogous to a surface pressure (see below) and R_h is the harmonic mean projected radius of the cluster,

$$R_h = \frac{1}{2} \frac{N(N-1)}{\sum_{i>j} R_{ij}^{-1}} \quad . \tag{2.6}$$

Here N is the number of galaxies in the system and R_{ij} is the projected separation between the ith and jth galaxies.

As observations of a cluster may not include the whole object (e.g. only galaxies within a certain projected radius are used), the lack of galaxies at large projected radius will reduce the apparent size of the cluster. Taken to an extreme, assuming that galaxies at large r are also moving radially within the halo (e.g. recently infallen), and would otherwise not contribute significantly to the observed velocity dispersions [Biviano, 2008; The and White, 1986], their omission will bias high estimates of the velocity dispersion. The and White [1986] account for these effects by introducing the "surface pressure" correction factor [see also, Biviano, 2008]. This is analogous to attempting to estimate the properties of a gas cloud by using a region inside the cloud, neglecting to account for the pressure exerted upon the region by any external gas. Without considering this extra confinement pressure, the virial theorem would overestimate the total mass required to maintain equilibrium. Typical values of P are $\simeq 0.8 - 0.9$ for a large

cluster [Biviano, 2008].

In addition to the surface pressure correction, this classical estimator may also be biased, giving a 10% overestimate in large samples ($\gtrsim 60$ members), increasing significantly to $\sim 50\%$ as sample size decreases to only ~ 15 members [Biviano et al., 2006]. Biviano et al. [2006] indicate that this is related to the interlopers in member selection that increase the estimated group radius. Galaxy type is also seen to cause a bias, also discussed in Biviano et al. [2006], though as late-type galaxies are more likely to have recently fallen into the halo than early-type galaxies, and therefore yet to fully reach equilibrium, this is not unexpected. Restricting virial analyses to early-type galaxies, galaxies that have been in halos the longest and are therefore more likely to be in virial equilibrium, would provide a better tracer of the underlying dark matter distribution. Clearly, from the result of Biviano et al. [2006], robust membership determination, regardless of galaxy type, is also important for reducing bias and scatter in the estimated virial masses.

Due to the varied definitions of membership, mass and radius, the virial theorem, reduced to $M = Ar\sigma^2/G$, is often calibrated on mock galaxy catalogues prior to use [e.g. Eke et al., 2004; Robotham et al., 2011]. This calibration also allows for the surface pressure term, assuming that this correction has a simple mass dependence. For example, groups masses for the 2PIGG catalogue [Eke et al., 2004], were calibrated such that $M = 5r_{rms}\sigma_g^2/G$, where r_{rms} is the root mean square radius of the group and σ_g is the gapper estimate of the velocity dispersion [Beers et al., 1990].

An alternative approach can be to use the virial theorem and the mean overdensity of a virialised halo to show that, at a given redshift, $r \propto \sigma$ [e.g. Carlberg et al., 1997a,b; Ramella et al., 2004]. Assuming a $\rho \propto r^{-2}$ density profile the

radius enclosing an overdensity of 200 relative to critical can be found to be

$$r_{200} = \frac{\sqrt{3}\sigma}{10H(z)} \quad , \tag{2.7}$$

where $H(z) = H_0\sqrt{\Omega_m(1+z)^3 + \Omega_\Lambda}$. This leads to an expression for M_{200} purely dependent on the velocity dispersion,

$$M_{200} = \frac{3\sqrt{3}}{10}\frac{\sigma^3}{H(z)G} \quad . \tag{2.8}$$

These estimators rely on estimating the velocity dispersion of a group or cluster. In a virialised system one would expect the velocity distribution of groups to be distributed as a Gaussian [Yahil and Vidal, 1977], the width of which characterises the groups' velocity dispersion (e.g. Figure 2.1). Already mentioned is the gapper technique, which determines the velocity dispersion using the difference in velocity between galaxies ordered by their velocity, v, [Beers et al., 1990],

$$\sigma = \frac{\sqrt{\pi}}{N(N-1)}\sum_{i=1}^{N-1} w_i g_i \quad , \tag{2.9}$$

where $w_i = i(N-i)$ and $g_i = v_{i+1} - v_i$ for a set of N galaxy velocities. Simpler estimates of galaxy velocity dispersion use a root mean square velocity estimate [e.g. Tago et al., 2008],

$$\sigma = \sqrt{\sum_{i=1}^{N}\frac{1}{N-1}(v_i - \bar{v})^2} \quad . \tag{2.10}$$

When applied to large redshift ranges, velocity dispersions are scaled by $1/1+\bar{z}$ to allow for the cosmological expansion of the universe where the low redshift

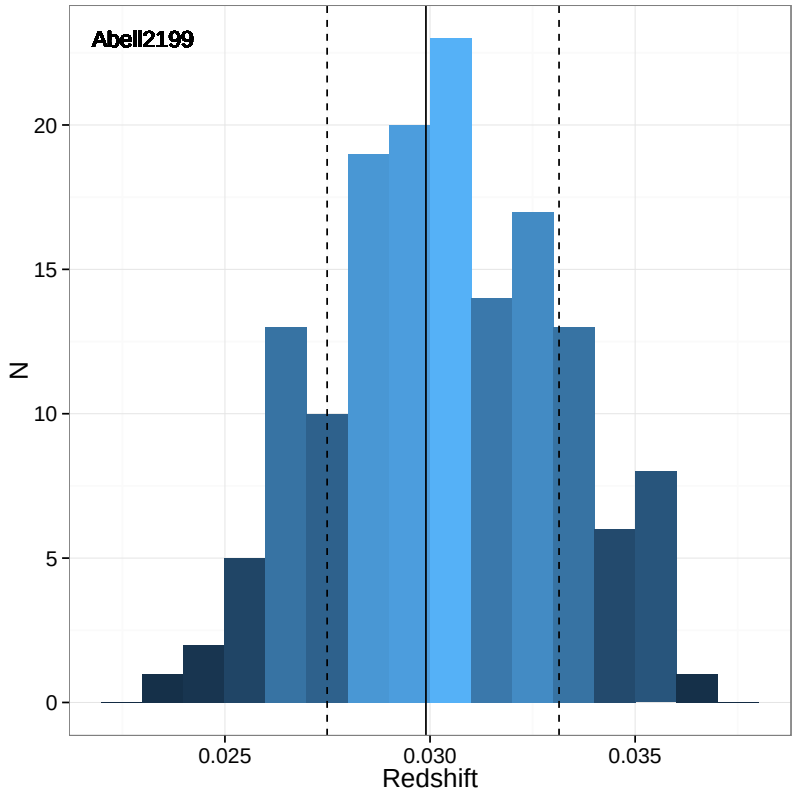

Figure 2.1: An example redshift histogram for Abell 2199 using galaxies within 1 Mpc and within a 3σ clip along the line-of-sight. The solid vertical line indicates the central redshift whilst the dashed vertical lines show the redshift limits equivalent to the observed 848 km s^{-1} velocity dispersion found from the gapper estimator, Equation (2.9).

approximation $v \approx cz$ no longer holds.

As this method assumes virial equilibrium, any processes that may disrupt this equilibrium, such as groups or cluster mergers, can result in biased virial theorem mass estimates. Virial mass estimates also show substantial scatter, increasing at lower masses [Biviano et al., 2006].

2.1.2 Caustics

An alternative use of galaxy kinematics is to define a "caustic" for a given cluster, allowing the mass profile to be measured to large radius [Diaferio, 1999; Serra et al., 2011, and references therein]. A caustic is a characteristic "trumpet" shape in the (r, v) plane (projected radius and line-of-sight velocity relative to the cluster centre) that is predicted through the spherical collapse model. An example phase space diagram is shown in Figure 2.2. The caustic contour splits galaxies into two populations: those contained within the caustic which are mostly inside the turnaround radius of a cluster, but also contain interlopers, and those outside the caustic which should be beyond the turnaround radius.

Following Diaferio [1999], the caustic links the escape velocity at a radius r to the gravitational potential within that radius,

$$v_e^2(r) = \Phi(r) \quad . \tag{2.11}$$

The caustic position, its amplitude $\mathcal{A}(r)$, is measured as a galaxy density contour in the redshift-space diagram. This contour is defined as the velocity above and below the central velocity in a smoothed (r, v) density distribution that first reaches some threshold value. Diaferio [1999] define a threshold density that minimises the difference between the escape velocity and the observed velocity at a given radius. This process will define an upper and lower caustic, the smallest of which is used to define $\mathcal{A}(r)$.

The measurement of $\mathcal{A}(r)$, however, cannot be linked directly to the gravitational potential due to velocity anisotropy within the infall region, $\beta(r)$. The

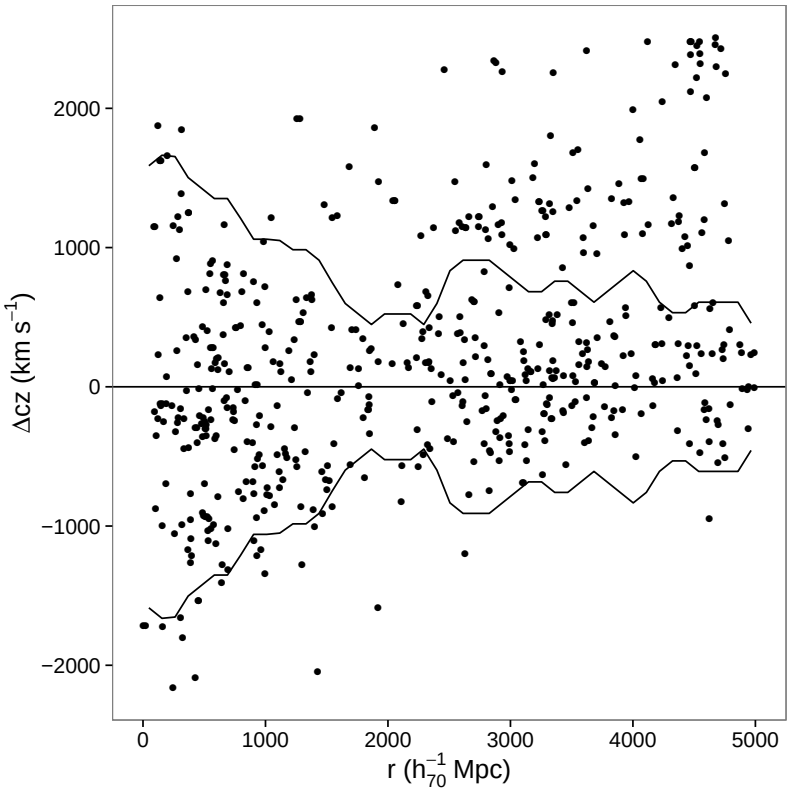

Figure 2.2: The cluster Abell 1367 in the redshift-space plane where the centre in both redshift and position are taken from NED. The higher density of galaxies about $\Delta cz = 0$ traces the distinctive caustic profile expected, with an example caustic (set to an arbitrary density threshold) shown.

potential can be modified to account for this,

$$\mathcal{A}^2(r) = \Phi_\beta(r) \quad , \tag{2.12}$$

where

$$\Phi_\beta(r) = \frac{2|\Phi(r)|}{g(\beta)} \quad \text{and} \quad g(\beta) = \frac{3 - 2\beta(r)}{1 - \beta(r)} \quad . \tag{2.13}$$

As described by Diaferio [1999], this modification also illustrates a possible origin of the caustic. If the galaxy velocities were purely radial ($\beta(r) = 1$) then

$\Phi_\beta = 0$, and no caustic is observed. This implies that the caustic is caused by any non-radial motion of galaxies within the cluster and infall region.

As potential for a spherical system relates to the enclosed mass as $-GM(<r)/r^2 = -\mathrm{d}\Phi/\mathrm{d}r$, we arrive at

$$GM(<r) = -\frac{r}{2}\mathcal{A}^2(r)g(\beta)\left[\frac{\mathrm{d}\ln\mathcal{A}^2}{\mathrm{d}\ln r} + \frac{\mathrm{d}\ln g}{\mathrm{d}\ln r}\right] \quad . \tag{2.14}$$

As measuring $\mathcal{A}(r)$ requires estimating the density of galaxies in the (r, v) plane, it can be too poorly constrained to differentiate. Instead, Diaferio [1999] recast Equation (2.14) as

$$GM(<r) - GM(<r_0) = \int_{r_0}^{r} \mathcal{A}^2(r')\mathcal{F}_\beta(r')\mathrm{d}r' \quad , \tag{2.15}$$

where r_0 is an inner radius from which to measure the mass. The term $\mathcal{F}_\beta(r) = \mathcal{F}(r)g(\beta)$ encapsulates information about the velocity anisotropy and makes additional assumptions regarding the density profile of the cluster. In the usual hierarchical formation scenarios this can be assumed to be slowly varying over most of the cluster and is reduced to a constant, $\mathcal{F}_\beta \approx 0.5$ [Diaferio, 1999; Rines et al., 2003]. This reduces Equation (2.15) to

$$GM(<r) - GM(<r_0) = \mathcal{F}_\beta \int_{r_0}^{r} \mathcal{A}^2(r')\mathrm{d}r' \quad , \tag{2.16}$$

allowing a mass profile to be constructed. Provided that the true mass density profile is consistent with, or between, an isothermal profile ($\rho \propto r^{-2}$) or an NFW profile ($\rho \propto r^{-3}$) at large radius, mass estimates are independent of the specifics of the density profile. Similarly, as long as any substructures or disturbances

are small compared to the cluster (e.g. random galaxy motions dominate and the cluster is not undergoing a major merger), mass estimates can be insensitive to the dynamical state and presence of substructure. Even if these assumptions are not valid, this method is a powerful tool for removing interlopers from a sample, using all 3 available dimensions (unlike, for example, a σ clip rejection). A caustic analysis can therefore also be used to select cluster members in addition to approaches described in Chapter 1.4.3.

The caustic method has been shown to work well on samples of both nearby clusters [e.g. CAIRNS, Rines et al., 2003] and a broader X-ray selected sample matched to the SDSS [CIRS, Rines and Diaferio, 2006]. Mass profiles agree well with NFW profiles and estimated masses are consistent with those estimated through X-ray and virial methods. As shown by Serra et al. [2011], masses estimated by caustic analyses, through the assumptions of spherical symmetry, are sensitive to projection effects. Furthermore, application to small haloes with few galaxies may be difficult, with Serra et al. [2011] demonstrating that reasonable mass profiles require a minimum of ~ 200 galaxies within $3r_{200}$.

2.2 The Intracluster Medium

2.2.1 X-ray Properties

The large hot gas reservoirs hosted within galaxy groups and clusters radiate strongly in X-ray wavelengths. As discussed in Sections 1.1.2 and 1.2, this emission can be related to halo mass through the assumption of hydrostatic equilibrium.

A review of early extragalactic X-ray astronomy is presented by Mulchaey [2000, and references therein], upon which this discussion is based. Whilst X-ray observations can be count-limited with extended sources showing only a few hundred to a few thousand counts in a typical exposure, observations benefit from the simultaneous, spatially resolved spectroscopy of which X-ray detectors are capable.

The typical emission spectrum of hot group and cluster gas (the intracluster medium, ICM) is expected to be a mix of thermal bremsstrahlung radiation and line emission from metal ions distributed in the ICM. The shape of this emission spectrum is controlled by the temperature of the gas. High temperature gas ($\gtrsim$ 3keV) radiates preferentially through bremsstrahlung, whilst line-emission dominates at low temperatures. Models, such as the APEC model [Astrophysical Plasma Emission Code, Smith et al., 2001], can be fit to the observed emission spectrum (e.g. Figure 2.3) to determine the temperature and metallicity of the hot gas.

With high quality data (i.e. observations with several thousand source counts) it is possible to bin and fit spectra radially, allowing a temperature profile to be determined. With assumptions of spherical symmetry and hydrostatic equilibrium, it is possible to determine the halo mass profile from the radial distribution of gas density and temperature,

$$M(r) = \frac{r k_{\rm B} T(r)}{G \mu m_p} \left[\frac{{\rm d} \ln \rho_g}{{\rm d} \ln r} + \frac{{\rm d} \ln T}{{\rm d} \ln r} \right] \quad , \tag{2.17}$$

where m_p is the proton mass, G is the gravitational constant and μ is the mean molecular weight of the gas. Using the binned data and the full set of annular

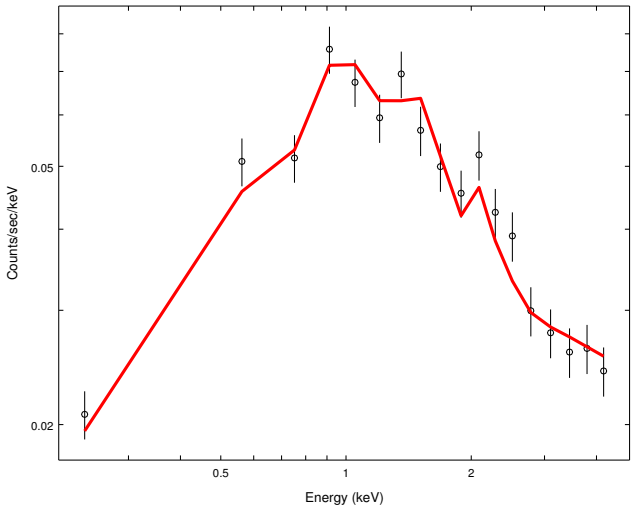

Figure 2.3: Example X-ray spectra from a *Chandra* observation of the group 200054 from the optically selected sample of Chapter 4. This spectrum, extracted within an aperture of $\sim 0.5r_{500}$ (see Figure 2.4) and fit with a background model, was found to have a temperature of 2.8 keV.

spectra, a deprojection analysis can be performed to determine the 3D mass and gas density profiles.

In cases of poor quality data where radial temperature profiles cannot be constrained, a common practice is to instead assume an isothermal gas (i.e. $\mathrm{d}\ln T/\mathrm{d}\ln r = 0$) and to use the mean temperature within an aperture to characterise the group or cluster. The gas density profile, $\rho_g(r)$, is found by fitting the surface brightness of the source with, for example, the β-profile, Equation (1.2) [e.g. Figure 2.4, Cavaliere and Fusco-Femiano, 1976]. This can be deprojected to give a 3D emission profile which is then converted to the gas density profile.

Physically, β is related to the energy in galaxies relative to the energy in the hot gas such that $\beta = \mu m_p \sigma^2 / k_B T = \beta_{spec}$, though comparisons of this to β

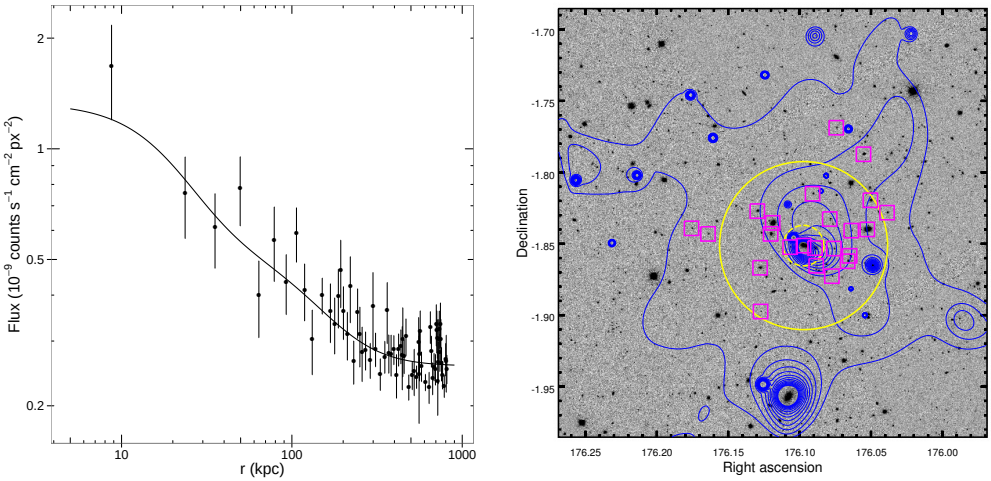

Figure 2.4: *Left:* Surface brightness profile of X-ray flux from the group 200054 (See Chapter 4). Counts have been exposure corrected and binned with at least 15 raw counts per bin The solid line is an example fit to the surface brightness, using two β-models to account for both a central emission core and large diffuse gas halo. A flat background has also been assumed in the fit. *Right:* Optical image (SDSS r-band) for group 200054 with adaptively smoothed X-ray contours overlaid (*blue contours*). Also shown are the position of the member galaxies from Robotham et al. [2011] (*magenta squares*) and apertures of 100 kpc (*yellow dashed circle*) and $0.5r_{500}$ illustrating the spectral extraction region (*yellow solid circle*).

found from fitting the surface brightness profile, β_{fit} are often in disagreement [e.g. Mulchaey, 2000; Osmond and Ponman, 2004]. However, these would only be expected to agree if the gas and galaxies were distributed isothermally and trace the dark matter distribution. In reality, we know the gas temperature is not isothermal and is distributed with a large core, the discrepancy between $\beta_{spec} \approx 1$ rather than the observed $\beta_{fit} = 2/3$ — decreasing to 1/2 at low masses [Mohr et al., 1999] — is not unexpected.

An even simpler mass estimation technique is to use the mass-temperature ($M - T$) relation. Already well known from the study of self-similarity within groups and clusters, and calibrated on systems with high quality data, the $M - T$

relation can be used as a scaling relation to relate a mean temperature to a mass [e.g. Sun et al., 2009]. Furthermore, results such as Le Brun et al. [2014] suggest that the $M - T$ relation is robust against processes such as feedback.

As with the virial theorem, estimated group or cluster masses from the hot intracluster medium are vulnerable to dynamical disturbances in the group. Recent merger activity, or extra heating of gas, will disturb the hydrostatic equilibrium of the system, introducing a bias into any mass estimates.

Finally, we reiterate that masses derived in this way are generally determined from an X-ray selected sample. The selection effects that are associated with an X-ray selection can introduce bias into the results, as discussed in the previous chapter.

2.2.2 Sunyaev-Zel'dovich Effect

Hot gas in the potential wells of galaxy clusters also affect observations of the Cosmic Microwave Background (CMB) — the Sunyaev-Zel'dovich Effect [SZ, Birkinshaw, 1999; Carlstrom et al., 2002; Sunyaev and Zeldovich, 1980]. It has been established that the CMB is well described by a blackbody spectrum of temperature $T_{CMB} = 2.73$ K [e.g. Fixsen, 2009] where the intensity, I, as a function of frequency, ν, is described by

$$I = \frac{2h\nu^3}{c^2}(e^{h\nu/k_B T_{CMB}} - 1)^{-1} \quad . \tag{2.18}$$

where h is the Planck constant and c is the speed of light. k_B is the usual Boltzmann constant.

CMB photons passing through the hot gas in the intracluster medium (ICM)

can undergo inverse Compton scattering, modifying the observed microwave spectrum behind the cluster. Due to the low energies of the incident photons, collisions within this hot gas will preferentially boost their energies. Following Birkinshaw [1999], this shift can be described as

$$\Delta I_{SZE} = g(x) I_0 y \quad , \tag{2.19}$$

where $x = h\nu / kT_{CMB}$, $I_0 = 2(kT_{CMB})^3/(hc)^2$ and

$$g(x) = \frac{x^4 e^x}{(e^x - 1)^2} \left(x \frac{e^x + 1}{e^x - 1} - 4 \right) \quad . \tag{2.20}$$

The final variable in Equation (2.19), y, is the Comptonisation parameter, given by

$$y = \int n_e(r) \sigma_T \frac{k_B T_e(r)}{m_e c^2} \mathrm{d}l \quad , \tag{2.21}$$

where n_e and T_e are the number density and temperature of the ICM electrons at a radius r in the cluster respectively. σ_T is the scattering cross-section. y, integrated along the line-of-sight, is a measure of the integrated gas pressure. As the strength of the SZ effect is proportional to y, y is often used as the main observable from SZ observations. Integrating y over a disk of projected radius r_{500} within a cluster, computes the integrated SZ effect, Y_{500}.

In comparison to the X-ray flux of a hot gas source, the SZ signal has two main differences: y is proportional to n_e, rather than n_e^2, and there is no distance / redshift dependence, allowing gas reservoirs to be seen at much higher redshifts than is possible for X-ray observations. The lack of a redshift dependence allows the SZ effect to be a powerful tool for detecting massive clusters at high redshifts.

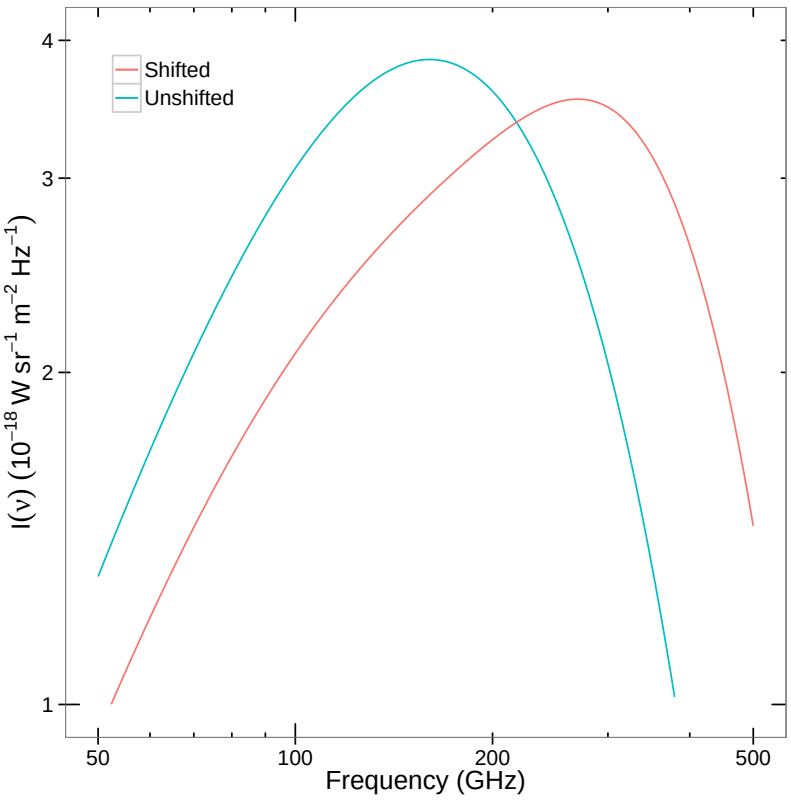

Figure 2.5: Exaggerated shift in the CMB spectrum (*blue curve*) due to the SZ effect (*red curve*). This shift is plotted according to Equation (2.19) with Comptonisation parameter $y = 0.1$.

The Planck mission [Planck Collaboration et al., 2011a] detected 189 cluster candidates from the analysis of their early results [Planck Collaboration et al., 2011b]. Of these, 20 clusters were newly discovered, with the whole sample spanning up to $z \sim 0.3$ and masses above 10^{15} $M_{\odot}$.

Moreover, the use of SZ Y rather than X-ray properties has been shown to produce much more rigorous scaling relations for estimating cluster masses. Simulated clusters, for example, find that $Y - M$ scaling relations are comparable to the self-similar expectation and with low levels of scatter [Motl et al., 2005; Nagai, 2006]. Observations of a sample of real clusters with masses derived from gravi-

tational lensing agree with these simulated predictions, though with marginally more scatter [Marrone et al., 2009, 2012].

As the SZ Y parameter is considered to be such a robust mass proxy, it has inspired a comparable estimator from X-ray analyses, $Y_X = M_g T_X$, where M_g is the gas mass of a cluster and T_X is its mean spectral temperature. Y_X has been found in simulations to produce better mass estimates than other X-ray mass estimators [Kravtsov et al., 2006]. However, Le Brun et al. [2014] caution that Y_X (and Y) is sensitive to the effects of feedback, affecting their reliability as a mass proxy.

We finally note that this discussion is based on the non-relativistic thermal SZ effect only. The SZ flux has additional components, smaller components in the form of a non-thermal component due to relativistic electrons within a cluster's radio halo; the kinetic signal, a Doppler shifted component that depends on the peculiar velocity of a galaxy cluster; and a polarisation, due to the scattering gas introducing a polarisation on the scattered photons.

2.3 Gravitational Lensing

The mass estimators discussed so far rely on the assumption that the properties or distribution of baryonic matter (the stars and gas) within a halo are informing us about the mass within that halo, the majority of which is dark and only interacts gravitationally. Through this gravitational interaction, one of the most direct mass estimation techniques is derived. Observations of galaxy clusters which are massive enough to distort the images of background galaxies — analogous to the distortion of light through a lens — contain a substantial amount of information

about the total projected mass of a cluster. Measuring the distortions due to these gravitational lenses can allow one to construct mass profiles. An example lensing system is shown in Figure 2.6. A comprehensive review of the principles of gravitational lensing are presented in Narayan and Bartelmann [1996, and references therein], upon which the following discussion is based.

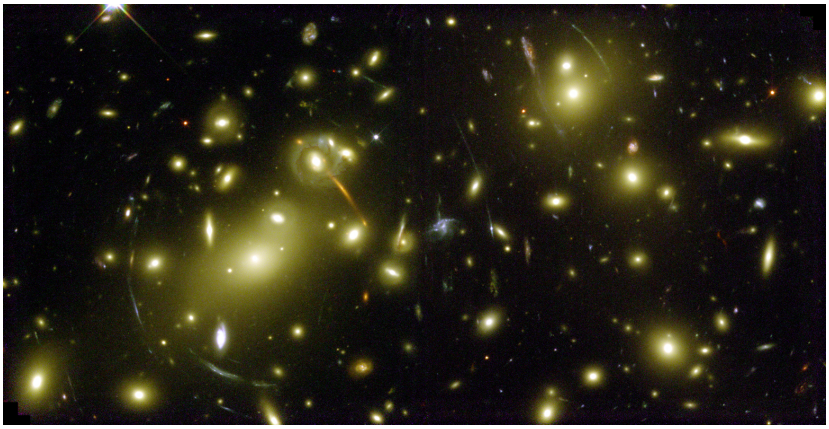

Figure 2.6: Example gravitational lensing system, Abell 2218, from the NASA Hubble Space Telescope archive (NASA/STSci, GPN-2000-000886).

Following the notation of Narayan and Bartelmann [1996], a lensing system is characterised by the lens equation,

$$\beta = \theta - \alpha(\theta) \quad , \tag{2.22}$$

where β is the true angle of the source relative to the optic axis between the lens and observer, θ is the angle from the optic axis of the image and α is the apparent, or reduced, deflection angle (Figure 2.7). The true deflection angle, $\hat{\alpha}$, is related to the reduced deflection angle as

$$\alpha = \frac{D_{ds}}{D_s}\hat{\alpha} \quad , \tag{2.23}$$

where D_{ds} is the distance from the source to the lensing object and D_s is the distance from the source to the observer.

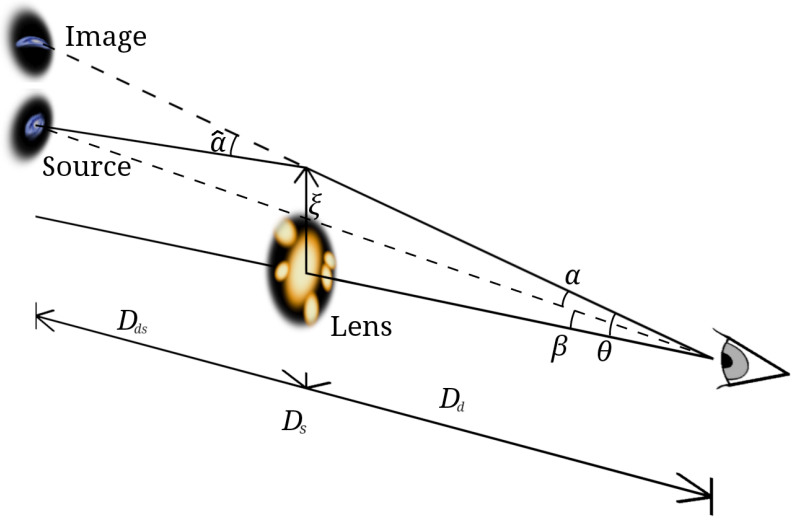

Figure 2.7: A cartoon of a lensing system illustrating the geometry leading to the lens equation (Equation 2.22) and the reduced deflection angle $\hat{\alpha}$ (Equation 2.23). We follow the notation of Narayan and Bartelmann [1996].

Again, summarising Narayan and Bartelmann [1996], for a point mass, the true deflection angle is $\hat{\alpha} = 4GM/c^2b$ where M is the mass of the lensing point mass and b the distance of closest approach for an unperturbed light ray (the impact parameter). G and c are the usual gravitational constant and speed of light. The majority of the lensing deflection occurs near the lens which, given the large distances between source, lens and observer, allows the lens to be treated as a projected mass sheet with surface mass density $\Sigma(\xi)$. In a circularly symmetric system, the deflection angle becomes $\hat{\alpha}(\xi) = 4GM(<\xi)/c^2\xi$ where $M(<\xi)$ is the projected mass enclosed within a radius ξ.

Determining the deflection angle therefore allows the projected mass profile to be estimated. The simplest realistic example of this is for an observation of an

"Einstein Ring", an example of strong lensing whereby the source is on the optic axis of the lens and its image forms a ring enclosing the cluster at the "Einstein radius", θ_E.

The Einstein radius encloses a mean surface mass density known as the critical density Σ_{cr}. Using the lens equation with $\beta = 0$ and assuming a constant surface mass density when estimating $\hat{\alpha}(\xi)$, the critical density can be defined as

$$\Sigma_{cr} = \frac{c^2}{4\pi G} \frac{D_s}{D_d D_{ds}} \quad . \tag{2.24}$$

The Einstein radius is

$$\theta_E = \left[\frac{4GM(< \theta_E)}{c^2} \frac{D_s}{D_d D_{ds}} \right]^{\frac{1}{2}} \quad . \tag{2.25}$$

The critical density can be used to characterise the two main varieties of gravitational lensing that are commonly used for mass estimation, *strong* lensing, where surface densities are comparable to Σ_{cr}, and *weak* lensing, where the surface densities are $< \Sigma_{cr}$. The Einstein ring is an example of strong lensing, however, the precise alignment and assumptions of symmetry required means few examples have been found, none of which are perfect rings. Strong lensing instead usually appears as giant arcs in cluster observations (e.g. Figure 2.6). Again, assuming circular symmetry, the surface mass density inside a circle traced by such an arc is the critical density, Σ_{cr}, allowing the enclosed projected mass to be estimated.

Weak lensing on the other hand appears as the aligned distortion of the background galaxy field. For these galaxies the gravitational lens will distort background images into small arclets, the galaxy shear. The degree of sheer is related

to density of the lens relative to the critical surface density. Mapping these distortions allows a map of the surface density to be constructed, leading to direct measure of the projected mass distribution. However, this effect is weak, and due to noise introduced by the intrinsic shape of galaxies, it can be difficult to measure on individual systems, especially on low mass systems where the weak lensing signal is small.

2.4 Other Methods

2.4.1 Galaxy Density

Whilst not a mass proxy, the galaxy number density profile has been used to characterise cluster sizes. We refer to the discussion of Hansen et al. [2005] who, on a sample of galaxy groups from the SDSS, were able to construct a galaxy density number profile by radially binning the members of a sample of clusters from the SDSS. Using this density profile, corrected for projection, and by reference to the global SDSS luminosity function [Blanton et al., 2003] to estimate the mean density of galaxies, they identified the radius at which the density of galaxies was $200\Omega_m^{-1}$ times the mean density of galaxies, $R_{200}^{\mathcal{N}}$. Though Hansen et al. [2005] note that $R_{200}^{\mathcal{N}}$ is not the same as r_{200} for a dark matter halo unless galaxies are completely unbiased tracers of mass. However, they suggest that the bias is close to unity and that $R_{200}^{\mathcal{N}}$ therefore is a reasonable approximation to r_{200}.

To determine their number profile, Hansen et al. [2005] fit a simple power law to the galaxy density profile split into several richness bins. Other results have

demonstrated that the galaxy distribution is comparable to the NFW density distribution, though with a different concentration [e.g. Budzynski et al., 2012]. In Chapter 3 we extend this idea to use an NFW distribution of galaxies to estimate the masses of groups and clusters.

2.4.2 Scaling Relations

With the exception of dynamical mass estimators, the previous mass estimators often require data beyond the scope of typical redshift surveys. We have also discussed that there are numerous challenges to overcome when applying such estimators to low mass objects. A simple alternative to this is to determine a scaling relation that relates an easily observable parameter — a mass proxy — to the group mass, calibrating on the subset of groups where both mass and mass proxy are available. This will be discussed and demonstrated more in Chapter 3. Here we discuss examples of previous work on this topic.

Cluster Richness

As structure builds hierarchically through the merger of smaller halos, it is simple to see that the number of galaxies within a halo should scale with the mass of the halo — a mass-richness relation. The details of this correlation are subject to processes such as galaxy mergers, which would reduce the number of galaxies in the group, as well as the variation in the luminosity function and star formation efficiency with mass, which modify the number of galaxies observable above a given luminosity limit.

When constructing a mass-richness relation, the definition of richness is important. For example, one could simply count the galaxies above some flux limit

and within an aperture [e.g. Section 3.3.1 Budzynski et al., 2012], correcting for background as required. The Budzynski et al. [2012] mass-richness relation was constructed to enable mass estimation on a large sample of groups and clusters, only a subset of which had X-ray masses available in the literature, which they used as a calibration sample. They measured richness as the number of galaxies within 1 Mpc with absolute magnitude $M_r \leq -20.5$, subtracting a background found from estimating the mean number density of galaxies in a series of annuli spanning $2.5 - 5$Mpc. Their mass-richness relation extended to moderately low mass ($M_{500} > 10^{13.7}$ $M_\odot$) and was found to have a slope of 1.4 ± 0.1 with intrinsic scatter 0.08 ± 0.01 dex.

Early robust measures of richness were based on a parameter used to quantify the environment around radio galaxies [Yee and López-Cruz, 1999, and references therein] and were found to correlate well with the dynamics and X-ray properties of massive clusters. This estimator, essentially the amplitude of the galaxy-cluster centre cross-correlation function, B_{gc} such that $\xi(r) = B_{gc} r^{-\gamma}$, is effectively the net number of galaxies within some aperture and brighter than some absolute magnitude scaled by the luminosity function and the spatial distribution function. Using an aperture of $0.5 h_{50}^{-1}$ Mpc, Yee and Ellingson [2003] found B_{gc} scaled with mass with a $B_{gc} - M_{vir}$ slope of 0.61 ± 0.10, consistent with their expectations of $\gamma/3$ where $\gamma = 1.8$, comparable to the slope of the density profile at their relatively small radius.

More recent estimators take advantage of the distinctive nature of cluster galaxies, predominantly selecting red galaxies [Andreon and Bergé, 2012; Andreon and Hurn, 2010], or developing a matched filter that not only gives an estimate of the richness but also computes the probably of a galaxy being a member of

the group [Rozo et al., 2009, 2011; Rykoff et al., 2012]. Selecting red sequence galaxies allows one to select a sample that is significantly different from the field (and therefore less likely to be contaminated). For a sample of cluster members Rozo et al. [2009] calculate richness $\lambda = \sum_i p_i$ where p_i is found by evaluating the ith galaxy's radial position, i-band luminosity and $g-r$ colour. As described in Rozo et al. [2009], these properties are matched against the projected NFW of Bartelmann [1996], a standard Schechter luminosity function [Schechter, 1976] with a passively evolving characteristic magnitude, and a Gaussian colour distribution centred on the red sequence at a given redshift. For a sample of 2000 maxBCG clusters with X-ray luminosity from the ROSAT All Sky Survey, this richness was found to have reduced scatter as a mass proxy compared to other available data where Rykoff et al. [2012] found $L_X \propto \lambda^{1.69\pm0.06}$ with a scatter of $63 \pm 2\%$. Though this scatter is larger than the scatter observed by Budzynski et al. [2012], equivalent to 19%, the differences in selection, definition of richness and the use of ROSAT L_X rather than mass make direct comparison somewhat difficult.

Rozo et al. [2011] examine this last richness estimator to further understand the sources of scatter in the mass proxy. They found that, in comparison to the expected Poisson noise, the scatter in the definition of the red sequence, as well as measurement errors on photometry or photometric redshifts had little impact on the scatter in richness. Halo triaxiality, where the assumption of spherically symmetric halos breaks down due to an ellipsoidal mass distribution, was found to introduce levels of scatter comparable to Poisson noise, whilst cluster miscentering was the most significant source of scatter. Rykoff et al. [2012] further experiment with the colour selection, adding a second Gaussian to their colour

filter to account for the "blue cloud", finding that it significantly increased scatter in a $L_X - \lambda$ relation.

As these recent richness estimators filter primarily against a general population of galaxies, this makes them difficult to use in lower mass systems where the red-fraction of member galaxies is significantly lower than in massive clusters. Allowing the definition of richness to include a broad array of galaxy types, background correction becomes significantly more important, and sources of scatter due to the evolution of this other population can have a substantial effect.

Cluster Luminosity

An early example of the attempted use of luminosity to estimate cluster mass is seen in Zwicky [1937], which, as noted in Chapter 1, lead to the inferred presence of dark matter. This early measurement was made assuming a mass-to-light ratio comparable to that of local stars, and instead computed the stellar mass of the cluster, rather than the total mass. Though cluster luminosity can be used to determine the stellar mass of a cluster [e.g. Gonzalez et al., 2007], this light can also be related to the total mass of the halo much like cluster richness.

An early review of the mass-to-light of galaxy groups and clusters can be found in the study of Girardi et al. [2002, and references therein]. Measurements initially found flat, mass independent mass-to-light ratios on cluster scales ($M/L_B \sim 200 - 300h^{-1}$ $M_\odot/L_\odot$). However, these estimates were lacking the statistical size and mass range of modern studies. Through an analysis of 294 systems with masses in the range $\sim 10^{12}$ $M_\odot$ to $\sim 10^{15}$ $M_\odot$, Girardi et al. [2002] found a mass-luminosity relation $M_{vir} \propto L_{B_j,vir}^{1.34\pm0.03}$, indicating a mass dependent mass-to-light ratio. They note however that this result is subject to biases introduced

by the short, blue filter they use. This wavelength is a better tracer of recent star formation activity, rather than the stellar mass of the galaxies. They instead recommend observations in the infrared to better probe the stellar mass.

Such a study was performed by Lin et al. [2003], finding that the deprojected infrared K-band luminosity of a sample of 27 clusters from 2MASS [Skrutskie et al., 2006] evolved with X-ray, $M-T$, derived masses as $L_{K,500} \propto M_{500}^{0.69\pm0.09}$ with 28% scatter at fixed mass. This corresponds to $M_{500} \propto L_{K,500}^{1.44}$ when compared to the Girardi et al. [2002] result. This result had two implications, that either star formation was more efficient in low mass halos or that stars are more easily stripped into the Intra-Cluster Light (ICL) at high mass. Current observations, whilst measuring substantial ICL [e.g. Zibetti et al., 2005], indicate that the stellar mass fraction, and therefore the efficiency of star formation, peaks in halos $\sim 10^{12}$ $M_{\odot}$, decreasing towards high mass [Budzynski et al., 2014; Leauthaud et al., 2012; Moster et al., 2010].

More recent results from the high-L_X sample of clusters from the Local Cluster Substructure Survey (LoCuSS) [Mulroy et al., 2014] found $M_{500} \propto L_{K,500}^{0.97\pm0.17}$ with only $10^{+0.07}_{-0.05}$% scatter. The main difference between this result and those of previous studies is the use of masses derived from weak lensing analyses rather than X-ray derived masses. Lin et al. [2003] indicate a large component of their scatter is the 17% scatter expected from the $M-T$ relation alone, and indeed, repeating their analysis with hydrostatic X-ray masses Mulroy et al. [2014] find that the scatter increases to 25^{+11}_{-10}%. The large difference in slope between Lin et al. [2003] and Mulroy et al. [2014] is possibly due to the larger range in masses available to Lin et al. [2003]. Accessing lower mass halos where the stellar mass fraction is higher than in cluster mass halos will steepen the observed mass-luminosity

relation.

Clearly the use of cluster luminosity is a powerful mass proxy, though care must be taken in how one measures the cluster luminosity. As we have discussed, the choice of wavelength can significantly bias results without first considering the group or cluster property that your choice of wavelength probes. However, even in the absence of K-band measurements, such a comparison is still possible. Popesso et al. [2007], for example, compute a mass-luminosity relation with SDSS r-band luminosities, finding $L_{op} \propto M_{200}^{0.92\pm0.03}$ using dynamical masses for a sample of clusters from the RASS-SDSS galaxy cluster survey.

Chapter 3

ON OPTICAL MASS ESTIMATION METHODS FOR GALAXY GROUPS

3.1 Introduction

An understanding of the mass of galaxy groups and clusters is essential to the study of these structures and their evolution. For example, use of the concept of self-similarity, whereby larger systems behave as scaled up versions of smaller ones [e.g. Alard, 2013; Kaiser, 1986; Navarro et al., 1997], requires knowledge of the mass of the objects in question. Studies of self-similarity based on cosmological simulations have direct access to dark matter particle information, which in turn allows the user to construct robustly defined halo masses. However, this luxury is not available in the case of observational studies, and comparisons of baryonic properties, such as X-ray luminosity and gas entropy, with self-similar

expectations require reliable estimates of the mass of the host halos.

In practice, groups and clusters are observed to depart from self-similar expectations [Arnaud and Evrard, 1999; Neumann and Arnaud, 2001; Osmond and Ponman, 2004; Ponman et al., 1999], and these departures offer valuable evidence about the nature of additional astrophysical processes, such as cooling and cosmic feedback, which break the symmetries observed in simple gravity-only models. Estimates of halo mass, and the corresponding characteristic overdensity radii of systems, are an essential element in the study of the baryon astrophysics. The effects of these additional processes are especially notable within poor galaxy groups ($M \lesssim 10^{14}$ $M_{\odot}$), so it is unfortunate that it is precisely in such systems that masses are most difficult to determine.

Most existing methods of mass estimation rely on the group or cluster mass distribution affecting a baryonic tracer population, which then provides a measurable mass proxy. The simplest, and oldest, of these approaches uses the dynamics of member galaxies within the cluster halo, whose velocity dispersion is related to system mass through the Virial Theorem [e.g. Zwicky, 1937]. This approach is often applied to large redshift surveys as a useful and relatively straightforward mass estimator [e.g. Eke et al., 2004; Ramella et al., 2004; Robotham et al., 2011]. This estimator requires that group membership be well-established, with limited contamination from foreground and background galaxies, though robust estimators of group velocity dispersion, such as the gapper estimator [Beers et al., 1990], help to reduce the impact of outliers in the galaxy velocity distribution. The method also requires that the galaxy tracers are relaxed – i.e. their motions are not strongly affected by dynamical disturbances such as group mergers or infall. Studies of simulated clusters by Biviano et al. [2006] indicate that virial

mass estimates are subject to biases of 10% or more. There are also indications, from comparisons between galaxy dynamics and X-ray temperatures, that in poor groups velocity dispersions may be subject to unexplained downward biases which can be substantially larger [Osmond and Ponman, 2004].

An alternative approach uses the hot gas within the dark matter halo of groups and clusters. This gas, heated by gravitational collapse to virial temperatures, radiates X-rays. The surface brightness distribution and spectrum of this radiation can be used to infer the radial distribution of gas density and temperature, and hence, via hydrostatic equilibrium, to estimate system mass [e.g. Mulchaey, 2000]. Such an analysis requires high quality X-ray data, with radially resolved spectroscopy. With poorer quality X-ray data, it is still possible to derive useful mass estimates if a mean X-ray temperature can be measured, applying well-established mass-temperature relations for groups and clusters [e.g. Sun et al., 2009]. However, even this may not be available for many galaxy groups, since they tend to have low X-ray surface brightness. Moreover, as X-ray data are expensive to acquire and existing all sky surveys such as RASS [*ROSAT* All Sky Survey, Voges et al., 1999] are too shallow on average, high quality X-ray spectral imaging is still not available for the majority of the sky. The upcoming surveys to be performed by the *eROSITA* instrument [Merloni et al., 2012], may help moderate this, though the detection of the lowest surface brightness groups may still be a challenge.

The most direct estimator of gravitating mass is gravitational lensing. The distortions imposed on the light from background galaxies as it passes through the gravitational potential of a foreground cluster allows the surface density of mass along the line of sight to be derived [Narayan and Bartelmann, 1996]. How-

ever, the magnitude of these lensing distortions is so small for poor groups that at present lensing studies at such low masses are largely confined to stacking analyses. These extract an average mass distribution, destroying information on the properties of individual groups [Parker et al., 2005].

Due to the availability of large galaxy surveys, the ability to estimate the masses of galaxy groups and clusters from their galaxy contents alone is an attractive possibility. The aim of this Chapter is therefore to explore ways of estimating masses given only basic properties of member galaxies available from surveys such as SDSS [Ahn et al., 2014] and GAMA [Driver et al., 2011]. We will evaluate the performance of these estimators using a sample of groups for which X-ray based masses have been well-constrained.

X-ray bright groups appear to constitute a particular subset of the group population [e.g. Rasmussen et al., 2006], so to check these results and obtain access to a wider range of groups, we will also investigate the performance of our mass proxies on a sample of groups drawn from a cosmological simulation.

In §3.2 we discuss the data used in this study. Section 3.3 presents the mass proxies that we use and in §3.5 we present the results for each methodology. In §3.6 and §3.7, we present and discuss analogous results for a sample of groups drawn from a cosmological simulation. Finally, in §3.8 we discuss the implications of our results for the practical problem of estimating the masses of galaxy groups.

Throughout the paper, we adopt a simple ΛCDM cosmology with $\Omega_m = 0.3$, $\Omega_\Lambda = 0.7$ and $H_0 = 70$ km s^{-1} Mpc^{-1}. When converting literature results to our cosmology we adopt $h = H_0/100$ km s^{-1} Mpc^{-1} $= 0.7$ when required. Due to the small range in current values of H_0 and the relatively large scatter in mass proxies observed the choice of cosmology is not a significant concern, we

therefore report values in physical units rather than as a function of h_{70}, where $h_{70} = H_0/70$ km s^{-1} Mpc^{-1}. The analysis performed here makes use of the R statistical package [R Development Core Team, 2009][1].

3.2 Data

This study requires a sample of galaxy groups with both optical data, for use in constructing mass proxies, and robust mass estimates that are independent of optical properties, against which mass-proxy scaling relations can be investigated and calibrated. We take our canonical masses from high quality X-ray analyses and use the Sloan Digital Sky Survey (SDSS) as the source of our optical data.

Throughout this work we take the mass derived from hydrostatic X-ray analyses as the canonical mass of a halo. We note however that in both simulations (where the true mass is known) and observations (using weak lensing mass estimates) the hydrostatic mass is found to be biased low by $\sim 10 - 30\%$ [e.g. Mahdavi et al., 2013; Nelson et al., 2014]. Though this bias is observed to be reduced for relaxed systems, it is probable that any X-ray selected sample we use here may be affected, which we do not attempt to correct for.

3.2.1 X-ray

Our galaxy group sample is primarily drawn from the Sun et al. [2009, hereafter S09] *Chandra* study of galaxy groups. This uses a sample of 43 groups with ACIS imaging from the *Chandra* archive. The groups were selected to have low temperature ($T_{500} \lesssim 2.7$keV) and redshift ($0.015 < z < 0.13$), together with a

[1] www.r-project.org

relaxed morphology (i.e. emission is not significantly substructured or disturbed). These criteria ensure that these groups have low mass and high quality X-ray data suitable for a hydrostatic mass analysis. The lower redshift limit ensures that r_{2500}, the radius enclosing a mean density 2500 times the critical density of the universe, for each group lies within the ACIS field of view, allowing S09 to trace gas properties to large radii.

The result is one of the most robust X-ray analyses of low mass groups currently available. Additionally, the low redshifts of these groups implies that their member galaxies should be well sampled by the SDSS for groups which lie within the Sloan survey area. It should be noted that this sample is an X-ray selected sample and may differ systematically from optically selected samples, as we will discuss later.

The groups of S09 were split into four tiers depending on the extent to which they were able to trace gas properties from the emission centre. We use the two best subsets for which M_{500} was either measured at r_{500} or was extrapolated based on gas properties at a large fraction of r_{500} ($\gtrsim 0.68 r_{500}$) – 'Tier 1' and 'Tier 2' respectively. There are 23 groups for which this was possible, 15 of which are covered by the SDSS.

To supplement this sample, and to usefully extend the mass range for calibration of mass proxies, we add 4 groups and 8 clusters with masses determined by Sanderson and Ponman. The cluster analysis is described in Sanderson and Ponman [2010, hereafter SP10]. The full sample included 20 high flux *Chandra* clusters drawn from the flux-limited sample of Ikebe et al. [2002]. The four groups were analysed in exactly the same way. Our superset sample therefore consists of 27 groups and clusters. However, in what follows we will exclude 5 groups for

which galaxy membership was not well-defined (section 3.2.2) or for which SDSS spectroscopic completeness was inadequate (section 3.2.2), leaving a final sample of 22 systems.

The position and redshift of each of our groups was extracted from the NASA Extragalactic Database (NED). We note that the cosmology used by S09 ($\Omega_m = 0.24$, $\Omega_\Lambda = 0.76$ and $H_0 = 73$ km s^{-1} Mpc^{-1}) differs from that used here and in SP10. Given the low redshift of our groups ($z \lesssim 0.1$) the effect of Ω_m and Ω_Λ is negligible. However, we apply a correction for H_0, scaling masses from S09 to $\mathrm{M}_\odot h_{70}^{-1}$.

3.2.2 Optical

Optical counterparts were selected from the Seventh Data Release (DR7) of the Sloan Digital Sky Survey (SDSS) [Abazajian et al., 2009]. Specifically we use data from the DR7 release of the Value-Added Galaxy Catalogue (VAGC) [Blanton et al., 2005]. This catalogue features improvements on the original survey, including photometric calibration [Padmanabhan et al., 2008] and source identification. The VAGC also provides a set of K-corrected absolute magnitudes [Blanton and Roweis, 2007] such that

$$M = m - 5\log\left(\frac{D_L(z)}{10\mathrm{pc}}\right) - K(z) + 5\log h \quad , \tag{3.1}$$

where $D_L(z)$ is the luminosity distance to the galaxy, M and m are the absolute and apparent magnitude respectively and $K(z)$ is the K-correction. We use K-corrected catalogues where the K-correction has been found for filters shifted to $z = 0.1$.

The original DR7 is nominally spectroscopically complete to an apparent Petrosian magnitude limit of $m_r \approx 17.77$, however this can vary somewhat across the sky. Following Berlind et al. [2006] we adopt a more conservative r-band magnitude limit of 17.5 to ensure more uniform coverage with an average completeness of $\sim 95\%$ as discussed below (Section 3.2.2). We further subset our galaxy sample by selecting only objects that meet the Blanton et al. galaxy criteria, i.e. have the bitmask `'VAGC_SELECT'>=4`, reducing potential contamination from spurious sources.

Group Membership

To explore the impact of galaxy selection methods on our mass proxies, we construct two optical group samples. A 'volumetric' sample, based upon selecting galaxies within a quasi-cylindrical volume about each X-ray group, and a 'Friends-of-Friends' (FoF) sample constructed by performing a friends-of-friends analysis on the galaxies in the vicinity of each group and matching the extracted groups to the X-ray groups. This allows us to examine effects such as the imposition of a fixed metric aperture and the differing treatment of interlopers.

The volumetric sample is initially built by selecting galaxies from the VAGC spectroscopic sample within cones of radius 5 Mpc about the group positions drawn from NED. An initial velocity cut of ± 1000 km s^{-1} about the group redshift, also drawn from NED, is also applied. We note that these position and velocity centroids are not consistently defined due to the heterogeneous nature of the NED service. The sample's centroids constitute a mix of X-ray, photometric and radio centroids. We do not refine these centres using the extracted spectroscopic galaxies, but comment on their impact in later sections.

Using galaxies from a smaller, 1 Mpc, aperture we then determine a velocity dispersion, σ, for the system using the *gapper* estimator from Beers et al. [1990]. This estimator is unbiased in low multiplicity systems and is robust against outliers. For a system of N galaxies each with a velocity v_i we first order these velocities and determine the gap between pairs as $g_i = v_{i+1} - v_i$ for $i = 1, ..., N-1$. Each gap is weighted by its position within the ordered list, $w_i = i(N-i)$. The *gapper* estimator is then defined as

$$\sigma_{gap} = \frac{\sqrt{\pi}}{N(N-1)} \sum_{i=1}^{N-1} w_i g_i \quad . \tag{3.2}$$

As discussed by E04, if we assume that the brightest group galaxy (BGG) is stationary within the group halo, then σ_{gap} needs to be modified by a factor $\sqrt{N/(N-1)}$ giving

$$\sigma = \sqrt{\frac{N}{N-1}\sigma_{gap}^2} \quad . \tag{3.3}$$

Our final volumetric group membership is then constructed iteratively by applying this 3σ clip until the number of galaxies within 1 Mpc converges (i.e. velocity dispersion converges). The galaxy sample within the 5 Mpc cone is then refined by applying a 3σ clip using the same value of σ. We assume that our galaxy sample consists of two populations, an interloper-contaminated group population within a 1 Mpc aperture, and a local background which we determine within an annulus of radius 3 – 5 Mpc about the group centre. Where possible, we use this local background to statistically subtract interloper contamination from our mass proxies. This annulus was chosen to be large enough to reduce any group contribution to this local background even for the largest systems (e.g. $r_{200} \sim 2$ Mpc for $M_{200} \sim 1 \times 10^{15}$ $M_\odot$, assuming a mean density $200\rho_c(z)$ at

$z = 0.1$). This background may include infalling galaxies or field galaxies in the Hubble flow that have similar redshifts to the group itself. Mamon et al. [2010] analysed an ensemble of halos from a cosmological simulation and found the surface density of interlopers within a σ clipped volume to be approximately uniform with radius, so our background subtraction should be effective so long as foreground or background structures contribute equally to our source and background regions. The application of this background correction is described in section 3.3.

Due to sparse spectroscopic coverage for one group our calculation fails to converge on a velocity dispersion and group membership. We exclude this group from our analysis, reducing the sample to 26 groups.

To generate the Friends-of-Friends group sample we follow the algorithm described by E04. This was originally developed for the 2-degree Field Galaxy Redshift Survey [2dFGRS, Colless et al., 2001]. We use the E04 linking length calibration, whereby perpendicular and parallel linking lengths are determined as $\ell_\perp = b/n^{1/3}$ and $\ell_\parallel = R\ell_\perp$ respectively. Following E04, the parameters b and R are found for each galaxy as

$$b = b_{\rm gal}\left(\frac{\Delta}{\Delta_{\rm fit}}\right)^{\epsilon_b} \quad \text{and} \quad R = R_{\rm gal}\left(\frac{\Delta}{\Delta_{\rm fit}}\right)^{\epsilon_R} \quad , \tag{3.4}$$

where Δ is the galaxy overdensity relative to the background galaxy density, taken to be n. Δ is estimated within a cylinder of comoving radius $1.5h^{-1}$ Mpc and depth R_{gal} times the width of this cylinder centred on each galaxy. This scaling is intended to reduce biases in recovered halo size introduced by mass-dependent properties such as halo concentrations [E04]. n is determined by integrating the

universal SDSS luminosity function [Blanton et al., 2003] to the magnitude limit at the redshift of a given galaxy. The parameters $b_{\rm gal}, R_{\rm gal}, \epsilon_b, \epsilon_R$ and $\Delta_{\rm fit}$ are taken from the E04 calibration.

We apply this to all galaxies within a cone with a radius of at least 5 Mpc and extending to a redshift of 0.2 about each volumetric group. This volume will contain more than one FoF group for a given X-ray system. We select the central group by matching the NED position to the centre of identified groups within a range of ± 0.05 in redshift.

The FoF group centre is determined using an iterative centre of light approach similar to that described in Robotham et al. [2011]. Weighting each galaxy by its luminosity and velocity offset from the mean, a centroid is derived at each step and the galaxy furthest from this is discarded. This process is repeated until only two galaxies remain, and the brightest of these is then taken as the group centre. The FoF group redshift is taken to be the median redshift of member galaxies.

Spectroscopic Completeness and Survey Coverage

Whilst the SDSS spectroscopy is nominally $\gtrsim 85\%$ complete to $m_r = 17.77$ [Blanton et al., 2005], variation in the target selection function, as well as incompleteness due to fibre collisions and obscuration from bright foreground objects, can lead to a variable level of completeness across the sky [Berlind et al., 2006]. Our initial apparent magnitude cut of $m_r \leq 17.5$ allows us to be confident of greater, and more uniform, completeness.

Correcting for fibre collisions is especially important in regions of high density such as the centres of galaxy groups and clusters. This problem is moderated slightly for the SDSS due to some overlap in its tiling pattern allowing for repeat

visits to regions of the sky. However, as this overlap covered only a small fraction of the observed field, fibre collisions still need to be considered. Failure to account for this would result in an underestimate of galaxy group richness and galaxy overdensities within these regions. We use the NYU-VAGC datasets in which each collided galaxy is assigned the spectroscopic redshift of the galaxy it collided with [Blanton et al., 2005]. This correction, found by Blanton et al. [2005] to affect $\sim 6\%$ of galaxies globally, is used for 10.4% of the galaxies in our sample. As we focus on regions with known groups or clusters, i.e. high density galaxy fields, this increase compared to the global average is to be expected.

The incidence of collided galaxies is larger in the dense central regions, and these central collisions are concentrated in 9 of the final 22 groups, with, on average, two corrected galaxies in each. In case the 'cloning' of redshifts in these systems introduces any significant bias into their calculated velocity dispersions, we will pay special attention to them in the analysis presented in §3.5.3.

We assess the level of any remaining spectroscopic incompleteness by direct comparison of the spectroscopic and photometric data. Selecting both photometric and spectroscopic galaxies (within our apparent magnitude limited sample) within a cone about a point on the sky, we can define completeness at each position as the ratio of the number of galaxies with a redshift to the total number photometric galaxies available. To control the statistical uncertainty on each point, yet ensure we have resolution as high as possible in dense regions, the size of the cone is adjusted to contain at least 25 spectroscopic galaxies. In most cases we find completeness close to unity, with an average value of $\sim 95\%$ within our groups. The inverse of the local completeness is included as a weight on each galaxy when applied to the majority of our methods as described in §3.3. As a

dynamical mass estimator is robust to the effects of incompleteness (assuming no velocity substructures), we do not attempt to correct for incompleteness in the case of dynamical mass proxies.

We also use the photometric data to derive a correction for fields located on the edge of the survey. Using a coarsely smoothed map of the photometric galaxy density we define the survey edge to be a contour $2\sigma_\Sigma$ below the mean surface density, where the mean and standard deviation, σ_Σ, are found iteratively, excluding regions of high (the group) and low (beyond the survey edge) density. Figure 3.1 illustrates an example completeness map for one of our groups which falls close to the SDSS survey boundary. We use this knowledge of the survey boundary to account for any missing area within each group, as described in §3.3.

To ensure that we do not use data requiring very large corrections for spectroscopic completeness or survey coverage, we examine the 26 groups remaining in the current sample, and exclude those which have a central or background completenesses $< 70\%$ (within a 1 Mpc aperture and a 3-5 Mpc annulus respectively), or have $< 70\%$ and $< 50\%$ footprint coverage, respectively, in the source and background regions. This excludes an additional four groups, reducing the sample to 23 systems, four of which intersect the survey edge. We exclude one last group due to a heavily contaminating background structure that could not be satisfactorily excluded. The final group sample consists of 22 groups. Their X-ray and initial optical properties are described in Table 3.1.

Luminosity Completeness

As our optical data are drawn from an apparent magnitude limited survey, which results in a redshift-dependent absolute magnitude limit, a final correction factor

Table 3.1: Our group + cluster sample.

Group	z[a]	RA[a] (deg)	Dec[a] (deg)	$N_{1\mathrm{Mpc}}$[b]	σ[c] (km s^{-1})	T_X (keV)	$M_{500,X}$ ($10^{13}\mathrm{M}_\odot$)	Reference[d]
3C442A	0.0263	333.70	13.840	47	409^{+41}_{-23}	1.34 ± 0.04	$4.07^{+0.23}_{-0.42}$	(1)
Abell0160	0.0447	18.21	15.515	54	825^{+95}_{-65}	1.68 ± 0.10	$8.24^{+1.11}_{-1.15}$	(1)
Abell1177	0.0316	167.37	21.695	27	326^{+52}_{-31}	$1.37^{+0.06}_{-0.07}$	$5.51^{+0.88}_{-0.76}$	(1)
Abell1275	0.0637	172.49	36.674	23	339^{+70}_{-39}	$1.46^{+0.08}_{-0.07}$	$7.20^{+3.13}_{-1.74}$	(1)
Abell1367	0.0220	176.19	19.698	164	842^{+53}_{-42}	3.22 ± 0.18	13.20 ± 2.88	(2)
Abell1692	0.0848	198.07	-0.932	25	678^{+131}_{-79}	$2.61^{+0.16}_{-0.24}$	$10.12^{+3.12}_{-1.99}$	(1)
Abell1795	0.0620	207.22	26.591	62	742^{+64}_{-43}	$5.62^{+0.36}_{-0.35}$	53.00 ± 7.50	(2)
Abell1991	0.0587	223.62	18.631	52	665^{+73}_{-53}	$2.68^{+0.10}_{-0.08}$	$13.97^{+2.61}_{-1.98}$	(1)
Abell2029	0.0770	227.73	5.745	74	1465^{+118}_{-79}	8.96 ± 0.30	71.50 ± 17.10	(2)
Abell2092	0.0669	233.33	31.149	34	567^{+84}_{-50}	$1.67^{+0.13}_{-0.12}$	$9.33^{+1.89}_{-1.69}$	(1)
Abell2142	0.0909	239.59	27.232	63	1294^{+151}_{-118}	$9.50^{+0.43}_{-0.42}$	125.00 ± 14.60	(2)
Abell2147	0.0350	240.57	15.963	147	924^{+61}_{-47}	3.69 ± 0.18	26.70 ± 3.72	(2)
Abell2199	0.0299	247.16	39.551	152	848^{+49}_{-37}	$4.50^{+0.20}_{-0.24}$	31.50 ± 4.25	(2)
Abell85	0.0594	10.46	-9.304	54	577^{+58}_{-37}	6.64 ± 0.20	47.40 ± 5.05	(2)
MKW04	0.0200	180.99	1.888	71	513^{+60}_{-41}	1.58 ± 0.09	$5.06^{+0.74}_{-0.71}$	(1)
NGC4104	0.0282	181.66	28.174	50	461^{+45}_{-27}	$1.41^{+0.09}_{-0.06}$	$5.06^{+0.57}_{-0.55}$	(1)
NGC4325GROUP	0.0252	185.78	10.621	29	305^{+49}_{-22}	1.00 ± 0.02	3.65 ± 0.44	(2)
NGC5098	0.0368	200.07	33.144	47	510^{+56}_{-37}	0.96 ± 0.04	$2.09^{+0.29}_{-0.48}$	(1)
NGC6338GROUP	0.0282	258.85	57.411	68	584^{+52}_{-35}	$2.03^{+0.12}_{-0.11}$	8.99 ± 0.51	(2)
RXJ1022.1+3830	0.0543	155.53	38.515	42	800^{+102}_{-63}	$1.94^{+0.20}_{-0.14}$	$8.34^{+1.37}_{-1.46}$	(1)
RXJ1159.8+5531	0.0808	179.96	55.534	14	354^{+74}_{-24}	$1.84^{+0.14}_{-0.08}$	$8.66^{+3.23}_{-1.17}$	(1)
UGC05088	0.0274	143.36	34.048	14	234^{+54}_{-20}	0.81 ± 0.03	$1.54^{+0.38}_{-0.25}$	(1)

[a] Coordinates as listed by the NED.

[b] Group multiplicity within 1 Mpc and brighter than $m_r = 17.5$.

[c] Velocity dispersions calculated for the innermost 1 Mpc galaxies of the volumetric selection.

[d] Masses and temperatures drawn from (1) Sun et al. [2009, S09]; (2) Sanderson and Ponman [2010, SP10]

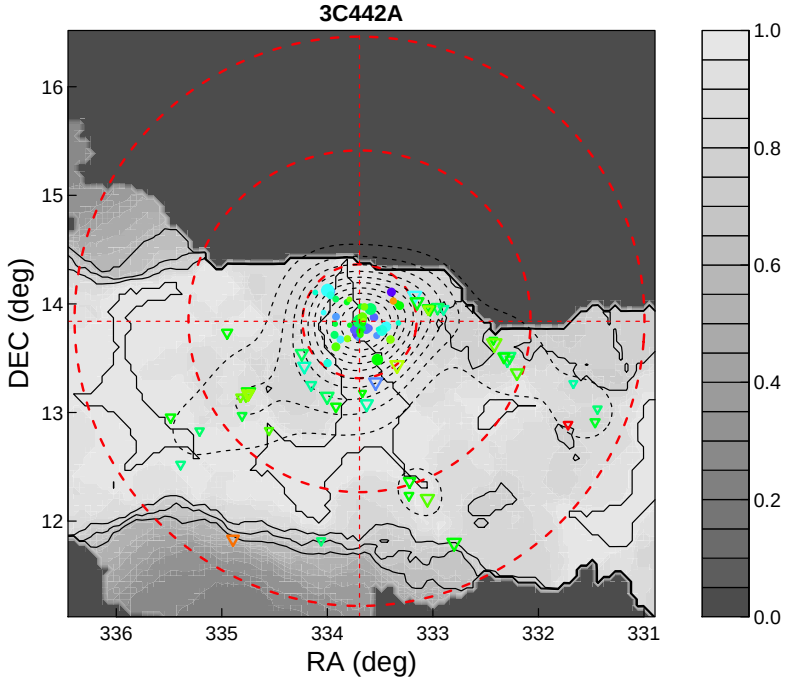

Figure 3.1: Completeness map for the group 3C442A. Greyscale contours indicate the measured spectroscopic completeness as described in the text, with black contours delineating 100, 80, 70 and 60% completeness levels. Dashed red circles indicate our 1, 3 and 5 Mpc boundaries representing the areas within which membership and background are determined respectively. The points represent the galaxies that pass through the 3σ clip, filled circles represent member galaxies, open triangles all galaxies beyond 1 Mpc, whilst colour represents redshift (galaxies at larger redshift are redder in the range $0.024 \lesssim z \lesssim 0.030$).

is needed to rescale results to the same absolute magnitude for those mass proxies which scale with the number or luminosity of galaxies.

To correct for this, we integrate over the galaxy luminosity function to calculate two factors,

$$c_N = \frac{\int_{L_r^{faint}(z)}^{L_r^{bright}} \Phi(L_r) \mathrm{d}L_r}{\int_{L_r^{faint}}^{L_r^{bright}} \Phi(L_r) \mathrm{d}L_r} \quad , \tag{3.5}$$

and

$$c_L = \frac{\int_{L_r^{faint}(z)}^{L_r^{bright}} L_r \Phi(L_r) \mathrm{d}L_r}{\int_{L_r^{faint}}^{L_r^{bright}} L_r \Phi(L_r) \mathrm{d}L_r} \quad , \tag{3.6}$$

to extrapolate number (c_N) and luminosity (c_L) estimates to a fixed absolute magnitude. We use $\Phi(L)$ to be a standard Schechter luminosity function [Schechter, 1976] with parameters from the r-band cluster luminosity function of Popesso et al. [2005] ($M_r^* - 5\log h = -21.35 \pm 0.19$ and $\alpha = -1.30 \pm 0.06$). We set the faint limit to be $M_r = -16.5$, comparable to the faintest absolute magnitude of galaxies within our sample and converted to luminosity assuming $M_{r,\odot} = 4.67$[1]. The correction is therefore ~ 1 for the closest groups, and reaches values of $c_N = 0.11$, $c_L = 0.65$ for our most distant, at $z \approx 0.09$.

3.3 Mass Proxies

3.3.1 Richness and Luminosity

One of the simplest mass proxies available to us is the number of galaxies brighter than a specific luminosity contained within a galaxy group. Through hierarchical formation we expect larger dark matter halos to have formed through the assimilation of smaller structures, and the total number of galaxies will be conserved during this process. Whilst there are processes that can reduce the final richness of groups, such as the orbital decay and merger of large galaxies, the impact of this on richness would be limited by the large dwarf populations in groups. In the

[1] http://mips.as.arizona.edu/~cnaw/sun.html

absence of major trends in star formation efficiency and trends in the luminosity function parameters with halo mass, we would naively expect richness to scale approximately linearly with mass. In practice this is not the case; star formation efficiency, and therefore stellar mass fraction, have been shown to vary with halo mass [e.g. Leauthaud et al., 2012; Moster et al., 2010], whilst luminosity functions have been found to become significantly more "field"-like in lower mass haloes [e.g. Hansen et al., 2005; Robotham et al., 2010; Zandivarez and Martínez, 2011], both of which will affect the number of galaxies observed above a given luminosity. We discuss the impact these have on our naive expectations in Section 3.5.1.

Richness-based mass proxies have previously been studied by a number of different authors. Budzynski et al. [2012], for example, use a mass-richness relation to determine the masses of their high mass group and cluster sample ($M_{500} > 10^{13.7}$ $M_{\odot}$). Other studies examine the mass-richness relation for a subset of galaxy types, such as red sequence galaxies [Rozo et al., 2009], and sources of scatter therein [Rozo et al., 2011], as well as Andreon and Hurn [2010] who similarly select only red galaxies. Rykoff et al. [2012] extend the richness estimator of Rozo et al. [2009] to include blue galaxies, finding that it increases the observed scatter in the L_X-richness relation. However, rather than restricting our analysis to a single class of galaxy, which would limit the diversity of groups suitable for analysis, we use all galaxies within each group.

To avoid the circularity involved in counting galaxies within some radius (e.g. an overdensity radius) which scales with mass, we employ a simple aperture-limited richness for our volumetric sample. Richness is defined as the number of galaxies within 1 Mpc of the group centre, corrected for incompleteness. Each

galaxy's contribution within the aperture is weighted by the inverse of its local spectroscopic completeness, and the number counts, after background subtraction, are corrected to our standard absolute magnitude range as described in §3.2.2 above. We make no correction for projection effects or for the imposition of a fixed aperture. Our aim here is to keep the procedure simple and to calibrate out these effects by comparison with the X-ray masses.

To correct for interloper contributions we first estimate the surface number density in a background annulus of radius 3 to 5 Mpc. Again, each galaxy contribution is weighted by its local spectroscopic completeness. If the annulus intersects the survey edge, we estimate the area that is covered and determine the surface density within this area. Using this surface density we estimate the number of background galaxies within the 1 Mpc aperture (again, correcting for the survey footprint if necessary). We subtract this background estimate from our total richness and rescale to a fixed absolute magnitude limit using equation (3.5) to determine our final corrected volumetric richness estimate, $\tilde{N}_{1\mathrm{Mpc}}$.

For our FoF sample, the procedure is simpler. Here no background subtraction is performed – it is assumed that background contamination is negligible – and the FoF multiplicity (N_{FoF}) is corrected for spectroscopic and survey incompleteness and scaled to our standard absolute magnitude, to give the corrected richness estimate, $\tilde{N}_{FoF}$.

A closely related mass proxy to richness is the total optical luminosity of a group. This has the advantage over richness of being less sensitive to variations in the faint end slope of the luminosity function. Furthermore, galaxy mergers conserve luminosity but not number, although in practice it is known that mergers and tidal interactions can remove stars from galaxies, forming an intra-cluster

light [ICL, see, e.g. Gonzalez et al., 2005; Zibetti et al., 2005] component. Our SDSS-derived luminosities do not include any contribution from ICL, and rather than attempting to correct for any trends in ICL, we assume that they can be calibrated out in our mass-luminosity analysis below. We convert absolute magnitudes to luminosities in solar units assuming $M_{\odot r} = 4.67$, and treat background and correction as for richness. The final luminosity-based mass proxies, $L_{1\mathrm{Mpc}}$ and L_{FoF}, are then derived by rescaling to our standard absolute magnitude using the c_L factor from Equation (3.6).

3.3.2 Overdensity

It is has been established that dark matter haloes in simulations are generally well represented by Navarro, Frenk and White density profiles [NFW, Navarro et al., 1996],

$$\rho(r) = \frac{\rho_0}{\frac{r}{r_s}\left(1+\frac{r}{r_s}\right)^2} \quad . \tag{3.7}$$

where r_s is the scale radius and ρ_0 is the normalisation of the NFW profile.

Under the assumption that galaxies trace mass, it is possible to use the galaxy density profile to infer the total mass of the system. A similar approach was employed by Hansen et al. [2005], who determined galaxy surface densities by counting galaxies within cylinders of increasing radius about each group or cluster. By applying a scale factor, these surface densities were converted into 3D densities and, comparing to the field density based on the Blanton et al. [2003] SDSS luminosity functions, characteristic overdensity radii were derived. These radii, $r_{200}^{\mathcal{N}}$, were defined to be the radius at which the estimated galaxy density was $200/\Omega_m$ times the mean galaxy density, where the factor of Ω_m allows conversion

from mean to critical density.

We expand on this approach by fitting a projected NFW profile to the observed galaxy number distribution and using the resultant NFW profile to determine the radius at which the density of galaxies is $500/\Omega_m$ times that derived from the global luminosity function. This radius should be equivalent to the radius enclosing a mean density of 500 times the critical density. Using a maximum likelihood method, we fit the projected NFW profile derived by Bartelmann [1996],

$$\Sigma_{NFW}(x) = \frac{2\rho_0 r_s}{x^2 - 1} f(x) \quad , \tag{3.8}$$

where $x = r/r_s$ and

$$f(x) = \begin{cases} 1 - \frac{2}{\sqrt{x^2-1}} \arctan \sqrt{\frac{x-1}{x+1}} & x > 1 \\ 1 - \frac{2}{\sqrt{1-x^2}} \operatorname{arctanh} \sqrt{\frac{1-x}{1+x}} & x < 1 \\ 0 & x = 1 \end{cases} \quad .$$

For the volumetric sample we add to this fit a background term, Σ_{bg}, to account for any background in the field, i.e.

$$\Sigma(r) = \Sigma_{NFW}(r) + \Sigma_{bg} \quad . \tag{3.9}$$

Incorporating this background term, we fit the galaxy distribution for each group within its full 5 Mpc, 3σ cone. For the FoF sample, the profile is fit to the FoF-linked galaxies assuming no background contribution.

The fit to the observed number distribution of galaxies involves using equation (3.9) to predict the number of galaxies within each annulus of width dr, centred

at projected radius r,

$$\mathrm{d}N(r) = 2\pi A(r) r \Sigma(r) \mathrm{d}r \quad . \tag{3.10}$$

The constant 2π assumes an annulus of radius r and width $\mathrm{d}r$ is fully covered, and in these cases $A(r) = 1$. As already discussed there are instances where the group intersects the survey edge. For these groups, the factor $A(r) \leq 1$ is used to rescale the area of the annulus as required.

The likelihood, $\mathcal{L}_i$, of observing a galaxy i at radius r_i is

$$\mathcal{L}_i = \frac{2\pi r_i \Sigma(r_i)}{\int_0^{r_{max}} 2\pi r \Sigma(r) \mathrm{d}r} \quad , \tag{3.11}$$

where r_{max} is the largest projected radius of the galaxies included in the fit. The likelihood function that we maximise with respect to r_s and Σ_{bg} is then

$$\mathcal{L} = \prod_i^N \mathcal{L}_i \quad . \tag{3.12}$$

The full analysis is an iterative process, in which we initially use all galaxies within a group's volume, with each galaxy weighted by the inverse of its local completeness. The fitted projected NFW and background terms are then renormalised to reproduce the observed number of galaxies used in the fit.

The group mass is then inferred by integrating the 3D NFW density profile, equation (3.7), using the values of r_s and ρ_0 determined from the fit. This gives a mean galaxy density profile from which we estimate r_{500} as the radius within which the mean number density is $500/\Omega_m$ times the mean galaxy number density. We determine the mean number density using a global luminosity function for the SDSS with r-band parameters of $M_r^* - 5\log h = -20.44 \pm 0.01$, $\alpha = -1.05 \pm 0.01$

and $\phi^* = (1.49 \pm 0.04) \times 10^{-2} h^3$ Mpc^{-3} from Blanton et al. [2003], and integrate from $M_r = -25$ to an absolute magnitude determined by the apparent magnitude limit at the group's redshift.

Using this initial estimate of r_{500} and the fit results as new initial guesses for r_s and Σ_{bg}, we then repeat the fit excluding the central galaxies ($r < 0.1 r_{500}$). This radial cut excludes central galaxies, which may be affected by orbital decay and galaxy merging at the centre of the group potential, and may therefore depart from the expected NFW distribution. We run this core-excised fit twice, iterating r_{500}.

We adopt a similar approach to define a *luminosity overdensity*. As with the richness/luminosity estimators, this extension provides an estimator which should be more robust against variations in the faint end slope of the luminosity function, since this contains many galaxies but not much light. The above analysis is simply modified to weight each galaxy in the likelihood fit by its luminosity. When determining luminosity overdensity we also explicitly add the BGG luminosity, which can represent a substantial fraction of the group total for poor groups, and estimate the mean global luminosity density from the Blanton et al. [2003] luminosity function.

We note that this approach assumes that an overdensity in the baryonic properties (e.g. galaxy number) of a group relates directly to the same overdensity in mass, essentially assuming that light-traces-mass. As demonstrated by the need to excise the core this is not necessarily the case. Indeed, it has been shown that galaxy density profiles are typically a factor of two less concentrated than those of dark matter profiles [e.g. Budzynski et al., 2012]. As we normalise galaxy profiles to recover the observed number and total light of galaxies, this concentration dif-

ference will trade against normalisation, ultimately reducing the observed group overdensity radius compared to what would be expected if the galaxies were concentrated as the underlying dark matter. This should however be a systematic bias we can calibrate out. More importantly, effects such as mass dependent variation in star formation efficiency will likely introduce substantial bias into this analysis which we will discuss more in Section 3.5.2.

3.3.3 Dynamical Mass

Dynamical mass estimation is one of the oldest and most well established techniques. The Virial Theorem, applied to a stable system, leads directly to

$$M \propto r\sigma^2 \quad . \tag{3.13}$$

Eke et al. [2004], calibrating this relation on simulated clusters for the 2dF Galaxy Redshift Survey, with a cosmology of $H_0 = 100h$ km s^{-1} Mpc^{-1} with $h = 1$, find

$$M_{vir} = 5\frac{r_{rms}\sigma^2}{G} \quad , \tag{3.14}$$

where r_{rms} is the RMS group radius and σ is the velocity dispersion found using the gapper estimator described in section 3.2.2. For the same H_0 with a different set of simulations, Robotham et al. [2011] find a substantially higher constant with

$$M_{halo} = 10\frac{r_{50\%}\sigma^2}{G} \quad , \tag{3.15}$$

where $r_{50\%}$ is the radius containing 50% of a group's galaxies. This constant is likely due to the different definition of radius.

Alternatively, this can be cast completely in terms of the velocity dispersion, σ, by assuming $r_\Delta \propto \sigma$ [e.g. Carlberg et al., 1997b; Ramella et al., 2004] such that,

$$M_\Delta = 3\frac{r_\Delta \sigma^2}{G} = 3\sqrt{\frac{6}{\Delta}}\frac{\sigma^3}{H(z)G} \quad , \tag{3.16}$$

where Δ is the overdensity, relative to the critical density, enclosed within r_Δ.

Despite the fact that these methods are well established, we include them to investigate the possible biases that have been reported in dynamical mass estimates of poor groups, as discussed in section 3.1. For each of these estimators we reduce the proxies to $M_{500} \propto r_{rms}\sigma^2$ and $M_{500} \propto \sigma^3$ respectively, taking radii and velocity dispersion within 1 Mpc for the volumetric sample, and using all member radii and velocities for the FoF sample.

3.3.4 Radii

At constant density it is easy to see that the mass and radius of groups are related by $M \propto r^3$. We initially examined a number of different estimates for the projected group radius, such as the half-light radius and harmonic mean radius, finding little difference in their behaviour. We use the root mean square radius, r_{rms}, of the group galaxies.

For the FoF sample, r_{rms} is simply the RMS radius of all the linked group galaxies. For the volumetric sample we use all velocity-selected galaxies within the 1 Mpc cone. Each galaxy is again weighted by its local completeness. This estimator ignores the expected background contamination, since we have no way of knowing exactly which galaxies are interlopers. Since the distribution of interlopers should be fairly uniform, we expect that this will bias estimated radii to

larger values. When applied to a volumetric sample, both this bias and the use of an aperture turn out to be serious flaws for this mass proxy.

3.4 Statistical analysis

Our aim is to calibrate the relationship between system mass and each of our mass proxies, and to examine the statistical performance of each method. In each case we evaluate the strength of correlations using the Spearman Rank correlation coefficient, and fit the mass-proxy relations with power laws of the form

$$\log_{10}\left(\frac{M_{500}}{10^{14}\mathrm{M}_{\odot}}\right) = \alpha \log_{10}\left(\frac{x}{x_0}\right) + \beta \quad , \tag{3.17}$$

where M_{500} is the X-ray determined mass and x is the relevant observable. To reduce correlation between the fitted slope and intercept we pivot the fit about $10^{14}\mathrm{M}_{\odot}$ and $x_0 = \bar{x}$.

3.4.1 Regression Methods

To avoid arriving at biased estimates of calibrated relations it is important to use the most appropriate regression method. Different methods make different assumptions regarding the dependent and independent variables and optimise scatter differently. These differences may result in biased estimates of any relation.

To explore this, we examine the performance of two different techniques which have been widely used – the frequentist BCES regression methods [Akritas and Bershady, 1996] and the Bayesian fitting approach of Kelly [2007] – and compare

them with a generative modelling technique of our own.

The BCES estimators are a general extension of the ordinary least squares estimator capable of accounting for intrinsic scatter and measurement errors in both axes. A number of forms of BCES are available: (Y|X) and (X|Y) regression which distinguish dependent and independent variables, and symmetric bisector and orthogonal techniques.

The Kelly [2007] estimator is a Bayesian linear regression estimator that models the mass-proxy relation, stressing the importance of correctly handling statistical errors. The method not only determines the optimum regression line but also provides an estimate of the intrinsic scatter in the relation.

The generative fitting method attempts to model the statistics of the process that produces measured mass and proxy values. The procedure is similar to some of the methods discussed in Hogg et al. [2010]; it is also similar in spirit, if not in detail, to the method of Kelly [2007]. However, whilst Kelly [2007] assumes an 'independent' variable upon which the 'dependent' second variable is conditioned, our generative model treats the two variables symmetrically. Further details of the generative fitting method can be found in Appendix A of the submitted paper with code available at `https://github.com/farr/galmassproxy`.

To decide which of these methods is the best method to use we generate an ensemble of mock mass-proxy datasets using a generative model and, through application of each fitting method, evaluate their accuracy in recovering the input relation. Our aim is to use a regression with the least biased slope, allowing, on average, accurate masses be recovered from a mass-proxy relation. Alternatively, we could optimise to a relation that recovers the lowest intrinsic scatter. Due to the sample size, we expect statistical errors and errors on the calibration to con-

tribute significantly to the scatter, therefore we prioritise recovering an unbiased relation over minimising the intrinsic scatter about that relation.

Each mock dataset consists of 22 mass values drawn from a log-uniform distribution with $13 \lesssim \log_{10}(M/\mathrm{M}_{\odot}) \lesssim 15$. We assume a mass-proxy relation as per Equation (3.17) with slope $\alpha = 0.8$ and intercept $\beta = 5$. From this, proxy values are found as

$$\log_{10}(x) = 1/\alpha \log_{10}(M) - \beta/\alpha + N(0, \sigma_{int}),$$

where $N(0, \sigma_{int})$ models intrinsic scatter in the proxy about the relation, assuming proxies are scattered as a Gaussian of width $\sigma_{int} = 0.3$ dex. The final step of constructing the mock dataset is to add statistical errors. To do this we rank both mock and observed mass-proxy pairs by mass and match them. The mock data are then assigned errors in mass and proxy based on the corresponding errors in the observational sample, where the proxy errors are drawn from the volumetric σ^3 proxy.

Each of the regression techniques are applied to the mass-proxy data for all 200 datasets. We collect the estimated slopes from each ensemble and determine the mean slope and standard error on this mean for each regression method. The results in Table 3.2 show that all methods apart from the frequentist BCES(X|Y) estimator return slopes which exhibit significant bias relative to the input value of 0.8.

Given these results, we adopt the BCES(X|Y) estimator to fit the mass-proxy calibration relations used for the remainder of this study.

Table 3.2: Results of regression tests — recovered slopes and their standard errors for each regression method.

Method	Mean Recovered Slope
Input	0.8
BCES(Y|X)	0.686 ± 0.005
BCES(X|Y)	0.808 ± 0.007
BCES(Bi)	0.745 ± 0.006
BCES(Orth)	0.727 ± 0.006
Kelly	0.687 ± 0.005
Generative	0.730 ± 0.008

3.4.2 Errors and Scatter Analysis

Measurement errors on masses are taken from the studies of S09 and SP10. Statistical errors on the proxies are derived in one of two ways. For the richness proxy, we simply assume Poisson noise on galaxy number counts. All other values have errors defined by a 68% confidence interval from a bootstrap analysis. For each group, and without redefining the galaxy selection (i.e. we do not repeat the FoF analysis), we resample from its input galaxy catalogue a new, random set of galaxies, with replacement, of equal size to the original. We then repeat our analysis to determine a revised set of mass proxies. This is performed 1000 times for each group, allowing a distribution of proxy values to be found.

We report all errors and scatter estimates as fractional errors in dex, where the statistical errors on each group are converted to dex[1] using $\sigma_{\log x} = \sigma_x / \ln(10) x$. Errors on our fitted calibration parameters are derived by bootstrap resampling from the group mass-proxy pairs. The resulting fits are presented in Table 3.3.

We illustrate the error on our fits as the shaded regions on Figures 3.2 and 3.3. At each point along the proxy axis we calculate a mass distribution using

[1] E.g. 0.1 dex is a factor of $10^{0.1}$

the spread of calibration parameters from the bootstrap resampling. The error region is then a 68 percentile contour in mass about the regression line.

One aim of this work is to explore the statistical performance of these mass proxies. We approach this by attempting to quantify the minimum error one would see if applying these relations to perfect data. That is, assuming no measurement error on a given proxy, how much uncertainty in a mass estimate would be introduced by the intrinsic scatter about these relations and the uncertainty in our calibration?

We estimate intrinsic scatter as

$$\sigma^2_{\log M,int} = \sigma^2_{\log M,tot} - \sigma^2_{\log M,stat} - \alpha^2\sigma^2_{\log x,stat} \quad , \tag{3.18}$$

where $\sigma_{\log M,tot}$ is the total fractional scatter in mass observed about the relation (i.e. the RMS fractional residuals) and $\sigma_{\log M,stat}$ the mean fractional statistical error in the mass (0.08 dex). The term $\alpha^2\sigma_{\log x,stat}$ accounts for the additional scatter in mass about the relation introduced by the statistical scatter of the proxy and propagated into the intrinsic scatter as $\sigma^2_{\log M} = (\mathrm{d}\log_{10}(M)/\mathrm{d}\log_{10}(x))^2\sigma^2_{\log x}$.

The mean uncertainty in mass introduced by the calibration is found by

$$\sigma^2_{\log M,cal} = \frac{1}{N}\sum_i^N \left[\left(\log_{10}\left(\frac{x_i}{x_0}\right)\sigma_\alpha\right)^2 + \sigma^2_\beta + 2\log_{10}\left(\frac{x_i}{x_0}\right)\mathrm{Cov}(\alpha,\beta)\right] \quad , \tag{3.19}$$

where $\mathrm{Cov}(\alpha,\beta)$ is the covariance of the relation parameters, accounting for any correlation in the errors. The sum $\sigma^2_{\log M,sys} = \sigma^2_{\log M,int} + \sigma^2_{\log M,cal}$ gives the

minimum fractional variance in mass one would expect for a given proxy. Our scatter analysis is also summarised in Table 3.3.

3.5 Results and Discussion

In this section we present the main results of this investigation. Using the statistical techniques described in the previous section, we calibrate each mass-proxy relation and examine its statistical performance. Where possible we also make comparisons with theoretical expectations to try to better understand these relations.

Table 3.3: BCES regression results for our sample corresponding to the best fit regression lines in Figures 3.2 and 3.3.

Method	α	β	$\log_{10}(x_0)$	ρ[a]	$\sigma_{\log x,stat}$[b]	$\sigma_{\log M,tot}$[b]	$\sigma_{\log M,int}$[b,c]	$\sigma_{\log M,cal}$[b]	$\sigma_{\log M,sys}$[b,d]
Volumetric Selection									
Richness	$1.62^{+0.21}_{-0.25}$	$0.22^{+0.06}_{-0.04}$	2.25	0.94	$0.08^{+0.01}_{-0.01}$	0.24	$0.19^{+0.08}_{-0.03}$	$0.08^{+0.02}_{-0.01}$	$0.21^{+0.08}_{-0.03}$
Luminosity	$1.74^{+0.26}_{-0.30}$	$0.23^{+0.07}_{-0.05}$	11.95	0.86	$0.11^{+0.01}_{-0.01}$	0.33	$0.25^{+0.12}_{-0.06}$	$0.10^{+0.03}_{-0.02}$	$0.27^{+0.11}_{-0.06}$
Overdensity (N)	$1.35^{+0.17}_{-0.20}$	$0.27^{+0.05}_{-0.05}$	14.34	0.88	$0.18^{+0.02}_{-0.02}$	0.26	$0.05^{+0.07}_{-0.05}$	$0.08^{+0.02}_{-0.01}$	$0.10^{+0.04}_{-0.05}$
Overdensity (L)	$1.20^{+0.16}_{-0.21}$	$0.30^{+0.06}_{-0.05}$	14.37	0.83	$0.20^{+0.03}_{-0.02}$	0.28	$0.13^{+0.11}_{-0.07}$	$0.09^{+0.02}_{-0.02}$	$0.16^{+0.08}_{-0.07}$
Dynamical ($r_{rms}\sigma^2$)	$1.33^{+0.22}_{-0.27}$	$0.31^{+0.09}_{-0.09}$	8.49	0.80	$0.09^{+0.01}_{-0.01}$	0.34	$0.31^{+0.09}_{-0.06}$	$0.11^{+0.03}_{-0.03}$	$0.33^{+0.10}_{-0.07}$
Dynamical (σ^3)	$0.99^{+0.19}_{-0.24}$	$0.42^{+0.10}_{-0.12}$	8.68	0.80	$0.13^{+0.01}_{-0.01}$	0.37	$0.34^{+0.10}_{-0.08}$	$0.12^{+0.04}_{-0.05}$	$0.36^{+0.11}_{-0.09}$
Radius	$12.68^{+1.82}_{-1.98}$	$0.08^{+0.10}_{-0.08}$	2.75	0.75	$0.03^{+0.004}_{-0.003}$	0.39	—	$0.11^{+0.03}_{-0.03}$	—
FoF Selection									
Richness	$1.03^{+0.13}_{-0.13}$	$0.34^{+0.07}_{-0.06}$	2.63	0.93	$0.06^{+0.01}_{-0.01}$	0.24	$0.21^{+0.07}_{-0.04}$	$0.08^{+0.02}_{-0.01}$	$0.23^{+0.07}_{-0.04}$
Luminosity	$1.06^{+0.15}_{-0.15}$	$0.33^{+0.08}_{-0.06}$	12.33	0.91	$0.08^{+0.01}_{-0.01}$	0.26	$0.23^{+0.08}_{-0.04}$	$0.09^{+0.02}_{-0.02}$	$0.25^{+0.08}_{-0.04}$
Overdensity (N)	$1.24^{+0.11}_{-0.12}$	$0.30^{+0.07}_{-0.06}$	14.33	0.88	$0.15^{+0.02}_{-0.01}$	0.29	$0.22^{+0.11}_{-0.05}$	$0.08^{+0.02}_{-0.01}$	$0.23^{+0.11}_{-0.05}$
Overdensity (L)	$1.17^{+0.15}_{-0.16}$	$0.33^{+0.07}_{-0.07}$	14.37	0.82	$0.19^{+0.02}_{-0.02}$	0.33	$0.24^{+0.09}_{-0.04}$	$0.10^{+0.02}_{-0.02}$	$0.26^{+0.09}_{-0.05}$
Dynamical ($r_{rms}\sigma^2$)	$0.94^{+0.14}_{-0.15}$	$0.39^{+0.09}_{-0.08}$	8.80	0.86	$0.08^{+0.01}_{-0.01}$	0.30	$0.28^{+0.08}_{-0.05}$	$0.10^{+0.03}_{-0.02}$	$0.30^{+0.09}_{-0.05}$
Dynamical (σ^3)	$1.05^{+0.15}_{-0.17}$	$0.35^{+0.07}_{-0.07}$	8.48	0.84	$0.12^{+0.01}_{-0.01}$	0.31	$0.28^{+0.08}_{-0.05}$	$0.10^{+0.03}_{-0.02}$	$0.29^{+0.09}_{-0.05}$
Radius	$2.33^{+0.41}_{-0.47}$	$0.21^{+0.09}_{-0.09}$	3.04	0.84	$0.04^{+0.004}_{-0.004}$	0.35	$0.33^{+0.10}_{-0.05}$	$0.12^{+0.03}_{-0.02}$	$0.35^{+0.10}_{-0.05}$

[a] Spearman rank correlation. All results have $> 95\%$ significance.

[b] Estimated fractional scatters in proxy and mass in dex.

[c] Intrinsic scatter in mass accounting for statistical scatter in the proxy (see Eq. 3.18). Where no value of $\sigma_{\log M,int}$ is shown, statistical errors dominate and $\sigma_{\log M,int}$ could not be constrained.

[d] The systematic scatter in mass, $\sigma^2_{\log M,sys} = \sigma^2_{\log M,int} + \sigma^2_{\log M,cal}$. Where $\sigma_{\log M,int}$ is unconstrained we show no value.

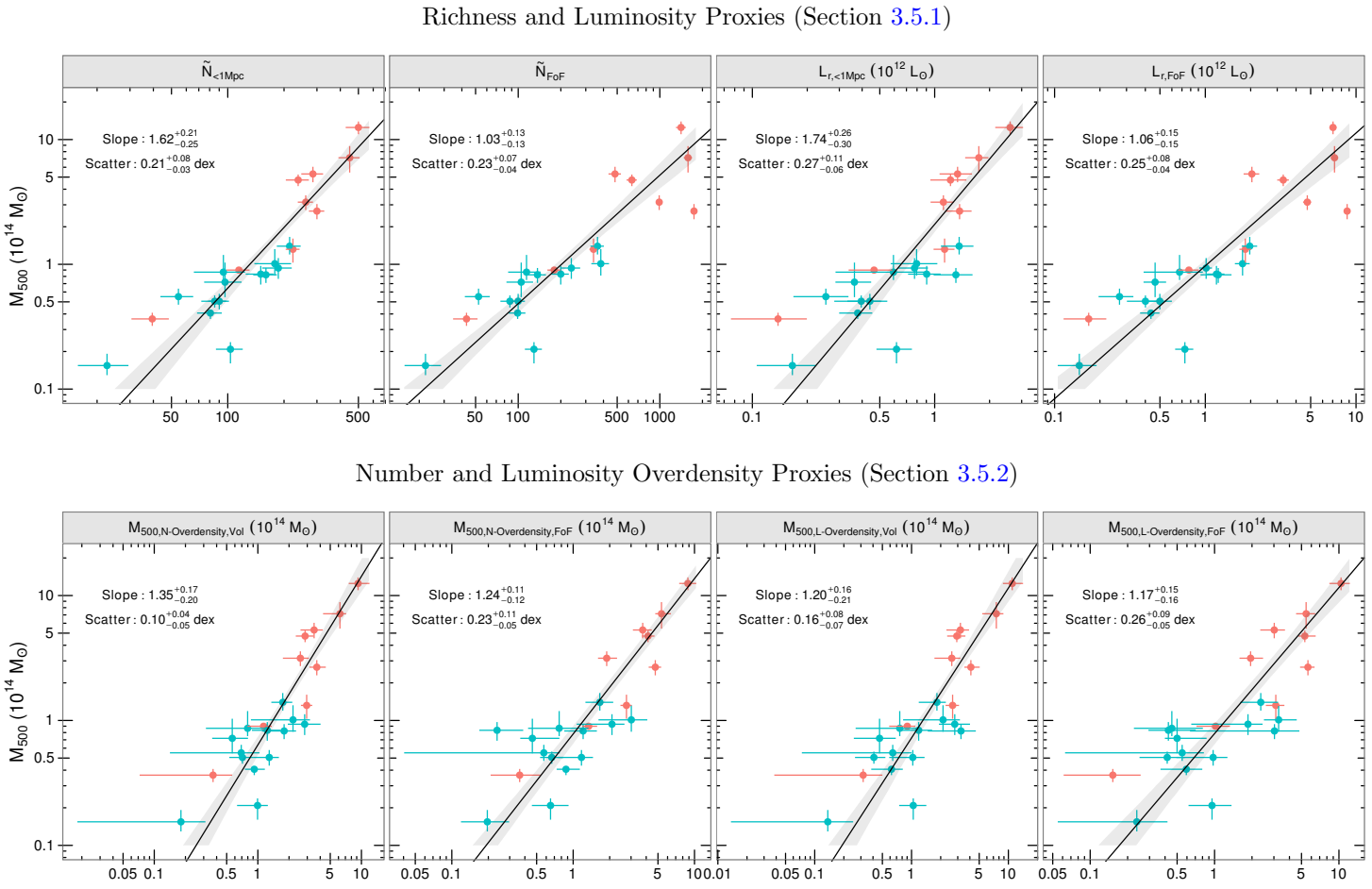

Figure 3.2: X-ray M_{500} plotted against from left to right, top to bottom, Richness, Luminosity, Number Overdensity and Luminosity Overdensity mass proxies. Alternating plots show results for the volumetric and FoF sample. Blue points are from the S09 sample, red points from the SP10 group and cluster samples respectively (see Table 3.1). The solid lines and shaded regions show the BCES(X|Y) regressions and a 68% percentile contour region drawn from the distribution of bootstrapped fit results.

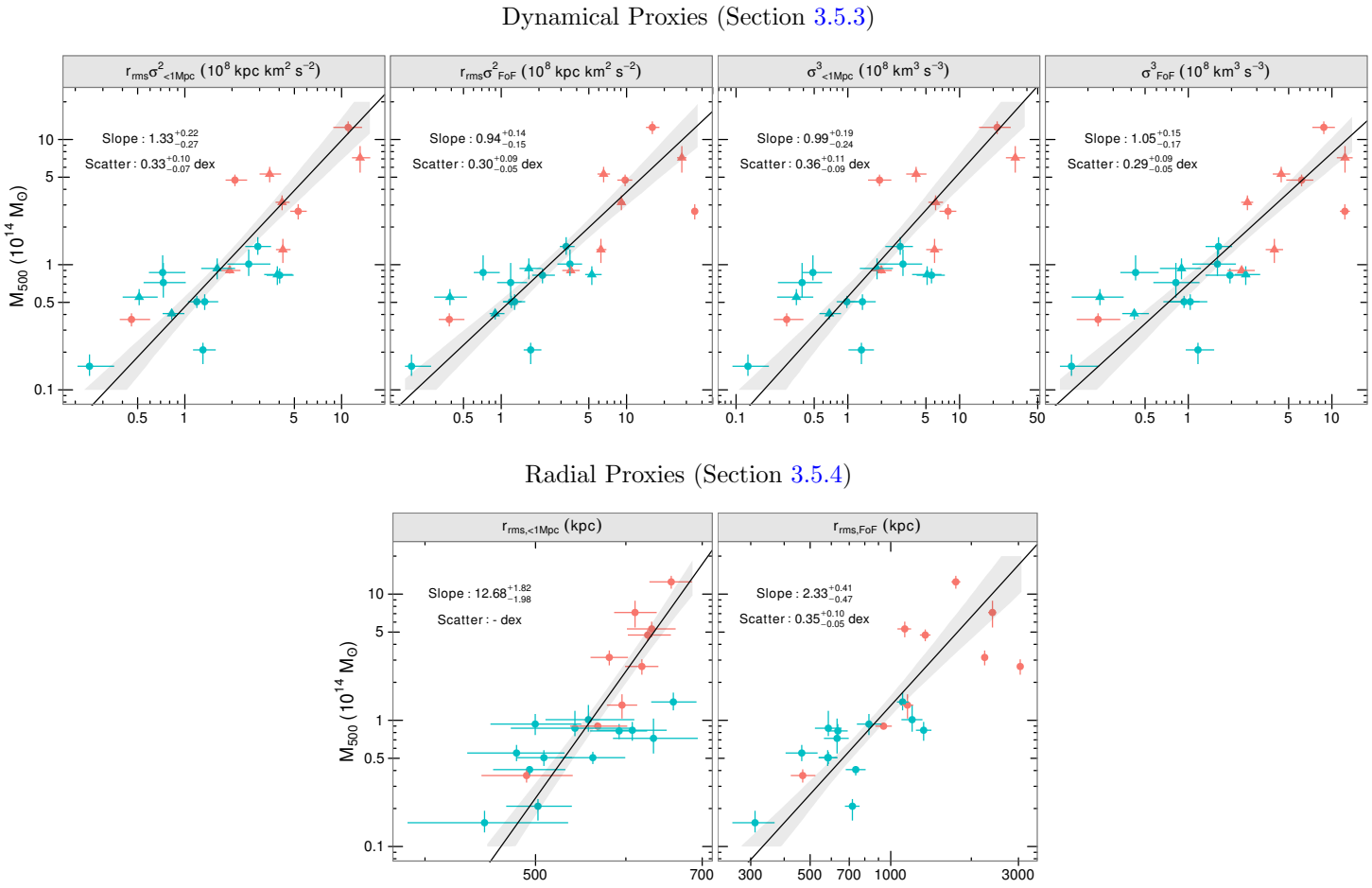

Figure 3.3: As Figure 3.2 with, from left to right, top to bottom, $r_{rms}\sigma^2$ Dynamical, σ^3 Dynamical and r_{rms} radius mass proxies. For the dynamical estimators (*top row*), groups with a large fraction of central galaxies with 'cloned' redshifts (see §3.2.2) are shown by triangular points.

3.5.1 Richness and Luminosity

The top row of Figure 3.2 shows the results of the richness and luminosity proxies, with fit estimates in Table 3.3. We find that for both galaxy selection methods these mass proxies are highly correlated with M_{500} with a low degree of scatter about the regression.

Comparing the volumetric $\tilde{N}_{1Mpc}$ against the literature, we note that Budzynski et al. [2012] compute a similar relation for high mass clusters ($M_{500} > 10^{13.7}$ $M_\odot$) and find that $M_{500} \propto N_{1\mathrm{Mpc}}^{1.4\pm0.1}$. This relation is shallower than ours, though it is (just) consistent within our 1σ error. Conversely, our FoF result is consistent with a 1:1 relation between mass and richness as one would expect if star formation efficiency and galaxy luminosity function were independent of halo mass.

Likewise, we compare the $L_{1\mathrm{Mpc}}$ result to the result of Popesso et al. [2007] who find a $L_{200} - M_{200}$ relation with a slope of 0.92 ± 0.03. Converting this to a $M_{500} - L_{1\mathrm{Mpc}}$ relation using the NFW model discussed below gives a slope of ~ 1.5, which is well within our estimated error. As with FoF richness, the FoF luminosity is also consistent with a slope of unity. A noticeable kink in the volumetric mass-luminosity data is apparent at $\sim 10^{14}$ $M_\odot$. There is some indication of a similar feature in a number of the other mass-proxy relations, though as it is not seen in any proxy-proxy relation and given the limited sample size it is hard to be confident of its reality.

We note from Table 3.3 that there is a significant difference between the slopes of the volumetric and FoF samples, indicating that, as one would expect, selection plays a significant role. This difference can be plausibly attributed to the use of a 1 Mpc aperture for the volumetric sample. For example, at low mass,

where $r_{500} \ll 1\text{Mpc}$ this would result in recovering $N_{1\text{Mpc}} > N_{500}$, and similarly recovering $N_{1\text{Mpc}} < N_{500}$ at high mass. Conversely, a friends-of-friends analysis should link galaxies together in a way that scales with the size of the group. Hence we expect the volumetric scaling relations to be steeper.

To investigate further, we construct a simple analytic model. We assume that galaxies are distributed as an NFW with a concentration half that of the dark matter [Budzynski et al., 2012], and take the dark matter concentration from the mass-concentration relation derived from simulations of relaxed halos by Duffy et al. [2008]:

$$c_{200} = 6.71 \pm 0.12 \left(\frac{M_{200}}{2 \times 10^{14} h^{-1} \mathrm{M}_{\odot}} \right)^{-0.091} (1+z)^{-0.44}. \tag{3.20}$$

We assume $z = 0.05$, close to the mean of our sample, and find that including scatter in mass-concentration relation has a negligible impact on our results, so we do not include it. We then model the aperture richness N_{ap} as,

$$N_{ap} = \int_0^{1\text{Mpc}} 2\pi r \Sigma(r, r_s(M_{200})) \mathrm{d}r \quad , \tag{3.21}$$

where Σ is the projected NFW from equation (3.8) and $r_s = 2r_{200}/c_{200}$. We then calculate N_{ap} for a set of equally spaced log M_{200} values in the range $12.5 \lesssim \log_{10}(M_{200}/M_{\odot}) \lesssim 15.5$. We also convert each M_{200} to M_{500} using the 3D NFW, equation (3.7), and concentration c_{200}.

Applying a BCES (X|Y) regression to the resulting points in the M_{500} - N_{ap} plane gives a slope of 1.42 ± 0.02. This is shallower than our observational result, though marginally within the errors. Whilst the effect of an aperture does indeed

appear to steepen the relation, this suggests that a second effect may be at work.

A possible second source of discrepancy could be variation of star formation efficiency as a function of halo mass [see, e.g. Behroozi et al., 2010; Budzynski et al., 2014; Leauthaud et al., 2012; Moster et al., 2010]. This would boost the stellar mass in lower mass halos relative to those of higher mass. Using the Budzynski et al. [2014] stellar mass fraction-M_{500} relation, and comparing it to a global stellar mass fraction from the SDSS, $\Omega_* = 1.9 \times 10^{-3}$ [Panter et al., 2007], we find that this scales our model to give a M_{500} – N_{ap} slope of 1.67 ± 0.03 – close to our observed relations for aperture richness and luminosity.

We can cast these two effects into two bias factors, $C_N = N_{ap}/N_{500}$ and $C_* = f_*/\bar{f}_*$ where $\bar{f}_* = \Omega_*/\Omega_m$. In Figure 3.4 we show the magnitude of these bias factors as a function of $N_{1\mathrm{Mpc}}$.

Unlike the volumetric sample, the richness and luminosity proxies for the FoF sample require no aperture correction. We attempt instead to correct N_{fof} and L_{fof} for star formation efficiency only. Scaling for C_* brings the observed slopes down to 0.92 ± 0.10 and 0.96 ± 0.11 respectively, both consistent with, though rather lower than, the expected slope of unity. We also note that even without this factor, both FoF selected proxies are already consistent with unity. This may relate to the nature of the FoF algorithm used. As we will discuss in §3.6, we believe that this is rather overgenerous in terms of linking galaxies together. If this effect is stronger for higher mass systems it would lead to some flattening of the observed mass-proxy relation.

We perform one final check on our data by examining the luminosity-richness relation for our sample. Popesso et al. [2007] found luminosity and richness to be well correlated, with a slope of 1.00 ± 0.03. Whilst we use a slightly different

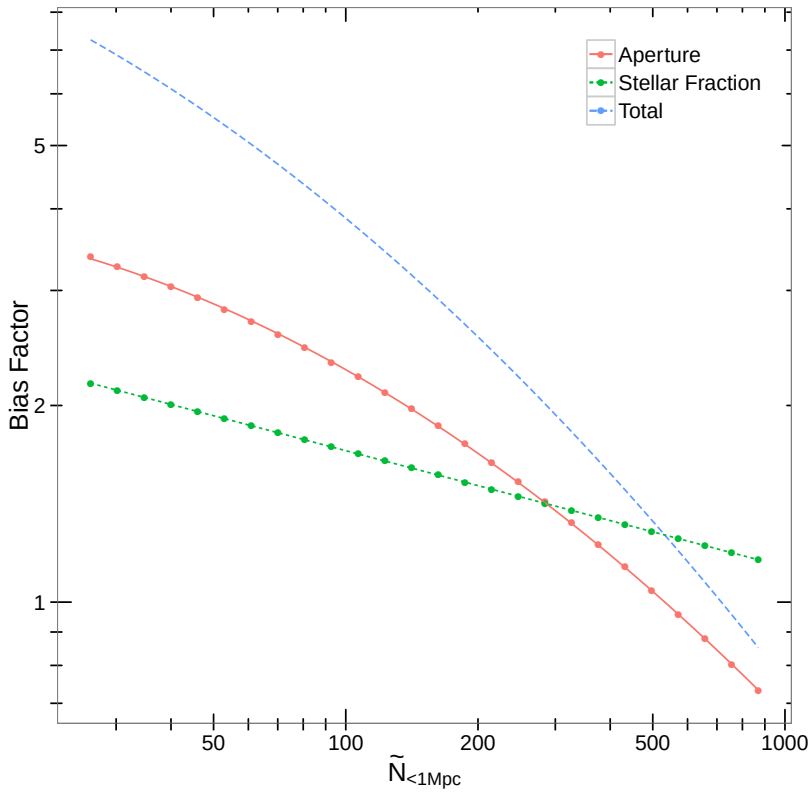

Figure 3.4: Modelled bias factors and best fit curves. These are required to rescale $\tilde{N}_{1\mathrm{Mpc}}$ to N_{500} (C_N, *red, solid line*) and to account for variation in star formation efficiency (C_*, *green, dotted line*). The combined scale factors, ($C_N C_*$) are shown as the *blue, dashed line*.

definition of both group richness and luminosity, we also find (Figure 3.5) that they are strongly correlated (Spearman rank correlations of 0.94 and 0.99 for volumetric and FoF samples respectively). BCES orthogonal regression slopes are $0.97^{+0.08}_{-0.07}$ and 0.98 ± 0.03 for our two selection methods, both in excellent agreement with each other and consistent with the Popesso et al. [2007] result. This suggests that there is no systematic trend in mean galaxy luminosity with system mass within our sample.

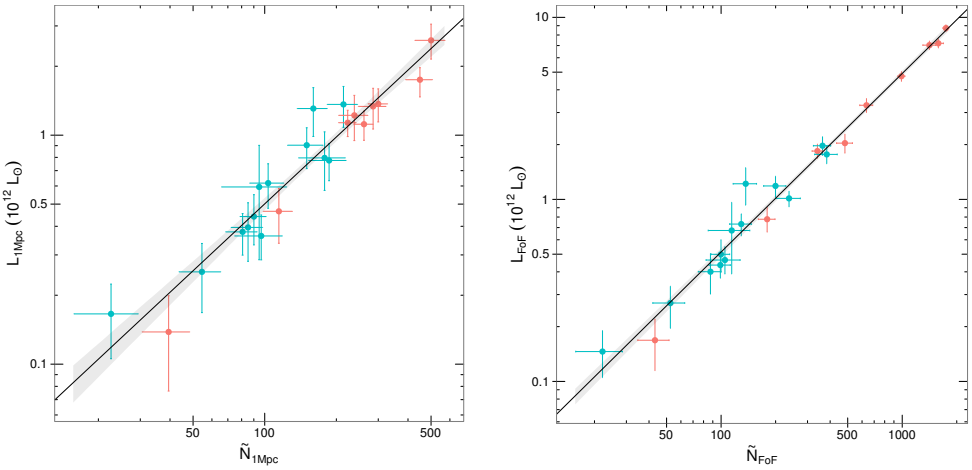

Figure 3.5: *Left:* background subtracted optical luminosity against richness within 1 Mpc, *Right:* Total FoF luminosity against FoF richness. Colour coding is as for Figure 3.2.

3.5.2 Overdensity

The second row of Figure 3.2 shows the observational results of the number and luminosity based overdensity analyses, with fit parameters given in Table 3.3. The number overdensity mass proxy performs well, exhibiting a strong correlation with mass and the lowest levels of intrinsic and calibration scatter for both volumetric and FoF selected groups. However, it also has the largest statistical errors on the measured proxy value.

As this proxy provides a direct measure of group mass, we would expect the mass-proxy relation to have a slope of unity. We observe however that whilst our overdensity masses are broadly consistent with X-ray masses, the slope of the relation is significantly steeper than unity. We find that the slope of the number overdensity relation is steeper than unity, implying that there is a mass dependent bias in the measured overdensities. A similar, though slightly less significant, bias

is observed for the luminosity overdensity. The reduced bias for luminosity may be due to its reduced sensitivity to the faint end slope of the luminosity function.

A fundamental assumption in the use of the galaxy (and galaxy luminosity) overdensity is that galaxies are a perfect tracer of the underlying dark matter. As noted previously however, it is well known that galaxy density profiles have concentrations different to that of their dark matter counterparts [see, e.g. Budzynski et al., 2012; Hansen et al., 2005]. However, this would be expected to make only a minor difference to the integrated galaxy density within r_{500}. More significant is likely to be the bias discussed in Section 3.5.1, which would arise from halo mass dependence in the efficiency of star formation. Some bias may also be introduced by the comparison between our observed mean density and the global mean density, which incoprorates an assumption about the stellar mass-to-light ratio.

It is well known that clusters and groups have different stellar mass-to-light ratios compared to the universe as a whole, a property that varies with the scale of the system [see, e.g. Davis et al., 1980; Ostriker et al., 1974]. We investigate this briefly here using the colour-dependent mass-to-light ratio of Bell et al. [2003], $\log_{10}(M/L_r) = -0.306 + 1.097(g-r) - 0.1$ [see also Budzynski et al., 2014]. Using the g and r absolute magnitudes from the NYU-VAGC catalogues from which our sample was drawn in section 3.2, we find that the mean mass-to-light ratio of the global sample in the range $M_r < -19$ and $0.01 \leq z \leq 0.1$ is 2.8. Repeating this for our clusters, using galaxies projected within 1 Mpc, we find a mean mass-to-light ratio of 3.7. This implies that our overdensity analysis would systematically underestimate the overdensity of haloes by a factor of 1.3. In practice, the mass-to-light ratio of clusters varies with halo mass [e.g. Budzynski

et al., 2014] so we also estimate the mass-to-light ratio of our groups in mass bins split at group masses of $M = 7.5 \times 10^{13}$ $M_\odot$ and $M = 2 \times 10^{14}$ $M_\odot$. We do not see any substantial change with group mass (mean mass-to-light values of 3.6, 3.6 and 3.8 respectively) so we adopt the mean factor above. This translates to underestimating masses by ~ 1.5, bringing our relation into agreement with expectations at high mass ($\sim 10^{15} M_\odot$). However, as this correction is mass independent it will have no effect on the measured slope.

As with Section 3.5.1, we again look to variation in star formation efficiency (SFE) and the consequent stellar mass fraction of halos as an effect that will modify the slope of our observed relation. This is also established to be different in groups and clusters compared to global values [see, e.g. Behroozi et al., 2010; Budzynski et al., 2014; Leauthaud et al., 2012; Moster et al., 2010]. It is also known to be mass dependent [e.g. Budzynski et al., 2014; Leauthaud et al., 2012], such that low mass halos have significantly higher stellar mass fractions compared to high mass systems, which are considerably closer to the global value. A halo with higher SFE will have a higher density of galaxies and light than might be expected for its mass overdensity (ignoring galaxy mergers). A correction for this would involve scaling the modelled halo densities by a factor that would allow a correct comparison to the global density. We define such a factor as $C_O = f_*(M_{500})/\bar{f}_*$ where $\log_{10}(f_*(M_{500})) = -0.11 \log_{10}(M_{500}/3 \times 10^{14} M_\odot) - 2.04$ [Budzynski et al., 2014] and $\bar{f}_* = \Omega_*/\Omega_m$. Again, we use $\Omega_* = 1.9 \times 10^{-3}$ derived from the SDSS [Panter et al., 2007].

Applying a correction for both a variable SFE and the difference between global and cluster mass-to-light ratios, we find that the overdensity mass – X-ray mass relations are consistent with our expectations. A richness based overdensity

recovers slopes of $1.12^{+0.14}_{-0.18}$ and 1.01 ± 0.10 for the volumetric and FoF samples respectively, with no significant bias in normalisation. Luminosity similarly is corrected to a slope of $0.99^{+0.13}_{-0.16}$ (volumetric) and $0.96^{+0.13}_{-0.14}$ (FoF). Given that we now understand the discrepancy between observations and expectations, we believe that it is safe to simply calibrate the uncorrected overdensity mass-X-ray mass relation.

3.5.3 Dynamical Mass

Results for the dynamical mass estimators are shown in the first row of Figure 3.3 and in Table 3.3. The 9 groups for which there is a central population of galaxies with cloned redshifts due to fibre collisions, as discussed in Section 3.2.2, are flagged in these Figures, but do not appear to be systematically offset. Excluding these systems from the fit results in only modest changes to the fitted slope (to $\alpha = 1.42$ and 1.07 for the volumetric $r_{rms}\sigma^2$ and σ^3 relations respectively). These changes lie well within the statistical errors, and we therefore retain the affected systems in our analysis.

Whilst the two proxies for both selection methods appear well correlated with the X-ray masses, they also show a large amount of scatter compared to some of our other mass estimators. From the Virial Theorem we expect these estimators to scale linearly with mass. We find that all but the volumetric $r_{rms}\sigma^2$ estimator are consistent with this expectation at the 1σ level. Given the highly discrepant behaviour of the r_{rms} proxy for the volumetric sample (discussed in §3.5.4), the behaviour of the $r_{rms}\sigma^2$ mass proxy is not surprising.

We note that our three good dynamical estimators – two FoF and one volu-

metric – have mass-proxy slopes which are consistent with each other, indicating that the extracted velocity dispersion is quite robust against the treatment of interlopers and the use of apertures. We also see no strong indication of the biased velocity dispersions at low mass suggested by previous work [e.g. Osmond and Ponman, 2004]. However, we note that our sample has been selected to be X-ray bright and morphologically relaxed, whilst the Osmond and Ponman [2004] study involved a more diverse set of galaxy groups.

3.5.4 Radii

The observed RMS radius-mass relation is shown in the second row of Figure 3.3, with fit parameters in Table 3.3. Based on $M \propto r^3$ at constant density (in this case, overdensity) we would expect the mass-radius relation to be have a slope of 3. We instead find that the relation for the volumetric sample is much steeper, whilst the slope for the FoF sample is somewhat shallower than expected by almost 2σ. This mass proxy is the worst performing of those discussed in this paper, with statistical errors large enough to prohibit the determination of the intrinsic scatter in mass for the volumetric sample, and the largest final systematic error for the FoF sample.

The difference in the fitted relations between the volumetric and FoF selection methods is likely to be due to the use of a metric aperture for the volumetric sample, coupled with the impact of interlopers. Interlopers, due to their uniform distribution, would be expected to increase the measured RMS radii, especially for poorer groups, steepening the observed slope. At the same time, the imposition of an aperture sets an upper limit to the radius. The result is a very small dynamic

range in r_{rms}, as can be seen in the bottom left panel of Figure 3.3.

To investigate these effects we construct a model to probabilistically sample projected NFW models, constructing halos of a given richness, and estimating their r_{rms} radii. We base our approach on the method Budzynski et al. [2012] used to estimate mass completeness. We first estimate the number of galaxies contributed by a halo of a given mass using our observed mass-aperture richness relation. This relation is calibrated to recover galaxies brighter than a fixed absolute magnitude, $\tilde{N}_{1\mathrm{Mpc}}$, whilst we require the number of galaxies that would actually be observed at some specific redshift, $N_{1\mathrm{Mpc}}$. We account for this by removing the correction given by equation (3.5), adopting a redshift of $z = 0.05$ for our simulated group. A projected NFW with a galaxy concentration as described in section 3.5.1 is then normalised to recover this halo richness. We add a background term to introduce interloper contamination and integrate the combined normalised NFW and interloper density profile within our aperture to estimate the 'observed' aperture richness.

To probabilistically construct a group with a halo of given mass, we draw the desired number of galaxies (N) from a Poisson distribution using the estimated richness as the mean. We then draw $N - 1$ radii from the projected NFW likelihood function, Equation (3.11), and add a single galaxy to the centre for the BGG. We generate 50,000 such simulated groups uniformly spanning the mass range $12.5 \leq \log_{10}(M_{200}/M_{\odot}) \leq 15.5$. We generate our simulations for two scenarios: one where we include no interloper contamination, and one where we assume an interloper population with galaxy number density $(1.0 \pm 0.3) \times 10^{-6}$ kpc^{-2}, based on the mean background measured by our overdensity method (Section 3.5.2).

Finally we bin these these two sets of 50,000 randomisations into bins of 0.1

dex in mass. The resulting mass-radius relations are shown in Figure 3.6. The small dynamic range in r_{rms} is similar to that seen in Figure 3.3, and power law fits to the sample including interlopers gives a slope of 27.4 ± 1.1 – far steeper than the naive expected value of 3. It can be seen that the inclusion of an interloper population does affect the recovered slope, especially in the lower mass regime where the 'clean' sample diverges significantly from the interloper contaminated model. However, the clean sample also appears to approach a slope of 3 at low r_{rms}, equivalent to groups with $r_{500} \ll 1$ Mpc. Our conclusion is that both interlopers and aperture effects play a significant role in biasing this relation, with interlopers dominating at low masses, increasing the RMS radius of a group, whilst the aperture dominates at high masses where it truncates the galaxy distribution, reducing the RMS radius. Ultimately, the derived radius for the volumetric selection is biased to the point where we observe a near constant r_{rms}, making it unsuitable for use as a mass proxy. As an aperture is not used for the FoF sample, interloper contamination will be the main source of bias at all masses.

3.5.5 Uncorrected effects

Throughout this section we have discussed mass dependent biases that can be introduced by failing to take into account properties of the sample selection (such as aperture effects) or of the groups themselves (such as variation in star formation efficiency). We have not, however, discussed the possible biases introduced by assumptions we have made. The most important is the implicit assumption, at various points in our analysis, of a universal galaxy luminosity function. In

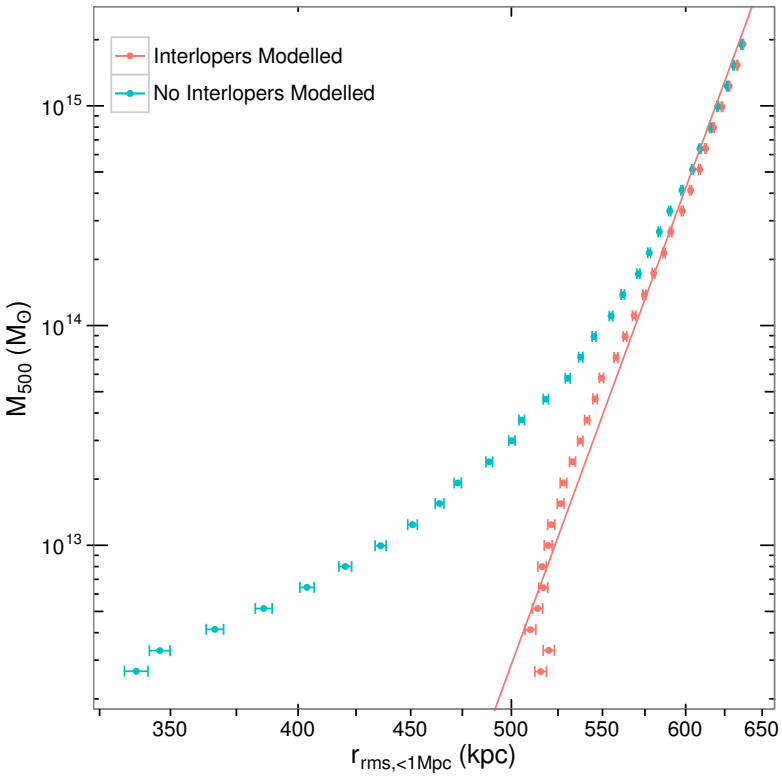

Figure 3.6: *Red:* Modelled r_{rms} radius including the interloper contamination. *Blue:* Modelled r_{rms} radius not including the interloper contamination.

practice, it has been observed [e.g. Hansen et al., 2005; Robotham et al., 2006, 2010; Zandivarez and Martínez, 2011] that the group luminosity function varies as a function of halo mass, becoming similar to the global galaxy luminosity function at low mass. As we use a single luminosity function for completeness correction, this has the potential to bias low mass systems whose luminosity function differs significantly from the Popesso et al. cluster luminosity function used. This will affect both luminosity and richness estimators and will be a larger effect for cases where a significant degree of extrapolation is required, i.e. at higher redshift. Whilst we do not attempt to correct for this, under the assumption that low mass

groups more closely resemble the field (i.e. global) luminosity function of Blanton et al. [2003], we can examine the degree of overcorrection that extrapolating with an inappropriate luminosity function can cause as a function of redshift. This is shown in Figure 3.7.

These differences are caused by the cluster luminosity function featuring a brighter turnover magnitude than the field ($M_* - 5\log_{10} h = -21.35$ [Popesso et al., 2005] rather than -20.44 [Blanton et al., 2003]) and a steeper faint end slope ($\alpha = -1.30$ compared to -1.05). When little extrapolation is required (at low redshift where only a small portion of the faint end is lost due to the survey limit), the low luminosities of galaxies below the survey flux limit result in little discrepancy between a cluster- and field-based luminosity correction, whilst their greater abundance in the field results in a cluster based richness correction underestimating rescale factors by $\sim 10\%$. Both factors converge to no discrepancy at $z \approx 0.015$ where the limiting magnitude is comparable to our adopted magnitude limit of $M_r = -16.5$. Conversely, at higher redshifts where it is necessary to extrapolate from near M_* ($M_{cut} \approx -20.8$ at $z = 0.1$), the excess of bright galaxies from the cluster luminosity function cause both the number and luminosity corrections to rise.

Hence, if our low mass groups have luminosity functions similar to the field, then attempting to correct them for incompleteness in faint galaxies using a cluster luminosity function will have two main effects as a function of redshift. At low redshift the degree of overcorrection will be negligible for a luminosity correction, rising to $> 20\%$ at $z = 0.1$. Conversely, richness corrections will be underestimated by $10 - 20\%$ until $z \sim 0.1$ at which point they become overestimated and continue to rise with increasing redshift. Correcting for these effects would

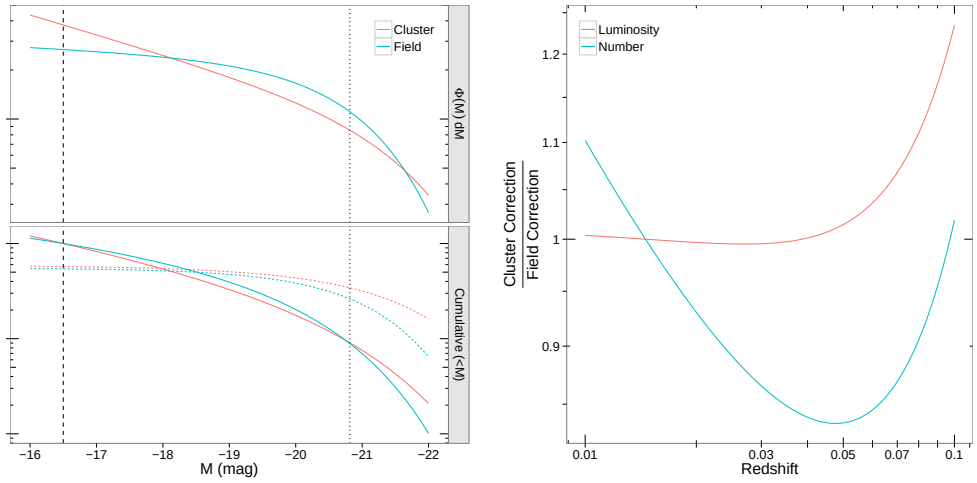

Figure 3.7: *Left, upper panel:* Luminosity functions used for the cluster correction (*red curve*) and the global luminosity function (*blue curve*) with arbitrary normalisation. *Left, lower panel:* the cumulative number (*solid coloured line*) and luminosity (*dashed coloured lines*) density the luminosity functions above. The vertical lines illustrate the magnitude we extrapolate to ($M_r = -16.5$) and the absolute magnitude corresponding to the flux limit at $z = 0.1$, $M_r = -20.8$. *Right:* The degree to which a high mass cluster luminosity function would overcorrect the richness and luminosity of a low mass group as a function of redshift. This assumes that low mass groups have a luminosity function comparable to a global luminosity function.

require knowledge of the way in which luminosity functions vary as a function of system mass. In practice, our fitted mass-proxy relations should calibrate out this effect, at least for the relaxed X-ray bright groups which constitute our sample.

Similarly, we have also not discussed the impact of galaxy mergers, which will affect the richness and luminosity estimators, as richness is reduced and stars are stripped to form the intracluster light. If these effects are mass-dependent, we assume their average effects can be calibrated out in our analysis. However, the varying merger histories of groups will also introduce scatter into the relevant mass-proxy relations.

Finally, it is important to emphasize that this study is based on a low redshift

sample, and apart from inclusion of the redshift dependence of ρ_{crit} (which is small over the redshift range of our sample) when calculating r_{500} for our systems, we do not take into account the evolution of mass proxies with redshift. Redshift correction of the dynamical and radius estimators is straightforward, and follows directly from the evolution in ρ_{crit}. The same is true of the overdensity estimators, provided that evolution in galaxy luminosities is the same in clusters as in the field. However, we would expect the richness and luminosity mass proxies to be strongly dependent on the evolution of the galaxy luminosity function within galaxy groups and clusters. Recent work implies that there may be little evolution in the mass-richness proxy [Andreon and Congdon, 2014], though as this work uses a specific subset of galaxies to define richness, the result cannot necessarily be extrapolated to our richness proxy.

We add a brief comment on the impact of miscentring on this analysis. We perform a post-analysis check on our volumetric sample, applying the centring algorithm used to determine the centres of the FoF group sample to the galaxies within the innermost 1 Mpc. We find that the new centres are offset from our adopted centres by at least 100 kpc in 13 of our 22 groups. Visually inspecting the 5 systems with the greatest offset (> 400 kpc) between the NED centre and our alternative central galaxy, in only one group is the alternative an obvious improvement. The remaining high-offset systems have either no obvious central galaxy or the chosen galaxy appears offset from a more obvious centre consistent with the NED centre. Furthermore, re-estimating the mass-proxy relations for the recentred sample we find minimal differences compared to those estimated here. The alternative slopes are shallower, and generally show reduced systematic scatters, compared to the results in Table 3.3. The difference in slopes is small-

est for the richness and luminosity estimators, though for all proxies, changes in slopes and systematic scatters are within the 1σ uncertainty presented in Table 3.3. As the the majority of our groups have centring offsets of less than r_{500}, the 1 Mpc aperture should contain a large number of the same galaxies for either centroid used. We would therefore not expect to see a significant difference for the number and luminosity based relations. However overdensity and radial based proxies, which rely on the distribution of galaxies, would understandably be more heavily affected. The difference between group redshifts from NED and the median redshift within the 1 Mpc cone is within the range given by the velocity dispersion for all but one system, with this group also showing the greatest change in velocity dispersion. In general, refinements to the group centres have no significant impact on the conclusions of this study.

3.5.6 Discussion

In general the majority of our proxies exhibit mass-proxy relations that are either consistent with theoretical expectations, or for which any discrepancy can be plausibly explained. The steepened slopes of volumetric aperture richness, luminosity and RMS radius proxies are consistent with the expected effects of imposing an aperture, and the behaviour of richness, luminosity and overdensity proxies are also influenced by known variations in star formation efficiency. Our approach is to calibrate out these effects in deriving our proxy-mass scaling relations.

What do our results suggest is the *best* mass proxy from the set we have studied? One reasonable definition of 'best' is the proxy which has the smallest

systematic error (arising from intrinsic population scatter and calibration error). Reference to the values of $\sigma_{\log M,sys}$ listed in Table 3.3 indicates that this is the richness overdensity taken from a volumetric sample. This may be the most reliable estimator when it can be measured to high precision, but it can be seen from the same table that this also has one of the largest *statistical* errors ($\sigma_{\log x,stat}$) of any of our proxies.

In the absence of a high quality galaxy surface density profile, we find that a simple richness estimator provides the most reliable result, with $\sim$ 0.2 dex (i.e. $\sim$ 50%) systematic scatter and relatively small statistical errors for galaxy samples of the size ($\gtrsim$ 15) used in this study. This is true for both volumetric and FoF selection methods.

However, we believe that there is substantial benefit in employing not just a single mass estimator, but a basket of them. We will return to this point in §3.8, but an indication of the extra information provided by using different mass proxies in conjunction can be gleaned by examining the *residuals* about our regression fits for the different proxies. Specifically, we look for evidence of correlations between residuals of different proxies, which might, for example, imply that if a group's mass is overpredicted by one proxy it will also be overpredicted by another.

Of course, it is self-evident that some proxies will be intrinsically correlated. For example, richness and luminosity, or the two dynamical estimators. However, others – such as luminosity and σ^3 – would appear to be quite independent of one another, apart from the relationship of both to system mass. We define residuals as the log-space difference between a mass predicted by the proxy (x) and the 'true' X-ray mass, $R_x = \log_{10}(M_{500}(x)) - \log_{10}(M_{500,X})$, and test for correlation between residuals from the different mass proxies using the Spearman

Rank statistic. The results are shown in Table 3.4 for both selection methods with errors derived from bootstrap resampling our residual estimates. Note however that the that the RMS radius proxy is intrinsically flawed for volumetric selection.

Surprisingly, the residuals are positively correlated in every case. To consider what this means, we focus on the correlation between the richness and σ^3 mass estimators. The residuals for these two are correlated with $\rho = 0.66^{+0.19}_{-0.15}$ and $0.81^{+0.05}_{-0.11}$ for the FoF and volumetric samples, both of which are significant at $> 95\%$ with errors, again, from a bootstrap analysis. We note that with the alternative, volumetric group centres the correlations are slightly reduced, though significant, moderate to strong correlations between residuals are still observed.

We plot the residuals from the fitted, FoF mass-proxy relations for these two mass estimators in Figure 3.8. Here a group which lies on both calibration relations would lie at the origin.

The clear correlation between the residuals indicates that for a group in which the richness proxy produces a mass overestimate (relative to its measured X-ray mass), the same tends to be true for the dynamical mass estimator, and similarly for underestimates. The colour coding in the Figure indicates the temperature of each system, and no correlation between this and location on the plot is apparent. There are two possibilities: either perturbations from the mean mass relations in richness and dynamics are related in some way, or there are errors in the X-ray masses. The latter would induce correlated offsets of the type we observe – a group with an overestimated X-ray mass would fall in the lower left quadrant, whilst an X-ray underestimate would move it towards the top right.

The fact that *all* our varied mass estimators show positively correlated residuals (see Table 3.4) suggests strongly that the X-ray masses are at fault. The

Table 3.4: Spearman rank correlations, with bootstrap errors, for the fractional offsets of masses predicted for, *Upper Triangle:* each volumetric selected proxy, and, *Lower Triangle:* FoF selected proxy from the X-ray mass.

	Richness	Luminosity	Overdensity (N)	Overdensity (L)	Dynamical ($r_{rms}\sigma^2$)	Dynamical (σ^3)	Radius
Richness	-	$0.89^{+0.08}_{-0.04}$	$0.89^{+0.09}_{-0.04}$	$0.85^{+0.10}_{-0.06}$	$0.81^{+0.12}_{-0.07}$	$0.81^{+0.11}_{-0.05}$	$0.36^{+0.24}_{-0.20}$
Luminosity	$0.91^{+0.09}_{-0.05}$	-	$0.78^{+0.13}_{-0.07}$	$0.82^{+0.11}_{-0.06}$	$0.76^{+0.14}_{-0.09}$	$0.74^{+0.14}_{-0.10}$	$0.40^{+0.23}_{-0.21}$
Overdensity (N)	$0.55^{+0.21}_{-0.17}$	$0.53^{+0.21}_{-0.16}$	-	$0.93^{+0.06}_{-0.02}$	$0.73^{+0.15}_{-0.08}$	$0.78^{+0.13}_{-0.06}$	$0.06^{+0.26}_{-0.22}$
Overdensity (L)	$0.56^{+0.20}_{-0.15}$	$0.66^{+0.19}_{-0.13}$	$0.89^{+0.08}_{-0.04}$	-	$0.74^{+0.13}_{-0.07}$	$0.80^{+0.11}_{-0.05}$	$0.05^{+0.26}_{-0.23}$
Dynamical ($r_{rms}\sigma^2$)	$0.84^{+0.12}_{-0.08}$	$0.80^{+0.11}_{-0.06}$	$0.46^{+0.23}_{-0.20}$	$0.46^{+0.22}_{-0.18}$	-	$0.99^{+0.02}_{-0.01}$	$0.87^{+0.10}_{-0.05}$
Dynamical (σ^3)	$0.66^{+0.19}_{-0.15}$	$0.64^{+0.18}_{-0.13}$	$0.52^{+0.20}_{-0.18}$	$0.54^{+0.19}_{-0.18}$	$0.90^{+0.10}_{-0.07}$	-	$0.64^{+0.19}_{-0.14}$
Radius	$0.91^{+0.08}_{-0.03}$	$0.78^{+0.15}_{-0.10}$	$0.32^{+0.26}_{-0.22}$	$0.28^{+0.24}_{-0.21}$	$0.42^{+0.22}_{-0.18}$	$0.31^{+0.24}_{-0.20}$	-

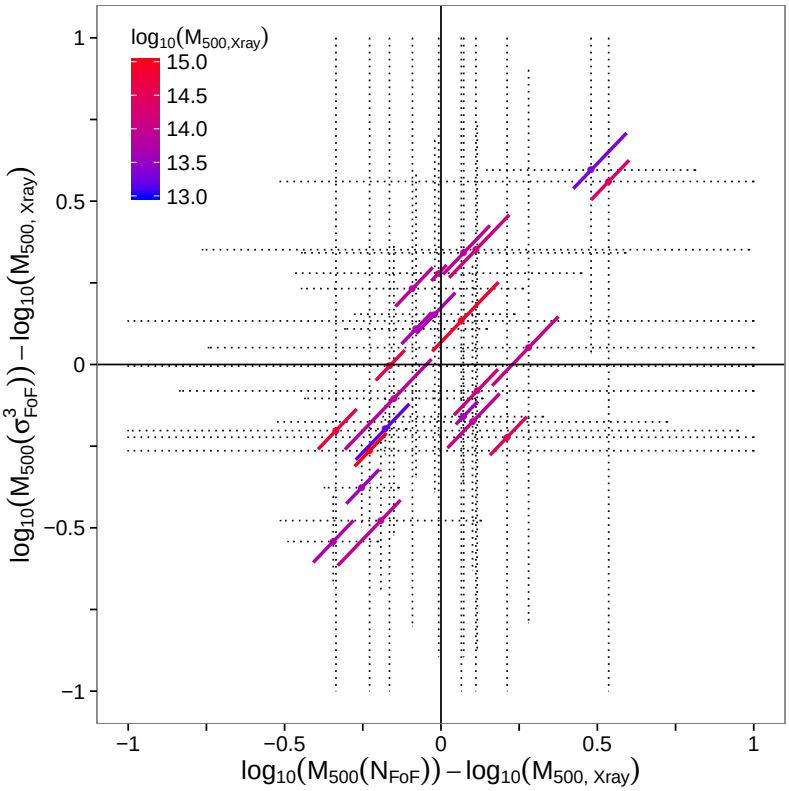

Figure 3.8: Fractional residuals about the regression lines for the FoF richness and σ^3 dynamical estimators defined as $R = \log_{10}(M_{500}(x)) - \log_{10}(M_{500,X})$. *Bold, solid lines:* the 1σ range due to statistical errors on the measured X-ray masses. *Dotted lines:* 1σ range due to the statistical errors on the mass proxies, intrinsic scatter in the relation and calibration errors added in quadrature. Each datapoint is coloured according to its X-ray mass, with blue $\sim 10^{13}$ $M_\odot$ and red $\sim 10^{15}$ $M_\odot$.

alternative would be some sort of conspiracy between the whole set of mass proxies to perturb together. Of course there are *statistical* errors on the X-ray mass measurements, and the effect of these is shown (diagonal bars) in the Figure. These would introduce some elongation of the distribution in the direction observed, but it is clear that in about a third of the systems these statistical errors cannot explain the magnitude of their offset from the centre. So, there is evidence here for errors in the X-ray derived masses, over and above the estimated statisti-

cal errors, in a significant subset of our group sample. For the worst cases, errors in the X-ray mass of a factor of two or more (in both directions) are implied.

The dotted error bars on the plot, in the x and y directions represent estimates of the error on the proxy mass arising from a combination of the measurement error in the proxy quantity, the calibration error in converting it to a mass and our estimate of the intrinsic scatter in the proxy value across the population (see §3.4.2). It is immediately apparent that these error bars are far too large – i.e. they are inconsistent with the observed scatter in the data. Table 3.3 shows that this error bar is dominated by the estimated contribution ($\sigma_{\log M,int}$) from scatter in the population. This in turn has been estimated (Equation 3.18) by subtracting the expected X-ray mass error and the propagated error in the proxy measurement from the observed scatter in mass about the regression relation. If there are offsets in the X-ray masses over and above their statistical errors, which it appears that there are, then $\sigma_{\log M,int}$ will be overestimated. It seems clear that this is the case.

Our analysis thus far has made use of X-ray masses derived from a hydrostatic mass analysis. However, a simpler X-ray mass estimate can be derived from the mean X-ray temperature, using a mass-temperature relation. We have checked that the overall picture seen in Figure 3.8 remains unchanged if such temperature-based masses are used. The most discrepant groups in the Figure, remain similarly offset with the alternative X-ray masses.

3.6 Mock groups

The results presented above are derived from a sample of relaxed X-ray bright systems. In practice, it would be very useful to have mass estimates for a wider range of groups, such as is generated by optical selection from a galaxy redshift survey. However, we have no such optically selected group sample for which robust mass estimates are available against which to compare our mass proxies. We therefore turn to simulations.

Applying our mass proxies to a set of groups and clusters generated from simulations, we have the advantage of a known halo mass that is *independent* of any X-ray selection biases. An additional advantage is availability of a larger sample size. On the other hand, conclusions drawn from simulated systems may be strongly affected by the assumptions and tuning which are incorporated into the simulated galaxy/group population.

For this study we make use of the mock galaxy catalogues generated for use by the GAMA consortium. The Galaxy And Mass Assembly [GAMA, Driver et al., 2011; Merson et al., 2013; Robotham et al., 2011] project aims to use a broad range of multi-wavelength observations to study cosmology and the formation and evolution of galaxies. The optical component of this project is a medium-deep galaxy redshift survey conducted by AAOmega multi-object spectrograph at the Anglo-Australian Observatory. Covering $\sim 250\,\mathrm{deg}^2$ of the sky, the GAMA project has spectroscopy for over 300,000 galaxies to $m_r < 19.8$.

A FoF analysis was conducted by Robotham et al. [2011] to identify galaxy groups within the survey. To support this analysis, a series of mock lightcones [Merson et al., 2013] were generated using the Millennium simulation [Springel

et al., 2005] populated with a semi-analytic galaxy formation model [Bower et al., 2006]. The galaxy luminosity functions of the mocks were adjusted to precisely mimic the observed r-band redshift dependent GAMA galaxy luminosity function of Loveday et al. [2012]. These mocks cover $\sim 144\,\mathrm{deg}^2$ in three $4\times12\,\mathrm{deg}^2$ regions, mimicking the original GAMA-I equatorial fields [Driver et al., 2011].

From these lightcones we select group galaxies using the methodology described in Section 3.2.2. We cut the initial galaxy catalogue to $m_r \leq 17.5$ to match our observational sample. Our volumetric group sample is then extracted from this catalogue, centring each extracted cylinder at the position of the original Robotham et al. [2011] GAMA FoF groups containing 10 or more galaxies. In addition, we run our implementation of the E04 FoF algorithm on the mock galaxy catalogue to construct a FoF group sample, retaining only groups with at least 10 members. We define the dominant group halo as the dark matter halo that contributes the most galaxies to either the initial GAMA FoF group (in the case of the volumetric sample) or to our FoF group for the FoF group sample. The mass of this halo is taken to be the true mass of the group. These masses, originally M_{Dhalo} [Jiang et al., 2014], have been converted to our cosmology and to M_{500} using a mass dependent scaling of $M_{500} = 10^{0.34} M_{\mathrm{Dhalo}}^{0.96}$. This conversion was derived from a set of median halo masses at $z = 0$ for the Millennium-I cosmology [Jiang et al., 2014]. To be comparable to our observational sample we restrict the redshift range of the mock sample to $0.01 \leq z \leq 0.1$ and only consider groups with $M_{500} \geq 10^{13}$ $\mathrm{M}_{\odot}$. The final simulated volumetric and FoF group samples consist of 179 and 313 groups respectively across 9 mock realisations, a significant improvement in sample size relative to our observational sample.

The larger number of FoF groups, compared to volumetric ones, results from

the fact that our FoF algorithm is more generous in linking galaxies than that of Robotham et al. [2011], as discussed below. These mock groups have halo M_{500} ranging from $\sim 10^{13}\mathrm{M}_{\odot}$ to $\sim 4 \times 10^{14}\mathrm{M}_{\odot}$. This upper mass is considerably lower than the highest mass cluster in the observational sample (Abell 2142 with $M_{500} \sim 1.3 \times 10^{15}$ $\mathrm{M}_{\odot}$) due to the larger volume probed by the X-ray + SDSS sample, compared to the GAMA mocks.

Considering briefly the performance of our FoF algorithm, it is clear that it recovers a greater number of FoF groups than the GAMA algorithm. As we discussed in §3.2.2, our algorithm is essentially that developed by Eke et al. [2004] to generate the 2PIGG group catalogue from the 2dF galaxy redshift survey. Conversely, the GAMA FoF algorithm has been carefully tuned on the GAMA mocks to optimise the fidelity of the grouping. The performance of the 2PIGG algorithm was examined by Robotham et al. [2010] finding that the 2PIGG algorithm was generous in terms of linking together subgroups. By application to the GAMA mocks we similarly find that the 2PIGG algorithm generously links together neighbouring structures. Indeed, 18% of groups have more than 50% contamination (i.e. of the linked members, less than half belong to the dominant halo), whereas this figure is only 10% for GAMA FoF groups. As the 2PIGG algorithm is more generous, we find it recovers a high fraction of true members, where 64% of our groups link together more than 90% of the dominant halo's galaxies, compared to only 10% of the GAMA FoF groups.

In summary, our algorithm will link most of the true member galaxies, but will also include a larger interloper fraction. Given that the GAMA galaxy luminosity function at low redshift is similar to that of SDSS [Loveday et al., 2012], it is likely that these conclusions are also applicable to the use of our algorithm on

our SDSS-based observational sample.

In the light of these differences in FoF performance, we have also examined the performance of our mass proxies on the original GAMA mock FoF catalogue (cut to our mass, magnitude and redshift range). We find little significant difference to the results with our own FoF groups, the most notable difference being that the richness overdensity and σ^3 proxies perform closer to theoretical expectations. For consistency with the observational sample we proceed using our own FoF selection, with reference to the original GAMA FoF selection where differences are significant.

3.7 Comparing Results for Observed and Mock Groups

In this section we discuss the results from the mock groups. We calibrate each mass-proxy relation, again using BCES (X|Y) regression, with the intention of examining whether they are consistent with observations. We do not attempt to bootstrap proxy errors for the mock groups. Instead, as we have selected mock groups to be comparable to our observational sample, we approximate the fractional statistical error in proxy and mass for all mock groups as the root mean square fractional statistical error in mass and proxy from the observational sample. Our analysis here is otherwise identical to that of the observational sample in Section 3.5.

Table 3.5: BCES regression results for the mock group sample corresponding to the best fit regression lines in Figures 3.9 and 3.10.

Method	α	β	$\log_{10}(x_0)$	ρ[a]	$\sigma_{\log M,tot}$[b]	$\sigma_{\log M,int}$[b,c]	$\sigma_{\log M,cal}$[b]	$\sigma_{\log M,sys}$[b,d]
Volumetric Selection								
Richness	$1.49^{+0.10}_{-0.11}$	$-0.10^{+0.02}_{-0.02}$	2.10	0.79	0.23	$0.19^{+0.03}_{-0.02}$	$0.03^{+0.00}_{-0.00}$	$0.19^{+0.03}_{-0.02}$
Luminosity	$1.41^{+0.13}_{-0.14}$	$-0.06^{+0.02}_{-0.03}$	11.80	0.68	0.34	$0.29^{+0.04}_{-0.04}$	$0.05^{+0.01}_{-0.01}$	$0.30^{+0.04}_{-0.04}$
Overdensity (N)	$0.87^{+0.08}_{-0.09}$	$0.01^{+0.03}_{-0.03}$	14.27	0.67	0.36	$0.31^{+0.04}_{-0.03}$	$0.05^{+0.01}_{-0.01}$	$0.31^{+0.04}_{-0.03}$
Overdensity (L)	$0.82^{+0.08}_{-0.11}$	$0.03^{+0.03}_{-0.03}$	14.31	0.62	0.42	$0.37^{+0.05}_{-0.04}$	$0.07^{+0.01}_{-0.01}$	$0.38^{+0.05}_{-0.04}$
Dynamical ($r_{rms}\sigma^2$)	$1.24^{+0.11}_{-0.13}$	$-0.01^{+0.03}_{-0.03}$	8.14	0.62	0.37	$0.34^{+0.05}_{-0.05}$	$0.05^{+0.01}_{-0.01}$	$0.34^{+0.05}_{-0.05}$
Dynamical (σ^3)	$0.87^{+0.07}_{-0.08}$	$0.05^{+0.03}_{-0.03}$	8.23	0.64	0.34	$0.31^{+0.04}_{-0.04}$	$0.05^{+0.01}_{-0.01}$	$0.32^{+0.04}_{-0.04}$
Radius	25.40^{+1996}_{-1971}	$0.01^{+11.75}_{-11.41}$	2.70	0.07 (66%)	2.25	2.09^{+146}_{-169}	$1.28^{+143000}_{-157000}$	$2.45^{+143000}_{-157000}$
FoF Selection								
Richness	$1.35^{+0.07}_{-0.07}$	$-0.17^{+0.02}_{-0.02}$	2.17	0.70	0.31	$0.29^{+0.03}_{-0.02}$	$0.03^{+0.00}_{-0.00}$	$0.29^{+0.03}_{-0.02}$
Luminosity	$1.28^{+0.08}_{-0.09}$	$-0.13^{+0.02}_{-0.03}$	11.86	0.64	0.41	$0.38^{+0.04}_{-0.04}$	$0.04^{+0.01}_{-0.01}$	$0.39^{+0.04}_{-0.04}$
Overdensity (N)	$0.76^{+0.05}_{-0.06}$	$-0.04^{+0.03}_{-0.03}$	14.14	0.66	0.45	$0.42^{+0.04}_{-0.04}$	$0.05^{+0.01}_{-0.01}$	$0.43^{+0.04}_{-0.04}$
Overdensity (L)	$0.71^{+0.05}_{-0.06}$	$0.00^{+0.03}_{-0.04}$	14.18	0.63	0.52	$0.50^{+0.07}_{-0.06}$	$0.05^{+0.01}_{-0.01}$	$0.50^{+0.07}_{-0.07}$
Dynamical ($r_{rms}\sigma^2$)	$1.08^{+0.06}_{-0.07}$	$-0.10^{+0.02}_{-0.02}$	8.17	0.66	0.36	$0.34^{+0.03}_{-0.03}$	$0.04^{+0.00}_{-0.00}$	$0.34^{+0.03}_{-0.03}$
Dynamical (σ^3)	$0.89^{+0.05}_{-0.06}$	$-0.07^{+0.02}_{-0.02}$	8.00	0.68	0.35	$0.33^{+0.03}_{-0.02}$	$0.03^{+0.00}_{-0.00}$	$0.33^{+0.03}_{-0.02}$
Radius	$5.90^{+0.94}_{-1.41}$	$-0.13^{+0.06}_{-0.08}$	2.86	0.27	1.01	$0.98^{+0.16}_{-0.24}$	$0.19^{+0.07}_{-0.11}$	$1.00^{+0.17}_{-0.25}$

[a] Spearman rank correlation. Unless shown in parentheses, all results have $> 95\%$ significance.

[b] Estimated fractional scatters in mass in dex.

[c] Intrinsic scatter in mass accounting for statistical scatter in the proxy (see Eq. 3.18). Statistical fractional scatter in mass and proxy are assumed to be equivalent to the mean fractional error from the observational sample reported in Table 3.3.

[d] The systematic scatter in mass, $\sigma^2_{\log M,sys} = \sigma^2_{\log M,int} + \sigma^2_{\log M,int}$.

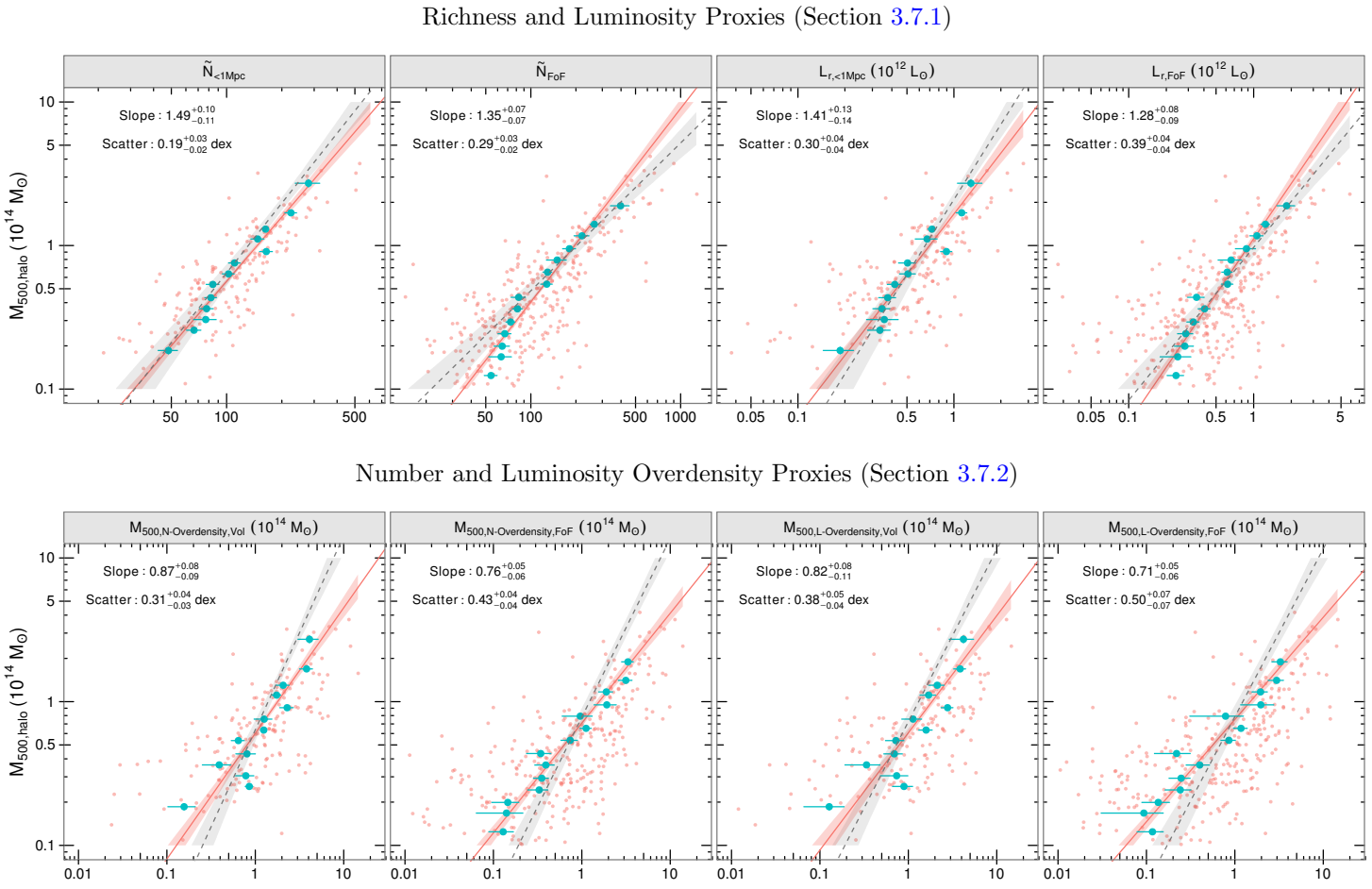

Figure 3.9: Mock group halo M_{500} plotted against, from left to right, top to bottom, Richness, Luminosity, Number Overdensity and Luminosity Overdensity mass proxies. Alternating plots show results for the volumetric and FoF sample. Faint red points show all mock groups whilst the blue points show horizontally binned averages and their standard errors. The red solid lines and shaded regions show the BCES(X|Y) regressions and a 68% percentile contour region drawn from the distribution of bootstrapped fit results for the mock data. The grey dashed lines and shaded regions show the same for the observational sample shown in Figure 3.2.

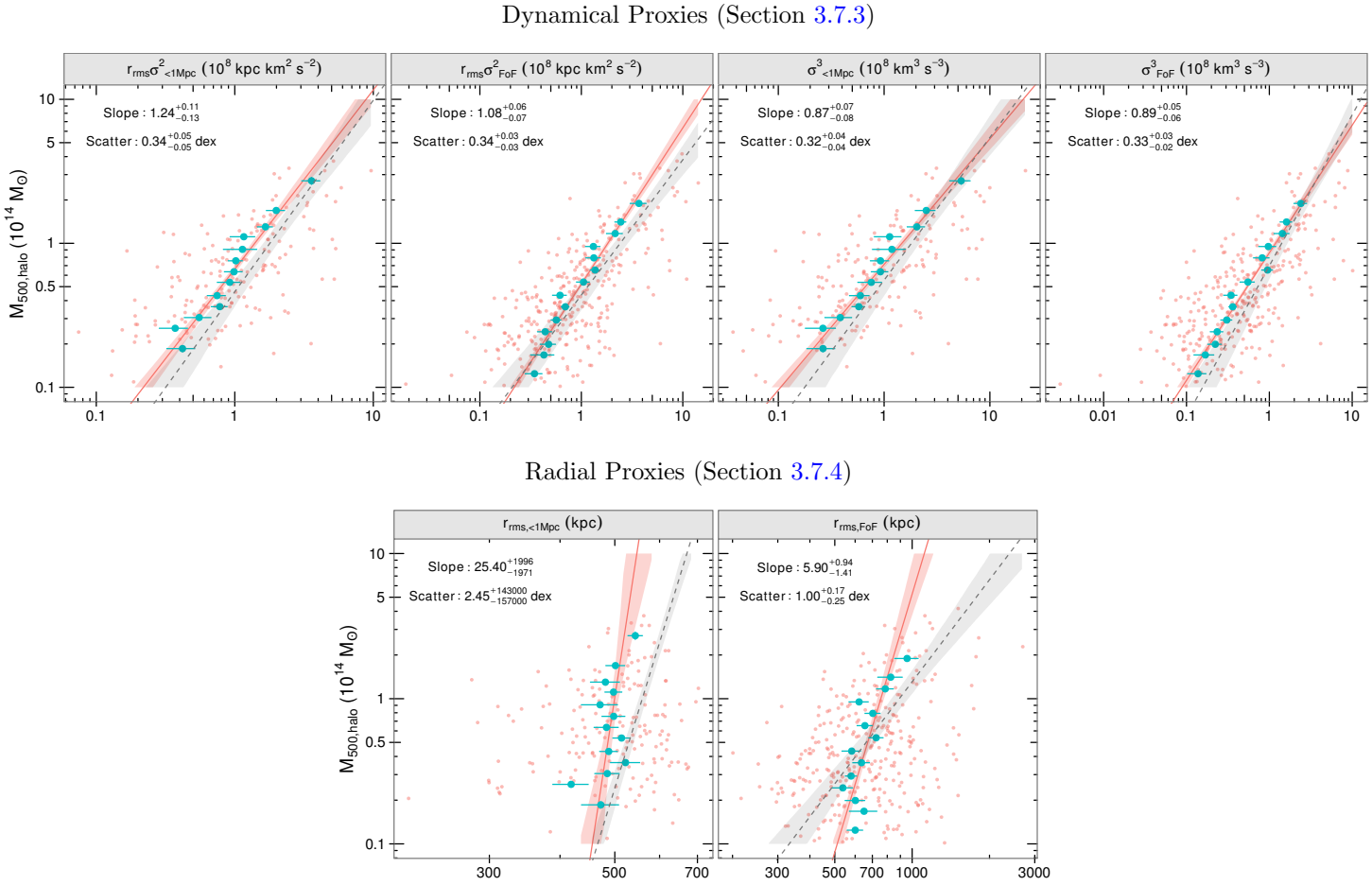

Figure 3.10: As Figure 3.9 with, from left to right, top to bottom, $r_{rms}\sigma^2$ Dynamical, σ^3 Dynamical and r_{rms} radius. The grey dashed lines and shaded regions show the same for the observational sample shown in Figure 3.3.

The Figures in this section follow those of Section 3.5, except that, for comparison to the observational sample, we overplot the mock mass – proxy data with the observational calibration line and error region. To aid in readability and highlight any trends we additionally bin our mock group's data. To avoid any biases introduced by the richness cut in the original GAMA catalogue this binning is performed horizontally, in $\log_{10}(M_{500})$ slices.

3.7.1 Richness and Luminosity

With Table 3.5 and the top row of Figure 3.9 we find that these GAMA mocks produce a mass-aperture richness relation that is in good agreement with observations, whilst the mass-aperture luminosity relation is shallower, but marginally consistent within the lower bound of the observational result. In general terms, these slopes are also consistent with the effect of an aperture, though not both an aperture and star-formation efficiency variation. Conversely, the FoF richness and luminosity estimators give results discrepant with the observational sample, both being significantly steeper.

We again consider the richness-luminosity relations, Figure 3.11. We find that the relation, whilst in good agreement with the observations and expected slope of 1 at high mass, deviates from the power law slope at low mass. Specifically we see an underluminous population of mock groups at low mass. This is possibly related to the galaxy formation models' implementation of satellite galaxy merging where a satellite galaxy is not resolved in its subhalo [Robotham et al., 2011]. If assigned too long a merging time, this will result in an excess of faint satellite galaxies in close orbits of central galaxies or the centre of the halo. This close satellite excess

will also affect other mass proxies.

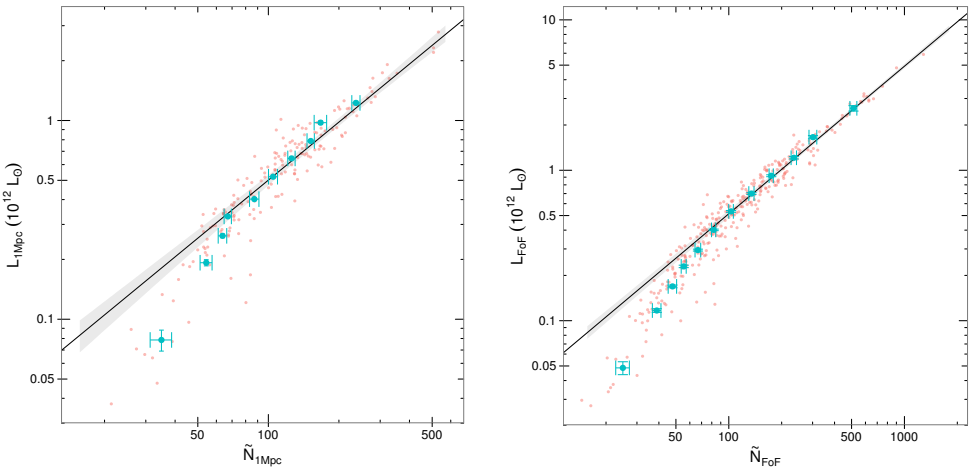

Figure 3.11: As Figure 3.9 with *Left:* background subtracted optical luminosity against richness within 1 Mpc, *Right:* Total FoF luminosity against FoF richness.

3.7.2 Overdensity

As shown in Table 3.5 and the second row of Figure 3.9, we find that the mock groups have a significantly shallower relation for overdensity masses than that of both the observed groups and the expectation of unity. This is true regardless of the selection method. In the case of the observed groups, we concluded that the steeper than unity slopes could be understood in the light of expected variations in star formation efficiency with halo mass. Another factor here may be the previously mentioned anomalies in the radial distribution of galaxies within mock groups [Han et al., 2014; Robotham et al., 2011].

For comparison, the GAMA FoF selection gives a slope of $0.95^{+0.12}_{-0.15}$ for the richness overdensity proxy, consistent with unity. Luminosity overdensity is also steeper for the GAMA FoF sample than for ours, though not significantly, and is

not consistent with unity.

3.7.3 Dynamical

The results of the $r_{rms}\sigma^2$ and σ^3 proxies are also shown in Table 3.5 and in the top row of Figure 3.10. As with the observational sample, we find that it is difficult to draw conclusions from the volumetric $r_{rms}\sigma^2$ relation due to the steepness of the r_{rms} relation (see below). Interestingly, we find that in contrast to the situation with the observed groups, the two σ^3 proxies, are also significantly discrepant from the expectation of unity slope. For comparison, the GAMA FoF selection gives a slope for the σ^3 proxy of $0.97^{+0.08}_{-0.10}$, consistent with unity.

3.7.4 Radii

Table 3.5 and the second row of Figure 3.10 show the results of the r_{rms} estimator. We first observe that the total scatter on this proxy is substantial for both selection methods (2.4 dex and 1.1 dex for the volumetric and FoF samples respectively). This makes it difficult to reliably constrain any calibration relation. Despite this, we find that the volumetric sample, which is again subject to interloper contamination and aperture effects, gives a relation that is steeper than the already very steep observed relation. The FoF estimator is also significantly steeper than the observational relation, and also steeper than the expected slope of 3.

3.7.5 Summary

In Tables 3.6 and 3.7 we bring together a summary of the comparison between the mass-proxy relations derived from the observational sample and the mocks, and a comparison of these with theoretical expectations. The proxies based on the mocks have relations which differ significantly from observations, with the exception of the σ^3 dynamical estimator, which agrees within the errors on the observational result. We also note that whilst the radius-mass relation is significantly different to the observationally derived relation, due to known issues with the orbits of satellite galaxies within the mocks [Han et al., 2014; Robotham et al., 2011], it behaves in a similar fashion, with an extremely steep relation for the volumetric sample.

The discrepancy for luminosity and overdensity might be explained by a difference in luminosity function (LF) between that assumed by the mocks and the observations. The semi-analytic galaxies were adjusted to reproduce a global luminosity function that matches that of the real GAMA fields [Robotham et al., 2011], however it does not follow that they will reproduce the luminosity function within groups and clusters. A study by McNaught-Roberts et al. [2014] examining the luminosity function of different density environments within the real GAMA fields and the GAMA mocks revealed no significant difference between simulations and reality. We note however that this study looked at the local density of each galaxy, rather than classifying galaxies as belonging to groups or the field.

The small difference between the global luminosity functions measured for the SDSS [Blanton et al., 2003] and GAMA [Loveday et al., 2012] is unlikely to

contribute greatly to the unexpectedly flat slope of the $M_{overdensity}$-$M_{\rm halo}$ relations for the mocks. A more likely cause is the radial distribution of galaxies in the mocks. As discussed in Han et al. [2014] [see also Robotham et al., 2011], who compared mass-observable relations for the GAMA fields and GAMA mocks, there is tension between the mocks and real data for the relationship between mass and $r_{50\%}$ (the radius containing 50% of a group's projected galaxies) which may have its origin in the approximate treatment of dynamical friction within the semi-analytic model, and consequent inaccuracies in the rate of orbital decay. This can be expected to modify the relationship with halo mass for both the overdensity and radius proxies.

Han et al. [2014] also find a systematic bias in the mass-velocity dispersion relation for the mocks compared to the real groups, again, due to known issues with the small scale dynamics of the GAMA mocks [Robotham et al., 2011]. This may be the cause of the lower slope in the mock mass-σ^3 relation relative to observation and to theoretical expectations.

Comparing the residuals of predicted masses with respect to the halo mass, in a similar fashion to that discussed in §3.5.6, we find much weaker correlation between unrelated proxies than was apparent in the observational sample. For example, the richness and σ^3 estimators show a weak, but still significant ($> 95\%$) correlation ($\rho = 0.18^{+0.07}_{-0.07}$ and $0.31^{+0.06}_{-0.05}$ for volumetric and FoF samples respectively) significantly different to the values of $0.81^{+0.05}_{-0.11}$ and $0.66^{+0.19}_{-0.15}$ seen observationally. The asymmetry in Figure 3.12 can be compared with that in the corresponding observational plot, Figure 3.8. The small error range from the mocks' bootstrapped correlations agrees with the high level of significance indicating that the mocks' residuals behave very differently to those of the obser-

vational sample, supporting the possibility that this effect is due to excess X-ray mass errors. The non-zero correlation seen for the mocks may arise from the effects of interlopers enhancing both richness and velocity dispersion. The fact that it is stronger in the FoF case, where no correction of richness for background galaxies has been included, supports this hypothesis.

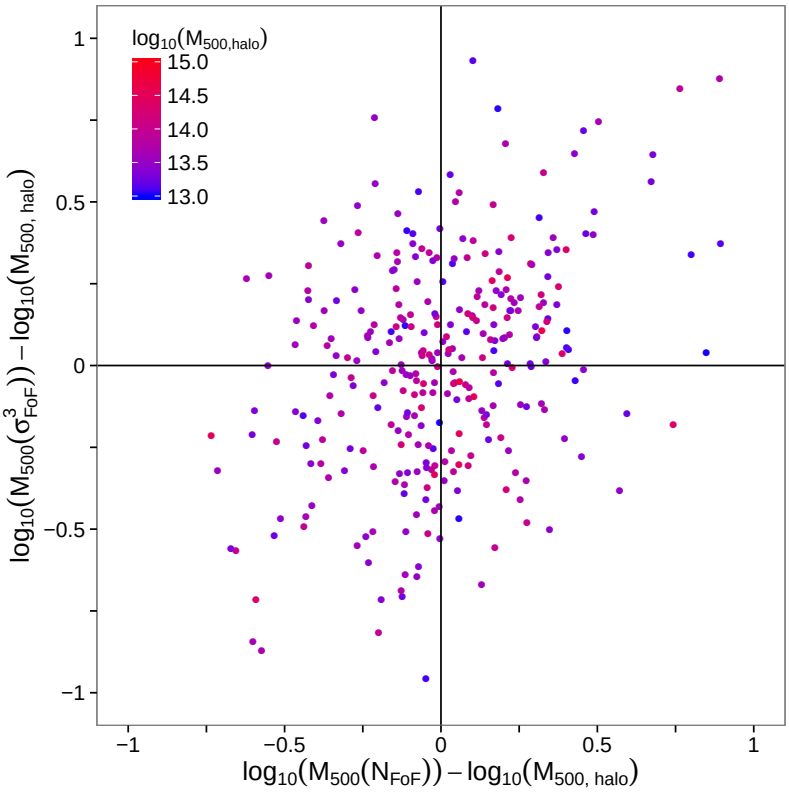

Figure 3.12: Fractional residuals about the regression lines for the mock groups' FoF richness and σ^3 dynamical estimators defined as $R = \log_{10}(M_{500}(x)) - \log_{10}(M_{500,halo})$. Each datapoint is coloured according to its halo mass, with blue $\sim 10^{13}$ $M_\odot$ and red $\sim 10^{15}$ $M_\odot$.

Comparing Table 3.5 with Table 3.3, it can be seen that the total scatter, $\sigma_{\log M,tot}$, about the mass-proxy relations for the mocks are mostly greater than the corresponding scatter for the observational sample. This suggests that, as

expected, we are sampling a more diverse group population in the mocks, in terms of their dynamics and evolutionary state, compared to the relaxed X-ray bright systems on which our observational sample is based. This emphasizes the importance of allowing for selection effects in any study of galaxy groups – samples selected in different ways can be expected to catch a different mix of dynamical and evolutionary states.

Finally, we comment briefly on the use of these proxies when the true galaxy membership is known. Thus far we have analysed the mocks by applying similar selections processes (volumetric and FoF) to those used on the observational data. Since our mass-proxy relations have been calibrated on observational data which will inevitably be contaminated by interlopers, we can expect to find different results for mocks groups if we use the *true* group membership, which is available for these simulated systems. Examining mass-proxy relations using the true galaxy membership can cast light on the fundamental nature of these proxies. Specifically considering the mass-richness relation (scaled to $M_r < -16.5$) and the mass-σ^3 these fit with BCES (X|Y) slopes of 1.07 ± 0.03 and 0.81 ± 0.05 with systematic scatters of $0.13^{+0.03}_{-0.02}$ dex and 0.29 ± 0.03 dex respectively, again assuming the masses and proxies have statistical errors comparable to the mean errors from the observational sample. Interestingly, the first relation, whilst significantly shallower than the mock mass-richness relations derived earlier, is still steeper than the expectation of unity by more than 2σ, even in the absence of aperture effects or FoF selection effects. This is likely related to the way galaxies populate the halos within the mocks, and to their merger history. Conversely, the mass-σ^3 relation is shallower than unity, as with other mock mass-σ^3 relations, illustrating the known concerns with the dynamics of the mock halos [Han et al.,

2014; Robotham et al., 2011]. Both relations show smaller systematic scatter than the corresponding relations with volumetric of FoF selection, indicating the scattering effects of interlopers.

3.8 Discussion and conclusions

In this paper we have investigated the behaviour of mass proxies based upon richness, luminosity, galaxy number and luminosity overdensity, characteristic radii and dynamics. We have applied these estimators to sets of group galaxies derived in two ways: a σ-clipped cylindrical volume and a Friends-of-Friends analysis. The mass proxies have been calibrated using masses derived from the X-ray properties of the hot intragroup gas, and the resulting calibrations compared with theoretical expectations. The performance of the same mass proxies has been assessed on a set of mock groups for which true halo masses are known. Our findings for each proxy are summarised in Tables 3.6 and 3.7. We conclude that:

1. The calibrated relationships between these mass proxies and the X-ray derived masses are consistent with theoretical expectations once aperture effects and the impact of mass-dependent variations in star formation efficiency are allowed for.

2. The most reliable mass estimate is provided by modelling the galaxy number density within a 5 Mpc cylinder (i.e. for a volumetric group sample). This mass proxy exhibits the smallest intrinsic scatter and the joint least uncertainty introduced by the calibration, resulting in only 0.1 dex (23%) systematic uncertainty in any final mass estimate. However, for our own

Table 3.6: Summary - comparison of the performance of the observations and mock results for the volumetric sample, noting any deviation from theoretical expectations.

Method	Observational	Mocks
Richness	Steeper than naive expectation of unity. Plausibly modified by aperture and star formation efficiency. Low systematic scatter.	Slope steeper than unity. Plausibly modified by aperture effects. Rough agreement with observational sample.
Luminosity	Steeper than naive expectation of unity. Plausibly modified by aperture and star formation efficiency.	Slope steeper than unity. Plausibly modified by aperture effects. Rough agreement with observational sample.
Overdensity (N)	Steeper than expected slope of unity. Plausibly modified by star formation efficiency and mass-to-light. Lowest systematic scatter, but high statistical scatter.	Shallower than expected slope of unity.
Overdensity (L)	Steeper than expected slope of unity. Plausibly modified by star formation efficiency and mass-to-light. Low systematic scatter, but highest statistical scatter.	Shallower than expected slope of unity.
Dynamical ($r_{rms}\sigma^2$)	Steeper than expected slope of unity. Possibly unreliable due to poor quality r_{rms}.	Steeper than expected slope of unity. Possibly unreliable due to poor quality r_{rms}.
Dynamical (σ^3)	Consistent with expected slope of unity. Greatest systematic scatter.	Shallower than expected slope of unity, but consistent within the errors on the observational sample.
Radius	Slope much steeper than naive expectation of 3. Plausibly modified by aperture effects. Errors dominated by statistical errors.	Slope much steeper than naive expectation of 3. Plausibly modified by aperture effects. Large scatter observed in the data.

Table 3.7: As Table 3.6 for the FoF Sample.

Method	Observational	Mocks
Richness	Consistent with expectations of unity before and after accounting for star formation efficiency. Low systematic scatter.	Steeper than expected slope of unity.
Luminosity	Consistent with expectations of unity before and after accounting for star formation efficiency.	Steeper than expected slope of unity.
Overdensity (N)	Steeper than expected slope of unity. Plausibly modified by star formation efficiency and mass-to-light. Low systematic scatter, but high statistical scatter.	Shallower than expected slope of unity.
Overdensity (L)	Steeper than expected slope of unity. Plausibly modified by star formation efficiency and mass-to-light. Low systematic scatter, but highest statistical scatter.	Shallower than expected slope of unity.
Dynamical ($r_{rms}\sigma^2$)	Consistent with expected slope of unity.	Steeper than expected slope of unity.
Dynamical (σ^3)	Consistent with expected slope of unity.	Shallower than expected slope of unity. Consistent within the errors on the observational sample.
Radius	Shallower than expected slope of 3. Largest systematic error.	Significantly steeper than expected slope of 3.

dataset this proxy also has the largest statistical scatter, and is therefore only likely to work well where one has high quality galaxy membership data, such that reliable galaxy density profiles can be fitted.

3. Richness, for either volumetric or FoF selection, is the next best method, and has the merit of being simple to apply, and working well even for fairly small galaxy samples. Of course, it is essential that this, and the overdensity and luminosity proxies, should be corrected for any incompleteness in survey coverage or spectroscopic observations.

4. Dynamical estimators show larger scatter, with a systematic uncertainty of $\gtrsim 0.3$ dex ($\gtrsim 70\%$). However, they do have the attractive feature that they are relatively robust against spectroscopic incompleteness. They may therefore become the preferred option for mass estimation where incompleteness is difficult to quantify. The $r_{rms}\sigma^2$ proxy should be avoided, in favour of σ^3, for volumetric galaxy samples, due to bias in the estimation of r_{rms}.

5. A r_{rms} radial estimator should not be used in cases where a restrictive aperture has been applied, such as our volumetric selection. It is more useful in the case of a FoF sample, however the scatter is substantial (0.35 dex, or 81%, systematic uncertainty).

The same set of mass proxies was applied to groups drawn from the mock galaxy data generated for the GAMA project. We find that in most cases the mass-proxy relations differ from those for the observational group sample, and that the scatter of the sample around the mean relationship is greater. This larger scatter suggests that our mock sample spans a more diverse collection of galaxy

groups than the relaxed X-ray bright systems which constitute the observational sample.

This greater diversity in the population might account for some of the differences in the mass-proxy relations which we see. However, the discrepancies between observational and mock samples are most striking for the overdensity and radius mass proxies, and these are affected by the radial distribution of group galaxies. This distribution is unreliable in the inner regions of the mock groups, due to the approximate treatment of orbital decay in the semi-analytic model on which they are based [Han et al., 2014; Robotham et al., 2011]. The richness, luminosity and σ^3 mass proxies are in better agreement for the observational and mock samples, though in general the fitted relations do not agree within the 1σ range.

The estimated systematic error ($\sigma_{\log M,sys}$) for each mass proxy, shown in the last column of Table 3.3, is an important quantity. This represents the uncertainty in the $\log_{10}$(mass) which results for each mass proxy even when the value of the proxy is precisely known. The low values of this for the overdensity proxies when applied to the volumetric sample are the basis for our statement above that this provides the most reliable single mass estimator where high quality galaxy data are available.

However, our estimate of this systematic error is subject to two opposing biases. As explained in §3.4.2, this quantity is derived from the observed scatter in mass about the fitted mass-proxy relation by subtracting the estimated statistical contributions to this scatter and then adding the variance which arises from uncertainty in the calibrated power law relation. However, we have seen (§3.5.6) that for a subset of our observational sample there appear to be errors in the X-

ray derived masses which exceed their statistical error estimates. Since we have not allowed for these, this will have inflated our estimates of $\sigma_{\log M,sys}$. On the other hand, we may expect the scatter in intrinsic group properties for a group sample more diverse than our observational sample to be larger, and this would naturally lead to *larger* scatter in the relation between true mass and proxy mass estimates, as we see from our mock sample. On the whole, it is probably best to regard the systematic error estimates for the mass proxies in Table 3.3 as being a useful indication, which is likely to be pessimistic for use with relaxed group samples, but not necessarily when used on a more diverse set of groups.

The diversity in the properties of galaxy groups has been documented by many authors [e.g. Balogh et al., 2011; Osmond and Ponman, 2004; Rasmussen et al., 2006; Zabludoff and Mulchaey, 1998]. In the light of this, there are considerable advantages to employing not just a single mass proxy, but a whole set of them, since different proxies will be robust against different effects. For example, mass estimates based on velocity dispersion are likely to be in error for dynamically disturbed groups which have recently experienced a major merger, whilst an estimate based on galaxy richness or luminosity should be relatively unaffected. On the other hand, variations in star formation efficiency, or in the fraction of stars stripped from galaxies will impact on richness, luminosity and overdensity estimates, but not on the velocity dispersion or radius proxies. The effects of orbital decay and merging in old groups will impact on the richness and the fitted galaxy profile, though the impact on the total overdensity within r_{500} should be modest. It would be very interesting to compare the performance of these different mass proxies across a wide range of groups and clusters with high quality X-ray data and optical photometry to explore such effects.

Finally, we remind the reader that the proxy-mass calibrations presented here are derived from a low redshift sample of relaxed groups and clusters, and should not be used without modification for systems at significant ($z \gg 0.1$) redshifts. In some cases, the nature of the required modification can be simply predicted theoretically – for example the velocity dispersion of a virialised system of given mass should scale as $H(z)^{1/3}$, where $H(z)$ is the Hubble parameter at redshift z – but in others (the effects of galaxy luminosity evolution, for example) calibration on a high redshift sample is really required.

Chapter 4

GAS ENTROPY IN A SAMPLE OF OPTICALLY SELECTED GROUPS

4.1 Introduction

Studies of the hot gas in groups and clusters have demonstrated that this gas exhibits entropies in excess of self-similar expectations [e.g. Lloyd-Davies et al., 2000; Ponman et al., 1999]. Determining how, why and when this entropy was raised is essential to better understand galaxy formation and evolution. For example, many of the processes that have been proposed to raise entropy are also implicated in maintaining the hot gas reservoir and preventing runaway cooling of gas into stars (the cooling catastrophe).

Early models suggested that entropy had been injected into the intracluster medium (ICM) prior to the full collapse of the halo [Evrard and Henry, 1991;

Kaiser, 1991]. Proposed sources of entropy include supernova feedback and active-galactic nuclei [Lloyd-Davies et al., 2000; Tozzi and Norman, 2001; Wu et al., 2000]. Due to the smaller potential wells of groups compared to massive clusters, the entropy injected into gas at group scales can be significant compared to the entropy accrued during halo assembly. Alternatives, such as cooling flows, which will preferentially cool low entropy gas into stars, raising the *mean* ICM entropy [see, e.g. Bryan, 2000; Voit and Bryan, 2001], have also been proposed.

Hydrodynamical simulations have explored the evolution of gas within group and cluster halos, examining the effect of the various proposed feedback models [e.g. the OverWhelmingly Large Simulations project, OWLS, Schaye et al., 2010]. Conclusions [e.g. McCarthy et al., 2010, 2011] suggest the observed entropy distribution is due to the pre-heating of gas by AGN feedback. The models used in these simulations also predict a distribution of central entropies broader than currently observed, where known X-ray groups and clusters populate the low entropy portion of the distribution. As a population of high entropy groups would have suppressed X-ray luminosity, they would be unlikely to appear in a typical X-ray selection where samples are constructed based on their X-ray properties, such as the group X-ray luminosity. To observe a high entropy population of galaxy groups, the group sample needs to be constructed independently of the X-ray properties.

In this chapter we select an optical sample of galaxy groups from the Galaxy And Mass Assembly [GAMA, Driver et al., 2011] project's Friends-of-Friends group catalogue [Robotham et al., 2011]. Despite being insensitive to any X-ray selection effects, optically selected samples can be affected by other selection effects, such as identified groups merely being chance alignments or are halos that

have yet to fully collapse. Selecting an uncollapsed or spurious group would have an effect similar to high entropy as the lower density gas in such systems would also show low X-ray luminosities (L_X). This makes it extremely important that our optical groups are also a relaxed sample.

The outline of this chapter is as follows: In §4.2 we discuss how we select our sample of relaxed optical groups using substructure in the distribution of member galaxies. §4.3 describes the X-ray analysis that we perform and §4.4 the results of our sample. We conclude this study in §4.5 and §4.6, examining the virialisation of these groups and understanding the limitations of our analysis that can affect entropy constraints. Throughout this chapter we adopt a simple ΛCDM cosmology with $\Omega_m = 0.3$, $\Omega_\Lambda = 0.7$ and $H_0 = 70$ km s^{-1} Mpc^{-1}, with $h = H_0/100$ km s^{-1} Mpc^{-1} $= 0.7$ and $h_{70} = H_0/70$ km s^{-1} Mpc^{-1} $= 1$. We reduce our X-ray data using CIAO 4.5 (CALDB 4.5.6 and SHERPA 1) and also make use of the R statistical package [R Development Core Team, 2009].

4.2 Data

To investigate whether a population of high entropy groups exists we need to select a sample of relaxed, optically selected groups. This removes ambiguity in the source of any observed low L_X groups. The GAMA project [Driver et al., 2011] provides an excellent platform from which to begin a study of this nature.

The Galaxy And Mass Assembly project is a broad multi-wavelength project covering $\sim 250\,\mathrm{deg}^2$ of the sky. The optical component of this project consists of a medium-deep redshift survey of more than 300,000 galaxies within the GAMA regions taken by the AAOmega multi-object spectrograph at the Anglo-Australian

Observatory. These galaxies have been grouped by Robotham et al. [2011] with a Friends-of-Friends (FoF) algorithm optimised on a sample of 9 realistic mock light cones [Merson et al., 2013]. These light cones were generated using the dark matter Millennium Simulation [Springel et al., 2005] populated with galaxies using the Bower et al. [2006] semi-analytic models of galaxy formation, with modifications to reproduce the observed r-band, redshift dependent GAMA luminosity function of Loveday et al. [2012].

At the time this study began the GAMA survey was complete to only $m_r < 19.4$ from which the G3Cv04 group catalogue was constructed [Robotham et al., 2011]. Since then, additional galaxy spectra were taken, extending the completeness to $m_r < 19.8$ and accompanied by an updated (v06) group finder. We performed our group selection using the v04 group catalogue. The subsequent analysis presented here makes use of the richer data available from the v06 group catalogue.

The G3Cv04 catalogue contains 14,388 FoF groups throughout the redshift range and with at least 2 members. We immediately cut the catalogue to contain $N \geq 12$ galaxies to reduce the likelihood of spuriously linked galaxies. This leaves a catalogue of 205 galaxy groups from which we chose a final sample of 10 with redshift ≤ 0.12. As halo mass has been found to correlate well with group optical luminosity [e.g. Popesso et al., 2007], we adopt the group r-luminosity as a predictor for group mass, in turn predicting their X-ray properties. We use the relation

$$M_{GAMA,DHalo} = 10^{3.406-(0.4364M_r)} \tag{4.1}$$

where M_r is the total r-band absolute magnitude of the early group catalogues,

calibrated on the mock group sample. We recast this in terms of L_r, the total r-band luminosity discussed in Robotham et al. [2011], for the v06 data as

$$M_{GAMA,DHalo} = 10^{1.37} L_r^{1.09} \tag{4.2}$$

assuming $M_{r,\odot} = 4.67$[1]. We specifically use the luminosity $L_{FoF} = BL_{obs}f(z)$ where L_{obs} is the total observed light, $f(z)$ is an extrapolation factor to account for GAMA's flux limit and B is a correction factor dependent on both group richness and redshift calibrated on the GAMA mock catalogues [Robotham et al., 2011]. As Equation (4.1) was calibrated using mock groups with dark halo masses M_{DHalo} [Jiang et al., 2014], these luminosity based masses $M_{GAMA,DHalo}$ are then converted into M_{500} using median relations between M_{DHalo}, M_{200} and M_{500} drawn from the dark matter distribution[Jiang et al., 2014]. These overdensities are relative to the critical density of the universe.

4.2.1 Selection

To select a relaxed sample of optically selected groups we assess the degree of substructure within the group. A highly substructured group, for example, is one that is likely to still be reaching equilibrium and virialising following a recent merger or may be collapsing for the first time. The ability to exclude such systems, or ones that are spuriously linked together by the group finder, should provide a good basis from which to select a sample of relaxed halos.

Due to the lack of obvious disturbance, we would also expect groups with low levels of substructure to produce reliable mass estimates. As we use optical mass

[1] http://mips.as.arizona.edu/~cnaw/sun.html

estimates to predict the X-ray properties of our groups, selecting a sample with reliable mass estimates is important for correctly judging target feasibilities. It is especially important to avoid selecting groups whose masses are overestimated, which would result in predicted exposure times that would be too short.

We therefore adopt a set of substructure statistics, calibrated on mock data, to select our group sample. Using the mock halos and their predicted and known masses, we tune the selection to discriminate against groups whose mass estimates are more than a factor of 2 larger than the halo mass.

Our calibration and selection algorithm is as follows. First, identify a set of substructure statistics that have useful discriminating power to select mock groups whose predicted masses satisfy the above constraint. Second, establish a set of thresholds for the adopted statistics that, in combination, can maximize the number of mock groups recovered with satisfactory mass estimates. Due to the importance of rejecting groups with overestimated masses, we allow this constraint to degrade the number of acceptable groups recovered. Finally, having tuned our selection criteria on mock groups, we apply this filter to the real G3Cv04 sample.

4.2.2 Substructure Statistics

We examined a number of different substructure statistics that probed the spatial and velocity distributions of the galaxies within a group. Six of these were drawn from the compilation of Pinkney et al. [1996]. Two more were based upon the output of the Robotham et al. [2011] group analysis, with a further statistic used specifically to examine the distribution of galaxy velocities. Our chosen set of

substructure tests consist of two spatial symmetry statistics, the β-test and the angular separation test [Pinkney et al., 1996], and the Anderson-Darling test for normality [Thode, 2002] in the velocity histogram implemented through the NORTEST R package [Gross and Ligges, 2012, and references therein].

The β test

This substructure test, originally discussed in West et al. [1988] with the following discussion based on Pinkney et al. [1996], looks for deviations from mirror symmetry caused by substructure within a group halo. The test proceeds by taking each galaxy and estimating the mean separation of the $\sqrt{N}$ nearest galaxies to that galaxy, d_i, where N is the total number of galaxies within the cluster. This distance is then compared to the same quantity calculated at a point diametrically opposite the galaxy, d_o.

For each galaxy, β is then defined as

$$\beta_i = \log\left(\frac{d_o}{d_i}\right) \quad . \tag{4.3}$$

The mean value of β for all galaxies is the unnormalised β-statistic. For an unsubstructured, symmetric system $\beta \approx 0$.

The Angular Separation Test

Similar to the β test, the angular separation test [hereafter AST, Pinkney et al., 1996; West et al., 1988], examines the angular distribution of galaxies within the cluster for an excess of small angular separations that substructure may cause. The AST first determines the mean harmonic separation of members,

$$\theta_{hm} = \left[\frac{2}{N(N-1)} \sum_{i=1;i>j}^{N} \theta_{ij}^{-1} \right]^{-1} \quad , \tag{4.4}$$

where N is again the number of galaxies in the group or cluster and θ_{ij} is the angular separation of two galaxies relative to the centre of the group. Subhalos would therefore reduce the value of θ_{hm} relative to a halo without any substructure.

The final statistics for both the β test and for AST, are normalised by their value from the "null hypothesis", a value of the statistic when no substructure is present. This accounts for any contributions to the measured statistic from statistical noise in the population. To generate the null hypothesis, we perform these tests on 1000 realisations of the cluster data where the azimuthal positions of the galaxies have been randomised. We then take the mean of these ensembles to represent the substructure-less null hypothesis. The final test statistics, ζ_β and ζ_{AST} are

$$\zeta_\beta = \beta/\beta_{null} \quad \text{and} \quad \zeta_{AST} = \theta_{null}/\theta_{hm} \quad . \tag{4.5}$$

Under this definition, substructure-less groups have statistic values of ≈ 1 whilst substructured systems will have statistics $\gg 1$. The significance of this statistic is equal to the fraction of the 1000 randomisations that have *more* substructure than the measured statistic.

Anderson-Darling test

Within a virialised structure, we expect the velocity of galaxies to be distributed as a Gaussian along the line-of-sight. Recent cluster merger activity or incomplete virialisation, as well as spurious grouping, would be expected to cause deviations

from this distribution, e.g. through introducing bimodality or asymmetries in the velocity histogram. The Anderson-Darling test [hereafter the AD test, Thode, 2002] examines if a sample is consistent with having been drawn from a normal distribution, and can therefore be useful for testing for such deviations. As a reasonable proxy for galaxy velocities, we apply this to the redshifts of member galaxies.

Here we describe the AD test as laid out by Thode [2002] and as implemented by the NORTEST R package [Gross and Ligges, 2012]. The AD test proceeds by first taking the data, in this case, galaxy redshifts, z, and scaling them relative to the mean, $\bar{z}$, and standard deviation, σ_z, of the sample,

$$z' = \frac{z - \bar{z}}{\sigma_z} \quad . \tag{4.6}$$

The statistic, A^2, is then determined as,

$$A^2 = -N - \frac{1}{N}\sum_{i}^{N}(2i-1)(\log(z'_i) + \log(z'_{N-i+1})) \quad , \tag{4.7}$$

where N is the sample size. The significance of A^2, $p(A^2)$, can then be found [D'Agostino, 1986],

$$p(A^2) = 1 - \exp(-13.436 + 101.14A^{2\star} - 223.73[A^{2\star}]^2)$$

for $A^{2\star} < 0.2$,

$$p(A^2) = 1 - \exp(-8.318 + 42.796A^{2\star} - 59.938[A^{2\star}]^2)$$

for $0.2 < A^{2\star} < 0.34$,

$$p(A^2) = \exp(0.9177 - 0.4279A^{2\star} - 1.38[A^{2\star}]^2)$$

for $0.34 < A^{2\star} < 0.6$ and

$$p(A^2) = \exp(1.2937 - 5.709A^{2\star} + 0.186[A^{2\star}]^2)$$

for $0.6 < A^{2\star}$, where

$$A^{2\star} = \left(1 + \frac{0.75}{N} + \frac{2.25}{N^2}\right) A^2 \quad . \tag{4.8}$$

We use $p(A^2)$ as our substructure indicator. To be consistent with ζ_β and ζ_{AST}, we define $\zeta_{AD} = 1/p(A^2)$ such that ≈ 1 indicates low levels of substructure, and $\zeta_{AD} \gg 1$ shows substantial non-Gaussian structure in the velocity histogram.

4.2.3 Calibration

Using these substructure statistics and the mock galaxy groups we calibrate a set of substructure thresholds that produce a mock group sample satisfying the mass criteria of Section 4.2.1. To ensure we jointly optimise the three substructure statistics, we explore a gridded $(\zeta_\beta, \zeta_{AST}, \zeta_{AD})$ parameter space, characterising each combination by the accuracy of the predicted masses for the groups that pass the filter. Using one of the GAMA mock volumes, we optimise to discard all groups with predicted masses greater than twice the true halo mass whilst maximising the number of groups with mass estimates within a factor of two of the true mass. We define the true mass of each mock FoF group as the mass of

the dark matter halo contributing the most galaxies to the group.

The resulting calibration accepts groups whose substructure measures are $\zeta_\beta < 1.9$, $\zeta_{AST} < 1.68$ and $\zeta_{AD} < 1.82$. Of the 220 groups within the calibration mock volume with $N_{FoF} \geq 12$ and $z \leq 0.12$ these thresholds were able to exclude all groups whose masses were overestimated by a factor of two whilst allowing 16% of the 141 groups with masses within a factor of two (i.e. 'accurate' mass estimates) to pass. Comparing with eight other mock volumes with 1731 groups, we find this should allow 18% groups with 'accurate' masses to pass whilst allowing only 2% contamination by groups whose masses are overpredicted. The sample will also be populated by groups whose masses are underestimated. However, as the X-ray luminosity predictions will be similarly reduced, their estimated exposure time should be sufficient for high quality data to be obtained. We therefore do not filter against such groups.

4.2.4 Group Sample

Applying the calibrated substructure filters to the observational group catalogue we identify a sample of 18 groups with $N_{FoF} \geq 12$ and $z \leq 0.12$. Using the luminosity based mass estimates, we predict their X-ray temperatures using the Sun et al. [2009] mass-temperature relation. Using these temperatures, X-ray luminosities are estimated using the $L_X - T$ relation of Slack and Ponman [2014]. As we are interested in high entropy groups, we would expect these groups to be underluminous relative to the known group population. We therefore predict fluxes and countrates assuming X-ray luminosities an order of magnitude below the $L_X - T$ relation. We then select the 10 groups with the shortest exposure

times required to reach a 3σ detection under these constraints (see Table 4.1). With a 2% chance that a selected group overestimates its mass, in a sample of 10 groups, there is a 21% chance (assuming the binomial distribution) that our sample is contaminated with at least one group whose predicted properties are significantly overestimated and therefore that the estimated exposure time is too short.

Of the 10 selected groups, 200130, is the only group in our sample that intersects the edge of a GAMA field, with approximately 79% of the group area (within $r_{100\%}$, the projected radius from the centre to the furthest group galaxy) covered by the survey footprint. Assuming galaxies follow an NFW with a concentration of half that of the dark matter with a predicted mass from Table 4.1, this is equivalent to missing $\sim$ 23% of group galaxies within the same radius. However, as we have full coverage of the group core and as this group is a known, relaxed X-ray group [MKW4, Fukazawa et al., 2004], we do not exclude this group from our sample.

ACIS-I observations of the 9 selected groups not already within the *Chandra* archive were completed by the *Chandra* X-ray Observatory in 2013. Observations of the group 200130, an ACIS-S image taken in 2002, were taken from the *Chandra* archive.

4.2.5 Group Centres

We observe X-ray emission in the majority of our sample. In most cases the centroid of the X-ray emission is coincident with a bright galaxy within the group. In these cases we adopt this galaxy as the centre of the group. One group, 200115,

Table 4.1: Summary of the predicted properties of our selected groups and X-ray observations.

Group ID[a]	α[b]	δ[b]	z[b]	N_{fof}	$M_{500,\mathrm{Pred}}$[c] (10^{13} h_{70}^{-1} $\mathrm{M}_{\odot}$)	$r_{500,\mathrm{Pred}}$[c] (h_{70}^{-1} kpc)	$T_{500,\mathrm{Pred}}$[d] (keV)	t_{exp} (ks)	Obsid
100053 (100072)	139.74	1.149	0.0874	32	5.8	573	1.5	9.9	14001
200015 (200011)	176.53	-1.094	0.1175	34	4.7	529	1.3	15.8	14002
200017 (200014)	182.26	-0.965	0.1132	22	3.9	499	1.2	34.3	14005
200043 (200018)	184.71	-1.047	0.1195	23	5.2	545	1.4	10.6	14003
200054 (200036)	176.10	-1.851	0.1069	23	4.5	524	1.3	24.7	14004
200099 (200034)	174.93	-1.030	0.0777	23	4.6	533	1.3	14.9	14000
200115 (200063)	176.28	-1.758	0.0276	18	2.6	445	0.93	24.7	14007
200130 (200003)	181.11	1.896	0.0200	35	7.1	626	1.7	30.0	3234
300008 (300006)	217.19	0.708	0.1027	23	3.5	483	1.1	52.6	14006
300067 (300028)	222.75	-0.036	0.0429	22	2.6	444	0.94	25.7	14008

[a] Group ID in parentheses shows the G3Cv04 group ID with $1xxxxx$, $2xxxxx$ and $3xxxxx$ indicating groups from GAMA regions G09, G12 and G15 respectively.

[b] Listed centres correspond to the galaxies associated with the X-ray peaks. In cases were no emission is detected we assign a central galaxy as described in the Section 4.2.5. For the group 200115 the X-ray centroid is offset from the brightest group galaxies, we use the X-ray centroid of this group. Redshifts are as defined by the Robotham et al. [2011] FoF group finder.

[c] r-band luminosity derived mass estimates as described in the main text. Predicted r_{500} assume the critical density of the universe at a redshift z.

[d] Temperatures estimated using the $M-T$ relation of Sun et al. [2009].

has its X-ray emission centroid offset from any bright galaxies. We use the X-ray centroid of the group as its centre.

We also define optical group centres using the v06 galaxy data, modifying the iterative centring algorithm of Robotham et al. [2011]. The G3Cv04 algorithm initially takes all member galaxies and calculates a centroid weighted by galaxy luminosity. The galaxy furthest from this centre is removed from the sample and the weighted centroid is recalculated. This is iterated until only two galaxies remain, the brightest of which is identified as the central galaxy.

We modify this algorithm by assuming that central galaxies should be near the centre of the velocity distribution. The weight of each galaxy in this centroid is modified to include the inverse of line-of-sight velocity offset from the mean of the halo, scaled by the standard deviation of the velocity distribution, $|z - \bar{z}|/\sigma_z$ — i.e. a galaxy at $3\sigma_z$ from the mean velocity will be weighted less than a galaxy offset by $0.1\sigma_z$. At each iteration the mean velocity is recalculated, whilst maintaining the standard deviation at its initial value. This modification should prevent excessively bright galaxies on the cluster outskirts dominating the weighted centroid of the group. We use this algorithm to define a central galaxy for each group.

In cases where an X-ray centroid is not possible, we use the optical central galaxy as the group centroid. The adopted centres of all 10 groups are listed with their predicted X-ray properties in Table 4.1.

4.3 X-ray Analysis

In this section we discuss our X-ray reduction and analysis. We use CIAO 4.5 and SHERPA 1 for this work including the reduction and analysis of spectra and radial profiles. We follow the method outlined by Pascut and Ponman [2014] for reduction and spectral modelling summarising here.

Our X-ray images were reduced from the initial level 1 event files with the calibration files from CALDB 4.5.6. These corrections include the effects of time dependent gain variation and charge transfer inefficiency. We additionally filter light curves for flaring events by removing periods where the count rate is 20% greater than the median rate.

These cleaned event files form the basis of our X-ray analysis. Using these files we also identify point sources in our sample using wavelet detection. In most cases, the quality of our data allows us to detect diffuse X-ray emission associated with a central galaxy, which we then use as the centre of the group for our analysis. In groups where we weakly detect, or don't detect, group emission, we instead calculate limits on X-ray properties as described in Section 4.3.5.

4.3.1 Spectral Modelling

We extract sources within a radius of $0.5r_{500}$ of our chosen centre, excluding any point sources detected in the cleaned events files. Initial estimates of r_{500} are based on the GAMA luminosity based mass estimates described previously. For many of our groups we find limited source counts in the usual $0.5-2.0$ keV soft band. To increase the signal-to-noise in the extracted photon counts we extend the energy range to $0.3-3.0$ keV for all groups. We model extracted regions as source

+ background where the background has been separately modelled. We fit the background, rather than subtracting, to allow fitting with a maximum likelihood method using Cash statistics [Cash, 1979]. As a likelihood based method relies on the Poisson nature of the data this should be robust against the effects of poor counts than other statistics, such as χ^2 [Humphrey et al., 2009].

To model the background we extract counts from ACIS-I chips 0–3, excluding point sources and the $0.5r_{500}$ source region. We run an additional CIAO routine, VTPDETECT, to search for other sources of diffuse emission to remove from the background region. The cleaned background region is fit in the range of $0.3-7.0$ keV and accounts for components such as the cosmic soft X-ray and particle background, galactic emission and instrumental lines introduced by material along the optical path. We refer to Pascut and Ponman [2014] for the specifics of the fit. In a small number of cases we note that an additional background term is required to account for the effect of solar wind charge exchange. In these cases we model these as an additional set of Gaussians corresponding to the OVII, OVIII, NeIX and MgXI lines at 0.56, 0.65, 0.91 and 1.34 keV respectively, [Koutroumpa et al., 2009; Kuntz and Snowden, 2008].

We rescale the background model to the area of the source region and fit the source as an APEC thermal plasma. We assume a fixed metalicity of $Z = 0.5Z_{\odot}$ [Sanderson et al., 2009] relative to the GRSA abundance model [Grevesse and Sauval, 1998] and absorption column from the galactic HI survey of Kalberla et al. [2005] extracted using NH tool from the HEASOFT software suite. We fit the source in two passes, the first in the range $0.3-7.0$ keV to rescale the particle background, allowing for differences in the vignetted photon background and non-vignetted particle background. This first pass also fits an initial estimate

of the temperature, T_{spec}, and normalisation, η, of the APEC model. We then fix all background components and fit the temperature and normalisation in the range $0.3 - 3.0$ keV.

Using T_{spec} we revise our estimate of r_{500} using the $r - T$ relation of Sun et al. [2009],

$$r_{500} = 602 h^{-1} \left(\frac{kT_{spec}}{3 \text{ keV}} \right)^{\frac{1.67}{3}} \text{ kpc} \quad . \tag{4.9}$$

We then re-extract and fit the source within the new $0.5 r_{500}$ aperture. If the newer estimate is larger than the initial, we additionally re-extract and model the background. We adopt the re-fitted T_{spec} as the estimate of the system's mean temperature. We estimate the masses of our groups using the $M - T$ relation of Sun et al. [2009],

$$M_{500} = 1.27 \times 10^{14} h^{-1} \left(\frac{kT_{spec}}{3 \text{ keV}} \right)^{1.67} \text{ M}_{\odot} \quad . \tag{4.10}$$

As shown by Le Brun et al. [2014], the $M - T$ relation is independent of feedback processes. Therefore, masses estimated in this way should be representative of the halo mass regardless of the thermal history of the group (i.e. low or high entropy gas).

4.3.2 Surface Brightness Profiles

We determine the surface brightness profiles of our groups by radially binning observed emission upon which an emission profile is fit. We centre the bins on the positions listed in Table 4.1, requiring at least 15 counts per bin in our $0.3 - 3.0$ keV energy band. We remove contaminating point sources and apply

an exposure correction. For groups without any strong cool core we assume that the surface brightness profile is well represented by a single β-model, [Cavaliere and Fusco-Femiano, 1976],

$$S(r) = S_0 \left(1 + \left(\frac{r}{r_c}\right)^2\right)^{-3\beta+0.5} \quad , \tag{4.11}$$

where r_c is the core radius, β is the slope of the emission profile and S_0 is the central surface brightness. In groups with a notable excess of central emission we modify the surface brightness profile to be the sum of two β-models, $S(r) = S_{core}(r) + S_{out}(r)$. This modification is simpler than those used by, for example, Ettori [2000] and Vikhlinin et al. [2006]. However due to the poor quality of the data in many of our groups, fitting more complicated models is unlikely to provide significant improvements.

We do not attempt to subtract background contamination, we instead assume that this can be approximated by a uniform emission source at all radii, S_{bg}. Due to the particle background not being affected by vignetting the photon and particle backgrounds will have different effective areas in regions where vignetting is significant. Exposure correction will flatten the photon background, but will introduce a radial dependent excess in the particle background, rendering our approximation of a flat background invalid at large radii. However, as the majority of our sources do not cover a very large fraction of the ACIS-I field (radial extent typically of $\lesssim$ few hundred pixels compared to a 2048 pixel wide field of view), and as our energy range does not extend into the hard X-ray regime, we do not expect this to be a significant effect.

We fit the surface brightness profiles using Sherpa. Again, due to limited

statistics we do not fit all β-model components, instead fixing $\beta_{out} = 0.5$, comparable to that observed for low temperature groups [e.g. Helsdon and Ponman, 2000], and $\beta_{core} = 2/3$, assuming that central emission has a standard slope comparable to those measured in Mohr et al. [1999]. For one group, 300008, we find the fit optimises the core profile with $\beta_{core} = 0.5$ and the outer profile with $\beta_{out} = 2/3$.

4.3.3 Luminosity

To determine the bolometric X-ray luminosity we use the spectral fit and the SHERPA algorithm CALC_ENERGY_FLUX in the energy range 0.01 to 15 keV, applying the appropriate conversion from flux to luminosity. As our extraction aperture is $0.5r'_{500}$, where r'_{500} is the radius derived from the previous iteration's T_{spec}, we rescale the measured luminosity to $L_{X,500}$, using the measured surface brightness profiles and the final estimate of r_{500}. These rescale factors range from $\sim 1.12 - 1.75$ in most cases, with one group, 300067, requiring little rescaling (1.04) due to its centrally concentrated emission profile. Three groups, 100053, 200099 and 200130, use scale factors of 3–6 due to the reduced, 100 kpc, aperture used for these systems, as discussed in Section 4.3.5.

4.3.4 Entropy

We calculate entropy, K, as described in Chapter 1,

$$K(r) = \frac{kT_{spec}}{n_e(r)^{2/3}} \quad , \tag{4.12}$$

where we assume an isothermal gas with temperature T_{spec} and $n_e(r)$ is the num-

ber density of electrons in the intragroup gas at radius r. To determine the gas density we analytically deproject our fitted surface brightness profile, assuming that the gas density has a density profile of

$$n_e(r) = n_{e,0}\left(1 + \left(\frac{r}{r_0}\right)^2\right)^{-\frac{3}{2}\beta} \quad , \tag{4.13}$$

where β and r_c are as per the surface brightness profile, Equation (4.11), and $n_{e,0}$ is a normalisation term defined as

$$n_{e,0} = \sqrt{\frac{n_{eH} 4\pi D_a(z)^2 (1+z)^2 10^{14} \eta J}{NV}} \quad . \tag{4.14}$$

Here $n_{eH} = 1.157$ is the ratio of electron to ion number densities within the gas [Sanderson et al., 2013] and $D_a(z)$ is the angular diameter distance to the group at redshift z. η is the normalisation of the APEC model fit in Section 4.3.1 and $N = \int_0^{r_{max}} 2\pi r S(r) \mathrm{d}r$ is the projected source count in the fit region. We calculate the gas density normalisation using the total emissivity within a spherical volume of radius 1 kpc, e.g. $J = \int_0^{1\mathrm{kpc}} 4\pi r^2 j(r) \mathrm{d}r$, such that

$$j(r) = j_0\left(1 + \left(\frac{r}{r_c}\right)^2\right)^{-3\beta} \quad , \tag{4.15}$$

where $j_0 = S_0 / \left(2 r_c \int_0^{\pi/2} \cos(\theta)^{2(3\beta-1)} \mathrm{d}\theta\right)$. In cases where we fit two β-models we determine the number density for each model and use the sum of the densities in Equation (4.12).

We determine group entropies at 10 kpc to probe the core of these groups.

4.3.5 Notes on individual groups

100053 and 200099

Due to surface brightness profiles consistent with no observed emission, the groups 100053 and 200099 are considered to be non-detections. We instead determine limits on the gas luminosity and entropy.

Examining the smoothed emission maps of these sources we find a small diffuse source associated with a bright member galaxy for 100053 (see Figure 4.1) and adopt this galaxy as the centre of our analysis. 200099 appears featureless in the smoothed images. We instead adopt an optical centre for 200099 based on the iterative centroid algorithm described in Section 4.2.5. We note that for both the iterative centre defined here and by Robotham et al. [2011], the identified central galaxy is near the group edge, markedly offset from any centre determined by a basic centre-of-light centroid.

To determine limits of gas properties, we extract X-ray spectra within 100 kpc, using a small, fixed aperture to increase the signal-to-noise relative to that within $0.5r_{500}$. Assuming the T_{pred} determined from the optical group luminosity, we fit an APEC model with fixed temperature and metallicity. Using the upper bound on the fitted APEC normalisation, we assume a 2σ upper limit on η. Surface brightness profiles are assumed to be single β-model distributions with $\beta = 0.5$ and $r_c = 0.2r_{500}$, comparable to the mean of the other 8 groups in the sample ($0.17 \pm 0.03\ r_{500}$). We assume r_{500} as predicted by the luminosity mass estimate.

Using the 2σ upper limit on normalisation and the assumed surface brightness profile, a 2σ upper limit on luminosity can be estimated. Deprojecting this surface brightness profile, a 2σ upper limit on number density, n_e can also be found. As

increased entropy acts to decrease gas density, this limit on n_e then allows 2σ *lower* limits on central entropy to be determined.

200130

The group 200130 is the known low redshift X-ray group MKW4 [Fukazawa et al., 2004]. This group was imaged in 2002 with *Chandra* in the ACIS-S configuration. We extract our spectra from the back-illuminated S3 chip. However, due to the low redshift of this group the predicted $0.5r_{500}$ aperture we would ordinarily use (313 kpc, 6.7 arcmin at $z = 0.02$), extends beyond the chip boundary. Additionally, this system is known to have traceable emission across the ACIS-S CCD [Sun et al., 2009], rendering our usual approach of measuring a local background unsuitable.

We instead use blank sky background datasets to estimate the background [Sun et al., 2009; Vikhlinin et al., 2005]. Using the S3 chip only we extract a spectrum within a 100 kpc aperture, comparable to the size of the chip. We do this for both the background and data. We scale the background to match the hard X-ray counts and subtract this from our source spectrum. We then fit with a source model only using χ^2 statistics.

To determine the radial profile, as we do not have data beyond 100 kpc, we again make use of the scaled blank sky background to constrain background emission. We use the core radius and slope of the outer gas halo determined by Vikhlinin et al. [1999] with $r_c = 204$ kpc and $\beta = 0.64$ using ROSAT imaging data that extended to much larger radius. We perform a two β-profile fit of the background subtracted radial profile where we fit only the amplitude of the outer β model but allow the inner, core profile freedom to optimise normalisation, core

radius and slope.

We calculate luminosity as described previously, extrapolating from 100 kpc to r_{500}. Whilst T_{spec} is widely available within the literature [e.g. Sun et al., 2009; Vikhlinin et al., 2006], to ensure the temperature estimated for 200130 is consistent with our other groups, we estimate T_{spec} using an emission weighted temperature profile. We use the temperature profile from Vikhlinin et al. [2006] and, weighting by the surface brightness profile, average within $0.5r_{500}$, where $r_{500} = 538$ kpc initially [Sun et al., 2009]. $r_{500}(T)$ is then recalculated and the estimation repeated, iterating until convergence. This temperature is used for estimating entropy.

200115

The group 200115 features a diffuse X-ray source not associated with any member galaxy. However, we also see no background groups or clusters in the GAMA survey that this emission may be associated with, nor are there any known groups or clusters within $1'$ of the emission found within the NASA Extragalactic Database (NED). We estimate the centroid of this emission in the 0.3–3.0 keV band within a 100 kpc aperture (at $z = 0.028$), finding this to be 130 kpc from the optical central galaxy, with another bright galaxy 32 kpc away. Though significant offsets between galaxies and X-ray emission can be an indication of recent disturbance, we assume the observed diffuse emission is associated with the group and use the centroid as the centre of our resulting analysis.

200054

When fitting group 200054 in our 0.3–3.0 keV band we find that this system fits with a temperature $5.2^{+4.9}_{-1.9}$ keV, dropping notably to ~ 3 keV as the energy band is increased. To avoid this ambiguity and to constrain any high temperature components, we opt to fit the spectrum within the $0.3-7.0$ keV band used when rescaling the background. We additionally use $\beta_{out} = 2/3$, consistent with high temperature systems, rather than $\beta_{out} = 0.5$ used for the cool groups within this work.

4.4 Results

Table 4.2: Results of the X-ray analysis for our sample of optically selected groups.

GroupID	T_{spec} [a] (keV)	$L_{X,500}$ [b] (10^{42}erg s^{-1})	M_{500} [c] ($10^{13}M_{\odot}$)	r_{500} [c] (kpc)	K_{10kpc} (keV cm^2)
100053	(1.52)	< 1.66	(5.82)	(573)	> 262
200015	$1.05^{+0.21}_{-0.12}$	3.02 ± 0.66	3.16 ± 0.83	480 ± 42	24.5 ± 11.5
200017	$1.34^{+0.56}_{-0.23}$	1.36 ± 0.46	4.74 ± 2.33	550 ± 90	29.3 ± 11.1
200043	$0.97^{+0.37}_{-0.25}$	1.63 ± 0.62	2.77 ± 1.47	460 ± 81	24.8 ± 16.6
200054	$2.80^{+1.03}_{-0.53}$	12.5 ± 1.61	16.2 ± 7.53	828 ± 129	47.2 ± 32.7
200099	(1.32)	< 0.96	(4.63)	(533)	> 235
200115	$0.59^{+0.09}_{-0.10}$	0.37 ± 0.06	1.20 ± 0.12	347 ± 30	64.5 ± 20.4
200130	$1.79^{+0.02}_{-0.02}$	27.2 ± 0.6	7.66 ± 0.15	645 ± 4	24.2 ± 0.3
300008	$1.67^{+0.31}_{-0.23}$	1.99 ± 0.30	6.80 ± 1.83	620 ± 56	40.1 ± 17.7
300067	$0.90^{+0.11}_{-0.08}$	0.39 ± 0.06	2.44 ± 0.44	440 ± 27	28.0 ± 3.5

Values in parentheses derived from GAMA mass and temperature estimates

[a] Mean temperature within an aperture of $\approx 0.5r_{500}$.

[b] Extrapolated using the surface brightness fits from the extraction aperture to r_{500}.

[c] Derived from the Sun et al. [2009] mass – temperature and radius – temperature relations for groups and clusters.

Table 4.3: X-ray surface brightness profiles.

GroupID	$r_{c,core}$[a] (kpc)	β_{core}[a]	$r_{c,out}$[a] (kpc)	β_{out}[a]
100053	-	-	(115)	(0.5)
200015	18 ± 17	(0.66)	107 ± 31	(0.5)
200017	10 ± 6	(0.66)	77 ± 28	(0.5)
200043	14 ± 23	(0.66)	87 ± 48	(0.5)
200054	25 ± 33	(0.66)	160 ± 24	(0.66)
200099	-	-	(107)	(0.5)
200115	-	-	36 ± 49	(0.5)
200130	4.0 ± 0.8	0.444 ± 0.004	(205)[b]	(0.64)[b]
300008	9.4 ± 19.1	(0.5)	88 ± 15	(0.66)
300067	15 ± 4	(0.66)	-	-

[a] Surface brightness profiles assuming the 2 β-model described in §4.3. In cases of non-detection or where only one β-model is sufficient we report only one set of model parameters. Values in parentheses are fixed as described in the text and not allowed to fit.

[b] Outer surface brightness profile parameters from Vikhlinin et al. [1999] fit to ROSAT PSPC data.

In this section we present our results for our sample of optically selected galaxy groups. We detect emission in 8 of our 10 groups, a larger fraction than detected in studies such as the XI project [only 1 bright source and 2 weak detections out of 9 targets Rasmussen et al., 2006] where substructure or virialisation was not considered when selecting groups. This detected fraction is consistent with the detected fraction of optically selected groups studied by Balogh et al. [2011] who found 5 groups were undetected in a sample of 18 targets. Interestingly, their sample, which was drawn from the 2PIGG catalogue [Eke et al., 2004] with a narrow mass range ($3 \times 10^{14} < M/\mathrm{M}_{\odot} < 6 \times 10^{14}$), was additionally selected to exclude groups with non-Gaussian velocity distributions. Whilst these samples are small, the difference between the XI result and that presented here, does

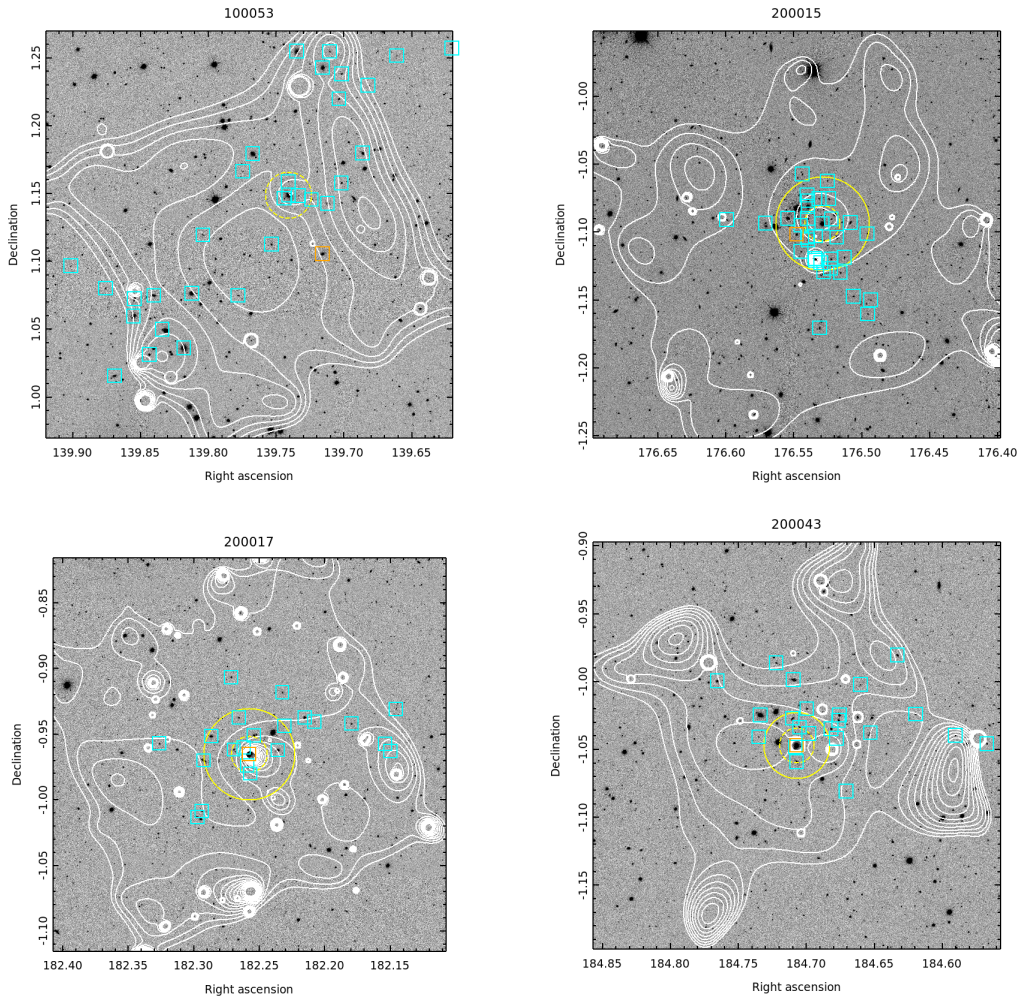

Figure 4.1: Optical images of groups 100053, 200015, 200017 and 200043 (*left to right, top to bottom*) from the SDSS with X-ray contours overlaid (*white lines*). The X-ray contours are derived from adaptively smoothed X-ray images in our analysis band (0.3–3.0 keV). Also shown are the member galaxies (*cyan squares*) with central galaxies shown (*orange squares*). For scale we illustrate a 100 kpc region with a *dashed yellow circle* and the extraction region, when different, by the *solid yellow circle*.

imply that selection by substructure can substantially improve the reliability of a group sample.

In Figures 4.1, 4.2 and 4.3 we show the optical SDSS images with X-ray

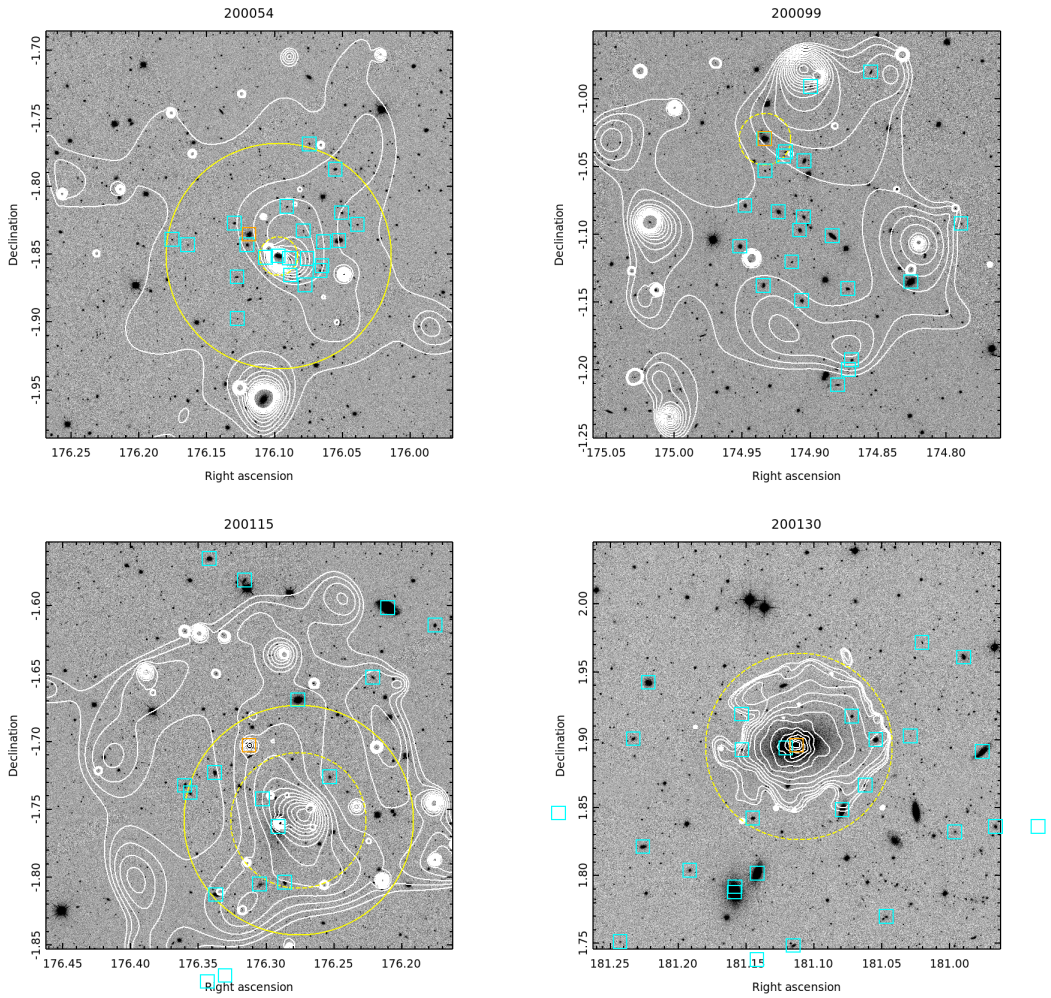

Figure 4.2: As Figure 4.1 for groups 200054, 200099, 200115, 200130.

contours overlaid. Of the 8 groups where we detect X-ray emission, there are 3 groups (200015, 200054 and 200115) where the central galaxy (Section 4.2.5) is not associated with the peak of the X-ray emission.

4.4.1 $L_X - T_{spec}$

An initial assessment of our sample can be made through their position on the X-ray luminosity-temperature relation ($L-T$). This relation, which has self-similar

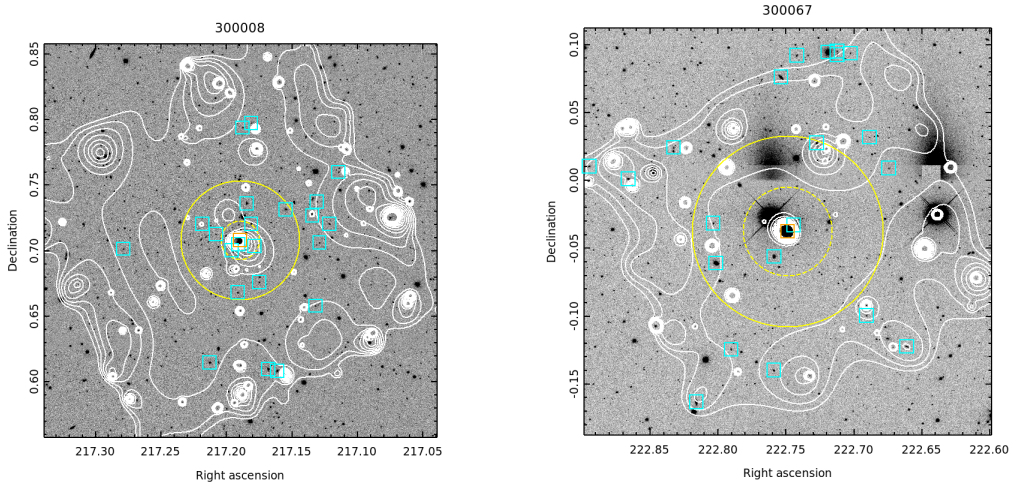

Figure 4.3: As Figure 4.1 for groups 300008 and 300067.

expectation of $L_X \propto T^2$ for systems with temperatures above ~ 3 keV, has been shown to be significantly steeper [e.g. Helsdon and Ponman, 2000; Osmond and Ponman, 2004; Pratt et al., 2009; Slack and Ponman, 2014] with slopes of 3 to 4. This similarity breaking is attributed to feedback processes that inject entropy into the gas halo [e.g. Voit and Bryan, 2001], suppressing X-ray luminosity in gas cores.

In Figure 4.4 we show our group sample overplotted onto the $L-T$ group data from the GEMS sample Osmond and Ponman [2004] and cluster results from the ACCEPT database[1] [Cavagnolo et al., 2009]. Also shown is the $L-T$ relation (for groups only) found by Slack and Ponman [2014] using a compilation of several group and cluster studies spanning nearly 2 orders of magnitude in temperature,

$$L_{X,500} = 1.27 \times 10^{44} \left(\frac{T}{3 \text{ keV}} \right)^{3.17} \text{erg s}^{-1} \quad . \tag{4.16}$$

[1] http://www.pa.msu.edu/astro/MC2/accept/

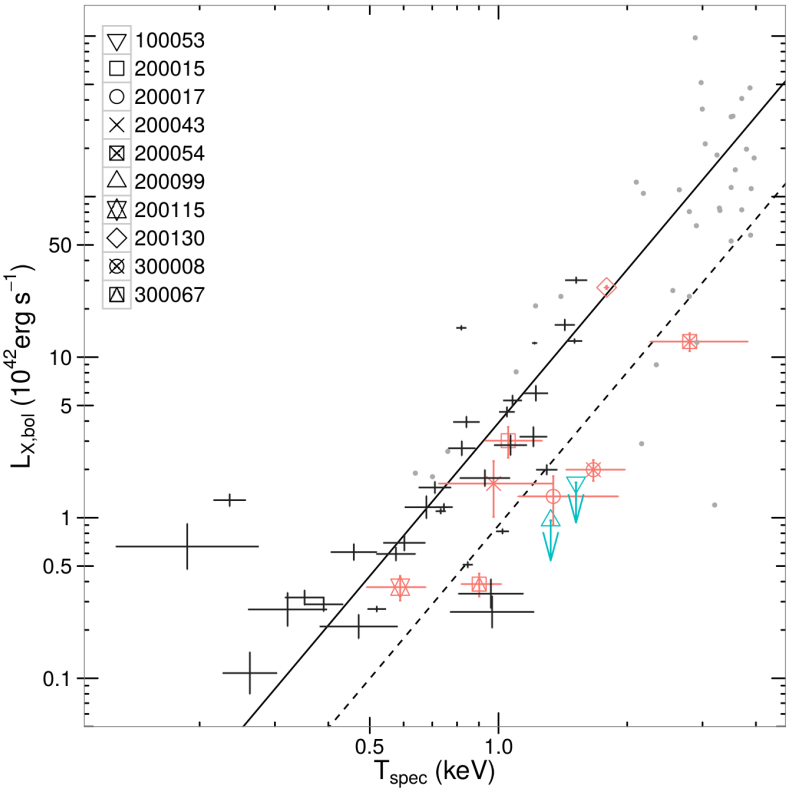

Figure 4.4: The luminosity – temperature relation for our group sample (*coloured points*). Overlaid are groups from the Osmond and Ponman [2004] (*black points*) sample and clusters from the ACCEPT sample [Cavagnolo et al., 2009] (*grey points*, constrained to clusters cooler than 4 keV and nearer than $z = 0.15$). The *solid line* represents the $L-T$ relation of Slack and Ponman [2014]. We show the $L-T$ relation of our sample, modified from the Slack and Ponman [2014] relation by refitting the normalisation only, excluding the undetected groups 100053 and 200099, as the *dashed line*.

With the exception of the archival group MKW4 (200130), we find that our groups have X-ray luminosities below those observed for the GEMS sample and expected from the $L-T$ relation, which agrees with both GEMS and ACCEPT samples. The few ACCEPT clusters at low temperature also suggest that our sample shows low X-ray luminosity. However, the ACCEPT project indicates that their luminosities are indicative only and determined within a non-uniform

set of apertures. Therefore, rigorous comparison with our r_{500} luminosities is difficult, though it is plausible that any extrapolation of ACCEPT luminosities to r_{500} would only serve to increase the disparity between ACCEPT and our sample, further increasing the significance of our luminosity offset. We observe a small number of ACCEPT systems with luminosities well below the $L-T$ relation. However, with the previously mentioned uncertainty in the nature of ACCEPT luminosities, it is unclear whether these underluminous systems are truly underluminous or if this is simply an artefact of the ACCEPT luminosity estimates (e.g. uncorrected for core-excision or reduced extraction apertures). As the central entropies of these underluminous groups are not significantly higher than the rest of the sample ($K_{10\mathrm{kpc}} < 100$ kev cm^2, see Section 4.4.2), it is unlikely that they are truly underluminous.

We briefly quantify the size of our luminosity decrement relative to the literature $L-T$ relation. Fitting just the normalisation of the $L-T$ relation to our data (excluding the two non-detections) implies that our optically selected sample is underluminous by a factor 4 relative to an X-ray selected one. This renormalisation is shown as the dashed line on Figure 4.4. This decrement is in qualitative agreement with the results of the Anderson et al. [2014] who find optical groups in a stacked analysis to be a factor 2 underluminous on the $L-M$ relation.

Despite our group luminosities being low compared to the standard relation, the group temperatures predicted from the optical luminosity based mass estimates with the Sun et al. [2009] $M-T$ relation show no significant bias. Excluding the two non-detections, and MKW4 whose analysis differed to that of the other groups, our predicted group temperatures have a mean offset ($\log_{10}(T_{pred})-$

$\log_{10}(T_{spec})$) of only -0.009 ± 0.072. This increases slightly to -0.011 ± 0.062 if MKW4 is included. This indicates that the mass estimation used here is on average unbiased, though substantially scattered. This scatter, totalling 0.18 dex, has 0.09 dex contributed by the measurement error on T_{spec}, with the remaining 0.15 dex introduced through uncertainty on the calibration of the optical luminosity mass estimation and intrinsic scatter on that relation.

4.4.2 Entropy

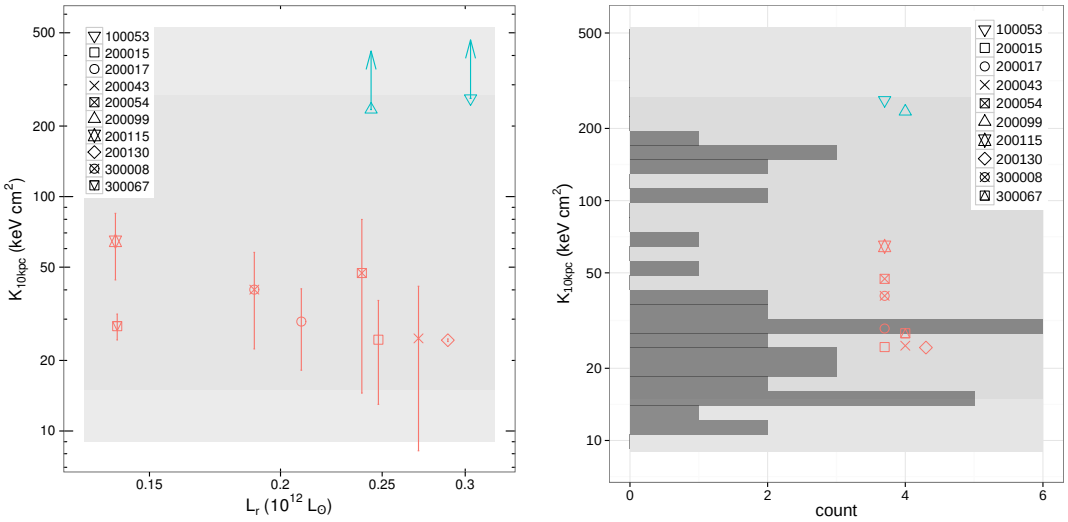

Figure 4.5: *Left:* Central (10 kpc) entropies against total optical r-band luminosity. *Right:* Histogram of group entropies at 10 Kpc using the entropy profiles of the ACCEPT sample [Cavagnolo et al., 2009] with $k_bT < 3$ keV with our measured entropies overlaid. In both figures we show the 1σ (*dark shading*) and 2σ (*light shading*) upper and lower limits at 10 kpc derived from the OWLS simulations [McCarthy et al., 2011].

We plot central entropies, calculated as Equation 4.12 using the surface brightness parameters in Table 4.3 to estimate gas density, against optical luminosity in Figure 4.5. We plot against L_r to avoid any correlation that may be introduced

by plotting against an X-ray derived quantity. As shown by the OWLS project, the feedback model that best reproduces observed entropy distribution as well as other halo baryon properties such as stellar mass fractions, uses metal line cooling and both AGN and supernova feedback [McCarthy et al., 2011]. The predicted range in central entropies from this model is shown in Figure 4.5 as the shaded regions. The majority of our groups are well within the 1σ range, however we note that our two non-detections have 2σ lower limits substantially higher than the central entropies of the rest of the sample.

We compare these results to the distribution of central entropies observed by Cavagnolo et al. [2009], available from the ACCEPT database. We use the entropy profiles $K(r) = K_0 + K_{100}(r/100\text{kpc})^{\alpha}$ with their fitted values of K_0, K_{100} and α to estimate group entropies at 10 kpc. For consistency with our sample we use only groups with $T_X < 3$ keV, reducing the ACCEPT sample from 241 systems to only 38. Our estimated entropies at 10 kpc are consistent with this range with few extending to high entropy ($\gtrsim 100$ keV cm^2, see Figure 4.5). The estimated lower limits for groups 100053 and 200099 are higher than the largest central entropies observed in the cut ACCEPT sample. We briefly comment on the quality of our entropy estimates using the overlap of these two samples, MKW4 (group 200130). As seen in Table 4.2 we determine a central entropy of 24.2 ± 0.3 keV cm^2, compared to the 28.4 keV cm^2 derived from the ACCEPT profile. Whilst the difference is significant, this significance is dominated by the high statistical quality of the data. Given the different approaches used in these analyses (e.g. assumptions of isothermal gas compared to a full temperature deprojection), we do not consider this discrepancy to be problematic.

To estimate the lower limits on group entropy for groups 100053 and 200099,

a series of assumptions needed to be made regarding the temperature and gas density profile. We investigate these assumptions and the impact deviations from them may have on the estimated limits in Section 4.5.

As entropy and cooling times are inherently linked properties of group gas (at the same temperature high gas entropy implies low gas density and therefore reduced a cooling rate), we can use our measured entropies to understand the cool core (CC) / non-cool core (NCC) nature of the group sample. To divide the population we guide the choice of threshold by the observed bimodality in central entropies reported by Cavagnolo et al. [2009], splitting the population at $30 - 50$ keV cm^2. Groups below this threshold are more likely to show features associated with active cooling [Cavagnolo et al., 2008]. Whilst the Cavagnolo et al. [2009] split is in the central entropy excess above that expected from a baseline value (K_0), our radius at 10 kpc should be small enough for a comparable split to be made. Pascut and Ponman [2014] approach this by splitting their group and cluster sample at $K_{0.01r_{500}} = 40$ keV cm^2. They also find that at a given entropy, groups have longer cooling times than clusters. We therefore take a comparable approach with our group sample, classifying groups with $K_{10kpc} < 30$ keV cm^2 as cool cores.

From Table 4.2 we see that half of our sample fall below this threshold and are therefore CC groups. However, most are weak CCs, marginally below our CC threshold. Cooling times can be estimated as $t_{cool} \propto K^{3/2}T^{-1/2}\Lambda(T)^{-1}$, e.g. $t_{cool} \propto K^{3/2}T^{-1}$ for pure bremsstrahlung emission where $\Lambda(T) \sim T^{1/2}$ [e.g. Donahue et al., 2006]. At low temperatures where bremsstrahlung is less dominant, such as the groups observed here, the temperature dependence flattens as the cooling function's dependence on temperature steepens [e.g. McKee and Cowie,

1977]. Assuming such a shallow temperature dependence, our five low entropy, CC groups should have the lowest cooling times of this sample, further implying that these groups are cool core.

We note however that one of our CC groups, 300067, is a group whose gas emission appears as a possible galaxy corona with little other emission observed. This corona is larger ($\sim$ 15 kpc) than those observed by Sun et al. [2007], $\sim$ 4 kpc, but is of comparable temperature. The Sun et al. [2007] coronas however were around galaxies within hot cluster environments. This is clearly different to the environment seen in 300067 where no other diffuse emission is observed. This may imply that any group gas within this halo is also high entropy, though as we do detect this compact central emission, we do not label this group as a high entropy candidate.

4.5 Discussion

4.5.1 High Entropy Limits

The results so far indicate that two of our groups have interestingly high lower limits on the central entropy of their intragroup gas. However, it is worth asking how realistic these limits are, especially given the assumptions that have gone into constructing them. The entropy calculation used here assumes an isothermal gas with temperature determined from the X-ray spectra, and a gas density profile derived from the deprojected emissivity profile of group emission. To determine limits we instead use the temperature predicted for each group predicted from their optical luminosity based masses, which have some uncertainty from the

scatter of the mass-L_r relation used. The uncertainty on mass also affects the shape of the density profile with the assumption of $r_c = 0.2r_{500}$ where r_{500} is also derived from optical luminosity based masses. Furthermore, the assumed factor of 0.2, comparable to the mean ratio of r_c to r_{500} for the rest of the sample may not be valid for groups with such high entropy — high entropy gas will redistribute itself within the halo, puffing up the intragroup medium and increasing the core radius. A small core radius should imply a denser gas core, which in turn, should be detectable.

It is interesting therefore to see how we can far we can push these assumptions before we reach entropy limits comparable to the rest of the sample. The most obvious question to ask is how reliably do we know the assumed temperature? We have already discussed that we believe the temperature estimates are, on average, unbiased for this sample. Whilst scatter is large, 0.15 dex, if we decrease the temperature by 0.15 dex and propagate this change into r_c, entropy lower limits decrease to only > 168 and > 150 keV cm^2 for 100053 and 200099 respectively. Therefore poorly estimated temperature alone cannot be responsible for the observed high entropy limits.

The alternative is to examine the effect of the core radius and the assumed fraction of r_{500} used. Specifically we examine the fraction of r_{500} required to reduce the measured limits to only 100 keV cm^2. Using the APEC normalisation upper limit, we find that this core radius would need to be $< 0.05r_{500}$ for both groups. Whilst an undetectably low surface brightness is plausible for a group with a large core, it is unlikely we would not observe such a cuspy distribution of emission at the same redshift. This distribution of gas should show low density outside the core, rising sharply near the middle to show a central compact core

Table 4.4: Substructure of the v06 Group Sample.

GroupID	ζ_β	ζ_{AST}	ζ_{AD}
100053	1.42 (0.93)	1.19 (0.70)	2.39
200015	1.22 (0.81)	0.82 (0.23)	1.11
200017	1.06 (0.63)	1.39 (0.78)	3.97
200043	1.86 (>0.99)	2.40 (0.98)	1.44
200054	0.78 (0.26)	1.24 (0.69)	3.41
200099	3.08 (>0.99)	2.08 (0.95)	2.19
200115	1.43 (0.89)	1.42 (0.76)	1.03
200130	1.78 (0.99)	1.23 (0.74)	3250
300008	1.11 (0.68)	0.79 (0.21)	1.03
300067	1.55 (0.94)	1.93 (0.93)	2.86

ζ_β, ζ_{AST} and ζ_{AD} show the mirror symmetry, angular separation test and velocity non-normality substructure indicators as described in Section 4.2.

whose emission would be detectable.

4.5.2 Substructure

The results above imply that the high entropy limits determined here are reliable. However, a third option remains for the lack of detectable emission: the groups 100053 and 200099 are still collapsing. Given the improvement in optical data quality since the initial selection, we can re-visit the question of substructure for the whole sample.

In Table 4.4 we show the recalculated substructure statistics of our group sample using the deeper data now available and centred on X-ray emission where possible. Whilst a quantitative comparison between these values and the thresholds used to originally select the groups is meaningless due to the updated galaxy catalogue, qualitatively this has a number of interesting implications.

The most apparent change is that the Anderson-Darling test has become much

more discriminating. Obviously, the inclusion of more galaxies will result in any deviation from normality in the velocity distribution becoming more significant, so this should not surprise us. However, the value of $\zeta_{AD} = 3250$ for 200130 (MKW4) indicates that the revised selection has introduced a significant perturbation in its velocities. Further examination indicates that there is a second structure linked into this group along the line-of-sight at $z \sim 0.0235$ causing the group velocities to be significantly skewed.

In contrast, the two spatial substructure tests do not appear to be substantially different with few showing more substructure than the original limits. Mirror symmetry gives a large, significant ($\geq 95\%$) substructure result for groups 200043, 200099 and 200130. The angular symmetry test similarly highlights groups 200043 and 200099 as groups with large, highly significant substructure statistics ($\geq 95\%$). The significant mirror symmetry result of 200130 is not surprising given its intersection with the survey edge.

We compare the substructure content of the two non-detected groups, noting a considerable difference spatially, but a very similar degree of velocity normality. The substructure statistics of group 100053 are comparable to the rest of our sample, suggesting that it is a virialised system. In contrast, group 200099 shows some of the highest substructure of the entire sample. This may be related to the poor centring already noted, where 200099 has no obvious bright central galaxy. Recalculating substructure around a simple centre-of-light centroid, without iterating, we observe considerably less projected substructure, where $\zeta_{\beta} = 1.47$ (0.94) and $\zeta_{AST} = 1.42$ (0.81). This poor centring may be a result of incomplete virial collapse, however as 200099 shows a velocity histogram consistent with the rest of the sample, and is much less substructured when a simple centroid is used,

it is plausible that the group is virialised. The lack of a central galaxy may be the result of extreme levels of pre-heating such that the halos from which member galaxies formed were unable to cool sufficient gas to form the large central galaxies we expect.

On the basis of substructure, we see no strong evidence that the groups 100053 and 200099 are not real, collapsed structures. This suggests that the observed high entropy limits are representative of the entropy in these systems.

4.5.3 Mass Estimation Quality

The ability to estimate masses is important for this work, both as a means of estimating the halo mass for predicting X-ray properties prior to observations and as the base predictor when determination of entropy limits. We again point out that we believe our predicted temperatures, and therefore mass estimates, are in general unbiased, though highly scattered. Using the broad range of mass estimates described in Chapter 3, we investigate our ability to estimate halo mass using galaxies. Furthermore, we also demonstrate that the use of these estimators in conjunction can help place further constraints on the virialisation state of the cluster.

We reselect galaxies for each group as described in Chapter 3, selecting a cylindrical volume with projected radius of 1 Mpc and depth $\pm 3\sigma$ along the line-of-sight using the gapper velocity dispersion [Beers et al., 1990]. This galaxy sample defines the volumetric group sample, in contrast to the GAMA Friend-of-Friends sample defined by Robotham et al. [2011]. With the volumetric sample, we construct a series of mass estimates based on the observed group richness and

Table 4.5: M_{500} estimates ($10^{13}\mathrm{M}_{\odot}$, assuming $h_{70} = 1$) for our group sample.

GroupID	$M_{L,GAMA}$	$M_{\sigma,GAMA}$	M_N	M_L	M_δ	M_{δ_L}	M_σ
100053	5.82	6.36	4.08	6.44	0.98	1.35	0.99
200015	4.71	6.51	15.0	9.63	21.7	25.0	6.73
200017	3.95	7.59	3.08	4.07	3.52	3.79	5.19
200043	5.16	7.93	6.35	11.0	4.45	7.99	5.37
200054	4.54	8.35	7.35	10.5	3.39	5.41	6.19
200099	4.63	3.27	1.94	3.32	0.25	0.41	1.37
200115	2.58	4.43	0.48	0.58	0.93	0.78	1.56
200130	7.10	12.9	4.44	7.63	4.75	2.35	10.5
300008	3.55	8.74	3.08	3.09	3.51	2.58	4.27
300067	2.59	2.98	1.28	1.00	0.40	0.43	1.61

luminosity (extrapolated from the $m_r = 19.8$ flux limit to $M_r = -16.5$ assuming SDSS cluster luminosity functions [Popesso et al., 2005]), galaxy and luminosity overdensity (fit to a Navarro, Frenk and White (NFW) density profile [Navarro et al., 1996]) and a dynamical estimator $\propto \sigma^{3\alpha}$. These mass estimates, labelled M_N, M_L, M_δ, M_{δ_L} and M_σ respectively, are based on mass-proxy relations that have been calibrated against M_{500} from a sample of X-ray selected groups. As a result of the different group selection applied with this sample, it will be interesting to see how these estimates compare to the X-ray based mass estimates, as well as to each other. In addition to the five mass estimators used here, we also include masses derived from GAMA FoF total light ($M_{L,GAMA}$, Section 4.2) and GAMA group masses derived from the FoF group velocity dispersion [$M_{\sigma,GAMA}$, Robotham et al., 2011], calibrated upon the GAMA mock data and later scaled to M_{500} as per the luminosity based masses.

We summarise the mass estimates in Table 4.5 and Figure 4.6. In Figure 4.6 we use the boxplot to show the spread of mass estimates according to their interquartile ranges for each group. The advantage of this representation is that

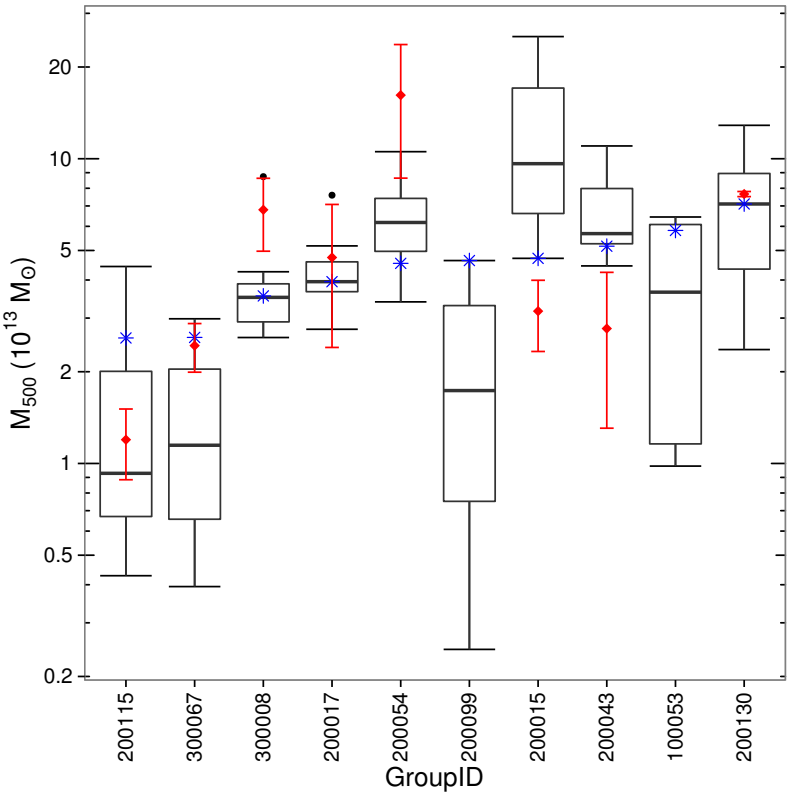

Figure 4.6: Distribution of predicted group M_{500} ordered by the GAMA luminosity predicted mass. Included in the boxplot are all mass estimates from Table 4.5. The *blue stars* are the predicted masses used for the X-ray feasibility (derived from the GAMA luminosity), the *red diamonds* are the $M-T$ based masses of Table 4.2. The boxes represent the 25th to 75th quartiles with outliers (outside of 1.5 times the inter-quartile range from the 25th and 75th quartiles) shown as black points.

it also allows outliers to be identified, defined as points outside of a region extending to 1.5 times the interquartile range above and below the 25th and 75th quartiles (the bounds of the box). Obviously, with only 7 masses going into each boxplot, the statistics here are poor and definitive conclusions are difficult to draw. Nonetheless, it is illustrative for understanding the nature of these mass estimates in a general sense.

We first note that the dynamical masses produced by Robotham et al. [2011] ($M_{\sigma,GAMA}$) are generally larger than those reported by the M_{σ} estimator. As both use similar mass proxies, this difference is interesting, though is likely is due to the differing calibration and definition details. The $M_{\sigma,GAMA}$ estimator is defined as $\propto A(N,z)r_{50\%}\sigma^2$, with $A(N,z)$ calibrated on mock groups as a function of FoF richness and redshift [Robotham et al., 2011]. M_{σ}, by contrast, is $= A\sigma^{3\alpha}$, where A and α are calibrated on a sample of X-ray selected groups. The mock galaxy catalogues have been shown to have galaxy dynamics biased low relative to observations [e.g. Han et al., 2014; Robotham et al., 2011], which will, in-turn, bias high the factor A in the calibration of $M_{\sigma,GAMA}$. Some groups, such as group 100053, also show a substantial difference between the centre as defined by the Robotham et al. [2011] algorithm and that used here. This difference would also raise the observed $r_{50\%}$, resulting in further raising the dynamical mass.

As seen in Figure 4.6, of the eight groups with detected X-ray emission we see only three groups where the X-ray derived masses are consistent (within 1σ) with the interquartile range (IQR) of mass estimates. We note that only one group had its mass overpredicted by more than a factor of two using the process described in Section 4.2, group 200115. As the probability of our sample containing at least one group with an overestimated masses was 21% from binomial estimation this is not surprising. We do note, however, that the X-ray derived mass for this system is contained well within the IQR of optical mass estimators, with the GAMA masses, $M_{L,GAMA}$ and $M_{\sigma,GAMA}$, producing the largest estimates of mass by more than a factor 2.

On the other end of the scale — groups where we underestimated halo mass by a factor of two or more — we see only one group, group 200054. As our selec-

tion process did not bias against groups with substantially underestimated halo masses, the fact that we only observe one group is interesting, further illustrating the utility of the substructure tests in selecting a sample with reliable masses. Though additional optical mass estimates appear to perform better on average than the predictor mass originally used for this group, they still underestimate the group mass by more than 1σ on the X-ray mass.

Comparing the size of the IQR for each group, we see that the two groups with no apparent X-ray emission also have the broadest IQR of the sample. Examining individual mass estimates we see that the both the dynamical, M_σ, mass for these groups and overdensity based masses, M_δ and M_{δ_L}, are low compared to masses estimated from a simple count of light and number. We interpret these low overdensity masses to be representative of small, overdense regions within a larger collapsing structure. This interpretation does however introduce some tension with the results of the substructure analysis, implying that though these groups are real, they are not fully virialised. Furthermore, a similar discrepancy is observed between the overdensity and richness mass estimates for the group 300067. As already noted, this group has little diffuse emission other than a concentrated halo of emission around the central bright galaxy.

4.6 Conclusions

In a small sample of groups selected to show little optical substructure we estimate X-ray temperatures, luminosities and central gas entropies. Two of our groups are high entropy candidates with high 2σ lower limits on central gas entropy. All other groups show gas entropies consistent with the typical range of central

gas entropies observed derived from the ACCEPT entropy profiles. All entropy estimates are consistent with the range predicted by the OWLS AGN feedback model. A third group shows a corona of emission extending to $\sim$ 15 kpc but otherwise shows little other diffuse emission, though we do not classify this as a high entropy group.

We have examined the robustness of our entropy limits against uncertainties in temperature or core radius. Temperature uncertainty alone cannot account for this difference. Reducing core radius from the $0.2r_{500}$ value used to $< 0.05r_{500}$ can produce entropies consistent with the low entropy population of groups, though at this scale we would expect to see some emission comparable to a hot gas corona.

More importantly, we examine the substructure statistics used to select these groups with the deeper v06 GAMA data. These results suggest that the high entropy candidate groups are real halos, rather than spurious FoF associations. A brief comparison of galaxy based mass estimators implies that these halos show very low overdensity based masses compared to estimates based on total number or luminosity, implying that they are still collapsing

It should be noted that our two high entropy candidates were observed with the shortest exposure times. Deeper observations of these groups would help constrain the true distribution of halo gas and its entropy. Furthermore, with a larger sample selected from the more recent GAMA data releases, repeating this study should allow for better placed constraints on the true distribution gas properties independent of X-ray selection effects. Similarly, repeating this work using a serendipitous sample of GAMA groups from the *Chandra* and *XMM-Newton* archives, whilst not providing a robust statistical sample, would allow the distribution of central entropies of groups and clusters to be examined. The

influence of substructure on a broader sample could then be studied.

Chapter 5

THE EFFECT OF SUBSTRUCTURE IN GROUPS ON GALAXY BASED MASS ESTIMATES

5.1 Introduction

The dynamical and evolutionary state of groups and clusters can significantly affect their observed properties. This can propagate into halo masses estimated from these properties, impacting upon their reliability. For example, the galaxy based mass estimators described in Chapter 3, which were calibrated on a sample of X-ray selected, relaxed groups, would likely give inaccurate results when applied to groups following a major merger or prior to full collapse. Whilst this was not investigated in Chapter 3, the mass-proxy relations for the X-ray selected

sample were compared to those of a sample of mock groups selected by richness and redshift only. The results show the scatter in the mock samples' mass-proxy relations is increased relative to the calibration sample, suggesting that a more diverse range of groups will increase the observed scatter.

Attempts to quantify the dynamical state of a halo can be made by considering substructure in the distribution of their member galaxies. This was used to define an optical sample of groups for the work in Chapter 4 in which a relaxed optical sample was essential to avoid X-ray selection effects. Whilst a battery of mass estimators were applied to the resulting sample, with such a small sample selected to show little substructure, rigorously relating the impact of substructure on mass estimates was not possible.

Due to its large number of mock halos and wide range of mass estimators, the Galaxy Cluster Mass Reconstruction project [GCMR, Old et al., 2014, Old et al., submitted] presents an opportunity to examine how substructure can affect mass estimates. The GCMR project is investigating how well the masses of mock cluster halos can be recovered using a variety of galaxy based mass estimators. In addition to the mass estimators discussed in Chapter 3, methods from other participants include estimators based on cluster richness, the virial theorem and caustic techniques such as those described in Section 2.1.2, and methods based on the broader galaxy phase-space and colour distribution within clusters.

The GCMR project consists of two phases. The first [Old et al., 2014, and references therein] used an idealised (e.g. substructure-less) halo occupation distribution (HOD) to populate dark matter halos drawn from the $z = 0$ snapshot of the Bolshoi Simulation [Klypin et al., 2011] with galaxies. The galaxy catalogue and a list of the position and velocity of the 1000 richest and most massive halos

were given to project participants. Galaxy membership and halo masses were then estimated using a range of techniques. When compared to the true halo mass it was found that estimates based on richness provided the most accurate and unbiased mass estimates, echoing the results of Chapter 3.

Phase 2, on which this chapter is based, extends Phase 1 by employing more realistic models for generating the mock galaxy population. The Phase 2 mocks are also extended to higher redshifts beyond the $z = 0$ snapshot used in Phase 1 [Old, et al., submitted, and references therein]. Two mock catalogues were generated, one a more realistic extension of the HOD model from Phase 1 that includes substructure [Skibba et al., 2011], the second a semi-analytic model (SAM) of galaxy formation (based on an updated version of the Croton et al. [2006] galaxy model). Preliminary indications are that richness-based methods again produce good, low scatter mass estimates, regardless of mock construction. Naturally, the added realism of the mocks has caused scatter to increase with respect to Phase 1.

5.2 Data

The Phase 2 mocks were constructed using SAM and HOD prescriptions applied to the N-body dark matter Bolshoi simulation. The details of the prescriptions are discussed in Old, et al. (submitted, and references therein), with a brief outline in Section 1.5.4. An important consequence of the two prescriptions is their different treatment of substructure when generating galaxy populations. In the SAM prescription, substructure arises as a natural consequence of the halo merger trees, resulting in a realistic distribution of substructure within halos.

By contrast, the HOD models introduce substructure into groups as populations of non-central bright galaxies, central galaxies with a velocity bias and clumped galaxy substructures following certain distributions [Skibba et al., 2011]. As the substructure in the SAM mock has a more physical origin than for the HOD prescription, we focus this analysis on the mock lightcone generated with the SAM prescription.

As with Phase 1, participants were given a luminosity limited galaxy catalogue (cut to $M_r < -19 + 5\log(h)$) and the halo positions of 1000 groups and clusters selected as 800 of the most massive clusters with 200 of the richest remaining clusters. The cluster sample spanned a mass range of $\sim 3\times10^{13}$ $M_\odot$ to $\sim 10^{15}$ $M_\odot$ over a redshift of $0 < z < 0.15$. The full range of GCMR mass estimators were applied to the mock halos by the respective participants, though for this analysis we focus on the subset of masses estimated using the methods described in Chapter 3.

Using the mock halo positions we selected member galaxies using the volumetric (within a 1 Mpc projected aperture and 3σ velocity cut) and Friends-of-Friends (FoF) selection methods described in Chapter 3. Using the calibrated relations from Table 3.3 we estimate M_{500} using the galaxy richness, galaxy number overdensity, dynamical σ^3 and RMS radial mass estimators described in Chapter 3, assuming SDSS galaxy luminosity functions when required. For the volumetric group samples we apply a background correction to richness, and fit the galaxy number overdensity with a projected NFW distribution and a constant background term. The FoF group samples assume the FoF groups are pure and make no correction for background.

We extrapolate the estimated masses to M_{200} assuming an NFW density pro-

file [Navarro et al., 1996] and the mass-concentration relation of Duffy et al. [2008]. For a halo with mass in the range 10^{13} $M_{\odot} < M_{500} < 10^{15}$ $M_{\odot}$ this extrapolation rescales mass by a factor of $1.36 - 1.47$ at $z = 0.1$. As established in both Chapter 3 and in Old et al. [2014] the volumetric RMS radius mass estimator has little practical value. We therefore remove it from this analysis. In the Galaxy Cluster Mass Reconstruction nomenclature we label our mass estimators as **PCN**, **PCO** and **PCS** (volumetric richness, overdensity and dynamical σ^3 estimators), and **PFN**, **PFO**, **PFS** and **PFR** (FoF richness, overdensity, dynamical σ^3 and radial estimators).

5.3 Substructure Statistics

We apply seven substructure tests to the galaxy samples. For the volumetric sample we apply these only to the galaxies within 1 Mpc, whilst we use all FoF member galaxies. In addition to the three tests described in Chapter 4, the β-test, the Angular Separation Test and the Anderson-Darling test, we use four more substructure statistics drawn from the Pinkney et al. [1996] compilation, the 2D and 3D Lee Statistics, the Dressler-Shectman test and the Centroid Shift. These tests are designed to be sensitive to bimodality in the projected distribution of galaxies or in the projection and velocity distribution of galaxies (the Lee Statistic) and to local deviations from the global velocity distributions (the Dressler-Shectman and the Centroid Shift) that substructures may cause.

5.3.1 The Lee Statistic

The Lee statistic, discussed in Pinkney et al. [1996, and references therein], examines the projected distribution of galaxies for bimodality. A bimodal distribution of galaxies may be expected during cluster mergers or when two halos have been mistakenly linked together by the grouping algorithm. To determine the Lee statistic, galaxies are first projected onto a line passing through the centre of the cluster. For N galaxies with a coordinate x along this line, a galaxy is chosen to split the sample into a left and right subsample. This is repeated for all galaxies to give $N-1$ variations of a left and right subsample, requiring at least 1 galaxy in each subsample. A value L is then

$$L = \max\left(\frac{\sigma_T}{\sigma_l + \sigma_r} - 1\right) \quad , \tag{5.1}$$

where $\sigma = \sum_i (x_i - \bar{x})^2$ for all galaxies (σ_T) and galaxies on the left and right of each of the $N-1$ subsets (σ_l and σ_r respectively). Rotating this line about the cluster centre and reprojecting allows a set of L values to be found. The statistic L_{2D} being the ratio of the maximum L to the minimum L (L_{rat} in the Pinkney et al. [1996] nomenclature).

This statistic can be extended to include velocity information as the 3D Lee Statistic. Again, following Pinkney et al. [1996], the 3D Lee statistic weights the left and right clumps by their velocity dispersion, modifying Equation (5.1) as

$$L = \max\left(\frac{2\sigma_T}{\sigma_l + \sigma_r + \sigma_{vl+vr}} - 1\right) \quad , \tag{5.2}$$

where

$$\sigma_{vl+vr} = \frac{\sigma_T}{4\sigma_v}(\sigma_{vl} + \sigma_{vr}) \quad . \tag{5.3}$$

All other σ values are defined as previously (e.g. $\sigma_v = \sum_i (v_i - \bar{v})^2$). The subscript v refers to the velocity of the relevant sample.

The statistic L_{3D} is defined as per L_{2D}.

5.3.2 The Dressler-Shectman Test

The implementation of the Dressler-Shectman test (hereafter, DS test) used here is that described by [Pinkney et al., 1996]. This test is sensitive to substructures in cluster halos such as recent infalling groups whose galaxies have not yet been mixed into the halo. As a result their local kinematics will not be representative of the larger halo. For each galaxy, this test compares the mean and standard deviation of velocity $(\bar{v}_{local}, \sigma_{local})$ for the $N_{nn} = \sqrt{N}$ nearest neighbours to the global mean and standard deviation of velocity $(\bar{v}, \sigma)$, calculating a deviation quantity, δ_i, as

$$\delta_i^2 = \left(\frac{N_{nn}+1}{\sigma}\right)\left[(\bar{v}_{local} - \bar{v})^2 + (\sigma_{local} - \sigma)^2\right] \quad . \tag{5.4}$$

The DS statistic is the sum of δ_i over all galaxies.

5.3.3 The Centroid Shift

Like the DS test, the centroid shift test [Pinkney et al., 1996] looks for deviations from global properties introduced by correlated spatial and velocity distributions. In this case it examines how the centroid of the group changes as one subsets the

galaxy population by velocity, For each galaxy a weighted centroid $(\bar{x}_i, \bar{y}_i)$ is calculated using its N_{nn} nearest neighbours in velocity. Weights are $w_i = 1/\sigma_i$ where σ_i is the velocity dispersion of the N_{nn} nearest neighbours in projection. By comparison with the centroid $(\bar{x}, \bar{y})$ of the whole sample, each galaxy can be attributed a centroid shift,

$$\alpha_i = \sqrt{(\bar{x} - \bar{x}_i)^2 + (\bar{y} - \bar{y}_i)^2} \quad . \tag{5.5}$$

The final statistic, α is the mean of all α_i.

5.3.4 Normalisation

With the exception of the Anderson-Darling test, each of these are normalised against a "null hypothesis", an idealised sample with no substructure, following the prescription of Pinkney et al. [1996]. For the two dimensional tests (β-test, AST and the Lee Statistic), the null hypothesis is generated by azimuthally randomizing the galaxy distribution. This azimuthal randomisation preserves the radial distribution of the galaxy population. The 3D tests were normalised against a null hypothesis generated by either shuffling galaxy velocities (DS test and the Centroid Shift) or by both shuffling the galaxy velocities and azimuthal randomisation (3D Lee statistic).

An average value of the null hypothesis was constructed from 1000 realisations as described above. As in Chapter 4, the ratio of the measured statistic and the mean null hypothesis gives the normalised statistic, ζ where $\zeta \gg 1$ indicates the presence of substructure. The fraction of the 1000 randomisations with *more* substructure than measured for the observed group also defines the significance

of this detection. Significances are reported as, e.g. 0.99, or 99%, being highly significant.

The Anderson-Darling (AD) statistic and significance is as described in Chapter 4 and the R package, NORTEST [Gross and Ligges, 2012]. As in Chapter 4, we adopt $\zeta_{AD} = 1/p(A^2)$ as our statistic for non-Normality.

To summarise, for each group we calculate seven measures of substructure: the deviation from mirror symmetry (β); the angular separation test (AST); the 2D and 3D bimodality Lee statistics (L_{2D}, L_{3D}); the deviation of local kinematics (DS); the velocity weighted centroid shift (α); and the degree of non-Normality in the velocity histogram (AD).

5.4 Results

In the following section we discuss how substructure can affect mass estimation. We expect substructure to affect mass estimates in two ways; to introduce bias, where increasing levels of substructure systematically increase or decrease estimated masses, and to introduce scatter, where increasing levels of substructure increase the variance of estimated masses.

To define mass bias we use the log-space difference between the recovered mass ($M_{200,rec}$) and the true mass ($M_{200,true}$). For each mass estimator, each mock cluster has a residual in mass of $\Delta M = \log_{10}(M_{200,rec}) - \log_{10}(M_{200,true})$. A strong correlation between substructure and residuals is indicative of a substructure-dependent bias in the estimated mass.

To examine the relation between substructure and scatter we first bin ΔM by the log of the normalised substructure statistic. It is important to estimate the

true scatter of the population in these bins, rather than the total scatter which may have a large statistical component. We estimate the total variance in each bin and subtract from this the statistical uncertainty in estimated masses. These statistical uncertainties are due to systematic uncertainties in the mass-proxy calibration (Equation 3.19) and errors propagated from the mass proxies found using either the Poisson uncertainty (for PCN, PFN based masses) or a bootstrap analysis of the galaxy population for each cluster (for the other mass estimators). The bootstrap analysis allows us to asses the error introduced through the use of a limited sample of galaxies, a larger source of error than uncertainty in, for example, the measured velocities. We then look for any correlation between this non-statistical scatter and substructure in each bin. In some bins the scatter is dominated by the statistical uncertainty in the estimated masses. In these cases we cannot constrain the non-statistical component of scatter, and therefore remove the affected bins from the correlation analysis.

At all times we use the Spearman Rank correlation coefficient to estimate correlation. We estimate the error on the correlation coefficients through bootstrap analysis with 1000 resamples of the mass-substructure data.

5.4.1 Overall Substructure

We show the overall level of substructure in the SAM mocks in Figure 5.1. There is a clear difference between the levels of substructure in the volumetric and FoF samples. For interest, in Figures 5.2 and 5.3 we compare the substructure for the two galaxy generation models in each selection method. We can see that, regardless of the galaxy selection method, the HOD clusters generally show lower

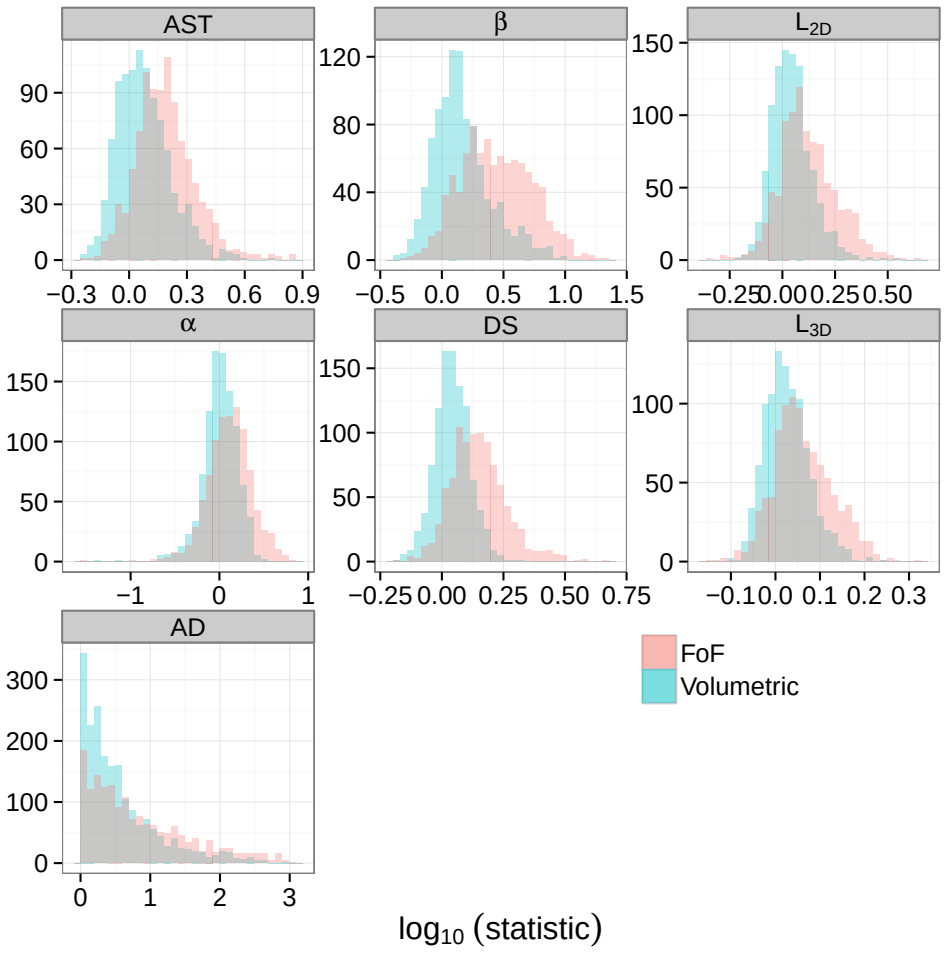

Figure 5.1: Comparison of substructure statistics for the volumetric and FoF galaxy selection. $\log(\zeta) = 0$ shows no substructure with larger values highlighting the presence of substructure in the halo.

levels of substructure compared to the SAM mock clusters.

5.4.2 Mass Bias

From Table 5.1 and Figures 5.4, 5.5, 5.6, 5.7 and 5.8, we see that the volumetric based mass estimators (PCx) show substantially less correlation with mass residuals than those of the FoF sample (PFx). However, despite showing weak

Table 5.1: Spearman Correlations between substructure statistics and mass residuals for the SAM mock samples.

Volumetric Galaxy Selection				
Statistic	PCN	PCO	PCS	Figure
β test	0.16 (>0.99)	0.15 (>0.99)	0.07 (0.98)	5.4
AST	-0.03 (0.61)	-0.03 (0.62)	0.02 (0.54)	5.4
Lee Statistic (2D)	0.10 (>0.99)	0.09 (>0.99)	0.05 (0.86)	5.4
Lee Statistic (3D)	0.10 (>0.99)	0.08 (0.99)	0.07 (0.97)	5.6
DS Test	0.16 (>0.99)	0.14 (>0.99)	0.23 (>0.99)	5.6
Centroid Shift	0.08 (0.98)	0.05 (0.90)	0.10 (>0.99)	5.6
AD	0.14 (>0.99)	0.13 (>0.99)	0.16 (>0.99)	5.8

FoF Galaxy Selection					
Statistic	PFN	PFO	PFS	PFR	Figure
β test	0.64 (>0.99)	0.18 (>0.99)	0.26 (>0.99)	0.75 (>0.99)	5.5
AST	0.38 (>0.99)	-0.03 (0.71)	0.12 (>0.99)	0.56 (>0.99)	5.5
Lee Statistic (2D)	0.52 (>0.99)	0.22 (>0.99)	0.20 (>0.99)	0.61 (>0.99)	5.5
Lee Statistic (3D)	0.53 (>0.99)	0.24 (>0.99)	0.21 (>0.99)	0.61 (>0.99)	5.7
DS Test	0.63 (>0.99)	0.32 (>0.99)	0.46 (>0.99)	0.62 (>0.99)	5.7
Centroid Shift	0.48 (>0.99)	0.22 (>0.99)	0.34 (>0.99)	0.47 (>0.99)	5.7
AD	0.45 (>0.99)	0.30 (>0.99)	0.36 (>0.99)	0.41 (>0.99)	5.8

Values in parentheses give the significance of the observed correlation.
The typical error on each correlation coefficient is ~ 0.03 from bootstrap analysis.

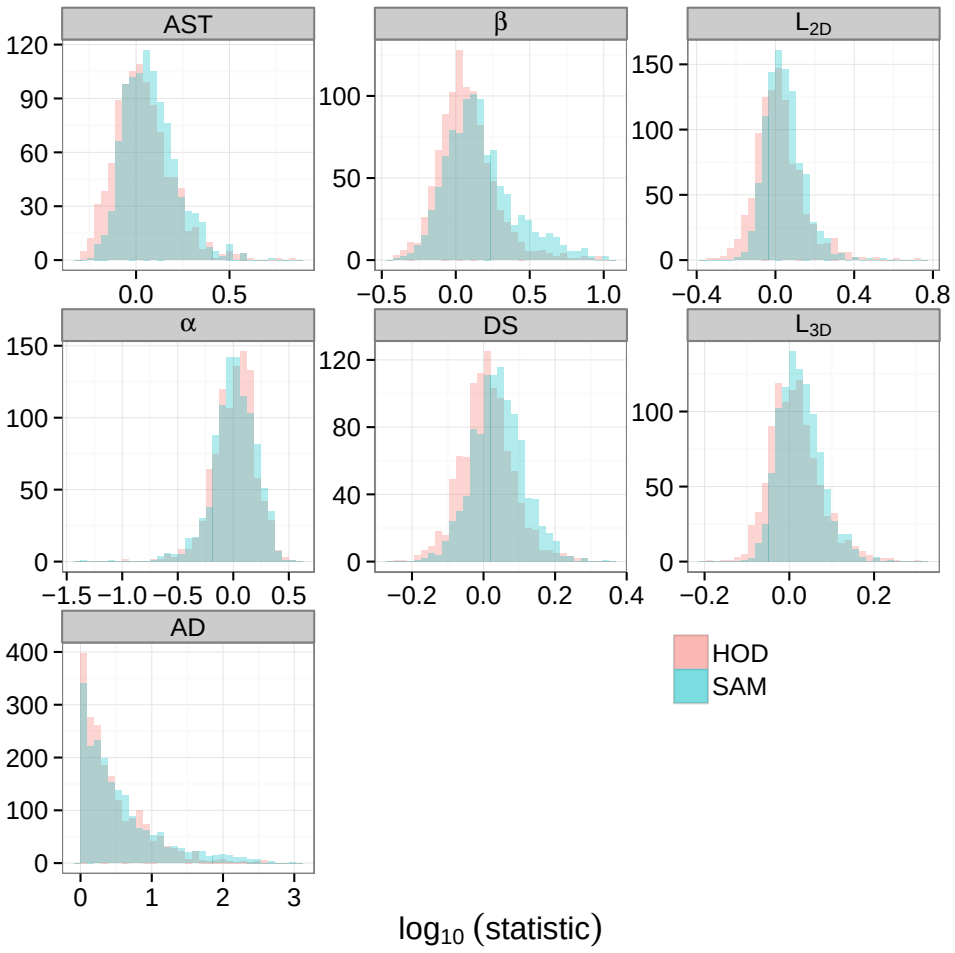

Figure 5.2: As Figure 5.1, comparing the substructure statistics for the SAM and HOD models using the volumetric sample.

levels of correlation, they are almost all highly significant. The strongest correlations observed for the volumetric sample involve the mirror symmetry statistic, β, with PCN and PCO mass estimates, and the Dressler-Shectman (DS) and Anderson-Darling (AD) tests with all PCx mass estimates. The strongest correlation observed is between the residuals of the dynamical PCS mass estimator and the DS test, though at $\rho = 0.23$, it is still fairly weak.

With the FoF sample, we again observe highly significant correlations of mass

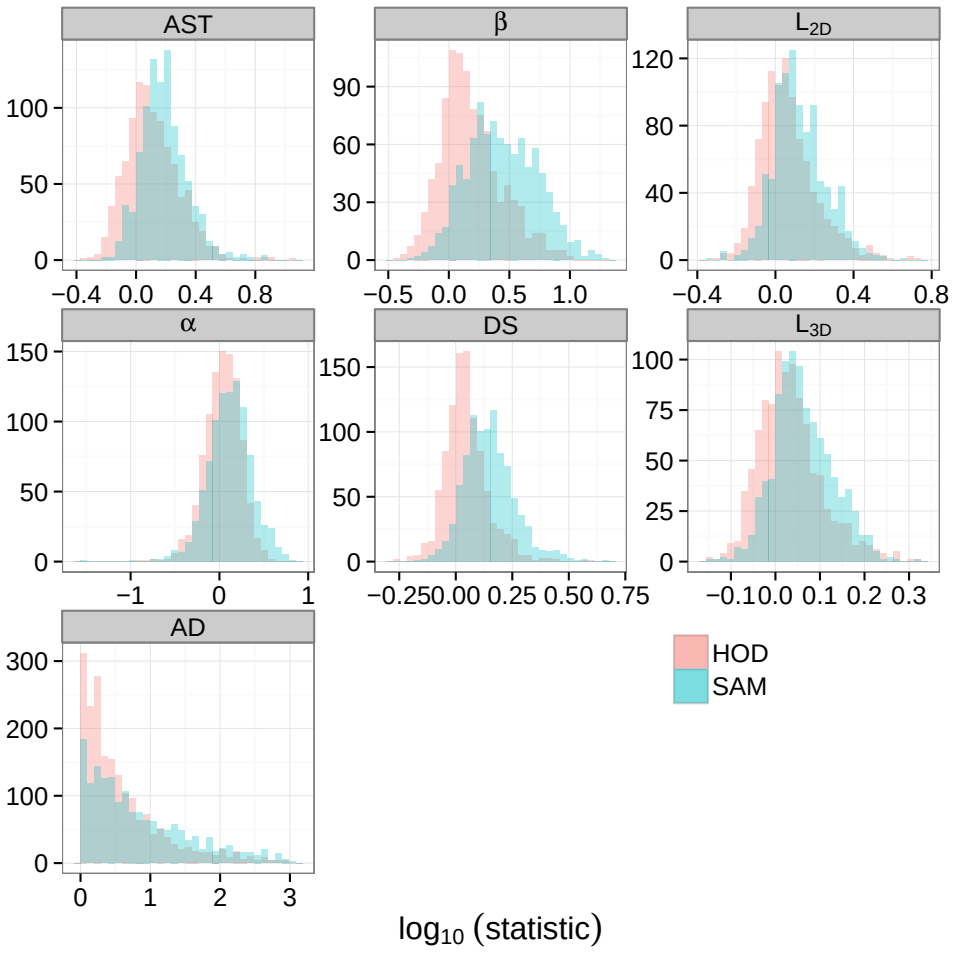

Figure 5.3: As Figure 5.1, comparing the substructure statistics for the SAM and HOD models using the FoF sample.

offsets with substructure, with bias in the number and radial based mass estimators showing the strongest correlation with substructure of any PFx mass estimator. Again, the β statistic appears to correlate well with the richness estimator, and gives the strongest result for the radial based estimator, PFR. The DS test again appears to be a good predicator of bias in all mass estimators.

The angular separation test (AST) generally shows the weakest correlation with bias in any of our mass estimators. The only exception to this is the corre-

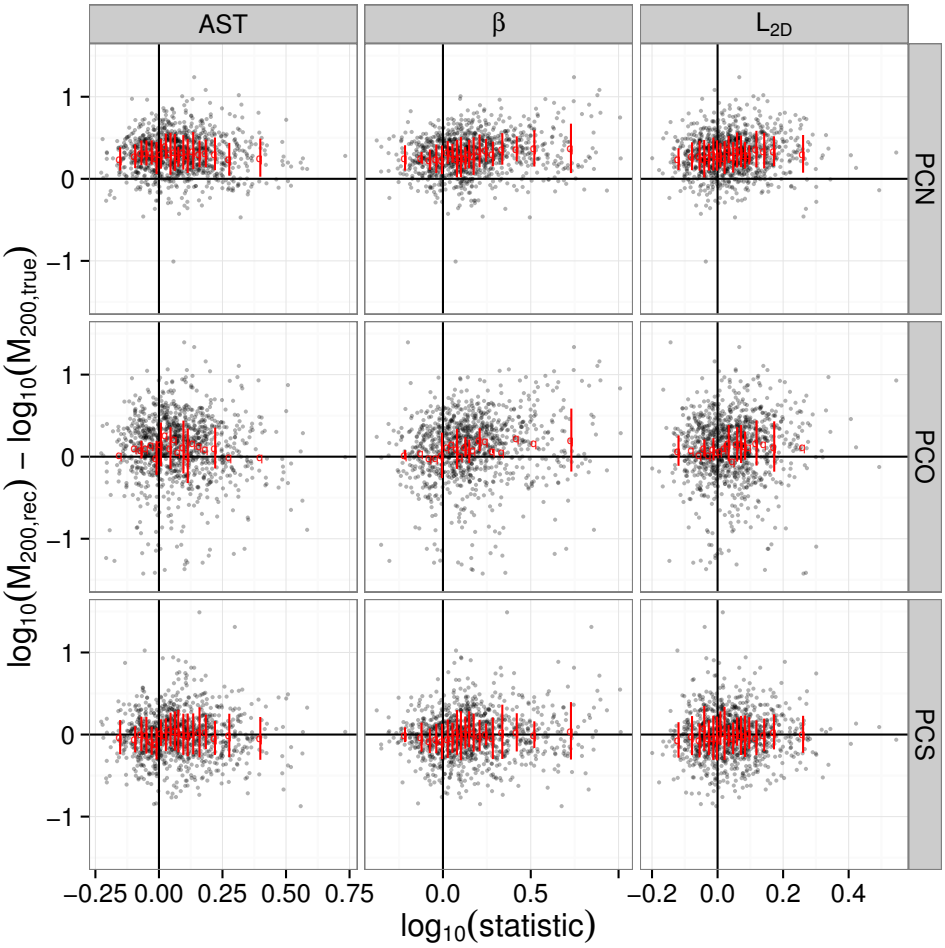

Figure 5.4: Normalised Substructure statistics against mass offset for the 2D substructure tests (β test, AST and 2D Lee Statistic) and the three mass estimators applied to the volumetric sample (PCN, PCO, PCS) from the SAM simulation. Points near the origin indicate levels of substructure comparable to the null hypothesis and no bias in mass measure. Large red points and errorbars show the binned mean and non-statistical scatter of the mass offset.

lation of AST with the FoF radial mass estimator.

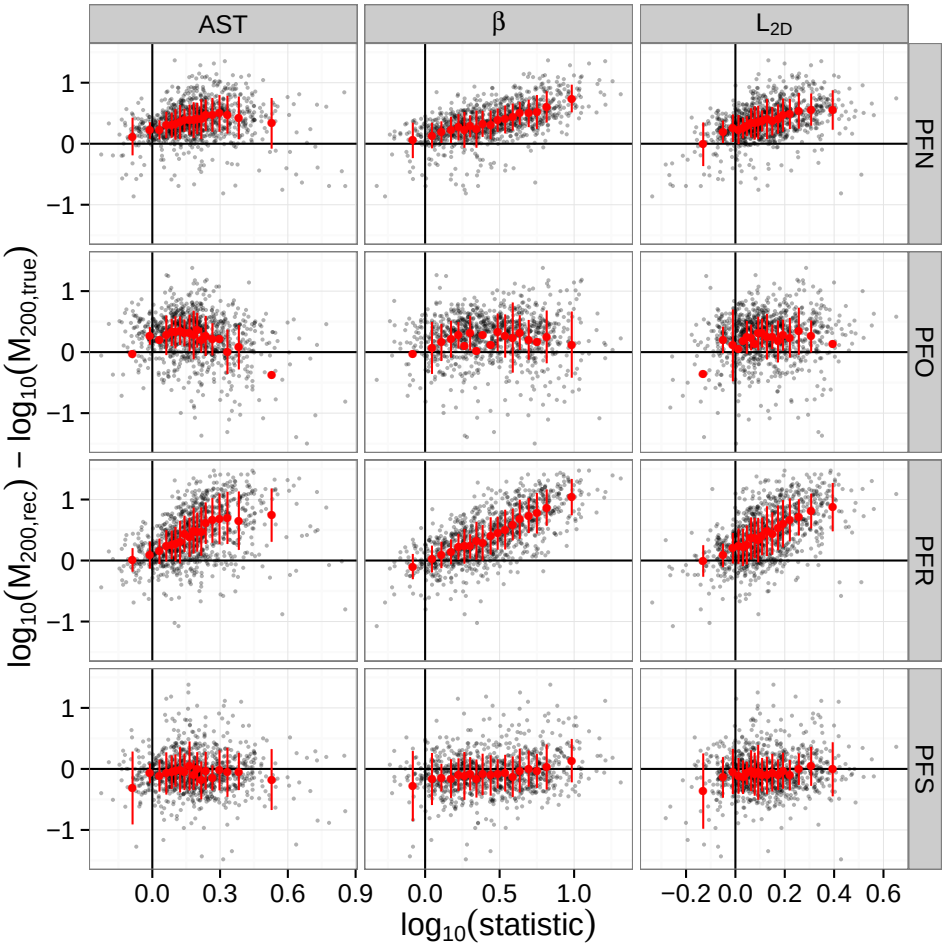

Figure 5.5: Normalised Substructure statistics against mass offset for the 2D substructure tests (β test, AST and 2D Lee Statistic) and the four mass estimators applied to the FoF sample (PFN, PFO, PFS, PFR) from the SAM simulation. Points near the origin indicate levels of substructure comparable to the null hypothesis and no bias in mass measure. Large red points and errorbars show the binned mean and non-statistical scatter of the mass offset

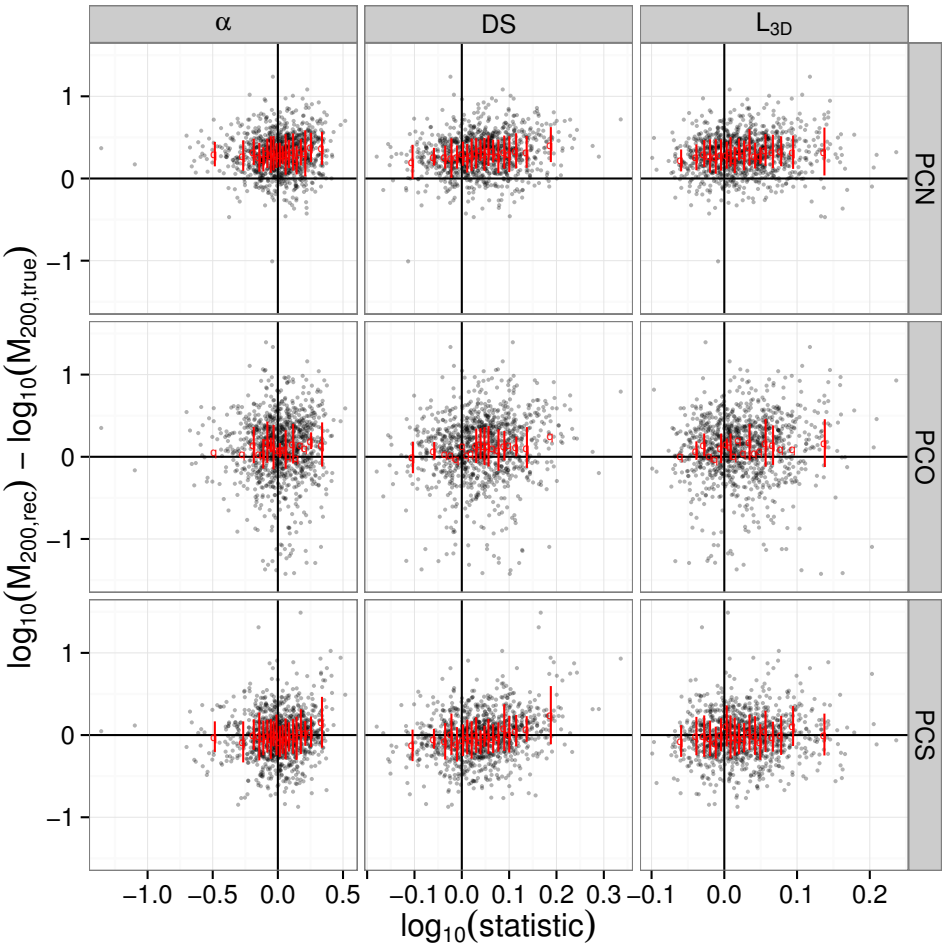

Figure 5.6: As Figure 5.4 with the 3D substructure statistics (3D Lee Statistic, DS test, Centroid Shift).

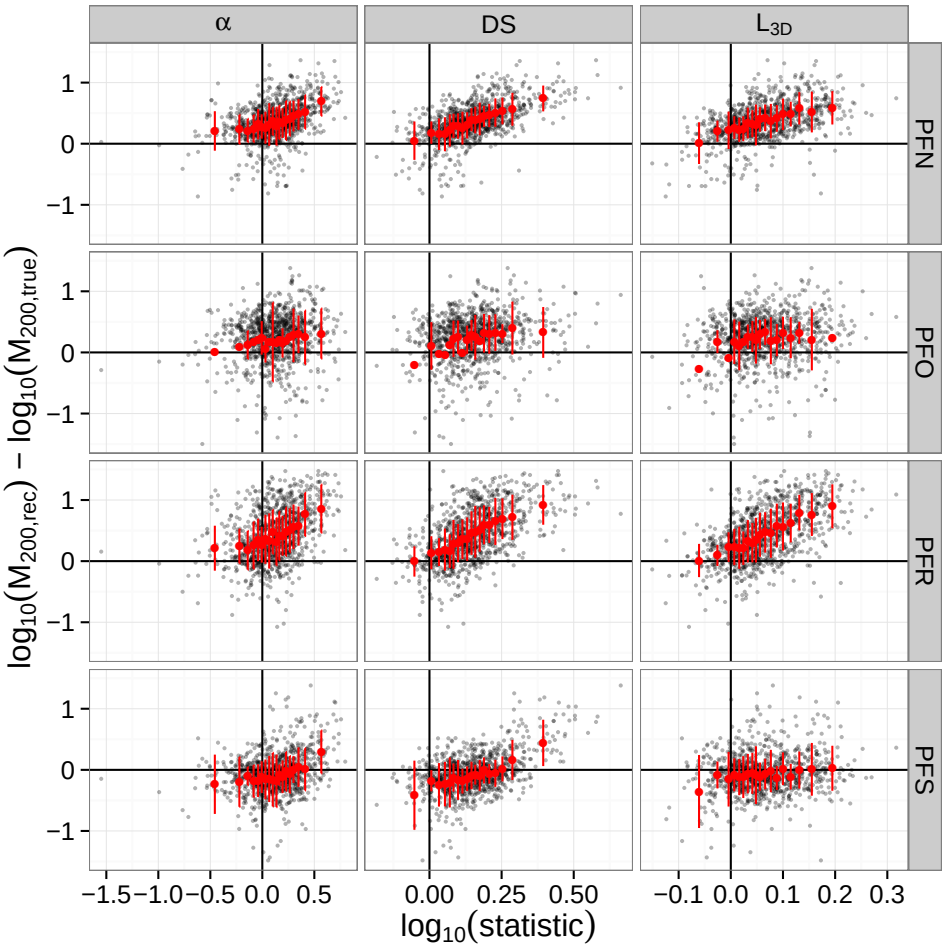

Figure 5.7: As Figure 5.5 with the 3D substructure statistics (3D Lee Statistic, DS test, Centroid Shift).

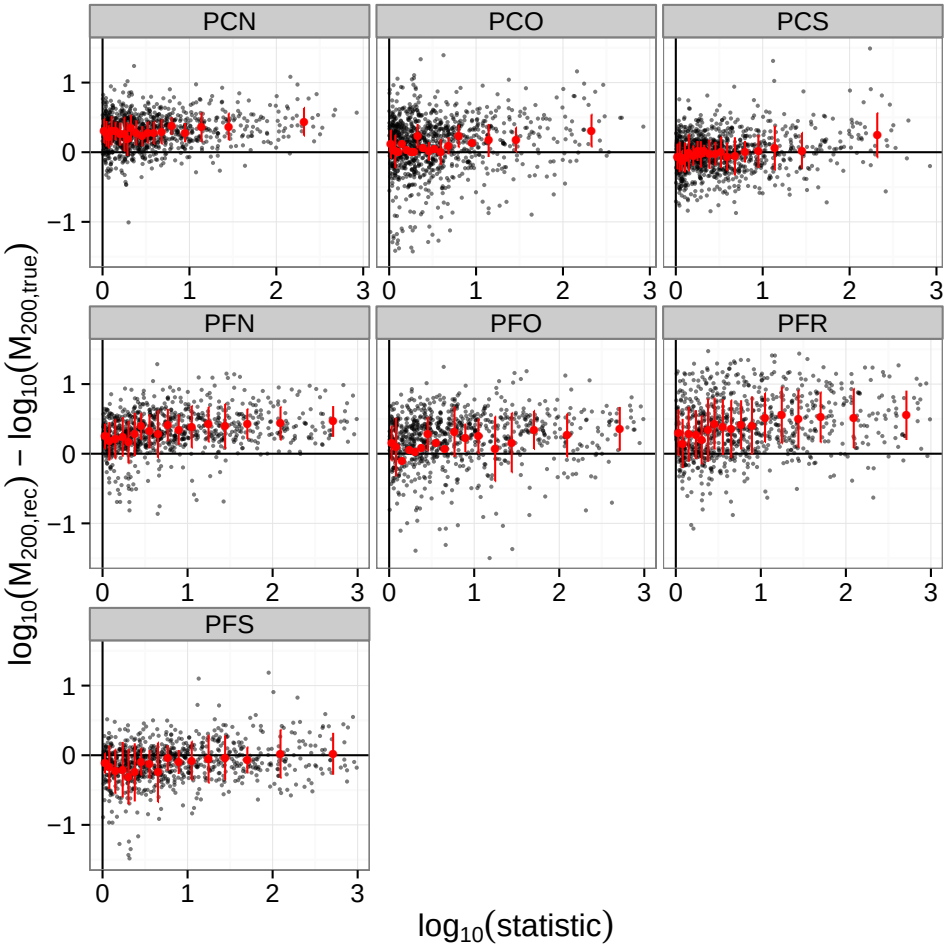

Figure 5.8: Anderson-Darling statistic and significance against mass offset for the volumetric sample (PCN, PCO, PCS) and FoF sample (PFN, PFO, PFS, PFR). Large red points and errorbars show the binned mean and standard deviation of the mass offset used to constrain the total scatter of the distribution.

5.4.3 Scatter

The correlations between substructure and the non-statistical scatter are shown in Table 5.2, with Figure 5.9 plotting the degree of non-statistical scatter observed in each bin against the mean statistic within that bin. With few exceptions we see that the majority of our mass estimators show scatter with little significant correlation with substructure. This is especially true for the groups with members identified with an FoF analysis where the measured correlation is consistent with no correlation for a large number of mass estimate – substructure test pairs. In other words, few of the types of substructure examined here have any significant impact on the scatter in mass estimates.

The most notable exception is the correlation of the angular separation test (AST). Despite showing little correlation with mass bias, the AST appears to correlate with moderate to high strengths at high significance with the scatter in most mass estimators. The only estimator where this is not true is the FoF dynamical estimator (PFS) whose correlation statistic with AST is consistent with no correlation. Whilst strong with AST, the scatter in PCO appears to be best predicted by the 2D and 3D bimodality statistic (L_{2D}, L_{3D}). The dynamical substructure (specifically the centroid shift, α) is also seen to correlate well with scatter in PFO.

In addition to correlating poorly with the AST statistic, the scatter in PFS appears to be consistent with no correlation for all substructure statistics. A slight *negative* correlation is observed with respect to the L_{2D}, L_{3D}, DS and α statistics, however they are not significant and as stated, are consistent with no correlation within $\sim 1\sigma$. A similar, highly significant negative trend is observed

Table 5.2: Spearman Correlations between substructure statistics and scatter in mass for the SAM sample.

Volumetric Galaxy Selection				
Statistic	PCN	PCO	PCS	Figure
β test	$0.45^{+0.21}_{-0.18}$ (0.95)	$0.10^{+0.53}_{-0.49}$ (0.16)	$0.46^{+0.24}_{-0.23}$ (0.95)	5.4
AST	$0.61^{+0.19}_{-0.15}$ (0.99)	$0.61^{+0.49}_{-0.39}$ (0.83)	$0.65^{+0.20}_{-0.14}$ (> 0.99)	5.4
Lee Statistic (2D)	$0.29^{+0.26}_{-0.24}$ (0.78)	$0.72^{+0.31}_{-0.19}$ (0.98)	$-0.25^{+0.17}_{-0.18}$ (0.69)	5.4
Lee Statistic (3D)	$0.40^{+0.23}_{-0.21}$ (0.91)	$0.85^{+0.22}_{-0.15}$ (0.99)	$0.21^{+0.26}_{-0.24}$ (0.61)	5.6
DS Test	$0.40^{+0.25}_{-0.24}$ (0.91)	$0.28^{+0.41}_{-0.37}$ (0.57)	$0.09^{+0.27}_{-0.26}$ (0.30)	5.6
Centroid Shift	$0.33^{+0.21}_{-0.19}$ (0.84)	$0.19^{+0.33}_{-0.30}$ (0.39)	$0.01^{+0.26}_{-0.26}$ (0.03)	5.6
AD	$-0.06^{+0.23}_{-0.23}$ (0.19)	$-0.02^{+0.37}_{-0.37}$ (0.03)	$0.49^{+0.22}_{-0.20}$ (0.97)	5.8

FoF Galaxy Selection					
Statistic	PFN	PFO	PFS	PFR	Figure
β test	$0.18^{+0.28}_{-0.23}$ (0.54)	$0.45^{+0.31}_{-0.24}$ (0.86)	$-0.04^{+0.30}_{-0.30}$ (0.12)	$0.69^{+0.14}_{-0.08}$ (> 0.99)	5.5
AST	$0.72^{+0.23}_{-0.16}$ (> 0.99)	$0.54^{+0.28}_{-0.20}$ (0.95)	$0.22^{+0.32}_{-0.25}$ (0.63)	$0.94^{+0.07}_{-0.04}$ (> 0.99)	5.5
Lee Statistic (2D)	$0.38^{+0.28}_{-0.23}$ (0.88)	$0.17^{+0.34}_{-0.31}$ (0.42)	$-0.27^{+0.25}_{-0.26}$ (0.71)	$0.59^{+0.21}_{-0.22}$ (0.99)	5.5
Lee Statistic (3D)	$0.23^{+0.32}_{-0.28}$ (0.64)	$0.14^{+0.34}_{-0.32}$ (0.36)	$-0.15^{+0.28}_{-0.26}$ (0.45)	$0.58^{+0.20}_{-0.18}$ (0.99)	5.7
DS Test	$-0.17^{+0.29}_{-0.24}$ (0.49)	$0.29^{+0.38}_{-0.31}$ (0.65)	$-0.25^{+0.30}_{-0.27}$ (0.68)	$0.48^{+0.25}_{-0.21}$ (0.95)	5.7
Centroid Shift	$0.20^{+0.27}_{-0.25}$ (0.58)	$0.57^{+0.36}_{-0.23}$ (0.88)	$-0.05^{+0.27}_{-0.28}$ (0.17)	$0.18^{+0.25}_{-0.23}$ (0.54)	5.7
AD	$0.01^{+0.22}_{-0.27}$ (0.04)	$0.22^{+0.25}_{-0.28}$ (0.52)	$0.21^{+0.24}_{-0.24}$ (0.61)	$0.23^{+0.25}_{-0.25}$ (0.65)	5.8

Values in parentheses give the significance of the observed correlation.

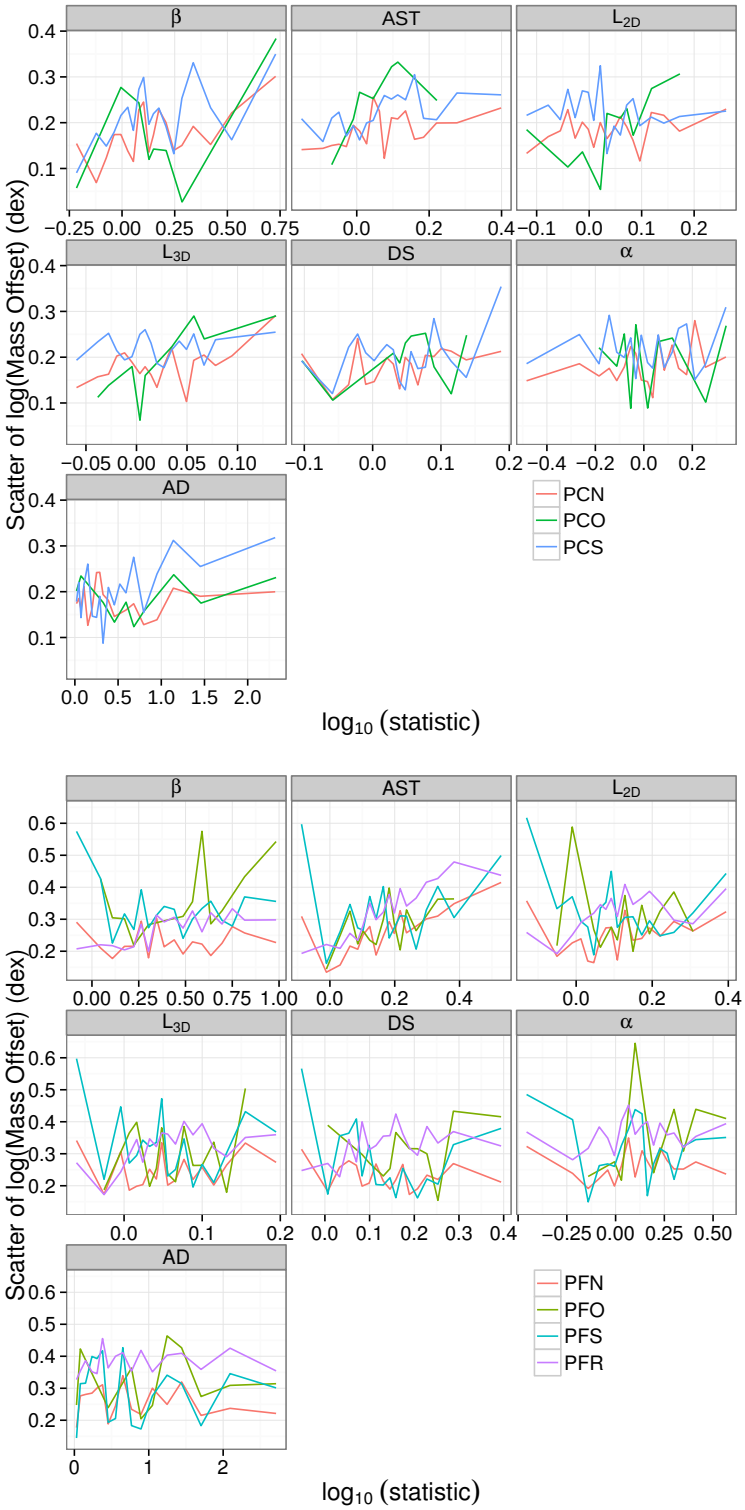

Figure 5.9: Total non-statistical scatter in each mass estimator against substructure from each statistic for the volumetric (*top*) and FoF (*bottom*) samples.

for the scatter in the volumetric dynamical mass estimator, PCS, against L_{2D}. This trend is inconsistent with no correlation with scatter.

5.5 Discussion

5.5.1 Physical Interpretation

Our observations indicate that the presence of substructure within a group can affect the quality of masses measured through galaxy based methods. This effect is clearest when correlating substructure with bias in mass estimates for a sample of FoF groups. For groups with members identified within an aperture, substructure correlates less well with bias in mass estimate. Interestingly, few substructure tests show any significant correlation with *scatter* in mass estimates. Given this difference in sample selection, and the performance of the different mass estimators and substructure statistics, it is useful to build a physical picture of what these results are telling us.

We expect substructure to relate to one of three physical circumstances: (1) incomplete virialisation, where the cluster halo is still establishing equilibrium following initial collapse; (2) early and late stage cluster mergers; (3) member selection constructing spurious groups, either linking together neighbouring, unassociated halos, or linking together field galaxies into a group. As we were given a set of known positions for our halos, the possibility of linking together chance associations of field galaxies is negligible. However, field galaxies can still significantly contaminate the galaxy membership, as can neighbouring halos.

Spurious Groups

As we have discussed in previous chapters, the FoF algorithm used here is generous in its linking properties, introducing a large interloper population. This would bias richness and radial measures, adding galaxies at large radius and may, depending on whether interlopers are isotropically distributed field galaxies, or neighbouring groups or clusters, result in biased and scattered dynamical mass estimates. This should also provide a source for symmetry and local kinematic deviations (β and DS substructures) and introduce bimodality (Lee statistic).

It is therefore probable that a large portion of the substructure observed within the FoF sample is due to contamination by these interloper galaxies. As the volumetric sample is a σ clipped selection within a fixed 1 Mpc aperture, a significant population of interloper groups are less likely to be observed. Indeed, we find over 60% of the volumetric sample are more than 75% pure within 1 Mpc (the ratio of true halo galaxies within the σ clip to all galaxies within the σ clip). The fraction of groups that are $> 75\%$ pure drops to only 12% for the FoF selection (the ratio of linked galaxies that are true halo members to all linked galaxies).

Additionally, as the contaminating galaxy population is distributed approximately uniform with radius within a σ clip [Mamon et al., 2010], we would also expect to see some dilution of substructure within the volumetric sample, reducing their measured strengths and significances (we refer back to Figure 5.1 for a comparison of substructure within a volumetric and FoF selected sample). However, as the volumetric sample is limited in radial and velocity extent, any substructures observed are more likely to represent real substructures in the group

or cluster halo, rather than spurious association from the grouping method — i.e. more likely to be representative of cases (1) and (2).

Incomplete Virialisation

Case (1), incomplete virialisation, should be somewhat more subtle in its effects on mass and substructure than we would see for spurious group selection. Lack of virialisation would be unlikely to bias mass estimators such as richness based estimators as groups would already have their full complement of galaxies, they simply have yet to fully reach equilibrium. However, this lack of equilibrium will cause bias and scatter in estimators that assume galaxy positions and velocities are distributed in a certain way, such as the overdensity and dynamical estimators.

Other than asymmetries in the galaxy distribution and non-normality in the velocity histogram, we would not expect to see any strong indications of substructure in this scenario. Assuming that the FoF member selection is accurately linking together structures, incomplete virialisation should have similar effects on both volumetric and FoF selection methods.

Mergers

The final circumstance, cluster mergers, would have effects on mass estimates and substructure measures that are comparable to the above scenarios. We make a distinction between early and late mergers to highlight the phases of a merger where clusters are infalling but yet to merge (early) and where the merger is mostly complete but a small halo of galaxies, such as the core of infallen halo, has survived and is orbiting within the larger structure (late). Without knowledge of the dark matter kinematics, early merger states should be indistinguishable from

spurious groups in lightcones such as those used here. In both merger states we would expect to see deviations from mirror symmetry and kinematic disturbances, though only early merger states should show significant bimodality.

Again, the similarity between early mergers and spurious groups should result in similar mass bias and scatter being observed. However, late mergers, where the full mass has been deposited into the halo, should show mass biases comparable to those of a system with incomplete virialisation. This form of substructure may also add to the difference between volumetric and FoF selection. Early merger states may only have one halo within the volumetric aperture, resulting in reliable mass estimates for that one halo, whilst FoF selection may link together both halos, biasing the mass estimates. Again, this would introduce substantial bimodality substructure into the FoF groups, and not into the volumetric sample.

5.5.2 Detected Substructure

Given these possibilities, are they in fact observable within the sample of groups we have? We have already indicated that the difference in bias correlation strength observed between the FoF and volumetric samples can be plausibly attributed to spurious group membership. Indeed, the strength of the correlation of mirror symmetry deviations, bimodality and local kinematic deviations with bias in richness, dynamical and radial estimators is qualitatively consistent with the spurious membership interpretation. Furthermore, if we define a purity statistic for the FoF groups as ($N_{FoF,true}/N_{FoF}$), we find a highly significant, moderate correlation of purity with substructure ($\rho = -0.32$ for mirror symmetry, -0.23 for 2D bimodality and -0.29 for the Dressler-Shectman test) indicating that the less

pure a group is, the more substructure it may show. In the volumetric sample, where purity is generally higher, these correlations are much weaker (-0.11, -0.08 and -0.07 respectively), further implying that a large degree of substructure is introduced as part of the FoF linking process.

A final check we make is to examine if these substructure statistics are acting together — i.e. if the group has spuriously linked in neighbouring halos, both mirror symmetry breaking and bimodality substructure should be apparent. We find that the mirror symmetry statistic, β, shows moderate correlation with bimodality and DS statistic of $\rho \sim 0.6$ with $> 99\%$ significance. This is much weaker in the volumetric case ($\rho \lesssim 0.25$ with $> 99\%$ significance).

Whilst the volumetric group selection provides a purer sample, it also recovers substantially less substructure than the FoF sample. Due to this and the large degree of interloper contamination with the FoF sample, it is difficult to examine the impact of other substructure scenarios without knowledge of the dynamical state of the dark matter.

The discussion so far has largely focussed on understanding bias in mass estimation in the context of substructure without much discussion of scatter. However, as shown in Section 5.4.3, our mass estimates generally show little correlation with substructure. The implication is that the types of substructure examined here preferentially bias mass estimates. Whilst it is easy to see how substructures can bias mass estimates (e.g. by adding extra galaxies or broadening velocity dispersions), it is difficult to see why they should also not introduce more scatter.

The most notable exception to this is the AST statistic which is observed to correlate well with mass scatter for most mass estimators, despite correlating

poorly with mass bias. This statistic looks for clumps of low angular separation material and is therefore similar to the mirror symmetry statistic, which examines the local projected density of galaxies. We would then expect the behaviour of the AST statistic to be comparable to the β statistic. This is clearly not the case, though β and AST are moderately correlated ($\rho \sim 0.44$ and 0.65 for the volumetric and FoF samples respectively). The implication is that there is a set of substructures that are detected by the β statistic that systematically bias mass estimates, whilst substructures detected by the AST statistic offset masses in both positive and negative directions, resulting in no net change in the average mass estimate whilst introducing considerable scatter. It is unclear why the substructure identified by the AST statistic should behave in this way.

The correlation of scatter in PCO with bimodality is potentially more understandable. Any overdensity estimator should be robust against minor substructures due to the assumptions of circular symmetry averaging over such substructures. However if substructure is a large subhalo — large enough to cause a significant bimodality result — the assumed galaxy density profile will clearly become inappropriate, introducing scatter.

5.5.3 Case study

To illustrate the difference between FoF and volumetric selection, we identify two groups in the FoF sample, one with high β statistic (deviations from mirror symmetry), and one with low β statistic. We identify Groups 205 and 951 as the high β and low β examples respectively. As these groups are at comparable redshift ($z = 0.148$ and 0.135 respectively), any differences should be related to

the properties of these groups, rather than any unaccounted for evolution in the halo. These are shown in Figure 5.10. The results of the mass and substructure estimation are shown in Table 5.3.

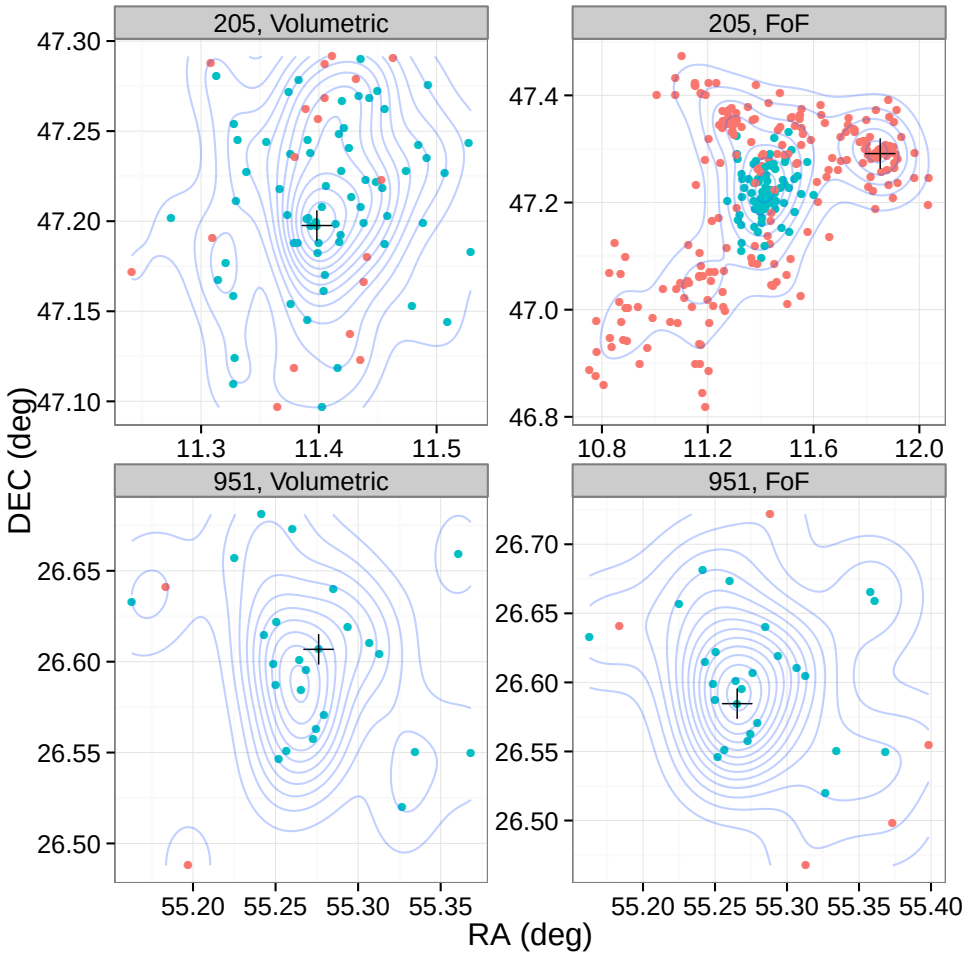

Figure 5.10: Galaxies within groups with a high FoF mirror symmetry substructure (ID 205, *top row*) and low FoF mirror symmetry substructure (ID 951, *bottom row*). Blue points show true halo member from the known SAM populations, red points show contaminating galaxies, which are a noticeably higher fraction of the FoF sample for group 205 than the volumetric sample. The faint blue contours illustrate the number density contours. Centres are marked by the black cross.

The difference between the FoF and volumetric selection for the high sub-

Table 5.3: Normalised substructure results and associated significances, and measured mass offsets for our example groups.

	205		951	
	Volumetric	FoF	Volumetric	FoF
ζ_{β}	1.21 (0.81)	20.6 (> 0.99)	1.47 (0.93)	1.00 (0.55)
ζ_{AST}	1.02 (0.56)	4.47 (> 0.99)	1.21 (0.70)	1.00 (0.51)
$\zeta_{L_{2D}}$	0.83 (0.03)	1.71 (> 0.99)	0.78 (0.14)	0.74 (0.06)
$\zeta_{L_{3D}}$	0.90 (0.02)	1.33 (> 0.99)	0.88 (0.15)	0.86 (0.06)
ζ_{DS}	1.00 (0.52)	1.65 (> 0.99)	1.12 (0.78)	1.15 (0.85)
ζ_{α}	2.04 (0.99)	2.01 (0.96)	1.46 (0.86)	1.03 (0.56)
ζ_{AD}	1.31 (0.24)	7.10 (0.86)	1.04 (0.04)	1.05 (0.05)
Bias - Richness (dex)	0.67	0.81	0.40	0.31
- Overdensity (dex)	0.62	0.22	0.50	0.54
- Dynamical (dex)	0.05	-0.22	0.01	0.08
- Radial (dex)	-	1.34	-	0.12

structure group is substantial. In fact, of the 294 galaxies identified as FoF group members for Group 205, only 26% of these galaxies are true members from the SAM realisation. There is also a marked difference in the defined centre of the group; the volumetric group uses the centre defined by the initial seed position supplied by the GCMR project; the FoF sample defines a centre iteratively using the algorithm discussed in Section 4.2.5. Mis-centring such as this will be an additional and important source of scatter for analyses such as the radial and overdensity mass estimator.

We also note that the FoF selected group 205 also shows a highly significant and large AST statistic.

5.5.4 'Grand' Substructure Statistic

Given the dramatic difference between the two groups in our case study, selecting a group sample without considering their substructure can lead to a sample heav-

ily contaminated by spurious structures. Removing such groups, preferentially selecting an unsubstructured, relaxed sample was important for the selection of groups for Chapter 4. For that selection we used substructures identified through the mirror symmetry statistic, angular separation test and the Anderson-Darling test to construct a group sample with masses based on the GAMA luminosity. Given this combination of statistics, is there a sensible way to combine them to construct a 'grand' substructure statistic?

The simplest combination to consider is a simple product of these, i.e. $\zeta' = \zeta_\beta \zeta_{AST} \zeta_{AD}$. This combination preserves the property of our statistics such that $\zeta' \approx 1$ shows no substructure and $\zeta' \gg 1$ indicates substantial substructure. We plot these the results of this combination in Figure 5.11 and with the non-statistical scatter shown in Figure 5.12

With this new statistic, we compare the strength of correlations of the grand statistic with mass offset and the scatter when binned by statistic. We again see weaker correlations with bias for the volumetric sample than for the FoF sample, with mass offset correlations of only 0.17 for PCN and 0.16 for both PCO and PCS (all $> 99\%$ significant). The FoF sample correlates with 0.57, 0.26, 0.36 and 0.60 for PFN, PFO, PFS and PFR respectively. We see scatter correlates with moderate strength in most cases (0.42 (0.93), 0.38 (0.69), 0.67 (> 0.99), 0.37 (0.88), 0.77 (> 0.99), 0.06 (0.20) and 0.85 (> 0.99) for PCN, PCO, PCS, PFN, PFO, PFS and PFR respectively). Only the scatter in PFS shows negligible correlation with scatter.

Is this grand estimator therefore an improvement over applying individual statistics? The observed correlations imply that it is at least comparable. Combining these statistics clearly allows the strengths of some substructure indicators

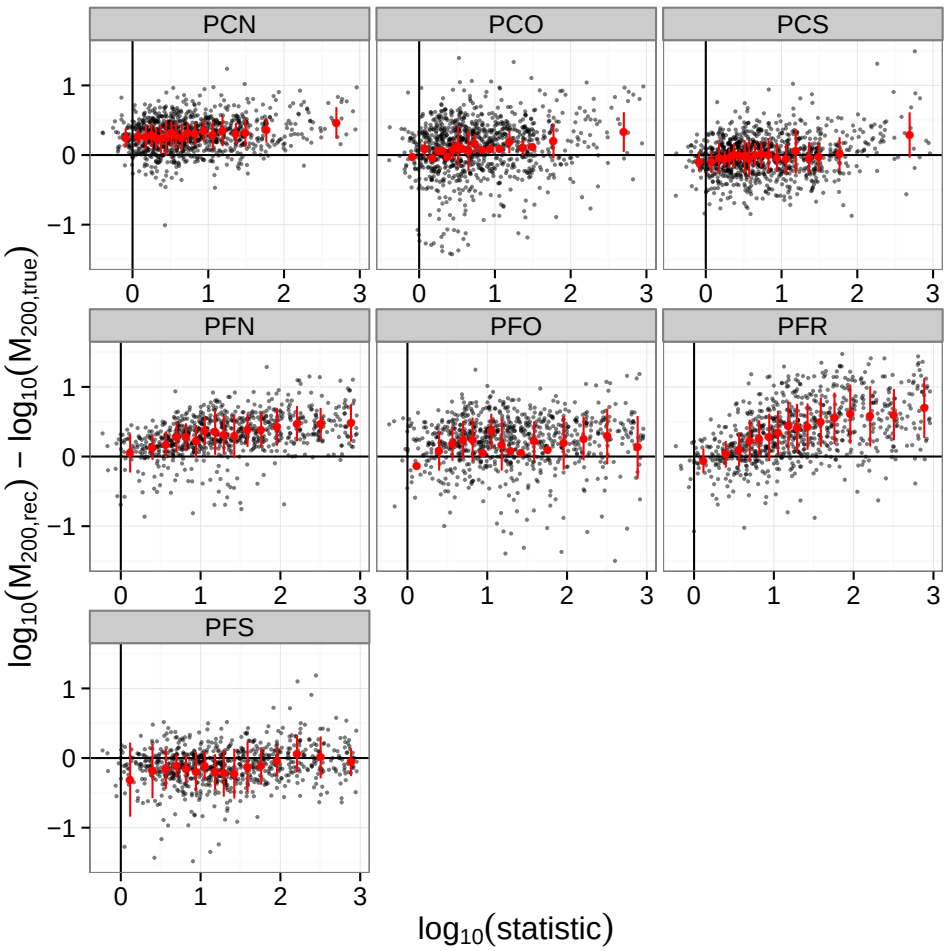

Figure 5.11: The grand substructure statistic against all mass estimators (both volumetric and FoF richness, overdensity, dynamical estimators and the FoF radial estimator). Large red points and errorbars show the binned mean and standard deviation of the mass offset used to constrain the total scatter of the distribution.

(such as β correlating well with mass bias) to balance against the weaknesses of others (e.g. the AST statistic with mass bias). Though this combination will also degrade the strong correlations observed in some cases, such as AST and scatter in PFR. The fact that this initial estimate of a grand statistic can perform comparably to most individual statistics is promising. Further work on optimising

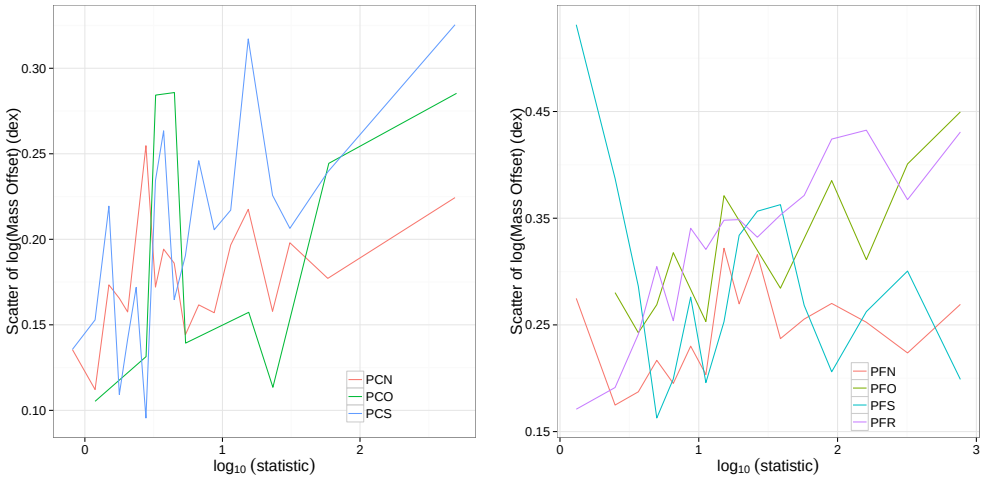

Figure 5.12: As Figure 5.9 with total non-statistical scatter in each mass estimator against the grand substructure for the volumetric (*left*) and FoF (*right*) samples.

this statistic should provide a basis for a good catch-all indicator of group or mass estimate quality that is sensitive to a range of substructure types.

5.6 Conclusion

In this Chapter we have examined the relationship between the bias and total scatter in mass estimation and the observed level of substructure in a sample of mock groups generated with a semi-analytic model of galaxy formation. Our broad conclusions are:

1. Deviations from mirror symmetry (the β statistic) and the Dressler-Shectman (DS) test correlate well with bias in most mass estimators. The DS test especially demonstrates a greater degree of correlation with the bias in dynamical PCS and PFS mass estimators whilst the β statistic correlates well with the richness based mass estimates PCN and PFN as well as the num-

ber overdensity based mass estimators PCO and PFO. Physically, this may be due to substructures from mergers or spurious associations within the volumetric aperture and FoF introducing galaxies to the halo as a coherent unit of structure. This would bias both number and the observed velocity dispersion.

2. The Angular Separation Test (AST) demonstrates the strongest correlation with scatter in mass estimates with otherwise little correlation with scatter shown for the rest of the substructure statistics. It is unclear why this is the case, especially as AST and β, for example, are similar in the substructure they look for.

3. Bias in mass estimates through galaxy overdensity (PCO and PFO) show the weakest correlation with substructure of any mass estimate. This may be due to assumptions made within the overdensity analysis, such as spherical symmetry which will average over any substructure, especially for a FoF analysis. This gives an advantage to overdensity based mass estimators, implying that they should be on average robust against substructure. In terms of scatter however, this estimator can show significant correlation with bimodality for PCO, implying subhalos can affect the scatter in PCO based mass estimates.

4. Galaxy selection is important with clusters populated with a Friends-of-Friends member selection showing a greater degree of correlation with mass bias than a simple volumetric member selection within 1 Mpc and 3σ clip in velocity. This is not unexpected; the FoF selection identifies galaxy overdensities so will be sensitive to associating nearby structures into a

group. It may also explain why the bias in FoF masses correlates better with bimodality than for the volumetric sample. A σ clip method effectively selects a cylindrical volume around a group. The combination of fixed aperture and the known, radially uniform population of interlopers [Mamon et al., 2010], will likely dilute any substructure signal from the real halo. As PCN and PCO also apply a background correction, this may also reduce any bias or scatter observed.

Given the results discussed in this work, and the results of Chapter 4, we conclude with an example 'grand' statistic. Such a statistic is one where a subset of statistics is combined into a single value with the aim of producing a single statistic that is sensitive to the range of substructure scenarios discussed here. Guided by Chapter 4, we take the product of the spatial mirror symmetry, angular separation and velocity non-normality statistics. We find that this statistic is comparable to the broad conclusions from the individual tests. Specifically it shows weak, but significant correlation with bias for the volumetric sample, independent of mass estimator, and moderate strength for the bias in FoF estimator, with PFN and PFR being the most sensitive. It also shows moderate correlation with scatter for all estimators except the FoF dynamical estimator, PFS, which we have observed is generally consistent with no correlation for individual cases. As a statistic that combines a set of spatial and velocity structure indicators, this grand statistic should show sensitivity to all forms of substructure. However no test that inherently combines this information (such as the DS test) is used.

Further work is needed to fully optimise such a grand statistic and to explore the range of combinations and methods of combination. Additionally, correlating these statistics with the full range of information available from mock halos, such

as the merger histories (e.g. the time since last major merger), would be beneficial to fully understand the physical scenarios these statistics are describing.

Chapter 6

CONCLUSIONS AND FUTURE WORK

In this thesis we have discussed the role knowledge of the masses of galaxy groups and clusters plays in understanding the assembly of structure within the universe. In Chapter 3 we demonstrated the calibration of simple scaling relations using mass proxies readily available from typical optical redshift surveys such as the Sloan Digital Sky Survey. This calibration process indicates that mass proxies based on the number of galaxies within a group (above some magnitude limit) or the galaxy number density profile (assumed to follow an NFW profile) provide the lowest scatter mass estimate. The effects of variation of star formation efficiency were examined and found to be a property we could safely fold into the mass-proxy calibration. However, we note that these richness and overdensity estimators (and similarly luminosity and luminosity overdensity mass proxies) require knowledge of the completeness of the survey as well as the global and cluster galaxy luminosity function. Dynamical masses were shown to be highly

scattered, though if the data has large uncertainties in its completeness, dynamical masses are also the only appropriate proxy. A group radius based mass proxy was also examined, however, it was found that for a volumetric selection this has no practical use due to the imposed aperture. However, if member galaxies are selected using a Friends-of-Friends (FoF) analysis this may be a useful alternative. As shown in Chapter 5 however, bias and scatter in the FoF radial estimator is highly sensitive to substructure and the quality of the grouping algorithm. We do note that whilst the specifics of a mass-FoF proxy calibration are sensitive to the tuning of the FoF algorithm used, broad conclusions are not substantially different.

A limitation of the calibration of Chapter 3 is the small sample of X-ray selected groups at low redshift. Extending this sample to both higher redshift and to a larger sample of groups and clusters may help understand these proxies and reduce their scatter. The sample could additionally be expanded using samples with caustic or lensing based masses, though extending such samples to group scale masses may be difficult.

In Chapter 4, we examined the effect of feedback on group gas. To avoid X-ray selection effects, which would result in a sample of groups less likely to show the high entropy properties predicted by hydrodynamic feedback models, we selected a sample of optical FoF groups. As an optical sample may be contaminated by unrelaxed groups, we used substructure in the distribution of member galaxies to select a sample of relaxed halos. Following observations by the *Chandra* X-ray Observatory, we find that this sample is underluminous in X-ray emission compared to an X-ray selected group sample, though most groups have low central entropies. Two groups however show remarkably high 2σ lower limits on entropy.

These two high entropy group candidates would require deeper X-ray imaging to confirm.

This study was based on a small pilot sample with *Chandra* observations of groups based on an early GAMA data release. Expanding the sample using groups from the updated, deeper GAMA database will allow further constraints to be placed on the impact of feedback on group gas. Additionally, matching GAMA groups to the *Chandra* and *XMM-Newton* archives to search for serendipitous observations, as well as the 20 deg^2 GAMA - XXL[1] overlap can be used to constrain gas properties over a diverse range of groups. A careful, substructure based group selection similar to that of Chapter 4 would allow such an archival search to retain a comparable group quality to our pilot sample. However relaxing this selection would allow a larger sample to be selected within which the impact of optical substructure on group gas could be studied.

We returned to mass proxies in Chapter 5, examining the effect substructure had on the bias — discrepancy from the true halo mass — and scatter of mass estimates on a large sample of mock groups and clusters. The largest effect noted was the impact of substructure attributed to an overly generous FoF grouping, introducing large populations of interloper galaxies or linking together neighbouring, unassociated halos. Such interlopers would inflate the measured richness and radius of a cluster, potentially also broadening its velocity dispersion. Therefore, halos with a large degree of grouping based substructure would show mass estimates biased relative to those with little. Mass bias was seen to have little relation to substructure for a sample of groups with members selected within an

[1] A large extragalactic X-ray survey mapping two 25 deg^2 fields with 10 ks observations using the *XMM-Newton* Observatory http://irfu.cea.fr/xxl.

aperture and σ clip. Interestingly, the scatter in mass estimate showed relatively little relation with substructure for any mass estimator. The notable exception to this was the correlation of scatter with substructure identified by their angular distribution.

We make a preliminary attempt at constructing a 'grand' statistic — a single statistic that is sensitive to a variety of classes of substructure — by combining the statistics used in Chapter 4 to select a group sample. This statistic, as with the individual statistics, shows reduced strength with mass bias in the aperture selected sample than for the FoF sample. Scatter however correlates well for most estimators except for those derived from FoF group dynamics. Further optimisation is needed to examine if a different combination of substructure indicators improves the performance of this grand statistic. Furthermore, as these statistics were examined for a sample of mock groups and clusters, a greater understanding can be derived from relating these statistics to the dark matter merger history of the halos. As the GCMR project used a wide variety of mass estimators, of which those discussed in Chapters 3 and 5 constituted only a third of the contributed methods, further insights could also be gained by repeating this analysis for all mass estimators contributed.

Bibliography

K. N. Abazajian, J. K. Adelman-McCarthy, M. A. Agüeros, S. S. Allam, C. Allende Prieto, D. An, K. S. J. Anderson, S. F. Anderson, J. Annis, N. A. Bahcall, C. A. L. Bailer-Jones, J. C. Barentine, B. A. Bassett, A. C. Becker, T. C. Beers, E. F. Bell, V. Belokurov, A. A. Berlind, E. F. Berman, M. Bernardi, S. J. Bickerton, D. Bizyaev, J. P. Blakeslee, M. R. Blanton, J. J. Bochanski, W. N. Boroski, H. J. Brewington, J. Brinchmann, J. Brinkmann, R. J. Brunner, T. Budavári, L. N. Carey, S. Carliles, M. A. Carr, F. J. Castander, D. Cinabro, A. J. Connolly, I. Csabai, C. E. Cunha, P. C. Czarapata, J. R. A. Davenport, E. de Haas, B. Dilday, M. Doi, D. J. Eisenstein, M. L. Evans, N. W. Evans, X. Fan, S. D. Friedman, J. A. Frieman, M. Fukugita, B. T. Gänsicke, E. Gates, B. Gillespie, G. Gilmore, B. Gonzalez, C. F. Gonzalez, E. K. Grebel, J. E. Gunn, Z. György, P. B. Hall, P. Harding, F. H. Harris, M. Harvanek, S. L. Hawley, J. J. E. Hayes, T. M. Heckman, J. S. Hendry, G. S. Hennessy, R. B. Hindsley, J. Hoblitt, C. J. Hogan, D. W. Hogg, J. A. Holtzman, J. B. Hyde, S.-i. Ichikawa, T. Ichikawa, M. Im, Ž. Ivezić, S. Jester, L. Jiang, J. A. Johnson, A. M. Jorgensen, M. Jurić, S. M. Kent, R. Kessler, S. J. Kleinman, G. R. Knapp, K. Konishi, R. G. Kron, J. Krzesinski, N. Kuropatkin, H. Lampeitl, S. Lebedeva, M. G. Lee, Y. S. Lee, R. F. Leger, S. Lépine, N. Li, M. Lima, H. Lin, D. C. Long, C. P. Loomis, J. Loveday, R. H. Lupton, E. Magnier, O. Malanushenko, V. Malanushenko, R. Mandelbaum, B. Margon, J. P. Marriner, D. Martínez-Delgado, T. Matsubara, P. M. McGehee, T. A. McKay, A. Meiksin, H. L. Morrison, F. Mullally, J. A. Munn, T. Murphy, T. Nash, A. Nebot, E. H. Neilsen, H. J. Newberg, P. R. Newman, R. C. Nichol, T. Nicinski, M. Nieto-Santisteban, A. Nitta, S. Okamura, D. J. Oravetz, J. P. Ostriker, R. Owen, N. Padmanabhan, K. Pan, C. Park, G. Pauls, J. Peoples, W. J. Percival, J. R. Pier, A. C. Pope, D. Pourbaix, P. A. Price, N. Purger, T. Quinn, M. J. Raddick, P. R. Fiorentin, G. T. Richards, M. W. Richmond, A. G. Riess, H.-W. Rix, C. M. Rockosi, M. Sako, D. J. Schlegel, D. P. Schneider, R.-D. Scholz, M. R. Schreiber, A. D. Schwope, U. Seljak, B. Sesar, E. Sheldon, K. Shimasaku, V. C. Sibley, A. E. Simmons, T. Sivarani, J. A. Smith, M. C. Smith, V. Smolčić, S. A. Snedden, A. Stebbins, M. Steinmetz, C. Stoughton,

M. A. Strauss, M. Subba Rao, Y. Suto, A. S. Szalay, I. Szapudi, P. Szkody, M. Tanaka, M. Tegmark, L. F. A. Teodoro, A. R. Thakar, C. A. Tremonti, D. L. Tucker, A. Uomoto, D. E. Vanden Berk, J. Vandenberg, S. Vidrih, M. S. Vogeley, W. Voges, N. P. Vogt, Y. Wadadekar, S. Watters, D. H. Weinberg, A. A. West, S. D. M. White, B. C. Wilhite, A. C. Wonders, B. Yanny, D. R. Yocum, D. G. York, I. Zehavi, S. Zibetti, and D. B. Zucker. The Seventh Data Release of the Sloan Digital Sky Survey. *ApJS*, 182:543–558, June 2009. doi: 10.1088/0067-0049/182/2/543. 30, 70

G. O. Abell. The Distribution of Rich Clusters of Galaxies. *ApJS*, 3:211, May 1958. doi: 10.1086/190036. 24

C. P. Ahn, R. Alexandroff, C. Allende Prieto, F. Anders, S. F. Anderson, T. Anderton, B. H. Andrews, É. Aubourg, S. Bailey, F. A. Bastien, and et al. The Tenth Data Release of the Sloan Digital Sky Survey: First Spectroscopic Data from the SDSS-III Apache Point Observatory Galactic Evolution Experiment. *ApJS*, 211:17, April 2014. doi: 10.1088/0067-0049/211/2/17. 29, 67

M. G. Akritas and M. A. Bershady. Linear Regression for Astronomical Data with Measurement Errors and Intrinsic Scatter. *ApJ*, 470:706–+, October 1996. doi: 10.1086/177901. 88

C. Alard. Dark matter haloes and self-similarity. *MNRAS*, 428:340–348, January 2013. doi: 10.1093/mnras/sts041. 64

M. E. Anderson, M. Gaspari, S. D. M. White, W. Wang, and X. Dai. Unifying X-ray Scaling Relations from Galaxies to Clusters. *ArXiv e-prints*, September 2014. 168

S. Andreon and J. Bergé. Richness-mass relation self-calibration for galaxy clusters. *A&A*, 547:A117, November 2012. doi: 10.1051/0004-6361/201220115. 59

S. Andreon and P. Congdon. The insignificant evolution of the richness-mass relation of galaxy clusters. *ArXiv e-prints*, June 2014. 111

S. Andreon and M. A. Hurn. The scaling relation between richness and mass of galaxy clusters: a Bayesian approach. *MNRAS*, 404:1922–1937, June 2010. doi: 10.1111/j.1365-2966.2010.16406.x. 59, 80

M. Arnaud and A. E. Evrard. The L_X-T relation and intracluster gas fractions of X-ray clusters. *MNRAS*, 305:631–640, May 1999. doi: 10.1046/j.1365-8711.1999.02442.x. 65

B. Ascaso, B. C. Lemaux, L. M. Lubin, R. R. Gal, D. D. Kocevski, N. Rumbaugh, and G. Squires. The violent youth of bright and massive cluster galaxies and their maturation over 7 billion years. *MNRAS*, 442:589–615, July 2014. doi: 10.1093/mnras/stu877. 28

M. L. Balogh, F. R. Pearce, R. G. Bower, and S. T. Kay. Revisiting the cosmic cooling crisis. *MNRAS*, 326:1228–1234, October 2001. doi: 10.1111/j.1365-8711.2001.04667.x. 18

M. L. Balogh, I. K. Baldry, R. Nichol, C. Miller, R. Bower, and K. Glazebrook. The Bimodal Galaxy Color Distribution: Dependence on Luminosity and Environment. *ApJL*, 615:L101–L104, November 2004. doi: 10.1086/426079. 12

M. L. Balogh, P. Mazzotta, R. G. Bower, V. Eke, H. Bourdin, T. Lu, and T. Theuns. The stellar and hot gas content of low-mass galaxy clusters. *MNRAS*, 412:947–959, April 2011. doi: 10.1111/j.1365-2966.2010.17957.x. 24, 137, 163

M. Bartelmann. Arcs from a universal dark-matter halo profile. *A&A*, 313:697–702, September 1996. 60, 83

V. Baumgartner and D. Breitschwerdt. Metal enrichment of the intracluster medium: SN-driven galactic winds. *Astronomische Nachrichten*, 330:898, December 2009. doi: 10.1002/asna.200911258. 8

T. C. Beers, K. Flynn, and K. Gebhardt. Measures of location and scale for velocities in clusters of galaxies - A robust approach. *AJ*, 100:32–46, July 1990. doi: 10.1086/115487. 40, 41, 65, 72, 176

P. S. Behroozi, C. Conroy, and R. H. Wechsler. A Comprehensive Analysis of Uncertainties Affecting the Stellar Mass-Halo Mass Relation for 0 ¡ z ¡ 4. *ApJ*, 717:379–403, July 2010. doi: 10.1088/0004-637X/717/1/379. 99, 103

E. F. Bell, D. H. McIntosh, N. Katz, and M. D. Weinberg. The Optical and Near-Infrared Properties of Galaxies. I. Luminosity and Stellar Mass Functions. *ApJS*, 149:289–312, December 2003. doi: 10.1086/378847. 102

A. A. Berlind, J. Frieman, D. H. Weinberg, M. R. Blanton, M. S. Warren, K. Abazajian, R. Scranton, D. W. Hogg, R. Scoccimarro, N. A. Bahcall, J. Brinkmann, J. R. I. Gott, S. J. Kleinman, J. Krzesinski, B. C. Lee, C. J. Miller, A. Nitta, D. P. Schneider, D. L. Tucker, and I. Zehavi. Percolation Galaxy Groups and Clusters in the SDSS Redshift Survey: Identification, Catalogs, and the Multiplicity Function. *ApJS*, 167:1–25, November 2006. doi: 10.1086/508170. 71, 74

M. Birkinshaw. The Sunyaev-Zel'dovich effect. *Phys. Rep.*, 310:97–195, March 1999. doi: 10.1016/S0370-1573(98)00080-5. 50, 51

A. Biviano. Galaxy systems in the optical and infrared. *ArXiv e-prints*, November 2008. 38, 39, 40

A. Biviano, G. Murante, S. Borgani, A. Diaferio, K. Dolag, and M. Girardi. On the efficiency and reliability of cluster mass estimates based on member galaxies. *A&A*, 456:23–36, September 2006. doi: 10.1051/0004-6361:20064918. 40, 42, 65

M. R. Blanton and S. Roweis. K-Corrections and Filter Transformations in the Ultraviolet, Optical, and Near-Infrared. *AJ*, 133:734–754, February 2007. doi: 10.1086/510127. 30, 70

M. R. Blanton, D. W. Hogg, N. A. Bahcall, J. Brinkmann, M. Britton, A. J. Connolly, I. Csabai, M. Fukugita, J. Loveday, A. Meiksin, J. A. Munn, R. C. Nichol, S. Okamura, T. Quinn, D. P. Schneider, K. Shimasaku, M. A. Strauss, M. Tegmark, M. S. Vogeley, and D. H. Weinberg. The Galaxy Luminosity Function and Luminosity Density at Redshift z = 0.1. *ApJ*, 592:819–838, August 2003. doi: 10.1086/375776. 57, 74, 82, 85, 109, 128

M. R. Blanton, D. J. Schlegel, M. A. Strauss, J. Brinkmann, D. Finkbeiner, M. Fukugita, J. E. Gunn, D. W. Hogg, Ž. Ivezić, G. R. Knapp, R. H. Lupton, J. A. Munn, D. P. Schneider, M. Tegmark, and I. Zehavi. New York University Value-Added Galaxy Catalog: A Galaxy Catalog Based on New Public Surveys. *AJ*, 129:2562–2578, June 2005. doi: 10.1086/429803. 2, 30, 70, 71, 74, 75

R. G. Bower, A. J. Benson, R. Malbon, J. C. Helly, C. S. Frenk, C. M. Baugh, S. Cole, and C. G. Lacey. Breaking the hierarchy of galaxy formation. *MNRAS*, 370:645–655, August 2006. doi: 10.1111/j.1365-2966.2006.10519.x. 3, 8, 18, 31, 34, 119, 142

G. L. Bryan. Explaining the Entropy Excess in Clusters and Groups of Galaxies without Additional Heating. *ApJL*, 544:L1–L5, November 2000. doi: 10.1086/317289. 140

J. M. Budzynski, S. E. Koposov, I. G. McCarthy, S. L. McGee, and V. Belokurov. The radial distribution of galaxies in groups and clusters. *MNRAS*, 423:104–121, June 2012. doi: 10.1111/j.1365-2966.2012.20663.x. 58, 59, 60, 80, 85, 97, 98, 102, 106

J. M. Budzynski, S. E. Koposov, I. G. McCarthy, and V. Belokurov. The similarity of the stellar mass fractions of galaxy groups and clusters. *MNRAS*, 437:1362–1377, January 2014. doi: 10.1093/mnras/stt1965. 14, 62, 99, 102, 103

C. Burke, C. A. Collins, J. P. Stott, and M. Hilton. Measurement of the intracluster light at z $\sim$ 1. *MNRAS*, 425:2058–2068, September 2012. doi: 10.1111/j.1365-2966.2012.21555.x. 13

R. G. Carlberg, H. K. C. Yee, and E. Ellingson. The Average Mass and Light Profiles of Galaxy Clusters. *ApJ*, 478:462–475, March 1997a. 40

R. G. Carlberg, H. K. C. Yee, E. Ellingson, S. L. Morris, R. Abraham, P. Gravel, C. J. Pritchet, T. Smecker-Hane, F. D. A. Hartwick, J. E. Hesser, J. B. Hutchings, and J. B. Oke. The Average Mass Profile of Galaxy Clusters. *ApJL*, 485: L13, August 1997b. doi: 10.1086/310801. 40, 87

J. E. Carlstrom, G. P. Holder, and E. D. Reese. Cosmology with the Sunyaev-Zel'dovich Effect. *ARA&A*, 40:643–680, 2002. doi: 10.1146/annurev.astro.40.060401.093803. 50

W. Cash. Parameter estimation in astronomy through application of the likelihood ratio. *ApJ*, 228:939–947, March 1979. doi: 10.1086/156922. 154

K. W. Cavagnolo, M. Donahue, G. M. Voit, and M. Sun. An Entropy Threshold for Strong Hα and Radio Emission in the Cores of Galaxy Clusters. *ApJL*, 683: L107–L110, August 2008. doi: 10.1086/591665. 171

K. W. Cavagnolo, M. Donahue, G. M. Voit, and M. Sun. Intracluster Medium Entropy Profiles for a Chandra Archival Sample of Galaxy Clusters. *ApJS*, 182:12–32, May 2009. doi: 10.1088/0067-0049/182/1/12. 19, 166, 167, 169, 170, 171

A. Cavaliere and R. Fusco-Femiano. X-rays from hot plasma in clusters of galaxies. *A&A*, 49:137–144, May 1976. 10, 48, 156

M. Colless, G. Dalton, S. Maddox, W. Sutherland, P. Norberg, S. Cole, J. Bland-Hawthorn, T. Bridges, R. Cannon, C. Collins, W. Couch, N. Cross, K. Deeley, R. De Propris, S. P. Driver, G. Efstathiou, R. S. Ellis, C. S. Frenk, K. Glazebrook, C. Jackson, O. Lahav, I. Lewis, S. Lumsden, D. Madgwick, J. A. Peacock, B. A. Peterson, I. Price, M. Seaborne, and K. Taylor. The 2dF Galaxy Redshift Survey: spectra and redshifts. *MNRAS*, 328:1039–1063, December 2001. doi: 10.1046/j.1365-8711.2001.04902.x. 1, 17, 73

D. J. Croton, V. Springel, S. D. M. White, G. De Lucia, C. S. Frenk, L. Gao, A. Jenkins, G. Kauffmann, J. F. Navarro, and N. Yoshida. The many lives of active galactic nuclei: cooling flows, black holes and the luminosities and colours of galaxies. *MNRAS*, 365:11–28, January 2006. doi: 10.1111/j.1365-2966.2005.09675.x. 34, 185

R. B. D'Agostino. *Goodness-of-Fit-Techniques*. Statistics: Textbooks and Monographs. Taylor & Francis, 1986. ISBN 9780824774875. 147

M. Davis, J. Tonry, J. Huchra, and D. W. Latham. On the Virgo supercluster and the mean mass density of the universe. *ApJL*, 238:L113–L116, June 1980. doi: 10.1086/183269. 102

A. Diaferio. Mass estimation in the outer regions of galaxy clusters. *MNRAS*, 309:610–622, November 1999. doi: 10.1046/j.1365-8711.1999.02864.x. 43, 44, 45

M. Donahue, D. J. Horner, K. W. Cavagnolo, and G. M. Voit. Entropy Profiles in the Cores of Cooling Flow Clusters of Galaxies. *ApJ*, 643:730–750, June 2006. doi: 10.1086/503270. 171

S. P. Driver, D. T. Hill, L. S. Kelvin, A. S. G. Robotham, J. Liske, P. Norberg, I. K. Baldry, S. P. Bamford, A. M. Hopkins, J. Loveday, J. A. Peacock, E. Andrae, J. Bland-Hawthorn, S. Brough, M. J. I. Brown, E. Cameron, J. H. Y. Ching, M. Colless, C. J. Conselice, S. M. Croom, N. J. G. Cross, R. de Propris, S. Dye, M. J. Drinkwater, S. Ellis, A. W. Graham, M. W. Grootes, M. Gunawardhana, D. H. Jones, E. van Kampen, C. Maraston, R. C. Nichol, H. R. Parkinson, S. Phillipps, K. Pimbblet, C. C. Popescu, M. Prescott, I. G. Roseboom, E. M. Sadler, A. E. Sansom, R. G. Sharp, D. J. B. Smith, E. Taylor, D. Thomas, R. J. Tuffs, D. Wijesinghe, L. Dunne, C. S. Frenk, M. J. Jarvis, B. F. Madore, M. J. Meyer, M. Seibert, L. Staveley-Smith, W. J. Sutherland, and S. J. Warren. Galaxy and Mass Assembly (GAMA): survey diagnostics and core data release. *MNRAS*, 413:971–995, May 2011. doi: 10.1111/j.1365-2966.2010.18188.x. 17, 28, 30, 67, 118, 119, 140, 141

A. R. Duffy, J. Schaye, S. T. Kay, and C. Dalla Vecchia. Dark matter halo concentrations in the Wilkinson Microwave Anisotropy Probe year 5 cosmology. *MNRAS*, 390:L64–L68, October 2008. doi: 10.1111/j.1745-3933.2008.00537.x. 7, 98, 187

D. Eckert, S. Molendi, M. Owers, M. Gaspari, T. Venturi, L. Rudnick, S. Ettori, S. Paltani, F. Gastaldello, and M. Rossetti. The stripping of a galaxy group diving into the massive cluster A2142. *ArXiv e-prints*, August 2014. 11

V. R. Eke, C. M. Baugh, S. Cole, C. S. Frenk, P. Norberg, J. A. Peacock, I. K. Baldry, J. Bland-Hawthorn, T. Bridges, R. Cannon, M. Colless, C. Collins, W. Couch, G. Dalton, R. de Propris, S. P. Driver, G. Efstathiou, R. S. Ellis, K. Glazebrook, C. Jackson, O. Lahav, I. Lewis, S. Lumsden, S. Maddox, D. Madgwick, B. A. Peterson, W. Sutherland, and K. Taylor. Galaxy groups in

the 2dFGRS: the group-finding algorithm and the 2PIGG catalogue. *MNRAS*, 348:866–878, March 2004. doi: 10.1111/j.1365-2966.2004.07408.x. (E04). 24, 26, 40, 65, 72, 73, 74, 86, 119, 120, 163

S. Ettori. β-model and cooling flows in X-ray clusters of galaxies. *MNRAS*, 318: 1041–1046, November 2000. doi: 10.1046/j.1365-8711.2000.03664.x. 156

A. E. Evrard and J. P. Henry. Expectations for X-ray cluster observations by the ROSAT satellite. *ApJ*, 383:95–103, December 1991. doi: 10.1086/170767. 139

D. J. Fixsen. The Temperature of the Cosmic Microwave Background. *ApJ*, 707: 916–920, December 2009. doi: 10.1088/0004-637X/707/2/916. 50

Y. Fukazawa, N. Kawano, and K. Kawashima. Very High Iron Abundance of the Hot Gas around the cD Galaxy of the MKW 4 Cluster. *ApJL*, 606:L109–L113, May 2004. doi: 10.1086/421345. 150, 160

S. Giodini, D. Pierini, A. Finoguenov, G. W. Pratt, H. Boehringer, A. Leauthaud, L. Guzzo, H. Aussel, M. Bolzonella, P. Capak, M. Elvis, G. Hasinger, O. Ilbert, J. S. Kartaltepe, A. M. Koekemoer, S. J. Lilly, R. Massey, H. J. McCracken, J. Rhodes, M. Salvato, D. B. Sanders, N. Z. Scoville, S. Sasaki, V. Smolcic, Y. Taniguchi, D. Thompson, and the COSMOS Collaboration. Stellar and Total Baryon Mass Fractions in Groups and Clusters Since Redshift 1. *ApJ*, 703:982–993, September 2009. doi: 10.1088/0004-637X/703/1/982. 5, 13, 14

M. Girardi, P. Manzato, M. Mezzetti, G. Giuricin, and F. Limboz. Observational Mass-to-Light Ratio of Galaxy Systems from Poor Groups to Rich Clusters. *ApJ*, 569:720–741, April 2002. doi: 10.1086/339360. 61, 62

A. H. Gonzalez, A. I. Zabludoff, and D. Zaritsky. Intracluster Light in Nearby Galaxy Clusters: Relationship to the Halos of Brightest Cluster Galaxies. *ApJ*, 618:195–213, January 2005. doi: 10.1086/425896. 13, 82

A. H. Gonzalez, D. Zaritsky, and A. I. Zabludoff. A Census of Baryons in Galaxy Clusters and Groups. *ApJ*, 666:147–155, September 2007. doi: 10.1086/519729. 5, 13, 14, 61

A. H. Gonzalez, S. Sivanandam, A. I. Zabludoff, and D. Zaritsky. Galaxy Cluster Baryon Fractions Revisited. *ApJ*, 778:14, November 2013. doi: 10.1088/0004-637X/778/1/14. 8, 11, 13, 14, 15

N. Grevesse and A. J. Sauval. Standard Solar Composition. *SSR*, 85:161–174, May 1998. doi: 10.1023/A:1005161325181. 154

J. Gross and U. Ligges. *nortest: Tests for Normality*, 2012. URL http://CRAN.R-project.org/package=nortest. R package version 1.0-2. 145, 147, 191

J. Han, V. R. Eke, C. S. Frenk, R. Mandelbaum, P. Norberg, M. D. Schneider, J. A. Peacock, Y. Jing, I. Baldry, J. Bland-Hawthorn, S. Brough, M. J. I. Brown, and J. Loveday. Galaxy and Mass Assembly (GAMA): The halo mass of galaxy groups from maximum-likelihood weak lensing. *ArXiv e-prints*, April 2014. 126, 128, 129, 131, 136, 179

S. M. Hansen, T. A. McKay, R. H. Wechsler, J. Annis, E. S. Sheldon, and A. Kimball. Measurement of Galaxy Cluster Sizes, Radial Profiles, and Luminosity Functions from SDSS Photometric Data. *ApJ*, 633:122–137, November 2005. doi: 10.1086/444554. 57, 80, 82, 102, 108

S. F. Helsdon and T. J. Ponman. The intragroup medium in loose groups of galaxies. *MNRAS*, 315:356–370, June 2000. doi: 10.1046/j.1365-8711.2000.03396.x. 157, 166

G. Hinshaw, D. Larson, E. Komatsu, D. N. Spergel, C. L. Bennett, J. Dunkley, M. R. Nolta, M. Halpern, R. S. Hill, N. Odegard, L. Page, K. M. Smith, J. L. Weiland, B. Gold, N. Jarosik, A. Kogut, M. Limon, S. S. Meyer, G. S. Tucker, E. Wollack, and E. L. Wright. Nine-year Wilkinson Microwave Anisotropy Probe (WMAP) Observations: Cosmological Parameter Results. *ApJS*, 208:19, October 2013. doi: 10.1088/0067-0049/208/2/19. 5, 15

D. W. Hogg, M. R. Blanton, J. Brinchmann, D. J. Eisenstein, D. J. Schlegel, J. E. Gunn, T. A. McKay, H.-W. Rix, N. A. Bahcall, J. Brinkmann, and A. Meiksin. The Dependence on Environment of the Color-Magnitude Relation of Galaxies. *ApJL*, 601:L29–L32, January 2004. doi: 10.1086/381749. 12

D. W. Hogg, J. Bovy, and D. Lang. Data analysis recipes: Fitting a model to data. *ArXiv e-prints*, August 2010. 89

J. P. Huchra and M. J. Geller. Groups of galaxies. I - Nearby groups. *ApJ*, 257:423–437, June 1982. doi: 10.1086/160000. 26

P. J. Humphrey, W. Liu, and D. A. Buote. χ^2 and Poissonian Data: Biases Even in the High-Count Regime and How to Avoid Them. *ApJ*, 693:822–829, March 2009. doi: 10.1088/0004-637X/693/1/822. 154

Y. Ikebe, T. H. Reiprich, H. Böhringer, Y. Tanaka, and T. Kitayama. A new measurement of the X-ray temperature function of clusters of galaxies. *A&A*, 383:773–790, March 2002. doi: 10.1051/0004-6361:20011769. 69

L. Jiang, J. C. Helly, S. Cole, and C. S. Frenk. N-body dark matter haloes with simple hierarchical histories. *MNRAS*, 440:2115–2135, May 2014. doi: 10.1093/mnras/stu390. 119, 143

N. Kaiser. Evolution and clustering of rich clusters. *MNRAS*, 222:323–345, September 1986. 64

N. Kaiser. Evolution of clusters of galaxies. *ApJ*, 383:104–111, December 1991. doi: 10.1086/170768. 15, 140

P. M. W. Kalberla, W. B. Burton, D. Hartmann, E. M. Arnal, E. Bajaja, R. Morras, and W. G. L. Pöppel. The Leiden/Argentine/Bonn (LAB) Survey of Galactic HI. Final data release of the combined LDS and IAR surveys with improved stray-radiation corrections. *A&A*, 440:775–782, September 2005. doi: 10.1051/0004-6361:20041864. 154

B. C. Kelly. Some Aspects of Measurement Error in Linear Regression of Astronomical Data. *ApJ*, 665:1489–1506, August 2007. doi: 10.1086/519947. 88, 89

A. A. Klypin, S. Trujillo-Gomez, and J. Primack. Dark Matter Halos in the Standard Cosmological Model: Results from the Bolshoi Simulation. *ApJ*, 740: 102, October 2011. doi: 10.1088/0004-637X/740/2/102. 6, 7, 34, 184

B. P. Koester, T. A. McKay, J. Annis, R. H. Wechsler, A. E. Evrard, E. Rozo, L. Bleem, E. S. Sheldon, and D. Johnston. MaxBCG: A Red-Sequence Galaxy Cluster Finder. *ApJ*, 660:221–238, May 2007. doi: 10.1086/512092. 27

D. Koutroumpa, R. Lallement, V. Kharchenko, and A. Dalgarno. The Solar Wind Charge-eXchange Contribution to the Local Soft X-ray Background. Model to Data Comparison in the 0.1-1.0 keV Band. *SSR*, 143:217–230, March 2009. doi: 10.1007/s11214-008-9381-9. 154

A. V. Kravtsov, A. Vikhlinin, and D. Nagai. A New Robust Low-Scatter X-Ray Mass Indicator for Clusters of Galaxies. *ApJ*, 650:128–136, October 2006. doi: 10.1086/506319. 53

K. D. Kuntz and S. L. Snowden. The EPIC-MOS particle-induced background spectra. *A&A*, 478:575–596, February 2008. doi: 10.1051/0004-6361:20077912. 154

A. M. C. Le Brun, I. G. McCarthy, J. Schaye, and T. J. Ponman. Towards a realistic population of simulated galaxy groups and clusters. *MNRAS*, 441: 1270–1290, June 2014. doi: 10.1093/mnras/stu608. 50, 53, 155

A. Leauthaud, M. R. George, P. S. Behroozi, K. Bundy, J. Tinker, R. H. Wechsler, C. Conroy, A. Finoguenov, and M. Tanaka. The Integrated Stellar Content of Dark Matter Halos. *ApJ*, 746:95, February 2012. doi: 10.1088/0004-637X/746/1/95. 14, 62, 80, 99, 103

Y.-T. Lin, J. J. Mohr, and S. A. Stanford. Near-Infrared Properties of Galaxy Clusters: Luminosity as a Binding Mass Predictor and the State of Cluster Baryons. *ApJ*, 591:749–763, July 2003. doi: 10.1086/375513. 62

E. J. Lloyd-Davies, T. J. Ponman, and D. B. Cannon. The entropy and energy of intergalactic gas in galaxy clusters. *MNRAS*, 315:689–702, July 2000. doi: 10.1046/j.1365-8711.2000.03380.x. 139, 140

J. Loveday, P. Norberg, I. K. Baldry, S. P. Driver, A. M. Hopkins, J. A. Peacock, S. P. Bamford, J. Liske, J. Bland-Hawthorn, S. Brough, M. J. I. Brown, E. Cameron, C. J. Conselice, S. M. Croom, C. S. Frenk, M. Gunawardhana, D. T. Hill, D. H. Jones, L. S. Kelvin, K. Kuijken, R. C. Nichol, H. R. Parkinson, S. Phillipps, K. A. Pimbblet, C. C. Popescu, M. Prescott, A. S. G. Robotham, R. G. Sharp, W. J. Sutherland, E. N. Taylor, D. Thomas, R. J. Tuffs, E. van Kampen, and D. Wijesinghe. Galaxy and Mass Assembly (GAMA): ugriz galaxy luminosity functions. *MNRAS*, 420:1239–1262, February 2012. doi: 10.1111/j.1365-2966.2011.20111.x. 119, 120, 128, 142

J. R. Lucey. An assessment of the completeness and correctness of the Abell catalogue. *MNRAS*, 204:33–43, July 1983. 25

A. Mahdavi, H. Hoekstra, A. Babul, C. Bildfell, T. Jeltema, and J. P. Henry. Joint Analysis of Cluster Observations. II. Chandra/XMM-Newton X-Ray and Weak Lensing Scaling Relations for a Sample of 50 Rich Clusters of Galaxies. *ApJ*, 767:116, April 2013. doi: 10.1088/0004-637X/767/2/116. 68

G. A. Mamon, A. Biviano, and G. Murante. The universal distribution of halo interlopers in projected phase space. Bias in galaxy cluster concentration and velocity anisotropy? *A&A*, 520:A30+, September 2010. doi: 10.1051/0004-6361/200913948. 25, 73, 206, 217

D. P. Marrone, G. P. Smith, J. Richard, M. Joy, M. Bonamente, N. Hasler, V. Hamilton-Morris, J.-P. Kneib, T. Culverhouse, J. E. Carlstrom, C. Greer, D. Hawkins, R. Hennessy, J. W. Lamb, E. M. Leitch, M. Loh, A. Miller, T. Mroczkowski, S. Muchovej, C. Pryke, M. K. Sharp, and D. Woody. LoCuSS: A Comparison of Sunyaev-Zel'dovich Effect and Gravitational-Lensing Measurements of Galaxy Clusters. *ApJL*, 701:L114–L118, August 2009. doi: 10.1088/0004-637X/701/2/L114. 53

D. P. Marrone, G. P. Smith, N. Okabe, M. Bonamente, J. E. Carlstrom, T. L. Culverhouse, M. Gralla, C. H. Greer, N. Hasler, D. Hawkins, R. Hennessy, M. Joy, J. W. Lamb, E. M. Leitch, R. Martino, P. Mazzotta, A. Miller, T. Mroczkowski, S. Muchovej, T. Plagge, C. Pryke, A. J. R. Sanderson, M. Takada, D. Woody, and Y. Zhang. LoCuSS: The Sunyaev-Zel'dovich Effect and Weak-lensing Mass Scaling Relation. *ApJ*, 754:119, August 2012. doi: 10.1088/0004-637X/754/2/119. 53

I. G. McCarthy, J. Schaye, T. J. Ponman, R. G. Bower, C. M. Booth, C. Dalla Vecchia, R. A. Crain, V. Springel, T. Theuns, and R. P. C. Wiersma. The case for AGN feedback in galaxy groups. *MNRAS*, 406:822–839, August 2010. doi: 10.1111/j.1365-2966.2010.16750.x. 3, 13, 18, 19, 20, 140

I. G. McCarthy, J. Schaye, R. G. Bower, T. J. Ponman, C. M. Booth, C. Dalla Vecchia, and V. Springel. Gas expulsion by quasar-driven winds as a solution to the overcooling problem in galaxy groups and clusters. *MNRAS*, 412:1965–1984, April 2011. doi: 10.1111/j.1365-2966.2010.18033.x. 18, 20, 24, 140, 169, 170

C. F. McKee and L. L. Cowie. The evaporation of spherical clouds in a hot gas. II - Effects of radiation. *ApJ*, 215:213–225, July 1977. doi: 10.1086/155350. 10, 171

T. McNaught-Roberts, P. Norberg, C. Baugh, C. Lacey, J. Loveday, J. Peacock, I. Baldry, J. Bland-Hawthorn, S. Brough, S. P. Driver, A. S. G. Robotham, and J. A. Vázquez-Mata. Galaxy And Mass Assembly (GAMA): the dependence of the galaxy luminosity function on environment, redshift and colour. *MNRAS*, 445:2125–2145, December 2014. doi: 10.1093/mnras/stu1886. 128

M. Merchán and A. Zandivarez. Galaxy groups in the 2dF Galaxy Redshift Survey: the catalogue. *MNRAS*, 335:216–222, September 2002. doi: 10.1046/j.1365-8711.2002.05623.x. 24

A. Merloni, P. Predehl, W. Becker, H. Böhringer, T. Boller, H. Brunner, M. Brusa, K. Dennerl, M. Freyberg, P. Friedrich, A. Georgakakis, F. Haberl, G. Hasinger, N. Meidinger, J. Mohr, K. Nandra, A. Rau, T. H. Reiprich, J. Robrade, M. Salvato, A. Santangelo, M. Sasaki, A. Schwope, J. Wilms, and t. German eROSITA Consortium. eROSITA Science Book: Mapping the Structure of the Energetic Universe. *ArXiv e-prints*, September 2012. 66

A. I. Merson, C. M. Baugh, J. C. Helly, V. Gonzalez-Perez, S. Cole, R. Bielby, P. Norberg, C. S. Frenk, A. J. Benson, R. G. Bower, C. G. Lacey, and C. d. P.

Lagos. Lightcone mock catalogues from semi-analytic models of galaxy formation - I. Construction and application to the BzK colour selection. *MNRAS*, 429:556–578, February 2013. doi: 10.1093/mnras/sts355. 31, 34, 118, 142

J. J. Mohr, B. Mathiesen, and A. E. Evrard. Properties of the Intracluster Medium in an Ensemble of Nearby Galaxy Clusters. *ApJ*, 517:627–649, June 1999. doi: 10.1086/307227. 49, 157

B. P. Moster, R. S. Somerville, C. Maulbetsch, F. C. van den Bosch, A. V. Macciò, T. Naab, and L. Oser. Constraints on the Relationship between Stellar Mass and Halo Mass at Low and High Redshift. *ApJ*, 710:903–923, February 2010. doi: 10.1088/0004-637X/710/2/903. 14, 62, 80, 99, 103

P. M. Motl, E. J. Hallman, J. O. Burns, and M. L. Norman. The Integrated Sunyaev-Zeldovich Effect as a Superior Method for Measuring the Mass of Clusters of Galaxies. *ApJL*, 623:L63–L66, April 2005. doi: 10.1086/430144. 52

J. S. Mulchaey. X-ray Properties of Groups of Galaxies. *ARA&A*, 38:289–335, 2000. doi: 10.1146/annurev.astro.38.1.289. 47, 49, 66

S. L. Mulroy, G. P. Smith, C. P. Haines, D. P. Marrone, N. Okabe, M. J. Pereira, E. Egami, A. Babul, A. Finoguenov, and R. Martino. LoCuSS: the near-infrared luminosity and weak-lensing mass scaling relation of galaxy clusters. *MNRAS*, 443:3309–3317, October 2014. doi: 10.1093/mnras/stu1387. 62

S. G. Murray, C. Power, and A. S. G. Robotham. How well do we know the halo mass function? *MNRAS*, 434:L61–L65, July 2013. doi: 10.1093/mnrasl/slt079. 2

D. Nagai. The Impact of Galaxy Formation on the Sunyaev-Zel'dovich Effect of Galaxy Clusters. *ApJ*, 650:538–549, October 2006. doi: 10.1086/506467. 52

R. Narayan and M. Bartelmann. Lectures on Gravitational Lensing. *ArXiv Astrophysics e-prints*, June 1996. 54, 55, 66

J. F. Navarro, C. S. Frenk, and S. D. M. White. The Structure of Cold Dark Matter Halos. *ApJ*, 462:563–+, May 1996. doi: 10.1086/177173. 6, 82, 177, 187

J. F. Navarro, C. S. Frenk, and S. D. M. White. A Universal Density Profile from Hierarchical Clustering. *ApJ*, 490:493, December 1997. doi: 10.1086/304888. 64

K. Nelson, E. T. Lau, D. Nagai, D. H. Rudd, and L. Yu. Weighing Galaxy Clusters with Gas. II. On the Origin of Hydrostatic Mass Bias in ΛCDM Galaxy Clusters. *ApJ*, 782:107, February 2014. doi: 10.1088/0004-637X/782/2/107. 68

D. M. Neumann and M. Arnaud. Self-similarity of clusters of galaxies and the L_X-T relation. *A&A*, 373:L33–L36, July 2001. doi: 10.1051/0004-6361:20010770. 65

L. Old, R. A. Skibba, F. R. Pearce, D. Croton, S. I. Muldrew, J. C. Muñoz-Cuartas, D. Gifford, M. E. Gray, A. v. der Linden, G. A. Mamon, M. R. Merrifield, V. Müller, R. J. Pearson, T. J. Ponman, A. Saro, T. Sepp, C. Sifón, E. Tempel, E. Tundo, Y. O. Wang, and R. Wojtak. Galaxy cluster mass reconstruction project - I. Methods and first results on galaxy-based techniques. *MNRAS*, 441:1513–1536, June 2014. doi: 10.1093/mnras/stu545. 34, 184, 187

J. P. F. Osmond and T. J. Ponman. The GEMS project: X-ray analysis and statistical properties of the group sample. *MNRAS*, 350:1511–1535, June 2004. doi: 10.1111/j.1365-2966.2004.07742.x. 16, 49, 65, 66, 105, 137, 166, 167

J. P. Ostriker, P. J. E. Peebles, and A. Yahil. The size and mass of galaxies, and the mass of the universe. *ApJL*, 193:L1–L4, October 1974. doi: 10.1086/181617. 102

N. Padmanabhan, U. Seljak, M. A. Strauss, M. R. Blanton, G. Kauffmann, D. J. Schlegel, C. Tremonti, N. A. Bahcall, M. Bernardi, J. Brinkmann, M. Fukugita, and Ž. Ivezić. Stellar and dynamical masses of ellipticals in the Sloan Digital Sky Survey. *New Astronomy*, 9:329–342, June 2004. doi: 10.1016/j.newast.2003.12.004. 30

N. Padmanabhan, D. J. Schlegel, D. P. Finkbeiner, J. C. Barentine, M. R. Blanton, H. J. Brewington, J. E. Gunn, M. Harvanek, D. W. Hogg, Ž. Ivezić, D. Johnston, S. M. Kent, S. J. Kleinman, G. R. Knapp, J. Krzesinski, D. Long, E. H. Neilsen, Jr., A. Nitta, C. Loomis, R. H. Lupton, S. Roweis, S. A. Snedden, M. A. Strauss, and D. L. Tucker. An Improved Photometric Calibration of the Sloan Digital Sky Survey Imaging Data. *ApJ*, 674:1217–1233, February 2008. doi: 10.1086/524677. 70

B. Panter, R. Jimenez, A. F. Heavens, and S. Charlot. The star formation histories of galaxies in the Sloan Digital Sky Survey. *MNRAS*, 378:1550–1564, July 2007. doi: 10.1111/j.1365-2966.2007.11909.x. 99, 103

L. C. Parker, M. J. Hudson, R. G. Carlberg, and H. Hoekstra. Mass-to-Light Ratios of Galaxy Groups from Weak Lensing. *ApJ*, 634:806–812, December 2005. doi: 10.1086/497117. 67

A. Pascut and T. J. Ponman. The Chandra Deep Group Survey – cool core evolution in groups and clusters of galaxies. *ArXiv e-prints*, December 2014. 153, 154, 171

J. Pinkney, K. Roettiger, J. O. Burns, and C. M. Bird. Evaluation of Statistical Tests for Substructure in Clusters of Galaxies. *ApJS*, 104:1, May 1996. doi: 10.1086/192290. 23, 144, 145, 187, 188, 189, 190

Planck Collaboration, P. A. R. Ade, N. Aghanim, M. Arnaud, M. Ashdown, J. Aumont, C. Baccigalupi, M. Baker, A. Balbi, A. J. Banday, and et al. Planck early results. I. The Planck mission. *A&A*, 536:A1, December 2011a. doi: 10.1051/0004-6361/201116464. 52

Planck Collaboration, P. A. R. Ade, N. Aghanim, M. Arnaud, M. Ashdown, J. Aumont, C. Baccigalupi, A. Balbi, A. J. Banday, R. B. Barreiro, and et al. Planck early results. VIII. The all-sky early Sunyaev-Zeldovich cluster sample. *A&A*, 536:A8, December 2011b. doi: 10.1051/0004-6361/201116459. 52

T. J. Ponman, D. B. Cannon, and J. F. Navarro. The thermal imprint of galaxy formation on X-ray clusters. *Nature*, 397:135–137, January 1999. doi: 10.1038/16410. 18, 19, 65, 139

T. J. Ponman, A. J. R. Sanderson, and A. Finoguenov. The Birmingham-CfA cluster scaling project - III. Entropy and similarity in galaxy systems. *MNRAS*, 343:331–342, July 2003. doi: 10.1046/j.1365-8711.2003.06677.x. 20

P. Popesso, H. Böhringer, M. Romaniello, and W. Voges. RASS-SDSS galaxy cluster survey. II. A unified picture of the cluster luminosity function. *A&A*, 433:415–429, April 2005. doi: 10.1051/0004-6361:20041870. 79, 108, 109, 177

P. Popesso, A. Biviano, H. Böhringer, and M. Romaniello. RASS-SDSS galaxy cluster survey. VII. On the cluster mass-to-light ratio and the halo occupation distribution. *A&A*, 464:451–464, March 2007. doi: 10.1051/0004-6361:20054708. 63, 97, 99, 100, 142

G. W. Pratt, J. H. Croston, M. Arnaud, and H. Böhringer. Galaxy cluster X-ray luminosity scaling relations from a representative local sample (REXCESS). *A&A*, 498:361–378, May 2009. doi: 10.1051/0004-6361/200810994. 166

W. H. Press and P. Schechter. Formation of Galaxies and Clusters of Galaxies by Self-Similar Gravitational Condensation. *ApJ*, 187:425–438, February 1974. doi: 10.1086/152650. 2, 4

R Development Core Team. *R: A Language and Environment for Statistical Computing*. R Foundation for Statistical Computing, Vienna, Austria, 2009. URL `http://www.R-project.org`. ISBN 3-900051-07-0. 68, 141

M. Ramella, W. Boschin, M. J. Geller, A. Mahdavi, and K. Rines. K-Band Properties of Well-Sampled Groups of Galaxies. *AJ*, 128:2022–2036, November 2004. doi: 10.1086/424862. 40, 65, 87

J. Rasmussen and T. J. Ponman. Temperature and abundance profiles of hot gas in galaxy groups - II. Implications for feedback and ICM enrichment. *MNRAS*, 399:239–263, October 2009. doi: 10.1111/j.1365-2966.2009.15244.x. 9

J. Rasmussen, T. J. Ponman, J. S. Mulchaey, T. A. Miles, and S. Raychaudhury. First results of the XI Groups Project: studying an unbiased sample of galaxy groups. *MNRAS*, 373:653–665, December 2006. doi: 10.1111/j.1365-2966.2006.11023.x. 24, 67, 137, 163

K. Rines and A. Diaferio. CIRS: Cluster Infall Regions in the Sloan Digital Sky Survey. I. Infall Patterns and Mass Profiles. *AJ*, 132:1275–1297, September 2006. doi: 10.1086/506017. 46

K. Rines, M. J. Geller, M. J. Kurtz, and A. Diaferio. CAIRNS: The Cluster and Infall Region Nearby Survey. I. Redshifts and Mass Profiles. *AJ*, 126:2152–2170, November 2003. doi: 10.1086/378599. 45, 46

A. Robotham, C. Wallace, S. Phillipps, and R. De Propris. Galaxy Luminosities in 2dF Percolation-Inferred Galaxy (2PIGG) Groups. *ApJ*, 652:1077–1084, December 2006. doi: 10.1086/508130. 108

A. Robotham, S. Phillipps, and R. de Propris. The variation of the galaxy luminosity function with group properties. *MNRAS*, 403:1812–1828, April 2010. doi: 10.1111/j.1365-2966.2010.16252.x. 80, 108, 120

A. S. G. Robotham, P. Norberg, S. P. Driver, I. K. Baldry, S. P. Bamford, A. M. Hopkins, J. Liske, J. Loveday, A. Merson, J. A. Peacock, S. Brough, E. Cameron, C. J. Conselice, S. M. Croom, C. S. Frenk, M. Gunawardhana, D. T. Hill, D. H. Jones, L. S. Kelvin, K. Kuijken, R. C. Nichol, H. R. Parkinson, K. A. Pimbblet, S. Phillipps, C. C. Popescu, M. Prescott, R. G. Sharp, W. J. Sutherland, E. N. Taylor, D. Thomas, R. J. Tuffs, E. van Kampen, and D. Wijesinghe. Galaxy and Mass Assembly (GAMA): the GAMA

galaxy group catalogue (GCv1). *MNRAS*, pages 1172–+, July 2011. doi: 10.1111/j.1365-2966.2011.19217.x. 26, 31, 40, 49, 65, 74, 86, 118, 119, 120, 125, 126, 128, 129, 132, 136, 140, 142, 143, 144, 151, 152, 159, 176, 177, 179

E. Rozo, E. S. Rykoff, B. P. Koester, T. McKay, J. Hao, A. Evrard, R. H. Wechsler, S. Hansen, E. Sheldon, D. Johnston, M. Becker, J. Annis, L. Bleem, and R. Scranton. Improvement of the Richness Estimates of maxBCG Clusters. *ApJ*, 703:601–613, September 2009. doi: 10.1088/0004-637X/703/1/601. 60, 80

E. Rozo, E. Rykoff, B. Koester, B. Nord, H.-Y. Wu, A. Evrard, and R. Wechsler. Extrinsic Sources of Scatter in the Richness-mass Relation of Galaxy Clusters. *ApJ*, 740:53, October 2011. doi: 10.1088/0004-637X/740/2/53. 60, 80

H. R. Russell, A. C. Fabian, B. R. McNamara, A. C. Edge, J. S. Sanders, P. E. J. Nulsen, S. A. Baum, M. Donahue, and C. P. O'Dea. The bow shock, cold fronts and disintegrating cool core in the merging galaxy group RX J0751.3+5012. *MNRAS*, 444:629–641, October 2014. doi: 10.1093/mnras/stu1469. 11

E. S. Rykoff, B. P. Koester, E. Rozo, J. Annis, A. E. Evrard, S. M. Hansen, J. Hao, D. E. Johnston, T. A. McKay, and R. H. Wechsler. Robust Optical Richness Estimation with Reduced Scatter. *ApJ*, 746:178, February 2012. doi: 10.1088/0004-637X/746/2/178. 60, 80

A. J. R. Sanderson and T. J. Ponman. X-ray modelling of galaxy cluster gas and mass profiles. *MNRAS*, 402:65–72, February 2010. doi: 10.1111/j.1365-2966.2009.15888.x. (SP10). 69, 70, 77, 91, 95

A. J. R. Sanderson, E. O'Sullivan, and T. J. Ponman. A statistically selected Chandra sample of 20 galaxy clusters - II. Gas properties and cool core/non-cool core bimodality. *MNRAS*, 395:764–776, May 2009. doi: 10.1111/j.1365-2966.2009.14613.x. 154

A. J. R. Sanderson, E. O'Sullivan, T. J. Ponman, A. H. Gonzalez, S. Sivanandam, A. I. Zabludoff, and D. Zaritsky. The baryon budget on the galaxy group/cluster boundary. *MNRAS*, 429:3288–3304, March 2013. doi: 10.1093/mnras/sts586. 5, 6, 8, 14, 158

C. L. Sarazin. Gas Dynamics in Clusters of Galaxies. In M. Plionis, O. López-Cruz, and D. Hughes, editors, *A Pan-Chromatic View of Clusters of Galaxies and the Large-Scale Structure*, volume 740 of *Lecture Notes in Physics, Berlin Springer Verlag*, pages 1–4020, 2008. doi: 10.1007/978-1-4020-6941-3_1. 8, 10, 19

J. Schaye, C. Dalla Vecchia, C. M. Booth, R. P. C. Wiersma, T. Theuns, M. R. Haas, S. Bertone, A. R. Duffy, I. G. McCarthy, and F. van de Voort. The physics driving the cosmic star formation history. *MNRAS*, 402:1536–1560, March 2010. doi: 10.1111/j.1365-2966.2009.16029.x. 7, 20, 140

P. Schechter. An analytic expression for the luminosity function for galaxies. *ApJ*, 203:297–306, January 1976. doi: 10.1086/154079. 60, 79

S. Schindler and A. Diaferio. Metal Enrichment Processes. *SSR*, 134:363–377, February 2008. doi: 10.1007/s11214-008-9321-8. 9

A. L. Serra, A. Diaferio, G. Murante, and S. Borgani. Measuring the escape velocity and mass profiles of galaxy clusters beyond their virial radius. *MNRAS*, 412:800–816, April 2011. doi: 10.1111/j.1365-2966.2010.17946.x. 43, 46

R. Skibba, R. K. Sheth, A. J. Connolly, and R. Scranton. The luminosity-weighted or 'marked' correlation function. *MNRAS*, 369:68–76, June 2006. doi: 10.1111/j.1365-2966.2006.10196.x. 8, 34

R. A. Skibba and R. K. Sheth. A halo model of galaxy colours and clustering in the Sloan Digital Sky Survey. *MNRAS*, 392:1080–1091, January 2009. doi: 10.1111/j.1365-2966.2008.14007.x. 34

R. A. Skibba, F. C. van den Bosch, X. Yang, S. More, H. Mo, and F. Fontanot. Are brightest halo galaxies central galaxies? *MNRAS*, 410:417–431, January 2011. doi: 10.1111/j.1365-2966.2010.17452.x. 185, 186

M. F. Skrutskie, R. M. Cutri, R. Stiening, M. D. Weinberg, S. Schneider, J. M. Carpenter, C. Beichman, R. Capps, T. Chester, J. Elias, J. Huchra, J. Liebert, C. Lonsdale, D. G. Monet, S. Price, P. Seitzer, T. Jarrett, J. D. Kirkpatrick, J. E. Gizis, E. Howard, T. Evans, J. Fowler, L. Fullmer, R. Hurt, R. Light, E. L. Kopan, K. A. Marsh, H. L. McCallon, R. Tam, S. Van Dyk, and S. Wheelock. The Two Micron All Sky Survey (2MASS). *AJ*, 131:1163–1183, February 2006. doi: 10.1086/498708. 62

N. W. Slack and T. J. Ponman. Next-generation X-ray cluster surveys. *MNRAS*, 439:102–122, March 2014. doi: 10.1093/mnras/stt2280. 16, 149, 166, 167

R. K. Smith, N. S. Brickhouse, D. A. Liedahl, and J. C. Raymond. Collisional Plasma Models with APEC/APED: Emission-Line Diagnostics of Hydrogen-like and Helium-like Ions. *ApJL*, 556:L91–L95, August 2001. doi: 10.1086/322992. 47

S. Smith. The Mass of the Virgo Cluster. *ApJ*, 83:23–+, January 1936. doi: 10.1086/143697. 37

V. Springel, S. D. M. White, A. Jenkins, C. S. Frenk, N. Yoshida, L. Gao, J. Navarro, R. Thacker, D. Croton, J. Helly, J. A. Peacock, S. Cole, P. Thomas, H. Couchman, A. Evrard, J. Colberg, and F. Pearce. Simulations of the formation, evolution and clustering of galaxies and quasars. *Nature*, 435:629–636, June 2005. doi: 10.1038/nature03597. 1, 6, 7, 31, 34, 118, 142

M. Sun, C. Jones, W. Forman, A. Vikhlinin, M. Donahue, and M. Voit. X-Ray Thermal Coronae of Galaxies in Hot Clusters: Ubiquity of Embedded Mini-Cooling Cores. *ApJ*, 657:197–231, March 2007. doi: 10.1086/510895. 172

M. Sun, G. M. Voit, M. Donahue, C. Jones, W. Forman, and A. Vikhlinin. Chandra Studies of the X-Ray Gas Properties of Galaxy Groups. *ApJ*, 693: 1142–1172, March 2009. doi: 10.1088/0004-637X/693/2/1142. (S09). i, 50, 66, 68, 69, 70, 77, 91, 95, 149, 151, 155, 160, 161, 162, 168

R. A. Sunyaev and I. B. Zeldovich. Microwave background radiation as a probe of the contemporary structure and history of the universe. *ARA&A*, 18:537–560, 1980. doi: 10.1146/annurev.aa.18.090180.002541. 50

E. Tago, J. Einasto, E. Saar, E. Tempel, M. Einasto, J. Vennik, and V. Müller. Groups of galaxies in the SDSS Data Release 5. A group-finder and a catalogue. *A&A*, 479:927–937, March 2008. doi: 10.1051/0004-6361:20078036. 41

L. S. The and S. D. M. White. The mass of the Coma cluster. *AJ*, 92:1248–1253, December 1986. doi: 10.1086/114258. 39

H. C. Thode. *Testing For Normality*. Statistics: Textbooks and Monographs. Taylor & Francis, 2002. ISBN 9780203910894. 145, 147

P. Tozzi and C. Norman. The Evolution of X-Ray Clusters and the Entropy of the Intracluster Medium. *ApJ*, 546:63–84, January 2001. doi: 10.1086/318237. 140

R. B. Tully. Nearby groups of galaxies. II - an all-sky survey within 3000 kilometers per second. *ApJ*, 321:280–304, October 1987. doi: 10.1086/165629. 1

R. van de Weygaert and J. R. Bond. Clusters and the Theory of the Cosmic Web. In M. Plionis, O. López-Cruz, and D. Hughes, editors, *A Pan-Chromatic View of Clusters of Galaxies and the Large-Scale Structure*, volume 740 of *Lecture Notes in Physics, Berlin Springer Verlag*, page 335, 2008. 4, 7, 21

M. P. van Haarlem, C. S. Frenk, and S. D. M. White. Projection effects in cluster catalogues. *MNRAS*, 287:817–832, June 1997. 25

A. Vikhlinin, W. Forman, and C. Jones. Outer Regions of the Cluster Gaseous Atmospheres. *ApJ*, 525:47–57, November 1999. doi: 10.1086/307876. 160, 163

A. Vikhlinin, M. Markevitch, S. S. Murray, C. Jones, W. Forman, and L. Van Speybroeck. Chandra Temperature Profiles for a Sample of Nearby Relaxed Galaxy Clusters. *ApJ*, 628:655–672, August 2005. doi: 10.1086/431142. 160

A. Vikhlinin, A. Kravtsov, W. Forman, C. Jones, M. Markevitch, S. S. Murray, and L. Van Speybroeck. Chandra Sample of Nearby Relaxed Galaxy Clusters: Mass, Gas Fraction, and Mass-Temperature Relation. *ApJ*, 640:691–709, April 2006. doi: 10.1086/500288. 156, 161

W. Voges, B. Aschenbach, T. Boller, H. Bräuninger, U. Briel, W. Burkert, K. Dennerl, J. Englhauser, R. Gruber, F. Haberl, G. Hartner, G. Hasinger, M. Kürster, E. Pfeffermann, W. Pietsch, P. Predehl, C. Rosso, J. H. M. M. Schmitt, J. Trümper, and H. U. Zimmermann. The ROSAT all-sky survey bright source catalogue. *A&A*, 349:389–405, September 1999. 25, 66

G. M. Voit and G. L. Bryan. Regulation of the X-ray luminosity of clusters of galaxies by cooling and supernova feedback. *Nature*, 414:425–427, November 2001. doi: 10.1038/35106523. 18, 19, 140, 166

G. M. Voit, G. L. Bryan, M. L. Balogh, and R. G. Bower. Modified Entropy Models for the Intracluster Medium. *ApJ*, 576:601–624, September 2002. doi: 10.1086/341864. 19

G. M. Voit, S. T. Kay, and G. L. Bryan. The baseline intracluster entropy profile from gravitational structure formation. *MNRAS*, 364:909–916, December 2005. doi: 10.1111/j.1365-2966.2005.09621.x. 19, 20

S. M. Weinmann, F. C. van den Bosch, X. Yang, and H. J. Mo. Properties of galaxy groups in the Sloan Digital Sky Survey - I. The dependence of colour, star formation and morphology on halo mass. *MNRAS*, 366:2–28, February 2006. doi: 10.1111/j.1365-2966.2005.09865.x. 27

M. J. West, A. Oemler, Jr., and A. Dekel. Subclustering in rich clusters of galaxies and their environs. *ApJ*, 327:1–24, April 1988. doi: 10.1086/166163. 145

K. K. S. Wu, A. C. Fabian, and P. E. J. Nulsen. Non-gravitational heating in the hierarchical formation of X-ray clusters. *MNRAS*, 318:889–912, November 2000. doi: 10.1046/j.1365-8711.2000.03828.x. 140

A. Yahil and N. V. Vidal. The Velocity Distribution of Galaxies in Clusters. *ApJ*, 214:347–350, June 1977. doi: 10.1086/155257. 22, 25, 41

H. K. C. Yee and E. Ellingson. Correlations of Richness and Global Properties in Galaxy Clusters. *ApJ*, 585:215–226, March 2003. doi: 10.1086/345929. 59

H. K. C. Yee and O. López-Cruz. A Quantitative Measure of the Richness of Galaxy Clusters. *AJ*, 117:1985–1994, May 1999. doi: 10.1086/300837. 59

D. G. York, J. Adelman, J. E. Anderson, Jr., S. F. Anderson, J. Annis, N. A. Bahcall, J. A. Bakken, R. Barkhouser, S. Bastian, E. Berman, W. N. Boroski, S. Bracker, C. Briegel, J. W. Briggs, J. Brinkmann, R. Brunner, S. Burles, L. Carey, M. A. Carr, F. J. Castander, B. Chen, P. L. Colestock, A. J. Connolly, J. H. Crocker, I. Csabai, P. C. Czarapata, J. E. Davis, M. Doi, T. Dombeck, D. Eisenstein, N. Ellman, B. R. Elms, M. L. Evans, X. Fan, G. R. Federwitz, L. Fiscelli, S. Friedman, J. A. Frieman, M. Fukugita, B. Gillespie, J. E. Gunn, V. K. Gurbani, E. de Haas, M. Haldeman, F. H. Harris, J. Hayes, T. M. Heckman, G. S. Hennessy, R. B. Hindsley, S. Holm, D. J. Holmgren, C.-h. Huang, C. Hull, D. Husby, S.-I. Ichikawa, T. Ichikawa, Ž. Ivezić, S. Kent, R. S. J. Kim, E. Kinney, M. Klaene, A. N. Kleinman, S. Kleinman, G. R. Knapp, J. Korienek, R. G. Kron, P. Z. Kunszt, D. Q. Lamb, B. Lee, R. F. Leger, S. Limmongkol, C. Lindenmeyer, D. C. Long, C. Loomis, J. Loveday, R. Lucinio, R. H. Lupton, B. MacKinnon, E. J. Mannery, P. M. Mantsch, B. Margon, P. McGehee, T. A. McKay, A. Meiksin, A. Merelli, D. G. Monet, J. A. Munn, V. K. Narayanan, T. Nash, E. Neilsen, R. Neswold, H. J. Newberg, R. C. Nichol, T. Nicinski, M. Nonino, N. Okada, S. Okamura, J. P. Ostriker, R. Owen, A. G. Pauls, J. Peoples, R. L. Peterson, D. Petravick, J. R. Pier, A. Pope, R. Pordes, A. Prosapio, R. Rechenmacher, T. R. Quinn, G. T. Richards, M. W. Richmond, C. H. Rivetta, C. M. Rockosi, K. Ruthmansdorfer, D. Sandford, D. J. Schlegel, D. P. Schneider, M. Sekiguchi, G. Sergey, K. Shimasaku, W. A. Siegmund, S. Smee, J. A. Smith, S. Snedden, R. Stone, C. Stoughton, M. A. Strauss, C. Stubbs, M. SubbaRao, A. S. Szalay, I. Szapudi, G. P. Szokoly, A. R. Thakar, C. Tremonti, D. L. Tucker, A. Uomoto, D. Vanden Berk, M. S. Vogeley, P. Waddell, S.-i. Wang, M. Watanabe, D. H. Weinberg, B. Yanny, and N. Yasuda. The Sloan Digital Sky Survey: Technical Summary. *AJ*, 120:1579–1587, September 2000. doi: 10.1086/301513. 1, 2, 17, 28, 29

A. I. Zabludoff and J. S. Mulchaey. The Properties of Poor Groups of Galaxies. I. Spectroscopic Survey and Results. *ApJ*, 496:39–72, March 1998. doi: 10.1086/305355. 137

A. Zandivarez and H. J. Martínez. Luminosity function of galaxies in groups in the Sloan Digital Sky Survey Data Release 7: the dependence on mass, environment and galaxy type. *MNRAS*, 415:2553–2565, August 2011. doi: 10.1111/j.1365-2966.2011.18878.x. 80, 108

S. Zibetti, S. D. M. White, D. P. Schneider, and J. Brinkmann. Intergalactic stars in z˜ 0.25 galaxy clusters: systematic properties from stacking of Sloan Digital Sky Survey imaging data. *MNRAS*, 358:949–967, April 2005. doi: 10.1111/j.1365-2966.2005.08817.x. 13, 62, 82

F. Zwicky. On the Masses of Nebulae and of Clusters of Nebulae. *ApJ*, 86:217–+, October 1937. doi: 10.1086/143864. 1, 5, 37, 61, 65